Interaction of Proteins and Ions at Different Tailor-made Solid-liquid Interfaces

A Dissertation Submitted in Partial Fulfillment for the Degree of

Doctor of Philosophy

by

Bedabrata Saha

(Roll No. 06615202)

Centre for the Environment

Indian Institute of Technology Guwahati

February – 2011

Interaction of Proteins and Ions at Different Tailor-made Solid-liquid Interfaces

A Dissertation Submitted for Partial Fulfillment for the Degree of

Doctor of Philosophy

by

Bedabrata Saha

(Roll No. 06615202)

Centre for the Environment

Indian Institute of Technology Guwahati

February – 2011

Dedicated to my Parents &
Everyone Gone Through This Phase

INDIAN INSTITUTE OF TECHNOLOGY GUWAHATI

Centre for the Environment

STATEMENT

I do hereby declare that the matter embodied in this thesis is the result of investigations carried out by me in the Centre for the Environment, Indian Institute of Technology Guwahati, India, under the guidance of Dr. Gopal Das, Associate Professor (Department of Chemistry) and Dr. Saswati Chakraborty, Associate Professor (Department of Civil Engineering), Indian Institute of Technology Guwahati, India.

In keeping with the general practice of reporting scientific observations, due acknowledgements have been made wherever this work is based on the findings of other investigators.

February, 2011 (**Bedabrata Saha**)

IIT Guwahati

INDIAN INSTITUTE OF TECHNOLOGY GUWAHATI

Centre for the Environment

CERTIFICATE

This is to certify that Bedabrata Saha has been working under our supervision since July, 2006 as a regular registered Ph. D. student. His thesis entitled **"Interaction of Proteins and Ions at Different Tailor-made Solid-liquid Interfaces"** is an authentic record of the results obtained from the research work carried out under our supervision in the Centre for the Environment, Indian Institute of Technology Guwahati, Assam, India. We are forwarding his thesis to submit for the award of degree of Doctor of Philosophy, from this institute. We certify that he has fulfilled all the requirements according to the rules of this institute regarding the investigations embodied in his thesis and this work has not been submitted elsewhere for a degree.

Dr. Gopal Das
(Thesis Supervisor)
Associate Professor
Department of Chemistry
IIT Guwahati
Assam - 781 039, India

Dr. Saswati Chakraborty
(Thesis Supervisor)
Associate Professor
Department of Civil Engineering
IIT Guwahati
Assam - 781 039, India

Acknowledgement

This opportunity to extend my gratitude should commence with my parents and family. I would not have made it this far without their love and support throughout my life. I wish to express my sincere gratitude towards my PhD supervisor Dr. Gopal Das and Dr. Saswati Chakraborty. Their motivation and encouragement helped me a lot to fit into this research field, after coming from a whole different background. Their understanding, wide knowledge and personal guidance have given me freedom to think, plan and execute my ideas towards my work, which has provided a good basis for the present thesis. Their efforts always encouraged me to work together in a group by helping each other to enrich a creative environment in our lab.

Besides my supervisors, I would like to thank my doctoral committee members, Dr. Biplab Mandal, Dr. P. K. Iyer and Dr. P. K. Ghosh for their advice and suggestion. I owe my gratitude to ex-Heads of the Centre for the Environment of IIT Guwahati, Dr. M. Jawed, Dr. M. Ray and current Head, Dr. C. Mahanta, for providing me with the necessary facilities. My sincere thanks to Chandan Borgohain and K. Senapati of Central Instruments facility, IIT Guwahati for their help and in hand guidance to several analytical instruments, required during my research work. I also wish to thank department of Chemistry for providing me the necessary instrumental facilities during the entire duration of my research tenure. I wish to acknowledge the ex-staffs of the Centre for the Environment, Partha da, Monojit da, Bhaben da and present staff Deepmoni di, Jyashree di and Rupinder Singh for their cooperation.

In the way of construction of this thesis throughout the last four years as I shuttled between centre and other departments, I made several connections which will certainly stay beyond. A thanks of appreciation to my group, BO, SD, Arghya, Jiban anna, Chiru, Nazbul, Romen and specially to my seniors *Doc*. BMB and *Doc*. OV. Without the frequent brainstorming tea breaks from the 'hectic' research work and 'relaxing' weekly parties with these people, it would never be possible for me to finish.

I really had a wonderful time working in lab at our centre and a sincere thanks goes to each of my friends here, Suresh, Atreyi, Naresh, Aditi, Anand, Bharti, Biju, Sushant, Bhaskar, Samarpita and others, for their co-operation in work and sharing light moments away from the 'serious' research.

I take this opportunity to thank my seniors and friends, *Doc*. Sahu, *Doc*. Sanpui, *Doc*. Subham Paul, *Doc*. S. Sen, *Doc*. Hari, *Doc*. Anirban Karmakar, *Doc*. Achlesh, *Doc*. Rama, *Doc*. Santanu Sinha, *Doc*. Sukhu, *Doc*. Mahanty and many others who have already completed work here, for their help and sharing. I also wish to thank my friends, Krishna da, Gunin da, Kasturi, Shadab, Vijay Ravi, Souvika, Kaushik da, Naresh (Kasoju), Asim da, Ramesh (Yella), Bachha and many others, for their unconditional support and all the help they extended from time to time whenever required. I am very much thankful to all of you for making my stay at IIT Guwahati memorable, your lights and humor, without which my life would have been too philosophical.

A special thanks to all M. Sc and B. Tech batches here in IIT Guwahati, and hostel mates I came across in these four years; and also the 'tea stalls' which supplied countless cups of tea for 'brainstorming' ideas throughout these years.

Hearty thanks to Arpita, to bear with me for so long throughout this phase even in frustrating times, and for all the fun and fight I shared with her.

I would also like to thank Mahesh, for the jokes, humor we shared here, and the night walks, all of which will surely remain with me.

I would like to thank Dhiman, Omkar, Priya di & Bhaiya, for being a source of encouragement and love throughout this time.

Finally, no words would suffice to express my feelings for my B. Tech friends, Sukesh, Paria, Iman, Lee, Malu, Victor, Tapan, Kaustav, Ash, Dabbu and many others, whose love and support have so luxuriously continued to enrich my life. We had started to work on our dreams on that struggling time, when I had no clue to come in this field.

Still many names are missing whose contribution and help is worth mentioning.

Bedabrata

Synopsis

The contents of this thesis entitled **"Interaction of proteins and ions at different tailor-made solid-liquid interfaces"** have been divided into five chapters based on the results of experimental work performed during the research period.

Chapter 1 highlights the properties and significance of solid-liquid interface and its interaction with various types of molecules with an emphasis on different ionic pollutants and proteins. The static and dynamic properties of solid–liquid interfaces are being used in many scientific and technological fields. Different tailor-made solid surfaces are of importance due to their capability of interacting with specific molecules. Combined and specific interaction of proteins and different pollutants on various tailor-made surfaces is a key process in many emerging fields like environmental remediation, bio-nanotechnology, bio-separation, material science etc. When such molecules in solution are exposed to solid surfaces it often leads to adsorption. Control over the adsorption process of these molecules can be achieved by controlling the surface properties or by introducing specific functional groups. The interactions of proteins on surfaces with ionic pollutants are significantly affected by surface modification with other small molecules, polymers and or proteins. Controlled/selective adsorption of various ionic pollutants on specific solid surfaces can be useful in environmental remediation technologies. In addition with flat surfaces, tailor-made nanoparticles are also in high demand due to their greater surface area and high scale efficiency. This chapter also describes the controlled interactions of different proteins and pollutants on specific nanoparticle surface. A detail mechanistic insight of tailor specific protein–surface interactions would benefit nanoscale materials and bio-nanoassembly technologies. Moreover, the structure-function relationship of proteins at specific solid-liquid interface can be also be used for specific interaction with different pollutant molecules. Selective surface properties can be produced by surface modification with different specific proteins which generates a tunable surface for selective interaction of different ionic pollutants. The first chapter summarizes the importance of the specific surface properties on controlled interaction of proteins and pollutants. It presents a thorough review of the contribution of important physicochemical phenomena at such tailored surfaces in combination with the molecular and structural knowledge of such solid surface interface.

Chapter 2 deals with the methodology followed to synthesize and characterize different solid surfaces. It also describes the general equipments and different experimental setup used to study the interaction of different proteins and pollutants on various tailor-made solid surfaces.

Chapter 3 describes the interaction of ionic pollutants and proteins on a acidic 'hard' (according to Pearson's Hard-Soft Acid Base principle) surface, prepared by surface modification of basic alumina with Benzene-*1,3,5*-tricarboxylic acid (Trimesic acid, TMA).

This chapter is divided into two sections. The first section describes the interaction of different cationic (Cu^{2+}, Fe^{3+} and Fe^{2+}) and anionic (PO_4^{3-}) pollutants with trimesic acid coated alumina surface (Figure S1). Due to the rigidity of TMA and strong co-ordination ability of three equally spaced carboxylate groups, metal centres should strongly bind with this organic ligand. From our studies, TMA grafted alumina has shown significant efficiency on removal of toxic Cu^{2+} ion from aqueous solution. Adsorption efficiency enhanced several times upon coating of TMA compared to that obtained with bare alumina. Maximum ~90-95% removal of Cu^{2+} was achieved at pH 5.0 with 100 mg L^{-1} Cu^{2+} solution. the adsorption behaviour of Fe^{3+} and Fe^{2+} from a competitive solution with a mixture of Fe^{2+} , Fe^{3+}, Co^{2+} and Ni^{2+} was also studied. A comparative study of Fe^{3+} adsorption with Fe^{2+}, Cu^{2+}, Co^{2+} and Ni^{2+} revealed that TMA coated alumina is more selective towards Fe^{3+} compared to other ions present, which can be explained well with HSAB principle. The TMA coated alumina has also been used in removal of anionic pollutant phosphate (PO_4^{3-}), one of the major causes for eutrophication in water bodies, along with Cl^-, NO_3^- and Br^- ions. Significantly, TMA coated alumina showed a selective and very high adsorption capacity for phosphate over the other anions studied throughout a wide pH range (pH ~1.0 - 8.0) in a multi-component system. Therefore, TMA coated alumina can be used as a prospective adsorbent for the removal of both cationic and anionic major pollutants from aqueous solution.

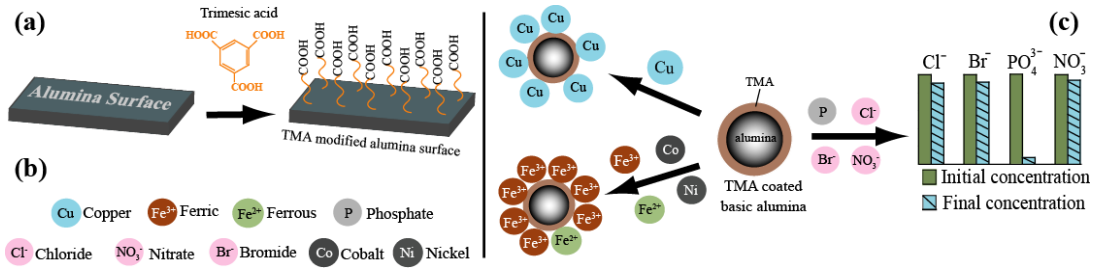

Figure S1. (a) Schematic representation of preparation of trimesic acid coated alumina surface, (b) different cationic and anionic pollutants used for adsorption study, and (c) adsorption patterns of different pollutants on TMA coated alumina.

The second section describes the competitive interaction of two different proteins, bovine serum albumin (BSA) and hen egg white lysozyme (HEWL) on TMA coated alumina surface (Figure S2). In this study we have demonstrated an efficacious approach for selective adsorption of lysozyme on TMA coated alumina at physiological pH (7.4) from a mixed solution of lysozyme and BSA. The selectivity of lysozyme adsorption can be attributed to the electrostatic interaction between surface TMA and proteins in this pH range which is affected by and isoelectric point and pK_a value of proteins and TMA molecule respectively. A binding stoichiometry of 0.86 for surface to lysozyme was obtained following the Job's plot. Selective adsorption of lysozyme was thermodynamically favourable and exothermic in nature. The adsorbed lysozyme was partially unfolded and remains in a molten-globule like structure as obtained from fluorescence spectra. However, the secondary helical structures of adsorbed lysozyme were almost retained (only ~2-3% loss in α-helical content) compared to native enzyme as analyzed from FT-IR study. Moreover, the adsorbed lysozyme was found to retain very high activity (~98%) relative to its native protein in solution. An enzymatic kinetic analysis revealed that adsorption phenomena did not affect the rate of enzymatic activity (v). Though the binding affinity of lysozyme (K_m) reduced, the rate of lysis of substrate was almost same. Therefore adsorption studies on TMA coated alumina surface can be an effective approach in tuning protein-surface interaction, where the selectivity of protein adsorption can meet with the retention of structural content and high enzymatic activity.

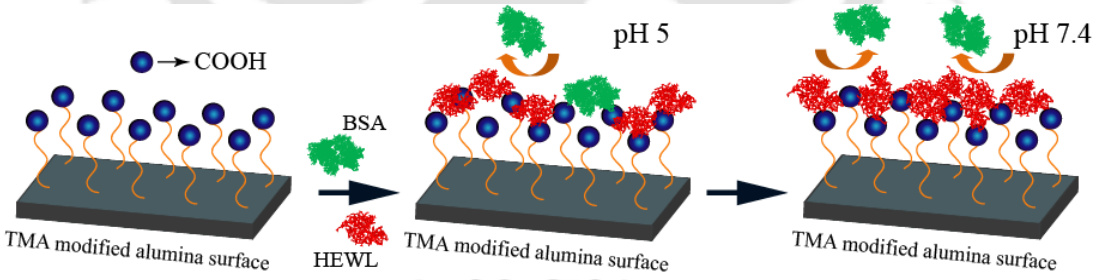

Figure S2. Schematic representation of competitive adsorption behavior of bovine serum albumin (BSA) and hen egg white lysozyme (HEWL) on TMA coated alumina surface at different pH.

Chapter 4. Progressing from the acidic surface described in previous chapter, this chapter describes the interaction of bovine serum albumin (BSA) and toxic metal ions with a basic 'hard' malachite [$Cu_2(OH)_2CO_3$] nanoparticle surface.

This chapter is divided into two section, first section describes the pH depended interaction of BSA with synthesized malachite nanoparticles. In this study, malachite

nanoparticles with an average size of 100−150 nm have been synthesized via a new and simple sodium dodecyl sulfate (SDS)-mediated reaction in aqueous solution. Malachite nanoparticles have been used for the first time as a new basic 'hard' surface for pH-controlled adsorption of BSA (Figure S3). We achieved an atypical surface coverage of BSA on malachite nanoparticle at pH beyond the isoelectric point (IEP) of BSA. Unlike other hydrophilic acidic surfaces like silica, an almost invariant surface coverage of BSA has been observed beyond its IEP up to pH ~7.0. Adsorption is reduced beyond pH ~7.0, and desorption is complete at pH > 10.0. In-depth conformational analysis of proteins in adsorption−desorption cycles has been done by circular dichroism (CD), fluorescence, and Fourier transform infrared (FT-IR) spectroscopic methods. Steady-state and time-resolved fluorescence study reveals partial unfolding and smaller lifetime of BSA upon adsorption to malachite surface. Secondary structural content of adsorbed BSA reduces as confirmed from CD and FT-IR analysis. The BSA molecule gains its secondary conformation partially after desorption from the malachite surface. Efforts were also made to understand the influence of surface modification of malachite nanoparticles (NPs) by stearic acid on protein interaction. Adsorbed stearic acid layers on malachite NPs have shown a reduced BSA adsorption compared to bare malachite nanoparticle surface. Moreover, detailed conformational analysis revealed that BSA undergoes a minor tertiary and secondary structural change upon interaction with stearic acid coated malachite NPs.

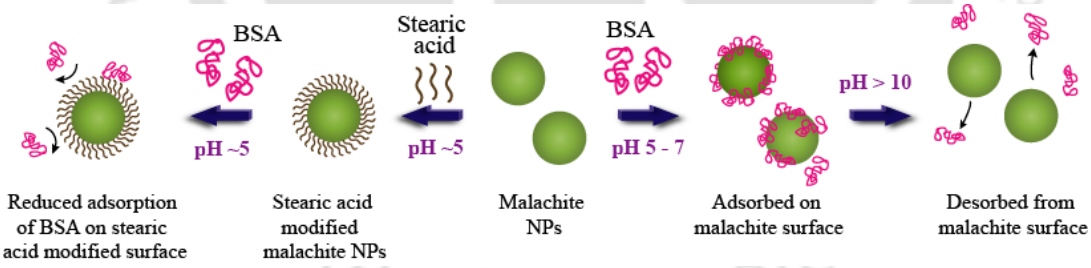

Figure S3. Schematic representation of pH controlled adsorption of BSA on malachite nanoparticles and influence of surface modification with stearic acid on protein adsorption.

The second section in this chapter describes the selective interaction of different toxic metal ions (Cr^{3+}, Cu^{2+}, Ni^{2+}, Zn^{2+}, Au^{3+}, Hg^{2+}, Pd^{2+}, Ag^{+} and Pb^{2+}) with malachite nanoparticles and BSA modified malachite nanoparticles. Herein, the BSA adsorbed malachite nanoparticles were further stabilized by crosslinking the adsorbed proteins with glutaraldehyde. The prepared BSA−malachite nanocomposite and bare malachite nanoparticles have been used for the adsorption of a series of toxic and precious metal ions from single- and multi-component aqueous solution. A reversal in adsorption

behavior of selected metal ions upon surface modification of malachite nanoparticle with BSA has been achieved (Figure S4). Among different metal ions studied, the "harder" ions (according to HSAB principle), likely Cr^{3+}, Cu^{2+}, Ni^{2+} and Zn^{2+}, were preferably adsorbed on bare malachite surface but show less adsorption on BSA−malachite nanocomposite. After surface modification with BSA, this situation was reversed, where the "soft" metal ions Hg^{2+}, Ag^{+}, Au^{3+}, and Pd^{2+} were highly adsorbed on BSA−malachite nanocomposite compared to the "harder" metal ions. However, Pb^{2+} was found to adsorb on both surfaces equally. The adsorption of metal ions has been investigated quantitatively with the help of adsorption kinetics, isotherm, and selectivity coefficient (*k*) analysis. The binding affinity of metal ions reduces $Cr^{3+} > Pb^{2+} > Ni^{2+} > Zn^{2+}$, Cu^{2+} on malachite nanoparticles, while on BSA−malachite nanocomposite, binding affinity is found in the order $Au^{3+} > Pd^{2+} > Hg^{2+} > Pb^{2+} > Ag^{+}$. We have also put our effort into studying the adsorption behavior of these metal ions from a synthetic wastewater solution containing a variable amount of metal ions. The results with synthetic wastewater solution also reflect the similar reversal adsorption phenomena of "harder" and "soft" metal ions on these two alternative surfaces, as was observed in previous case.

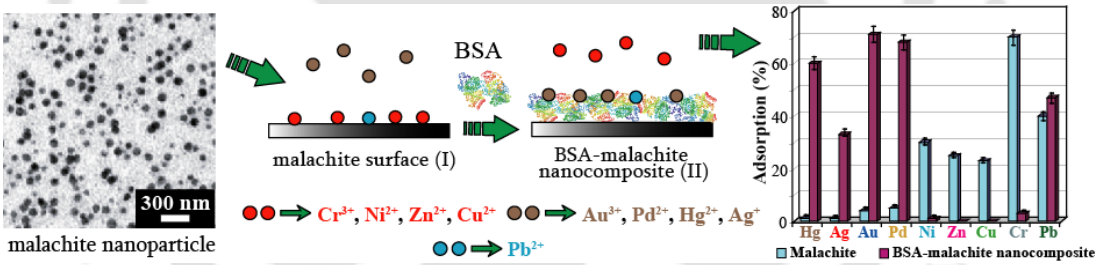

Figure S4. Schematic representation of controlled metal ion adsorption on bare malachite nanoparticle and BSA-malachite nanocomposite surface.

Chapter 5. After studying the interaction on 'hard' surfaces, this chapter advances to describe the interaction of trypsin, a proteolytic enzyme, on sulfur based 'soft' CuS nanoparticles and its preliminary application on treating dairy wastewater.

The 'soft' CuS nanoparticles of an average size of 30 nm have been prepared by passing H_2S into a complex of copper—pyridine dicarboxylic acid, in a basic solution. Adsorption studies revealed a very high adsorption capacity of trypsin on CuS nanoparticles at pH 8.0 (Figure S5). Influence of different parameters like temperature, concentration of protein and nanoparticles etc. have been studied in detail. The adsorption process was thermodynamically favourable and exothermic in nature. The structural features of adsorbed enzyme on nanoparticle surface have been analyzed with steady state and lifetime fluorescence spectroscopy, anisotropy and FT-IR spectroscopy. This chapter also

describes the in-depth structure-function relationship of trypsin on CuS nanoparticles. The adsorption of trypsin on CuS nanoparticles reaches steady state within 2-3 h. The quenching in steady state fluorescence emission of trypsin with time indicates a partial unfolded structure of the protein upon adsorption on CuS surface. The increase in anisotropy values of trypsin also indicates a motional restriction of the adsorbed protein with time. Lifetime of adsorbed trypsin was also affected with continuous addition of CuS nanoparticles. The tertiary structure of adsorbed trypsin unfolded more with a loss of enzymatic activity at a higher temperature of ~40^{o}C. Isotherm studies revealed a maximum monolayer surface coverage of trypsin of ~42 mg m^{-2} as obtained from Langmuir model analysis. Significantly we observed, the increase in surface crowding of trypsin (at higher concentration of trypsin) imposes a spatial restriction on the CuS nanoparticle surface, which affect the tertiary structure of the enzyme, as observed from fluorescence spectroscopy. This alteration in tertiary structure of adsorbed trypsin further leads to the decrease in enzymatic activity. Almost ~99% of native enzymatic activity was retained at lower surface coverage of trypsin (~3 mg m^{-2}) on CuS nanoparticles, which was decreased to ~77% when the surface coverage of trypsin increased (~14 mg m^{-2}). The enzymatic kinetic analysis of free and immobilized trypsin revealed that the rate of enzymatic activity (v) and the binding affinity of (K_m) of native enzyme remain almost same after adsorption on CuS nanoparticle surface at low surface coverage. Surface immobilized trypsin-CuS nanocomposites were also used for some preliminary studies in treating dairy wastewater. The immobilized trypsin retained same proteolytic activity as the free enzyme, in degrading the total protein content in the dairy wastewater. Moreover, the immobilized trypsin showed same efficiency to that of free enzyme in reducing the COD content of the dairy wastewater. This chapter provides an in-depth analysis of enzyme-surface interaction which can help to control the enzyme structure and activity on a specific surface.

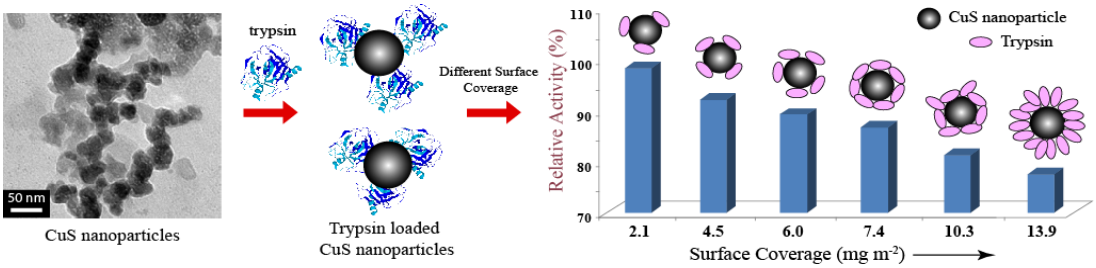

Figure S5. Adsorption of trypsin on CuS nanoparticles (average size of ~30 nm), and surface coverage depended retention of enzymatic activity of adsorbed trypsin.

At the end of the thesis an overall conclusion of the research carried out during the research period is presented and a discussion for the scope of future and further research in the area of interaction of proteins and environmental pollutants at different solid-liquid interfaces is provided.

Contents

Chapter 1

Introduction

Chapter 1

1.1. Solid-liquid interface

Solid surface constitution and surface-structure specific properties at different liquid interfaces have long defied interest of chemists, physicists, metallurgists, engineers, and biologists. The difficulties have been especially vexing to those who have tried to understand in fundamental terms the great variety of phenomena occurring at solid-liquid interfaces. Solid-liquid interface is where the solid and liquid phases separate from each other. The behavior at solid-liquid interface is quite different from that of in bulk liquid phase, and largely controlled by the surface properties of the solids having high interface-to-volume ratio. The phenomena occurring at different solid-liquid interfaces play critical roles different natural process; such as in regulating the composition and the ecology of oceans and fresh waters, in the development of soils and the supply of plant nutrients, in preserving the integrity of waste repositories. The interaction of solute from liquid phase on different micro- to nano- scale solid particles gains a significant importance in various emerging technical applications such as in remediation technologies, biotechnology, material sciences, nanotechnology etc.

1.2. Interaction/Adsorption at solid-liquid interface

It is a well known fact that liquid molecules tend to accumulate on a solid surface upon exposure, mainly due to attractive intermolecular forces. At solid-liquid interface, the molecules in the liquid phase posses a higher standard free energy compared to that of bulk-phase. This is because, in a bulk material, all the bonding requirements of the constituent atoms of the material are filled; but atoms on the (clean) surface experience a bond deficiency (unbalanced force component) as they are not wholly surrounded by other atoms.[1.1] Therefore, it is energetically favorable for the molecules in the surface to bond with whatever happens to be available (Figure 1.1). In other term, if the molecules of the liquid have a stronger attraction to the molecules of the solid surface than to each other (the adhesive forces are stronger than the cohesive forces) at solid-liquid interface, wetting of the surface occurs. Alternately, if the liquid molecules are more strongly attracted to each other than the molecules of the solid surface (the cohesive forces are

stronger than the adhesive forces), the liquid beads-up and does not wet the surface of the part.[1.2]

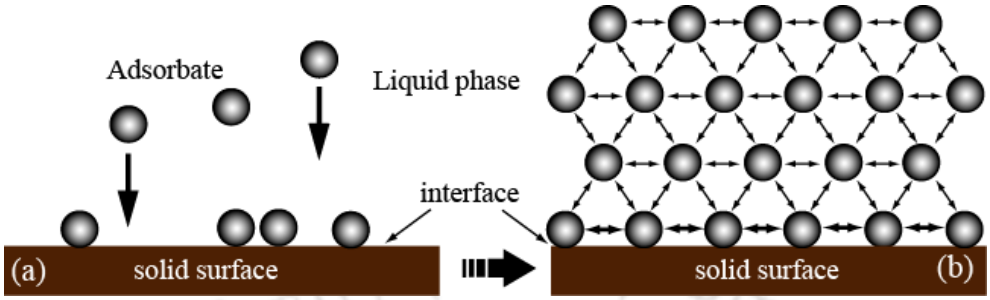

Figure 1.1. (a) Accumulation of solute from liquid phase onto solid surfaces and (b) uneven force distribution of molecules at solid-liquid interfaces which can lead to adsorption.

Upon adsorption on the surface, the rotational and vibrational freedom of the adsorbed molecules usually reduces. Some molecules may diffuse laterally through the pores of the surfaces or might react on the surface. Moreover, molecules might again desorb from the surface into liquid phase. Thus sorption phenomena may vary from complete reversibility to total irreversibility. These processes are highly important to understand the actual phenomena at solid-liquid interfaces.

1.3. Mechanism and features of interaction at solid-liquid interface

Adsorption mechanisms represent probably the most important interaction phenomena exerted by solid surfaces at a solid-liquid interface.[1.3] The extent of adsorption depends on the amount and properties of both solid phase and solute substances in liquid phase (Figure 1.2).

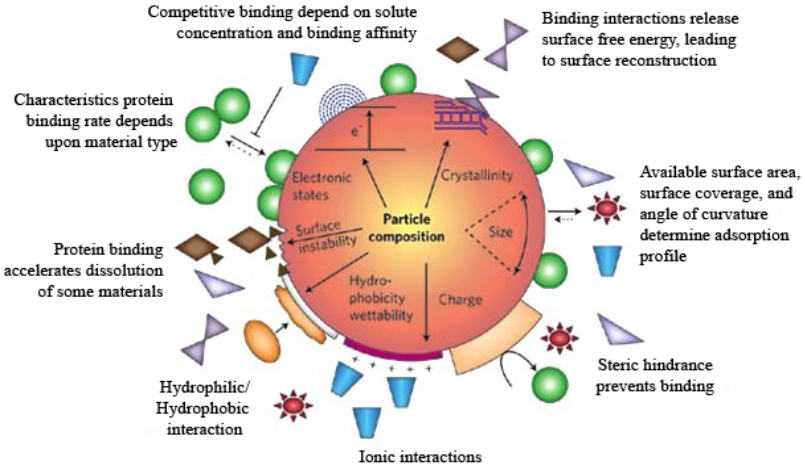

Figure 1.2. Various types of interactions at solid-liquid interfaces (Adopted from reference 1.4)

The most important properties of a molecule which determine its mode of interaction with a solid surface, are the chemical character of the molecule, shape and configuration, acidity (pK_a) or basicity (pK_b), water solubility, polarity, molecular size, polarizability, and charge distribution. The quantitative amount of a material adsorbed to an interface is a significant aspect of adsorption process. This can be determined experimentally, which indicates the number of adsorbed molecules per unit area or mass.

1.3.1. Different forces of adsorption

When a molecule adsorbs on a surface, it can bind broadly through either a chemical interaction (chemisorption) or a physical interaction (physisorption).[1.5] Chemisorption involves the formation of chemical bond between the adsorbate (in liquid phase) and the surface. Physisorption involves weaker interactions involving the polarization of the adsorbate and the surface rather than electron transfer between them.[1.5,1.6] A full understanding of this adsorption process requires that the interaction of the solute with the surface be characterized in terms of the fundamental physical and chemical properties of the solute, the sorbent and the solvent.[1.7] The different intermolecular forces play roles in adsorption process are –

- *Forming chemical reactions with surfaces* — Surface hydrolysis, Surface complexation by ionic bonding, Surface-ligand exchange, Hydrogen bond formation.
- *Forming electrical interactions at surfaces* — Electrostatic interaction, Polarization interaction.
- *Forming interaction with solvent* — Hydrophobic interaction
- *Weak interaction*— van der Waals interaction

1.3.2. The adsorption time

A useful parameter to characterize adsorption is the adsorption time. Upon exposure of a molecule to a solid surface, it gets adsorbed onto the specific or non-specific binding sites of the adsorbent surface. As more molecules approaching towards the surface it occupies the more binding sites on the surface gradually. Thus, the total binding sites available on the surface are occupied by the molecule with time, which represents an adsorption steady state for that respective system.

1.3.3. The adsorption kinetics

The study of adsorption kinetics is significant as it provides valuable insights into the reaction pathways and mechanisms of adsorption reactions. Various possible steps are involved in the transfer pathway of an adsorbate to the adsorption layer. These includes, transport of the adsorbate to the surface by convection or molecular diffusion, attachment to the surface, surface diffusion and formation of a bond with the surface constituents. These steps can be broadly explained with the help of different kinetic models such as, first-order, second order and intra-particle diffusion model (Chapter 2). Kinetics describe the solute uptake rate that controls the residence time of adsorbate uptake at the solid-liquid interface, and are important because to design appropriate large scale adsorption process, the rate at which any solute is removed from aqueous solutions must be predicted.

1.3.4. The adsorption isotherm

An adsorption isotherm can be represented by the relation between the amount adsorbed per unit area (or weight) of adsorbent and the solute concentration in the solution at equilibrium.[1.8] Isotherms can be broadly categorized in four different types (Figure 1.3)—

S-type isotherm — this type of isotherm indicates that, the adsorbate at low concentration possess low affinity towards the surface, but increases at higher concentrations.

L-type (Langmuir) isotherm— such adsorption behavior could be explained by the high affinity of the adsorbent for the adsorbate at low concentrations, which then decreases as concentration increases.

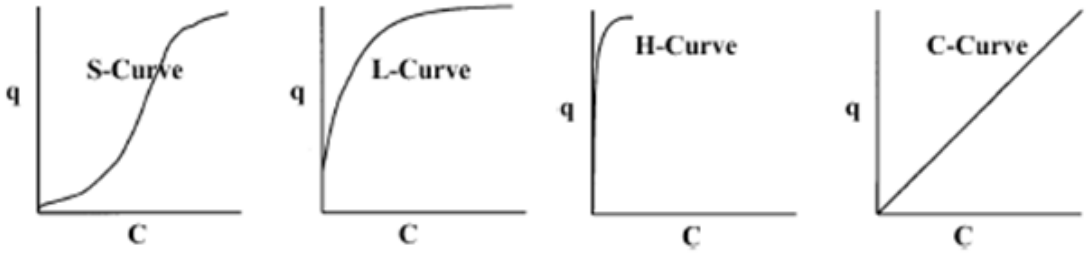

Figure 1.3. Schematic plot of four different types of adsorption isotherm generally observed at solid-liquid interface (Adopted from reference 1.5)

H-type (high affinity) isotherm — isotherm is indicative of strong adsorbent-adsorbate interactions such as inner sphere complexes.

C-type isotherm — indicates a linear increase in adsorbed amount with the increase in solute concentration.

In addition, there are several equilibrium-based mathematical models which have been used to describe adsorption on solid surfaces. These include the widely used *Freundlich* equation, a purely empirical model, and the *Langmuir* equation as discussed in the following sections (Chapter 2).

1.3.5. The adsorption thermodynamics

One of the major factors that control the adsorption mechanism at solid-liquid interface is the partitioning of the solute molecules which is mainly governed by free energy change. The concept of net free energy (ΔG) is in accord with the laws of thermodynamics and assumes that it is the natural tendency of a system to seek spontaneously a condition of minimum energy and maximum disorder[1,9] which can facilitate by adsorption on solid surface at interface. The value of the free energy relation is that spontaneous adsorption process must always be associated with a negative change in free energy (i.e. $\Delta G < 0$). Moreover, the change in free energy significantly depends on the absolute temperature (T), change in entropy (ΔS) and the change in enthalpy (ΔH) of the system. The determination of free energy change along with enthalpy and entropy are discussed later (Chapter 2)

1.3.6. Factors affecting the adsorption interaction mechanism

There are several factors which affects the interaction mechanism at solid-liquid interface which includes –

- Interfacial tension – of solute molecules at solid-liquid interface
- pH of the system
- Temperature of the system
- Colloid stability at interface and solute concentration
- Functional groups of the adsorbate and adsorbent interacting with each other

1.4. Controlled/Selective adsorption: influence of different Micro- to Nano- scale surface properties

The development and applications of selective/controlled adsorption technologies have undergone significant advances in recent years. Notably, the recent fusion of synthetic chemistry and chemical biology has seen the development of some very powerful and efficient site-specific attachment methods for inorganic, organic and biomolecules. The physical and chemical structure of the surface will strongly influence the adsorption

patterns of the molecules. Tailor-made solid surfaces coupled with a well defined morphology and chemistry can offer unique adsorption selectivities. Different tailor-made solid surfaces are of importance due to their capability of interacting with specific molecules. Controlled and specific interaction at various tailor-made surfaces is a key process in many emerging fields like environmental remediation, bio-nanotechnology, bio-separation, material science etc.[1.10]

1.4.1. Micro-scale surfaces for controlled interaction

Various micro-structured surfaces, including micro-to-mesoporous solids are widely used in size and shape selective adsorption processes for different inorganic and biomolecules. For *e.g.* Humphrey *et al.* demonstrated a size selective adsorption of proteins with molecular weights of ~40 KDa and below on propylthiol functionalized mesoporous silica SBA-15 (Figure 1.4).[1.11] In the proposed adsorption model for size selective screening, reversible physisorption is followed by irreversible chemisorption. Moreover, selective adsorption of several ionic molecules on different functionalized mesoporous solid surfaces has also been achieved. Lam *et al.* reported a selective adsorption of gold from a binary mixture on mesoporous silica (MCM-41) functionalized with organic amine groups.[1.12] Similar results were also reported in other studies where, metal ions like Au^{3+}, Pt^{2+}, Pd^{2+} and Hg^{2+} were preferably adsorbed on thiol or imidazole modified mesoporous silica.[1.13]

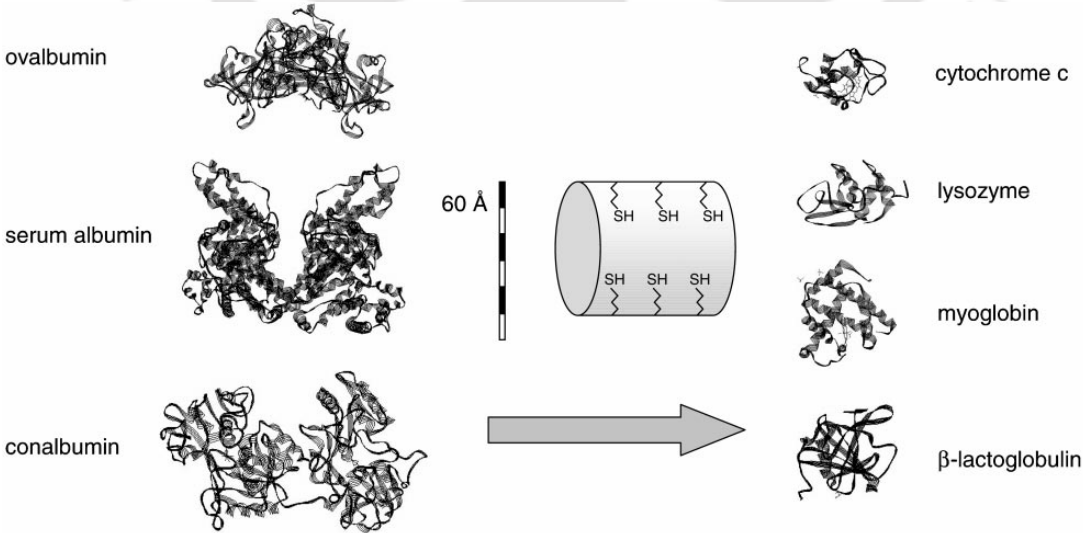

Figure 1.4. Schematic representation for size and shape selective adsorption of different proteins on the propylthiol functionalized pores of silica SBA-15. (Adopted from reference 1.11)

1.4.2. Nano-scale surfaces for controlled interaction

In addition with flat or micro-scale surfaces, the nano-structured materials are also a major tool in controlled/selective adsorption of different molecules. Throughout the past decade, there has been increasing interest in using nanotechnology to solve problems in several emerging fields likely, environmental remediation, drug delivery, medicine, sensor designing etc.[1.14]. Nanoparticles, having a very large surface to volume ratio, can provide an efficient tool for controlled interaction of molecules with high adsorption capacity. Different types of nano-structured materials, from inorganic minerals to polymeric nanoparticles are often used for adsorption studies. The properties at nano-scale level and its surface certainly affect the interaction mechanism of different molecules like, Hamada *et al.* reported an adsorption selectivity of proteins with carboxyl group surface modified irregular shaped polystyrene nanoparticles (Figure 1.5). According to them, the irregular carboxyl modified nanoparticles were able to immobilize the protein concanavalin A more efficiently than spherical nanoparticles of the same size[1.15].

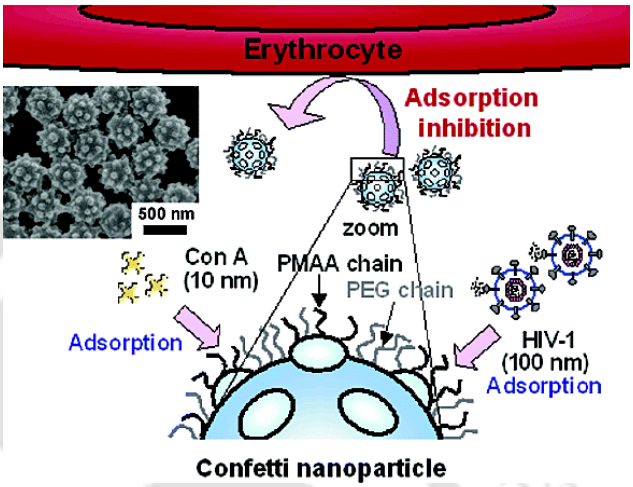

Figure 1.5. Size selective adsorption properties of materials on carboxyl modified irregular shaped '*confetti*' polymeric nanoparticles (Adopted from reference 1.15)

In addition with biomolecules, several studies report the use of nano-structured materials for controlled adsorption of inorganic/ionic molecules, for *e.g.* Magnetite-chitosan nanocomposite has been applied for potential removal of heavy metals such as, Pb^{2+}, Cu^{2+} and Cd^{2+} from aqueous solution (Figure 1.6).[1.16] As the interaction between chitosan and heavy metal ions is reversible, the synthesized magnetite-chitosan nanocomposites were used as a useful recyclable tool for heavy metal ion removal. Therefore, different micro-to-nano structured materials with proper modification can be used for controlled interaction of different ionic as well as biomolecules at solid-liquid interface.

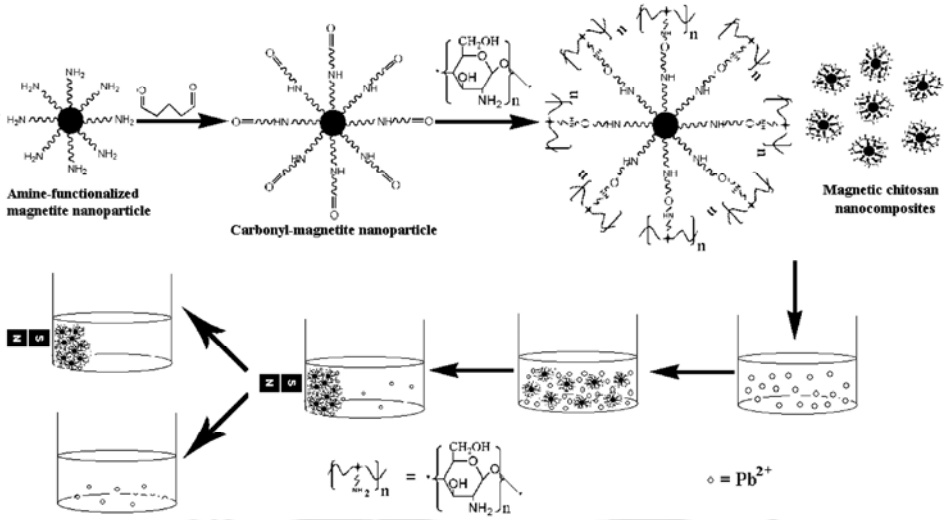

Figure 1.6. Synthesis route of magnetic chitosan nanocomposites and their use as a facile tool for heavy metal removal with the help of an external magnetic field (Adopted from reference 1.16)

1.4.3. General strategies for controlled interaction

Control over the interactions at solid-liquid interfaces can be achieved by several methods. This broadly includes,

1) *Controlling the surface properties of micro- to nano- scale solid surfaces*. Surface properties in terms of hydrophilicity/hydrophobicity and acidic or basic nature of the surface are a crucial factor in controlled interaction of molecules. Lindman *et al.* reported hydrophobicity and radius of curvature dependent interaction pattern of proteins on a co-polymer nanoparticle (Figure 1.7).[1.17] Polyacrylamide-copolymer (made with *N*-iso-propylacrylamide and N-tert-butylacrylamide monomer) nanoparticles was prepared with different surface hydrophobicity and radius of curvature. Human serum albumin (HSA) was found to bind in higher quantity upon increasing the hydrophobicity of the nanoparticles. Moreover, the surface curvature controlled the binding of protein as less amount of HSA get adsorbed on nanoparticles having smaller diameter and higher curvature.

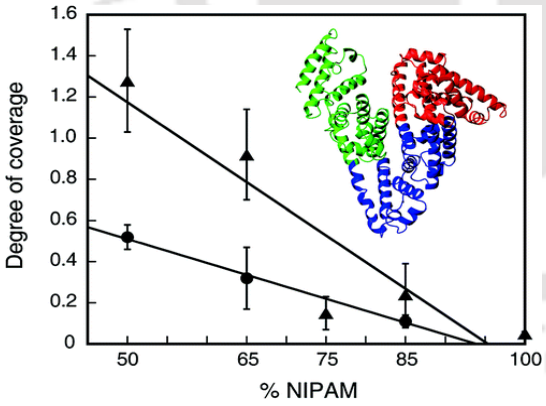

Figure 1.7. The controlled HSA coverage for the different hydrophobicities of 70 (●) and 200 nm (▲) particles. (Adopted from reference 1.17)

2) *Surface modification by introducing specific small, polymer, and/or biomolecules for specific interaction with solute*. The chemical modification of the surface of nanoparticles is a very important for control the interaction at solid-liquid interfaces. The techniques for tuning the surface capping materials of nanoparticles allow more methods to tailor the properties of these materials. Various organic and inorganic materials have been utilized as capping materials on the surface of nanoparticles through covalent or ionic interactions. These capping groups can stabilize nanocrystals in solution and connect the nanoparticle surface with other molecules. For *e.g.* poly(ethylene oxide) or poly(L-lysine)-*graft*-dextran modified surfaces can act as a protein repulsive surfaces (Figure 1.8),[1.18] whereas, several biomolecules or small imidazole and/or thiol modified surfaces can be used as selective adsorption for different soft metal ions.[1.13]

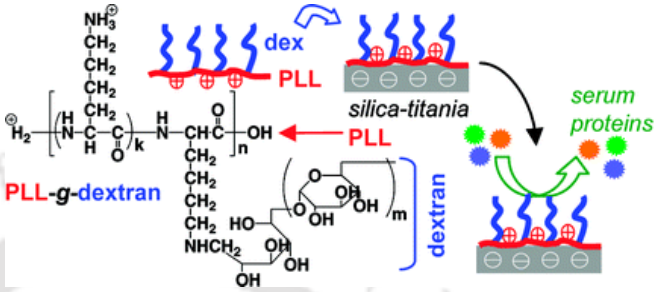

Figure 1.8. Controlled inhibition in adsorption of serum proteins on poly(L-lysine)-graft-dextran modified surface (Adopted from reference 1.18b)

3) *Generating a specific pattern on surfaces.* Recently, micro- and nanopatterned surfaces have attracted increasing interest for electronic, separation membrane and biological device fabrication due to demonstrations of selective metal deposition and adsorption in only the desired areas.[1.19] Patterned surfaces with tailored composition and architectures can be a promising tool in controlled adsorption of several inorganic and biomolecules. A variety of methods have been described for preparing pattern surfaces, including photolithography, microcontact printing, microspotting, pin spotting, and microfluidics, which allow different substrate properties and

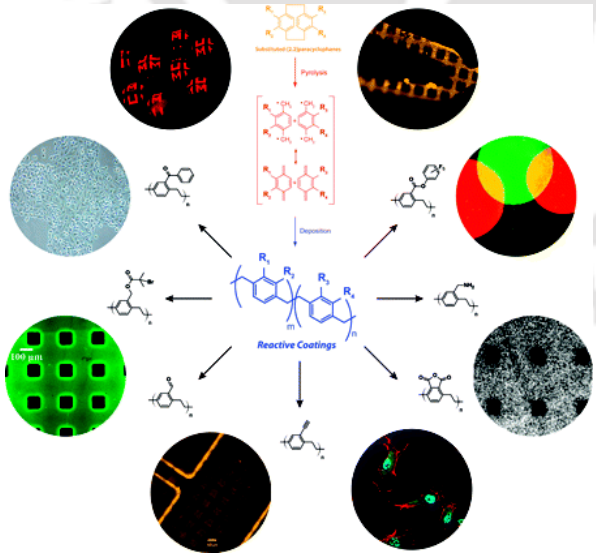

Figure 1.9. Different designable patterned surfaces using vapor-based reactive polymers for controlled interaction of biomolecules (Adopted from reference 1.20)

attachment chemistries. Several studies report the controlled interaction of biomolecules on patterned surfaces. For *e.g.* recently, an overall description on preparation of various patterned bio-array, by controlled adsorption of different proteins on patterned reactive polymer (poly-p-xylylene) substrate has been reported by Chen and Lahann (Figure 1.9).[1.20] On the other hand, the patterned substrate can be useful for controlled binding of small inorganic ions as well; as reported by Lancaster *et al.*, patterned Ni^{2+} deposition onto a polystyrene (PS) substrate,[1.21] is an potential example of this general patterning method in controlled interaction at solid-liquid interfaces.

1.5. Adsorption of proteins

The interaction of proteins with solid surfaces is not only a fundamental phenomenon but is also a key to several important and novel applications. Adsorption of proteins on a surface and its interaction are major concerns in medicine, biotechnology, separation technology, food processing and bio-nanotechnology. In the biomaterials field, protein adsorption is the first step in the integration of an implanted device or material with tissue.[1.22] In nanotechnology, protein–surface interactions are pivotal for the assembly of interfacial protein constructs, such as sensors, activators and other functional components at the biological/electronic junction.[1.23] A detailed mechanistic understanding of the protein–surface interaction would be of value to these fields, and the ability to tailor specific protein–surface interactions would benefit nanoscale materials and bio-nano-assembly technologies. Fundamentally, the interaction of proteins and surfaces involves both protein binding and unfolding; studies may therefore increase our knowledge on the biophysical properties of the protein at the interface in general (Figure 1.10).[1.4,1.24] Because of the great relevance of the protein–surface interaction phenomenon, much effort has gone into the development of protein adsorption experiments and models. The

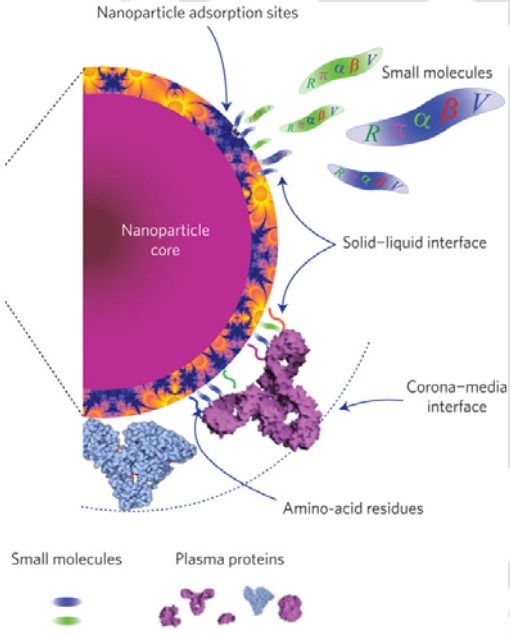

Figure 1.10. Competitive interaction of proteins and small peptides onto adsorption sites of solid surfaces (Adopted from reference 1.24b)

ultimate goals of such studies would be to measure, predict and understand the protein conformation, surface coverage, superstructure and kinetic details of the protein–surface interaction.

Different strategies for controlled adsorption of proteins at tailor-made solid-liquid interface

On the other hand, protein adsorption can be desirable if it proceeds under controlled and well-characterized conditions. Well-controlled interactions between surfaces and biomolecules are important for the development and optimization of biomaterials, biosensors, and other bio-analytical applications.[1.25] Therefore, with understanding of protein-surface interactions, control over the conformation and activity of immobilized species may ultimately allow tailor-made surfaces to be generated for the development and improvement of bio-analytical applications. Several studies found in literature, which describes the different approaches for controlled adsorption of proteins governed through careful consideration of surface structure, allowing the fabrication of materials/surface coatings with tailored bioactivity. A simple surface topography controlled adsorption of lysozyme on different sized silica nanoparticles was reported by Vertegel *et al.*[1.26] According to their report, greater loss of helical structure and subsequent activity was observed for the lysozyme adsorbed onto larger nanoparticles compared to smaller one. A similar study on surface topography and curvature depended adsorption of two proteins serum albumin and fibrinogen (differing in size and shape) on different sized hydrophilic and hydrophobic silica nanoparticles was later illustrated by Roach *et al*. (Figure 1.11).[1.27] They reported that, albumin is increasingly less ordered on larger particles, while fibrinogen, in contrast, loses secondary structure to a greater extent when adsorbing onto smaller particles (high surface curvature). Again, surface hydrophilicity can be an important tool for controlling the interaction of proteins. Koutsopoulos *et al.* reported a higher initial adsorption affinity of trypsin on hydrophobic

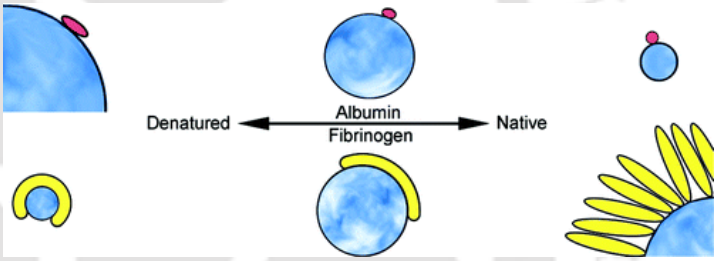

Figure 1.11. Surface topography controlled different adsorption pattern of serum albumin and fibrinogen on different sized silica nanoparticles (Adopted from reference 1.27)

polystyrene surface than that for the hydrophilic silica surface.[1.28] However, after adsorption on silica, the enzymatic activity of trypsin was ten times lower but the activity of trypsin on polystyrene surface was completely suppressed.

Moreover, surface modification with various small molecules to polymers is being used as a potential tool for controlled adsorption of different proteins. For *e.g.* an inhibition in myoglobin adsorption on alendronate (bisphosphonates) modified hydroxyapatite nanoparticles has been reported by Iafisco *et al.* (Figure 1.12).[1.29] In addition with small molecules, several polymer modified surfaces have been used for specific immobilization of proteins or as an antifouling surface. For *e.g.* poly(ethylene oxide) or polysaccharides like dextran modified surfaces was found to possess an antifouling properties which inhibits nonspecific adsorption of proteins on a tailor-made surface. Adsorption of proteins depends on grafting density, and was almost completely suppressed at high grafting densities of these polymers. On the other hand, poly(acrylic acid) modified surfaces were found to adsorb proteins with retention of their native structure.[1.18,1.30]

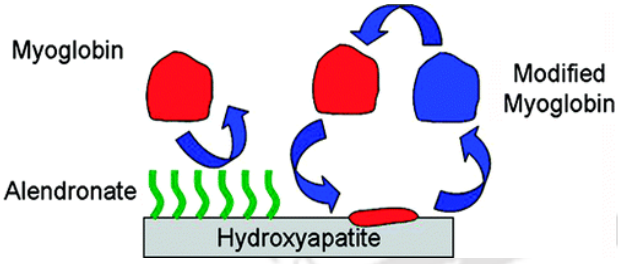

Figure 1.12. Control over the adsorption of myoglobin on hydroxyapatite nanoparticles after surface modification with alendronate (Adopted from reference

Moreover, specific attachment of desired proteins could also achieve through grafted antibody-antigen on a protein repellent surface. In this case generally, a covered surface is prepared using polymers like poly(ethylene glycol), branched poly(ethyleneimine), or hydrophilic phosphorylcholine groups, to suppress the non-specific adsorption of undesired proteins; which is followed by the conjugation of antibodies specific to the desired proteins on the polymer modified protein repellent surface (Figure 1.13).[1.31]

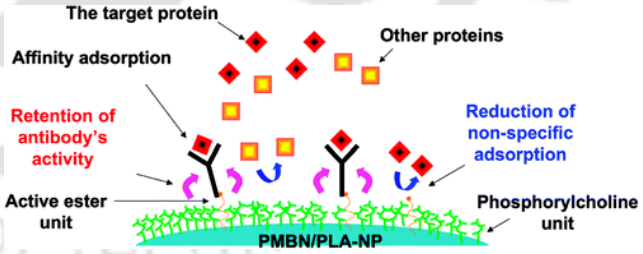

Figure 1.13. Specific attachment of desired proteins through antibody recognition on phosphorylcholine modified surface (Adopted from reference 1.31)

1.6. Adsorption of different ionic pollutants

Interaction of several environmentally and economically significant cationic and anionic species (such as precious and toxic heavy metal ions, anionic pollutants etc.) on different

tailor-made solid surfaces is an important phenomenon in bio-separation, environmental remediation and various analytical technologies. Different cationic pollutants, likely the toxic metal ions are the major concern in environmental pollution encountered in many industrial areas. Toxic metal ions such as, lead (Pb^{2+}), chromium (Cr^{6+}/Cr^{3+}), cadmium (Cd^{2+}), copper (Cu^{2+}), zinc (Zn^{2+}), mercury (Hg^{2+}) etc. are released to ecosystem at elevated concentrations as a result of unregulated application and inappropriate waste-disposal practices. Moreover, recovery different precious metal ions such as gold (Au^{3+}), palladium (Pd^{2+}), platinum (Pt^{2+}) and silver (Ag^{+}) is in high demand in industrial as well as economical point of view, as it contaminates the water bodies after discharging from several metal plating industries into the environment. These toxic and precious metal ions are of special concern because they are nondegradable and therefore persistent, which can be a threat for mankind and environment.[1.32]

In addition with metal ions, several anionic pollutants such as, phosphate, fluoride, nitrate etc. also contributes significantly in environmental pollution. For *e.g.* phosphates are used in many industrial applications in large quantities. Phosphorus has been considered as a key element causing eutrophication, an important environmental problem. This directly affects water quality and other aquatic life through oxygen depletion, because of high biological oxygen demands, and acidification. Therefore, the removal of phosphates from contaminated wastewater is absolutely necessary to avoid any kind of environmental and health hazardous problems.[1.33]

In recent years, industrial wastewater and effluent treatment have gained much importance because of increased concern about the environment. Among the different techniques employed for toxic heavy metal removal from waste aqueous sources, adsorption at solid substrate materials (adsorbents) is preferred because of its high efficiency, easy handling, and cost-effectiveness, as well as the availability of different types of adsorbents. The adsorption pattern of different metal ions is mostly dependent on the physicochemical properties of the adsorbent such as surface area, particle size, porosity, residual electric charges (ú potential) on the adsorbent and adsorbate, capacity for aggregation, and degrees of dissociation, solubilization, and ionization. In addition with the surface properties, the surrounding system, likely the nature of the solvent, concentration, temperature, pH, presence of foreign ions, etc., greatly influence the process of adsorption. Moreover, by controlling the above mentioned parameters, a controlled and selective adsorption of metal ions can be achieved.

Different strategies for controlled adsorption of ionic pollutants at tailor-made solid-liquid interface

Several studies in literature have been found which reports the controlled and high-fold adsorption behaviour of different cationic and anionic pollutants on wide varieties of micro-to-nano scale tailor-made solid surfaces. For *e.g.* mesoporous silica with specific surface modification has been widely used for toxic and precious metal ions adsorption studies. Brown *et al.* reported thiol functionalized silica nanoparticles with uniform porosities exhibit selective binding affinity for Hg^{2+}, while other metal ions like Cd^{2+}, Pb^{2+}, Zn^{2+}, Co^{2+}, Fe^{3+}, Cu^{2+} and Ni^{2+} have little or no binding ability with the adsorbents.[1.13c] In a similar study, Kang *et al.* reported that imidazole moiety containing organic ligand functionalized mesoporous silica was able to bind Pd^{2+} and Pt^{2+} selectively in presence of Cd^{2+}, Cu^{2+} and Ni^{2+} (Figure 1.14).[1.13e] Lam *et al.* reported an approach for selective and controlled separation of Ag^{+} and Cu^{2+} ions on tailor-made silica surface based on hard-soft, acid-base (HSAB) principle. Silica surface was modified with 'hard' Lewis base ($-NH_2$) for adsorption of the 'hard' Lewis acid Cu^{2+}; and with 'soft' thiolpropyl base for selective adsorption of 'soft' Ag^{+} (Figure 1.15).[1.34] Moreover, several other tailor-made surfaces like bare and surface modified iron oxide nanoparticles, goethite and hematite nanoparticles, siderite, mixed metal oxide like jacobsite ($MnFe_2O_4$) nanoparticles, metallic nanoparticles like silver and gold nanoparticles etc. are being widely used for controlled metal ion adsorption.[1.35] In addition with cations, there are several studies on controlled adsorption of anionic pollutants such as, phosphate, fluoride etc. For *e.g.* where nano-scale materials like magnetite based nanoparticles were successfully used for phosphate adsorption,[1.36] micro-

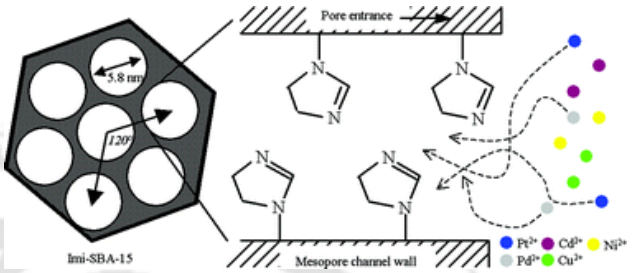

Figure 1.14. Imidazole functionalized mesoporous silica for controlled adsorption of Pd^{2+} and Pt^{2+} (Adopted from reference 1.13e).

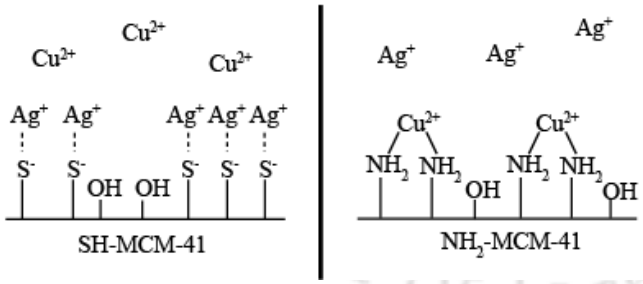

Figure 1.15. Tailor-made approach for selective adsorption of Cu^{2+} and Ag^{+} on functionalized silica (Adopted from reference 1.34).

scale silica particles functionalized with cationic metal− ethylenediamine complex has also been reported to adsorb phosphate with high efficiency.[1.37]

Moreover, in addition with biomolecules, controlled interaction of different ionic species with in-depth understanding of physicochemical phenomena on various tailor-made surfaces can lead to a combine tool for remediation and bio-nanotechnologies. In other words, ionic species assisted binding of biomolecules or the surface bound biomolecules assisted selective binding of desired ionic species can be a useful assembly for construct of various for environmental as well as biotechnological application. For *e.g.* as reported by Hayden et al., adsorption of Cu^{2+} on a lipid bi-layer can rapidly form a self-assembled micro-domain, which posses a high affinity for His-tagged proteins and further assist in controlled binding of His-tagged proteins on specific locations.[1.38] Another report by Kiyoyama *et al.* suggests a high-fold immobilization of protein on a microcapsule and its adsorption performance with respect to precious-metal ions (Figure 1.16).[1.39] Proteins including lysozyme, bovine serum albumin, chicken egg albumin, and soybean protein were immobilized on a microcapsule and further investigated for adsorption of several metal ions. Immobilized proteins could selectively adsorb precious-metal ions like (gold, platinum, and palladium) over base-metal ions (zinc and copper) from a solution. Therefore, these studies indicate that suitable tailor-made surfaces can be efficiently used for the controlled interaction of different proteins and ionic species or in a combine adsorption process.

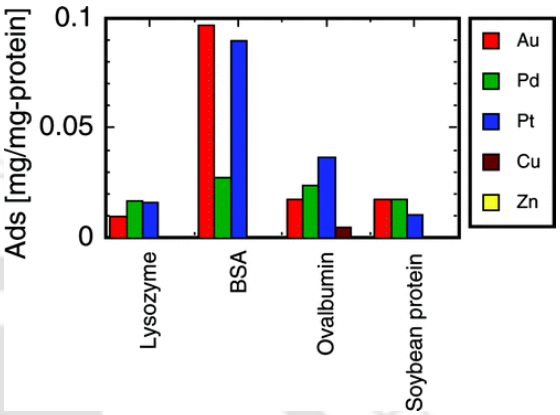

Figure 1.16. Different surface immobilized proteins for selective adsorption of precious metal ions (Adopted from Kiyoyama *et al.*).[1.39]

1.7. Objective of thesis work

Based on the extensive literature survey in previous sections, this thesis aimed to study the influence of different tailor-made surface properties on the interaction of different proteins and ionic pollutants at solid-liquid interface. Broadly, various inorganic mineral based micro-to-nano structured 'hard'/'soft' and acidic/basic particles have been prepared and used for these interaction studies. Focus has been given towards the different approaches to control the interaction phenomena of proteins and ionic pollutants with proper understanding of the physiochemical phenomena at the solid-liquid interfaces, on these tailor-made surfaces. In-depth interaction process has been studied in terms of different regulating parameters such as pH, temperature, solute concentration etc., which are the central parameters to achieve control over interaction. The influence of different surface modification with small molecule to biomolecules on the interaction phenomena has also been studied. Efforts were also made to understand the in detail structural-functional phenomena of the biomolecules at different solid-liquid interfaces using various analytical techniques. Moreover, the combine interaction of both the ionic pollutants and biomolecules at different regulating condition has also been studied.

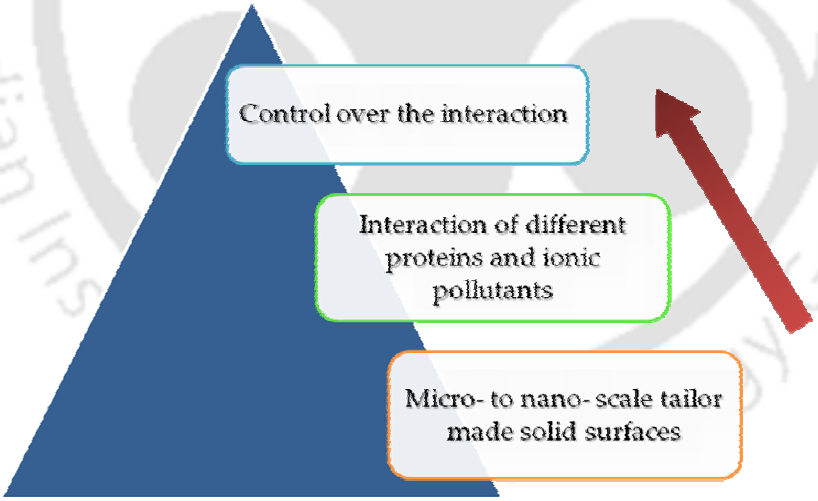

References

[1.1] Adamson, A.W.; Gast, A.P. *Physical Chemistry of Surfaces*, 1997, 6th ed., John Wiley & Sons, New York.

[1.2] Stumm, W. *Chemistry of the Solid-Water Interface*, 1992, John Wiley & Sons., New York.

[1.3] (a) Stumm, W.; Morgan, J. J. *Aquatic chemistry* 1981, 2nd ed.Wiley. (b) Schlebaum, W.; Schraa, G.; van Riemsdijk, W. H. *Environ. Sci. Technol.* 1999, 33, 1413. (c) Xia, G.; Ball, W. B. *Environ. Sci. Technol.* 1999, 33, 262.

[1.4] Nel, A. E.; Mädler, L.; Velegol, D.; Xia, T.; Hoek, E. M. V.; Somasundaran, P.; Klaessig, F.; Castranova, V.; Thompson, M. *Nat. Mater.* 2009, 8, 543 – 557.

[1.5] Lyklema, J. *Fundamentals of Interface and Colloid Science II: Solid-Liquid Interfaces*, 1995, Academic Press, San Diego.

[1.6] (a) Hunter, R.J. *Foundations of Colloid Science*, 2001, 2nd ed., Oxford University Press, Oxford. (b) Dabrowski, A. *Adv. Colloid Interface Sci*. 2001, 93, 135.

[1.7] Westall, J., *Adsorption Mechanisms in Aquatic Surface Chemistry, Aquatic Surface Chemistry*, Ed. Stumm, W., 1987, John Wiley and Sons, New York.

[1.8] (a) Chiou, C. T.; Kile, D. E. *Environ. Sci. Technol.* 1998, 32, 338. (b) Grant, P. G.; Phillips, T. D. *J. Agric. Food Chem.* 1998, 46, 599. (c) Huang, W.; Young, T. M.; Schlautman, M. A.; Yu, H.; Weber, W. J. Jr. *Environ. Sci. Technol.* 1997, 31, 1703.

[1.9] (a) Jang, M.; Kamens, R. M.; Leach, K. B.; Strommen, M. R. *Environ. Sci. Technol.* 1997, 31, 2805. (b) Luehrs, D. C., Hickey, J. P.; Nilsen, P. E.; Godbole, K. A.; Rogers, T. N. *Environ. Sci. Technol.* 1996, 30, 143.

[1.10] (a) Christman, K. L.; Enriquez-Rios, V. D.; Maynard, H. D. *Soft Matter* 2006, 2, 928. (b) Mendes, P. M.; Yeung, C. L.; Preece, J. A. *Nano. Res. Lett.* 2007, 2, 373. (c) Bajaj, A.; Rana, S.; Miranda, O. R.; Yawe, J. C.; Jerry, D. J.; Bunz, U. H. F.; Rotello, V. M. *Chem. Sci.* 2010, 1, 134.

[1.11] Yiu, H.P.H.; Botting, C. H.; Botting, N. P.; Wright, P. A. *Phys. Chem. Chem. Phys.*, 2001, 3, 2983.

[1.12] Lam, K.F.; Yeung, K.L.; Mckay, G. *J. Phys. Chem. B* 2006, 110, 2187.

[1.13] (a) Olkhovyk, O.; Antochshuk, V.; Jaroniec, M. *Colloids Surf. A* 2004, *236*, 69. (b) Aguado, J.; Arsuaga, J. M.; Arencibia, A. *Ind. Eng. Chem. Res.* 2005, 44, 3665. (c) Brown, J.; Mercier, L.; Pinnavaia T. J. *Chem. Commun.* 1999, 69. (d) Fryxell, G. E.; Liu, L.; Hauser, T. A.; Nie, Z.; Ferris, K. F.; Mattigod, S.; Gong, M.; Hallen, R. T. *Chem. Mater.* 1999, 11, 2148. (e) Kang, T.; Park, Y.; Choi, K.; Lee, J. S.; Yi, L. *J. Mater. Chem.* 2004, 14, 1043

[1.14] (a) Rosi, N. L.; Giljohann, D. A.; Thaxton, C. S.; Lytton-Jean, A. K. R.; Han, M. S.; Mirkin, C. A. *Science* 2006, 312, 1027. (b) Michalet, X.; Pinaud, F. F.; Bentolila, L. A.; Tsay, J. M.; Doose, S.; Li, J. J.; Sundaresan, G.; Wu, A. M.; Gambhir, S. S.; Weiss, S. *Science* 2005, 307, 538. (c) Dobrovolskaia, M. A.; McNeil, S. E. *Nat. Nanotechnol.* 2007, 2, 469.

[1.15] Hamada, K.; Kaneko, T.; Chen, M.Q.; Akashi, M. *Chem. Mater.* 2007, 19, 1044.

[1.16] Liu, X.; Hu, Q.; Fang, Z.; Zhang, X.; Zhang, B. *Langmuir* 2009, 25, 3.

[1.17] Lindman, S.; Lynch, I.; Thulin, E.; Nilsson, H.; Dawson, K. A.; Linse, S. *Nano Lett*. 2007, 7, 914.

[1.18] (a) Unsworth, L. D.; Sheardown, H.; Brash, J. L. *Langmuir* 2008, 24, 1924. (b) Perrino, C.; Lee, S.; Choi, S. W.; Maruyama, A.; Spencer, N. D. *Langmuir* 2008, 24, 8850.

[1.19] (a) Harris, J. J.; DeRose, P. M.; Bruening, M. L. *J. Am. Chem. Soc.* 1999, 121, 1978. (b) Balachandra, A. M.; Dai, J. H.; Bruening, M. L. *Macromolecules* 2002, 35, 3171. (c) Wang, B. Q.; Rusling, J. F. *Anal. Chem.* 2003, 75, 4229.

[1.20] Chen, H.Y.; Lahann, J. *Langmuir* 2011, 27, 34.

[1.21] Lancaster, J. R.; Jehani, J.; Carroll, G. T.; Chen, C.; Turro, N. J.; Koberstein, J. T. *Chem. Mater.* 2008, 20, 6583.

[1.22] (a) Ratner, B. D.; Hoffman, A. S.; Schoen, F. J.; Lemons, J. E. (Eds), *Biomaterials Science: an Introduction to Materials in Medicine*, San Diego: Academic Press, 1996. (b) Horbett, T.A. *Biological activity of adsorbed proteins*, Surfactant Science Series 2003, 110, 393.

[1.23] Texter, J.; Tirrell, M.; *AIChE J.* 2001, 47, 1706.

[1.24] (a) Lynch, I.; Dawson, K. A. *Nano Today* 2008, *3*, 40–47. (b) Xia, X. R.; Monteiro-Riviere, N. A.; Riviere, J. E. *Nat. Nanotech.* 2010, 5, 671.

[1.25] Lundqvist, M.; Stigler, J.; Elia, G.; Lynch, I.; Cedervall, T.; Dawson, K. A. *Proc. Natl. Acad. Sci.* USA 2008, 105, 14265.

[1.26] Vertegel, A. A.; Siegel, R. W.; Dordick, J. S. *Langmuir* 2004, 20, 6800.

[1.27] Roach, P.; Farrar, D.; Perry, C. C. *J. Am. Chem. Soc.* 2006, 128, 3939.

[1.28] Koutsopoulos, S.; Patzsch, K.; Bosker, W. T. E.; Norde, W. *Langmuir* 2007, 23, 2000-2006.

[1.29] Iafisco, M.; Palazzo, B.; Falini, G.; Foggia, M. D.; Bonora, S.; Nicolis, S.; Casella, L.; Roveri, N. *Langmuir* 2008, 24, 4924-4930

[1.30] (a) Bosker, W. T. E.; Patzsch, K.; Stuart, M. A. C.; Norde, W. *Soft Matter* 2007, *3*, 754. (b) Reichhart, C.; Czeslik, C. *Langmuir* 2009, 25, 1047. (c) Belegrinou, S.; , Mannelli, I.; Lisboa, P.; Bretagnol, F.; Valsesia, A.; Ceccone, G.; Colpo, P.; Rauscher, H.; Rossi, F. *Langmuir* 2008, 24, 7251.

[1.31] (a) Goto, Y.; Matsuno, R.; Konno, T.; Takai, M.; Ishihara, K. *Biomacromolecules* 2008, *9*, 828. (b) Erol, M.; Du, H.; Sukhishvili, S. *Langmuir* 2006, 22, 11329.

[1.32] (a) Schwarzenbach, R. P.; Escher, B. I.; Fenner, K.; Hofstetter, T. B.; Johnson, C. A.; Gunten, U.; Wehrli, B. *Science* 2006, 313, 1072. (b) Molinari, R.; Poerio, T.; Cassano, R.; Picci, N.; Argurio, P. *Ind. Eng. Chem. Res.* 2004, 43, 623. (c) Nriagu, J. O.; Pacyna, J. M. *Nature* 1988, 333, 134.

[1.33] Chen, J.; Kong, H.; Wu, D.; Hu, Z.; Wang Z.; Wang, Y. *J. Colloid Interf. Sci.* 2006, 300, 491.

[1.34] Lam, K. F.; Yeung, K. L.; McKay, G. *Langmuir* 2006, 22, 9632.

[1.35] (a) Liu, J.; Zhao, Z.; Jiang, G. *Environ. Sci. Technol.* 2008, 42, 6949. (b) Wang, J.; Zheng, S.; Shao, Y.; Liu, J.; Xu, Z.; Zhu, D. *J. Colloid Interf. Sci.* 2010, 349, 293. (c) Liu, Y.; Liu, C.; Chen, L.; Zhang, Z. *J. Colloid Interf. Sci.* 2003, 257, 188. (d) Chen, Y. H.; Li, F. A. *J. Colloid Interf. Sci.* 2010, 347, 277. (e) Erdem, M.; Ozverdi, A. *Sep. Purif. Technol.* 2005, 42, 259. (f) Hu, J.; Lo, I. M. C.; Chen, G. *Langmuir* 2005, 21, 11173.

[1.36] Daou, T. J.; Begin-Colin, S.; Grenche, J. M.; Thomas, F.; Derory, A.; Bernhardt, P.; Legar, P.; Pourroy, G. *Chem. Mater.* 2007, 19, 4494.

[1.37] Chouyyok, W.; Wiacek, R. J.; Pattamakomsan, K.; Sangvanich, T.; Grudzien, R. M.; Fryxell, G. E. *Environ. Sci. Technol.* 2010, 44, 3073.

[1.38] Hayden, C.C.; Hwang, J.S.; Abate, E.A.; Kent, M.S.; Sasaki, D. Y. *J. Am. Chem. Soc.* 2009, 131, 8728.

[1.39] Kiyoyama, S.; Maruyama, T.; Kamiya, N.; Goto, M. *Ind. Eng. Chem. Res.* 2008, 47, 1527.

Chapter 2

Experimental Section

Chapter 2

This chapter deals with the generalized materials and methodology followed to synthesize and characterize different micro- to nano-scale solid surfaces. It also describes the general equipments and different experimental set ups/calculations used to study the interaction of different proteins and pollutants on various tailor-made solid surfaces.

2.1. Materials

All the chemicals used here are of analytical grade analytical grade quality and were used without further purification unless otherwise specified. Benzene-*1,3,5*-tricarboxylic acid (trimesic acid, TMA) and basic aluminum oxide active (Al_2O_3) were purchased from *Alfa Aesar*, USA and *Loba Chemie Pvt. Ltd.*, India, respectively. Stearic acid, sodium dodecyl sulfate (SDS), glutaraldehyde (25% aq.) were purchased from *Merck India Ltd*. Different metal salts used as source for cationic pollutants like copper and ferrous sulfate; ferric nitrate; mercuric, zinc, cobalt and nickel and chromium chloride etc., were purchased from *Merck India Ltd*. and *CDH analytical reagent*, India. Precious metal ions like gold chloride, palladium and silver nitrate were procured from Sigma-Aldrich Chemicals, USA. Potassium hydrogen phosphate, potassium bromide, potassium nitrate, potassium chloride etc. were used as the source of anionic pollutants and were procured from *CDH analytical reagent*, India. Different proteins like bovine serum albumin (BSA, fraction V), hen egg white lysozyme (HEWL, from bovine pancreas) and trypsin (1:250, from porcine pancreas) were purchased from *Sigma Chemicals*, USA. The substrates for these enzymes, N_α-Benzoyl-L-arginine ethyl ester hydrochloride (BAEE) and lyophilized *M. lysodeikticus* were also purchased from *Sigma Chemicals*, USA. Other general chemicals used for different purpose for *e.g.* buffer preparation etc. were purchased from *Merck India Ltd*. and *CDH analytical reagent*, India. All the solvents used for spectroscopic studies were of spectroscopy grade and the distilled water and deionized water (Milli-Q system at 18.2 MΩ, Millipore, USA) was used in all experiments.

2.2. Different calculations used for quantification of adsorption process at solid-liquid interface

2.2.1 Adsorption capacity

Adsorption capacity is defined as the amount of solute adsorbed on the surface per unit amount or surface area of the adsorbent. Adsorption capacity generally denotes as q_e (mg g^{-1}) and can be calculated using the following equation:

$$q_e\ (mg\ g^{-1}) = \frac{C_0\ (mg\ L^{-1}) - C_e\ (mg\ L^{-1})}{D\ (g\ L^{-1})} \quad (2.1)$$

Where, C_0 is the initial solute concentration (mg L^{-1}), C_e is the steady state solute concentration (mg L^{-1}), and D is the adsorbent concentration (g L^{-1}). The adsorption capacity can also be determined in term of per unit surface area of the adsorbent (q_e value, mg m^{-2}) from the steady state mass balance and specific surface area of the adsorbent.

2.2.2. Adsorption kinetics

The kinetics of adsorption process can be validated with the different kinetic models. The surface kinetics can be evaluated with first order and second order kinetic model.[2.1] The linearized first order kinetics model is expressed as,

$$\log\ (q_e - q_t) = \log\ (q_e) - \frac{1}{2.303} k_1 t \quad (2.2)$$

And the linearized second order kinetic is expressed as,

$$\left(\frac{t}{q_t}\right) = \left(\frac{1}{q_e^2 k_2}\right) + \left(\frac{t}{q_e}\right) \quad (2.3)$$

Where, q_t and q_e (mg g^{-1} or mg m^{-2}) are the adsorption capacities at time t and at steady state respectively. The k_1 and k_2 are the first and second order rate constant respectively. To perform the error analysis and evaluate the better fitting χ^2 test has been performed using the following equation:

$$\chi^2 = \sum \frac{(q_e - q_{em})^2}{q_{em}} \quad (2.4)$$

Where, q_t and q_{tm} are total adsorption capacity at time t, using experimental data and kinetic model respectively.

Another empirically established functional relationship proposed by Weber and Morris,[2.2] the intraparticle diffusion model is also being used to fit the kinetic experimental results. The root time dependent equation is given by,

$$q_t = K_i t^{1/2} + C \quad (2.5)$$

Where K_i (mg g^{-1} $min^{-0.5}$) is an intraparticle diffusion rate constant and C (mg g^{-1}) is the intercept. The slope in the linearized fitted curve using intraparticle model characterizes the rate parameter corresponding to the intraparticle diffusion, whereas the intercept of this portion is proportional to the boundary layer thickness.

2.2.3. Adsorption isotherm

Adsorption isotherm of different process is evaluated from the fitting with different isotherm models. Most widely used adsorption isotherms models *viz.* Langmuir, Freundlich, and Temkin isotherm were utilized for adsorption processes. The main consideration of Langmuir isotherm is sorption takes place at specific homogeneous sites within the adsorbent, indicating a monolayer adsorption (constant heat of adsorption for all sites). Langmuir isotherm is expressed as,

$$\frac{C_e}{q_e} = \frac{1}{Q_m b} + \frac{1}{Q_m} C_e \qquad (2.6)$$

Where, Q_m is the maximum monolayer uptake by the adsorbent (mg g^{-1}), and b is the energy (heat) constant of the adsorption. Now a constant separation factor as described by Hall *et al.* (1966),[2.3] called "constant separation factor" or "equilibrium parameter", R_L is defined as

$$R_L = \left(\frac{1}{1 + bC_0}\right) \qquad (2.7)$$

R_L informs about the favourability of the sorption process. For a favourable reaction process, $0 < R_L < 1$; whereas $R_L = 0$ for the irreversible case, $R_L = 1$ for the linear case and $R_L > 1$ for unfavourable reaction. The Freundlich adsorption isotherm is generally based on multilayer adsorption on heterogeneous surface this holds the assumption that the adsorption sites are distributed exponentially with respect to heat of adsorption. Freundlich isotherm is given as,

$$q_e = K_f C_e^{1/n} \qquad (2.8)$$

Where, K_f in the equation denotes the Freundlich's uptake factor and n denotes Freundlich's intensity factor. The value of n in the range of 1 to 10 denotes favourable adsorption, could be find out from the linearized form of Freundlich isotherm plot. In addition with these two isotherm model, isotherm data can also be evaluated with Temkin model. This isotherm considers the heat of adsorption that decreases linearly with coverage of the interaction between adsorbate and adsorbent components. The Temkin isotherm[2.4] is given as,

$$q_e = (\frac{RT}{b}) \ln(AC_e) \quad (2.9)$$

Where A (L g^{-1}) and b are the Temkin constants. Moreover the assumption of uniform distribution of binding energies up to some maximum binding energy is also considered in this model.

2.2.4. Thermodynamic analysis

The standard Gibbs free energy change (ΔG^0) of an adsorption process indicates its thermodynamic favourability ($\Delta G^0 < 0$ for a favourable process). The standard Gibbs free energy change (ΔG^o) was calculated from

$$\Delta G^0 = -RT \ln(k_c) \quad (2.10)$$

Where R is the universal gas constant (8.314 J mol^{-1} K^{-1}) and T is temperature in Kelvin. k_c is the equilibrium stability constant, which was calculated at each temperature using the relation,

$$k_c = (\frac{C_s}{C_e}) \quad (2.11)$$

Where, C_s and C_e is the equilibrium solute concentration on adsorbent (mmol g^{-1}) and aqueous phase (mmol mL^{-1}) respectively. Moreover, the average standard enthalpy change (ΔH^0) and entropy change (ΔS^0) can be determined from Van't Hoff equation[2.5],

$$\ln(k_c) = (\frac{\Delta S^0}{R}) - (\frac{\Delta H^0}{R})\frac{1}{T} \quad (2.12)$$

ΔH^0 and ΔS^0 were calculated from the slope and intercept of plot between $\ln(k_c)$ vs (1/T).

2.3. Particulars of Instruments/Equipments used for different types of studies

2.3.1. Atomic absorption spectra

The initial and residual metal ion concentrations after adsorption and desorption were measured by *AA240* atomic absorption spectrometer (*Varian Inc.*) in each case using different cathode lamp.

2.3.2. Scanning electron microscope

Scanning electron micrograph (SEM) images of each samples glued on an aluminum stub and gold sputtered were obtained by means of a *LEO-1430 VP* electron microscope.

2.3.3. Transmission electron microscope

Samples were characterized by transmission electron micrograph (TEM) in a *JEOL 2100* UHR-TEM instrument. An amount of 5 μL of dispersion solution was drop-cast on carbon-coated copper grids and subsequently air-dried before TEM analysis.

2.3.4. Powder X-ray diffraction

Powder X-ray diffraction (PXRD) data were recorded with Seifert powder X-ray diffractometer (XRD 3003TT) with Cu K_α source (λ =1.54 Å) on a glass surface of an air-dried sample. The average crystallite size of the particles was estimated using the Debye−Scherrer equation.[2.6]

2.3.5. FT-IR spectra

FT-IR spectra were recorded at 4 cm^{-1} resolution with required scans with a *Perkin-Elmer* Spectrum One FT-IR spectrometer from 4000 to 450 cm^{-1}.

2.3.6. Steady state fluorescence spectra

The steady state fluorescence spectra of different samples were recorded on a steady state *FSP-920* spectrofluorimeter (Edinburgh instrument) using 10 mm path length quartz cuvettes.

Steady-state anisotropy measurement was also performed in *FSP-920* spectrofluorimeter (Edinburgh Instrument). Steady-state anisotropy (r) was defined by

$$r = \frac{I_{VV} - GI_{VH}}{I_{VV} + 2GI_{VH}} \qquad (2.13)$$

where, I_{VV} and I_{VH} are the intensities obtained with the excitation polarizer orientated vertically and the emission polarizer oriented vertically and horizontally, respectively. The *G* factor is defined as,

$$G = \frac{I_{HV}}{I_{HH}} \qquad (2.14)$$

The "*I*" terms refer to the parameters similar to those mentioned above for the horizontal position of the excitation polarizer and vertical and horizontal position of the emission polarizer, respectively.

2.3.7. Time-resolved Fluorescence Spectra

Time-resolved intensity decays of the proteins were measured using a *Life Spec II* spectrofluorimeter (Edinburgh Instrument). The sample was excited by Pico-quant 290 nm laser source, and the decay was measured in a time scale of 0.0488 ns/channel. The decay curves were analyzed by FAST software using the discrete exponential method, provided by Edinburgh Instrument along with the fluorescence instrument. The generated curves for intensity decay were fitted in the functions

$$I(t) = \sum_i \alpha_i \exp(\frac{-t}{\tau_i}) \qquad (2.15)$$

where α_i is the initial intensity of the decay component i, having a lifetime τ_i. The mean lifetime (τ_m) of the proteins in different experimental conditions was calculated following the equation[2.7]

$$\tau_m = \frac{\sum_i \alpha_i \tau_i}{\sum_i \alpha_i} \qquad (2.16)$$

2.3.8. Absorption spectra

UV-Visible spectra of the samples were recorded, on a *Perkin Elmer Lambda 25* UV-Visible spectrophotometer using 10 mm path length quartz cuvettes.

2.3.9. Circular dichroism spectra

The secondary conformational characteristics of proteins were investigated by far-UV CD spectra in a *J-810* (*JASCO*, Japan) spectropolarimeter. Spectra were analyzed for secondary structure content by a curve-fitting method described by Yang *et al.*[2.8] An average molar mass of 115 Da per amino acid residue was used for calculating the molar ellipticity, [θ].

2.3.10. Atomic Force Microscope (AFM)

AFM imaging of different samples were taken on Picoplus microscope (*Molecular Imaging*, USA) under non contact or MAC MODE to avoid damages of biological samples like proteins. For the data analysis, molecular imaging software was employed, which provided height patterns and cross sections.

2.3.11. Ion chromatography

Ion chromatography of the samples was performed in a Metrohm ion meter (*Basic IC 792*, Switzerland) equipped with a *METROSEP DUAL3* separation column (4 mm × 100 mm). The column was packed with polymethacrylate with quaternary ammonium groups. The samples were filtered through 0.2 μm Millipore filter paper prior to chromatogram analysis. The eluent was prepared using 2 mmol L^{-1} $NaHCO_3$ mixed with 1.3 mmol L^{-1} Na_2CO_3 solutions as recommended. The primary standard used for these experiments was PRIMUS multi-anion solution (10 mg Kg^{-1} ± 0.2 % of each ionic species) from *Fluka*.

2.3.12. Specific surface area measurement

Specific surface area and pore volume of particle were determined using a *Beckman Coulter SA3100* surface area analyzer by measuring N_2 adsorption and adopting the well-known BET procedure.[2.9]

2.3.13. Thermo-gravimetric analysis

The thermo-gravimetric analysis (TGA) of materials was performed by using an SDTA 851 e TGA thermal analyzer (*Mettler Toledo*) with a heating rate of 2 °C/min in a N_2 atmosphere.

2.3.14. Surface charge analysis

Zeta potential (ζ-potential), which indicates the surface charge of the material at different pH was measured using a ζ-potential analyzer (model *1200 Micromeritics*) at room temperature.

2.3.15. Lyophilization

Lyophilization of protein samples was performed by first quench-freezing the solutions or suspensions in liquid nitrogen and subsequent drying in a *Christ Alpha* (Germany) for 1 day at ~0.2 mbar and -60 °C.

2.3.16. pH measurement and sonication

pH of the different solutions were measured and adjusted with a *Varian* digital pH meter. Sonication of the samples was performed in a *Cyberlab* (model. 405) water bath ultra-sonicator.

References

[2.1] (a) Kumar, P. A.; Ray, M.; Chakraborty, S. *J. Hazard. Mater.* 2007, 143, 24. (b) Ho, Y. S. *Water Res.* 2006, 40, 119.

[2.2] Weber, W. J.; Morris, J. C. *Proceedings of 1st International Conference on Water Pollution Symposium*, 1962, vol. 2, 231, Pergamon Press, Oxford.

[2.3] Hall, K. R.; Eagleton, L. C.; Acrivos, A.; Vermeulen, T. *Ind. Eng. Chem. Fund.* 1966, 5, 212.

[2.4] Kim, Y.; Kim, C.; Choi, I.; Rengaraj, S.; Yi, J. *Environ. Sci. Technol.* 2004, 38, 924.

[2.5] Kalavathy, M. H.; Karthikeyan, T.; Rajgopal, S.; Miranda, L. R. *J. Colloid Interface Sci.* 2005, 292, 354.

[2.6] Yu, C. H.; Al-Saadi, A.; Shih, S. J.; Qiu, L.; Tam, K. Y.; Tsang, S. C. *J. Phys. Chem. C* 2009, 113, 537.

[2.7] Swaminathan, R.; Krishnamoorthy, G.; Periasamy, N. *Biophys. J.* 1994, 67, 2013.

[2.8] Yang, J. T.; Wu, C. S. C.; Martinez, H. M. *Methods Enzymol.* 1986, 130, 208.

[2.9] Brunauer, S. P.; Emmet, P. H.; Teller, E. *J. Am. Chem. Soc.* 1938, 60, 309

Chapter 3

Interaction of Proteins and Ions on an Acidic 'Hard' Surface

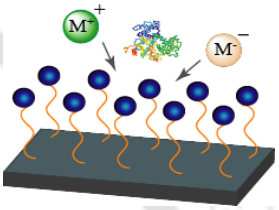

Chapter 3

3.1. Introduction

In order to investigate the interaction of protein and ions on different tailor-made surfaces, this chapter describes the interaction of cationic (Cu^{2+}, Fe^{3+}, Fe^{2+} etc.), anionic (PO_4^{3-}, NO_3^- Br^- etc.) pollutants and proteins (BSA and HEWL) on an acidic 'hard' surface. The acidic 'hard' surface has been prepared by surface modification of alumina support with benzene-*1*,*3*,*5*-tricarboxylic acid (trimesic acid, TMA). Trimesic acid has proved to be widely used class of ligands in metal-organic framework research. Due to its rigidity and strong co-ordination ability of three equally spaced carboxylate groups, metal centers can strongly bind with organic ligands. It has also been found that TMA acts as a multidentate ligand for various divalent and trivalent metal ions.[3.1] Moreover, acidic surface represented by the carboxylic groups on the surface can also bind well with the amino acid side chains of protein molecules. TMA can exhibit different types of binding mode, resulting various 3D structure.[3.1,3.2,3.3]

Inorganic oxides such as alumina, iron oxide and silica can be used as solid support for coating of the adsorbent. In the present work, TMA was coated onto the surface of basic alumina as solid support. It is well studied that carboxylic acids are strongly adsorbed on the surface of basic alumina, with adsorption energies much larger than those of other organic compounds.[3.4] A very common procedure to deposit an organic coating on inorganic oxide is to dissolve the acid in a proper organic solvent and mixed with inorganic oxide particles for a period of time, followed by evaporation of the solvent.[3.5]

3.2. Preparation of the acidic 'hard' surface/trimesic acid coated alumina surface

The preparation of trimesic acid coated alumina surface is facile and reproducible. In a typical preparation, 500 mg (~24 mM) of TMA was dissolved in 100 mL of methanol followed by continuous addition of 5 g of basic alumina in portion wise with continuous stirring. The solution pH was maintained at ~2.5, which was close to the pK_a^1 value of TMA.[3.6] After addition of alumina the solution was stirred continuously for further 6 h. The resulting mixture was vacuum-filtered and washed with cold water to remove

unadsorbed acids. Thus prepared surface modified particles were air dried before the interaction studies.

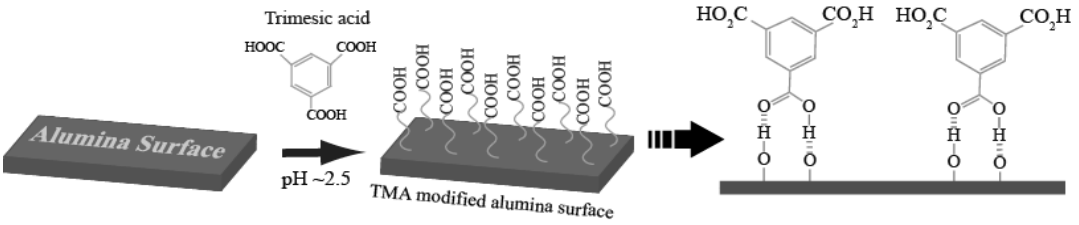

Figure 3.1. Schematic illustration of preparation of trimesic acid coated alumina surface.

3.3. Characterization of trimesic acid coated alumina surface

Trimesic acid was successfully coated on alumina surface. The degree of dissociation of TMA and surface complexation with alumina surface was highly affected by the pH of the solution. Different mechanisms for sorption of carboxylated organic acids were found to be reported.[3.7,3.8] Mao and Fung reported that the acid sorption onto alumina take place through hydrogen bonding.[3.7] At pH < pK_a value of the organic acid, less than half of the acid molecules are completely dissociated in the solution. Hence, it is less likely that the acid deposition is a dissociative adsorption process on to the solid surface. Rather, a strong hydrogen bond established at this condition where a hydrogen atom is shared between each oxygen atom in carboxylic group and the oxygen atom on alumina surface. Possibility of formation of two hydrogen bonds with each of the oxygen of TMA functional group was also reported which might further stabilize the acid coating.[3.9] Moreover, the surface charge of alumina also might have a crucial role in the coating process, as the point of zero charge (*i.e.*, pH value at which surface charge is zero) or PZC for the alumina is ~9.1.[3.7] Therefore, at pH < 9.0, the alumina surface becomes positively charged. This might have an effect on TMA coating. Mao and Fung had also supported that optimal adsorption of carboxylated acids onto alumina surface occurs when the pH is close to but slightly lower than the pK_a value of the acids. If the acid has multiple acidic functional groups then optimal adsorption occurs at a pH of slightly lower than pK_a^1 value.[3.7,3.8,3.10] When the pH becomes very low than the pK_a^1 value of acid, the alumina surface become completely protonated and formation of two hydrogen bonds with each carboxylic acid functional group is not favourable. This might result in the decrease in TMA coating onto alumina surface. Again, TMA coating on alumina surface might also be aided by electrostatic interaction. Here, the surface complex formation between acidic functional groups of the organic acid and surface hydroxyl groups on metal oxides at lower pH plays an important role in TMA coating. As the metal oxide

surface is negatively charged in the pH ~9.0 or above, surface oxygen atom is strongly bound; therefore not favourable for exchange with acidic functional group in solution. As pH decreases further, metal oxide surface become neutral and then positively charged (below pH 9). The aluminium–oxygen bond is weakened due to decreased electron density of the bond, and an electrostatic bond forms with acidic functional groups. With increase of carboxylic groups in benzene ring, the possibility of formation of surface complex increases due to the enhanced strength of the acid. This might lead to enhanced sorption. Evanko and Dzombak[3.8] found that the maximum sorption for TMA on metal oxide surfaces occurred at higher acidic pH values. This also supports the optimal coating of TMA at a pH value ~2.5, performed in our study.

FT-IR spectroscopy was used to identify the vibration frequency changes in the functional groups present in the TMA, coated on alumina. The background obtained from the scan of pure KBr, was automatically subtracted from the sample spectra. All spectra were plotted using the same scale on the transmittance axis. The FT-IR spectra of pure TMA and alumina were also taken for the comparison. All three FT-IR spectra are shown in Figure 3.2. Only TMA shows the C=O, O-H, and C-O stretching vibration at 1700, 1450, and 1275 cm^{-1} respectively corresponds to the aromatic acid.[3.11] Alumina shows a characteristic stretching band at 1650 cm^{-1}, while TMA coated alumina shows the peaks correspond to carboxylic acid at 1710, 1450, and 1275 cm^{-1} along with a shoulder at 1610 cm^{-1} characteristic to alumina.[3.11]

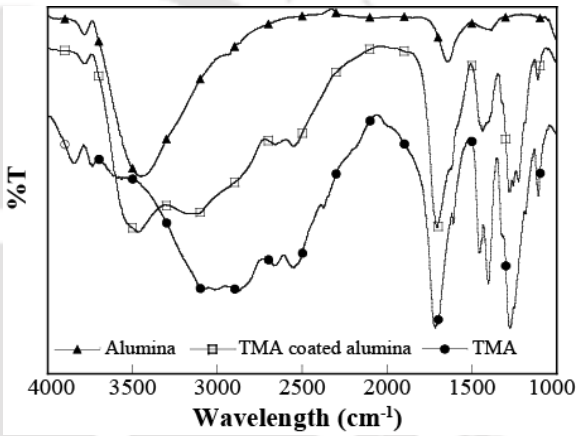

Figure 3.2. FT-IR spectroscopy of bare alumina, trimesic acid and trimesic acid coated alumina

The surface morphology of the alumina, TMA coated alumina and metal adsorbed on adsorbent was studied by scanning electron microscopy. Figure 3.3a shows that alumina is an aggregate of small crystalline structure of average dimension of ~2 μm. EDX spectra shows the presence of only Al and O. TMA coated alumina is the aggregates of smaller crystallites with average dimension of < 1 μm (Figure 3.3b) and EDX shows the presence of C after coating.

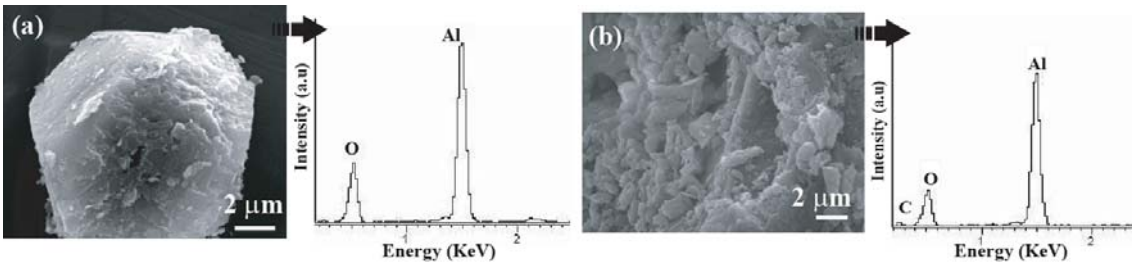

Figure 3.3. SEM images and EDX spectra of (a) bare alumina and (b) TMA coated alumina

Now, based on the types of solute molecules, this chapter has been divided in two sections,

Part 1: Interaction of ionic pollutants on trimesic acid coated alumina surface.

Part 2: Interaction of proteins on trimesic acid coated alumina surface.

Part 1:

3.4. Interaction of ionic pollutants on trimesic acid coated acidic 'hard' surface

This section describes the different cationic (Cu^{2+}, Fe^{3+}, Fe^{2+} etc.) and anionic (PO_4^{3-}, NO_3^- Br^- etc.) pollutants on trimesic acid coated surface.

3.4.1. Interaction of Cu^{2+} on trimesic acid coated alumina surface

3.4.1.1. Background

Aquatic pollution by heavy metals is a rising concern at hazardous waste sites around the world. Several heavy metals like cadmium, chromium, copper, lead, mercury, nickel, zinc, etc. are included on the U.S. Environmental Protection Agency's (EPA) list of priority pollutants.[3.12] Cu^{2+} ion is one of the ubiquitous and frequently found toxic metals in surface water. The potential sources of Cu^{2+} ions are, essentially, pulp, paper and wood preservative-employing mills, industrial waste streams of metal cleaning and plating baths, fertilizer industry, etc.[3.13] Cu^{2+} has high affinity for N and S donor containing ligands.[3.14] Hence, enzymes, whose activities depend on sulhydryl and amino groups,[3.15] are strongly inhibited by Cu^{2+} ions. Moreover it also has several toxic effects on human.[3.16] Considering deleterious effects of heavy metals on living systems, strict regulation had been placed on their concentration in potable water supplies and effluent discharges by various agencies throughout the world. Hence, the need of efficient techniques to reduce the heavy metal content in the aqueous waste streams is highly important. In addition, there is continuous increase in demand of most of the known metals as their availability decreases continuously. This also strengthens the need of effective waste processing method, so that the water can be recycled and the metals can

also be reused. Adsorption is considered to be an effective and versatile method for reduction of Cu^{2+} ions in wastewater. When adsorption is combined with appropriate desorption step, it solves the problem of sludge disposal.[3.17] Several enhanced adsorbents like activated carbon, inorganic colloids, functionalized silica, polyurethane foams, and low cost adsorbent like chitosan, zeolites, fly ash, cellulose, saw dust, TiO_2, waste iron oxide etc. were used in Cu^{2+} adsorption previously.[3.18]

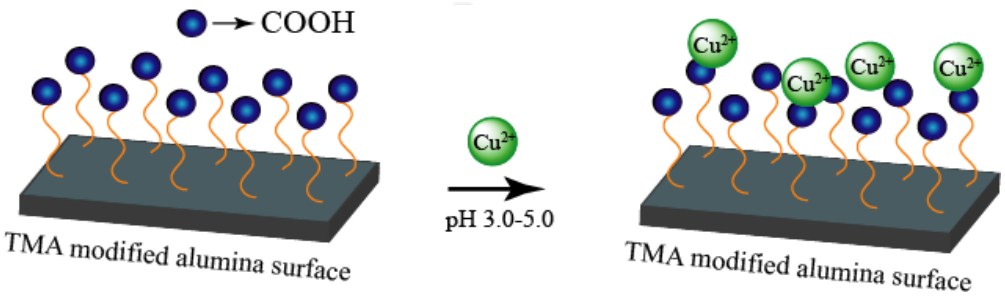

Scheme 3.1. Illustration of Cu2+ interaction on trimesic acid coated alumina surface.

The purpose of present study is to use the alumina supported by benzene-*1,3,5*-tricarboxylic acid (trimesic acid, TMA) as an adsorbent materials for the adsorption of toxic Cu^{2+} ion. Moreover, not many studies were found before where aromatic carboxylated acids like TMA were used as an adsorbent for divalent toxic cations. Hence we are interested to use this aromatic acid as an adsorbent for divalent toxic Cu^{2+} ions from wastewater. This study provides the insight into Cu^{2+} ion adsorption from aqueous solutions in terms of equilibrium, kinetics, isotherm and thermodynamic parameters. It also provides the optimizing conditions in terms of various system parameters such as initial ion concentration, time, pH, temperature and adsorbent dose for Cu^{2+} ion adsorption. Besides, recovery of metal ion, and regeneration of adsorbents were conducted which is very important to assess the practical utility of the adsorbent.

3.4.1.2. Materials and methods

The Cu^{2+} concentration was measured in atomic absorption spectrophotometer. After addition of adsorbent, the metal solution was stirred in a temperature controlled shaking incubator at a fixed rpm (*Labtech Co. Ltd*., Model No. LSI-3016R).

Adsorption studies. Adsorption experiments were carried out in batch mode. An amount of 500 mg L^{-1} stock solution of $CuSO_4$ was prepared and diluted to different desired concentration as required for adsorption study. After addition of different amounts of

adsorbent (20 to 100 g L^{-1}), specimen tubes were kept in a temperature controlled shaker for proper mixing. Kinetic experiments were performed by adding fixed amount of adsorbent (100 g L^{-1}) in known concentration of Cu^{2+} solution. The samples were taken out at regular interval and centrifuged to obtain suitable aliquots for analysis of Cu^{2+} concentration. Rate constants of kinetic models were also calculated from the conventional rate equations. Reaction pH, concentration of TMA coated alumina, amount of TMA per gm of alumina in coating, duration of mixing and initial Cu^{2+} concentration were the variables in this study. Solution pH was adjusted by adding 0.1 M NaOH and 0.1 M HCl, and once optimized, rest of experiments were performed in the optimized pH. Isotherm experiments were performed with different initial Cu^{2+} concentration solution (50–250 mg L^{-1}) by adding a constant amount of adsorbent of 15 g L^{-1}. Initial pH of the solution was adjusted to ~5.0 as optimized and mixed until equilibrium reaches. Adsorption capacity or the qe value (mg g^{-1}) for Cu^{2+} was calculated in each case. Control experiments were carried out in each case with only Cu^{2+} solutions, to validate the adsorption phenomenon. The detail sets of experiments are shown in Table 3.1. All the adsorption experiments were performed in duplicate for data consistency.

Table 3.1. Detail adsorption experimental set for Cu^{2+} interaction on TMA coated alumina surface.

Set	*Variable parameter*	*Controlled/fixed parameter*
1.	Uncontrolled initial pH ~ 4, vary stirring time until equilibrium reached.	250 mg L^{-1} Cu^{2+}, adsorbent 100 g L^{-1}, temp 25°C.
2.	Controlled pH: 2, 3, 4, 5, 6 and 7	250 mg L^{-1} Cu^{2+}, adsorbent 100 g L^{-1}, time 2 h., temp. 25°C.
3.	Reaction temperature variation: 25, 30, 35, 40, 45 and 50 °C.	Reaction pH 5, 250 mg L^{-1} Cu^{2+}, adsorbent 100 g L^{-1}, time 2h.
4.	Adsorbent dose (g/L): 20, 40, 60, 80 and 100.	Reaction pH 5, 250 mg L^{-1} Cu^{2+}, time 2h, temp. 25°C,
5.	Initial Cu^{2+} concentration: 50 to 250 mg/L	Reaction pH 5, time 2 h, temp. 25°C, adsorbent 15 g L^{-1}.
6.	Different coating ratio (mg TMA/gm alumina): 50, 100 and 200; and uncoated alumina	250 mg L^{-1} Cu^{2+}, adsorbent dose 100 g L^{-1}, time 2h, temp 25°C

Desorption and multi-cyclic adsorption studies. Once steady state reaches in adsorption process, the adsorbent (containing adsorbed Cu^{2+}) was separated by centrifugation and air dried. After drying, the adsorbent was treated with 0.2–1.0 M HCl and H_2SO_4 solution

separately to study the desorption phenomena of Cu^{2+} ion from the adsorbent. On completion of desorption, the mixture was then again centrifuged and the supernatant was measured for the concentration of desorbed Cu^{2+} in solution. Multi-cyclic adsorption efficiency of the adsorbent was performed by air drying of the adsorbent after desorption and re-use of it for the five continuous adsorption cycles under same conditions.

3.4.1.3. Equilibrium studies of Cu^{2+} adsorption

Adsorption equilibrium studies were performed with the Cu^{2+} concentration varied from 100 to 250 mg L^{-1} with a constant adsorbent dose of 100 g L^{-1} separately (Table 3.1, Set 1). Solution pH left uncontrolled at ~4.0 for this equilibrium study. Final solution pH was found in between 4–5 which indicates little variation in solution pH during adsorption process. Initially adsorption of Cu^{2+} increased with increase in contact time and remained nearly constant after it reached equilibrium (Figure 3.4). The steady state reached within 120 min irrespective of initial Cu^{2+} concentration at 25 °C. About 85% removal of Cu^{2+} was observed with 100 mg L^{-1} sample at this uncontrolled pH, which decreased to 75% with 250 mg L^{-1} sample. More than 50% of the equilibrium Cu^{2+} uptake was adsorbed rapidly within first 10 min of contact with adsorbent. However, the q_e value changed from 1.8 to 0.85 mg g^{-1} when sample concentration was decreased from 250 to 100 mg L^{-1}, respectively. This indicates that Cu^{2+} adsorption by TMA coated alumina is also significant in at lower concentrations such as 100 mg L^{-1}. Crystalline nature of the adsorbent before and after adsorption of heavy metal was confirmed by powder XRD pattern. Figure 3.5a shows the XRD pattern of the adsorbent before and after metal adsorption. In case of TMA coated alumina, the adsorbent, no significant peak found in this interval, which indicate the amorphous nature of the adsorbent. After adsorption of the Cu^{2+} ion on the surface of the adsorbent, crystalline nature became more prominent. The surface of alumina became smoother after TMA coating. Cu^{2+} adsorption on adsorbent changes the overall surface morphology drastically. It became highly crystalline in nature and forms aggregates of micron size

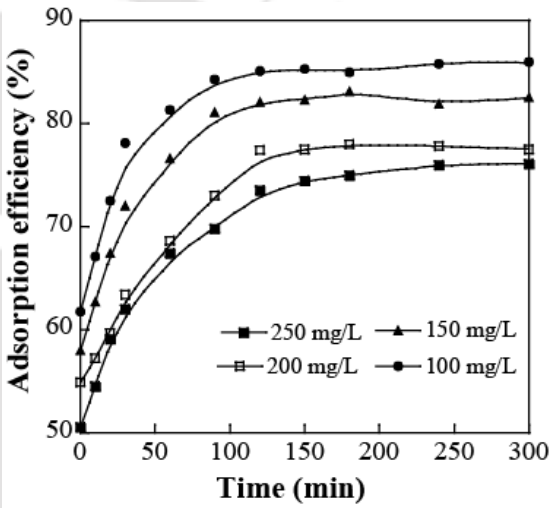

Figure 3.4. Equilibrium study with different initial concentration Cu^{2+} solution.

plates (Figure 3.5b). The presence of copper on the surface of the adsorbent was confirmed by EDX spectrum.

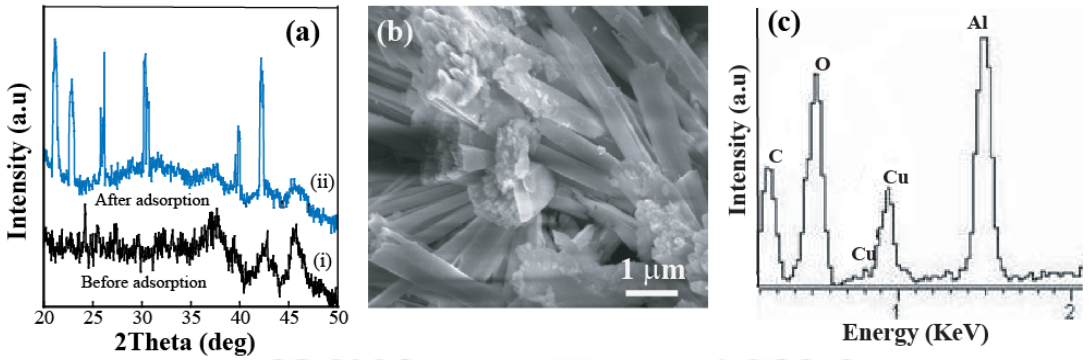

Figure 3.5. (a) Powder XRD pattern of TMA coated alumina (i) before and (ii) after Cu^{2+} adsorption and (b) SEM image of TMA coated alumina after Cu^{2+} adsorption and (c) EDX confirms the presence of copper.

In case of TMA coated alumina, the adsorbent, no significant peak found in this interval, which indicate the amorphous nature of the adsorbent. After adsorption of the Cu^{2+} ion on the surface of the adsorbent, crystalline nature became more prominent. The surface of alumina became smoother after TMA coating. Cu^{2+} adsorption on adsorbent changes the overall surface morphology drastically. It became highly crystalline in nature and forms aggregates of micron size plates (Figure 3.5b). The presence of copper on the surface of the adsorbent was confirmed by EDX spectrum.

3.4.1.4. Effect of solution pH on Cu^{2+} adsorption

To study the influence of pH, the adsorption experiment of Cu^{2+} was carried out in a pH range of 2.0 to 7.0. The concentration of Cu^{2+} and adsorbent dose were kept constant at 250 mg L^{-1} and 100 g L^{-1}, respectively, at 25 °C during pH variation (Table 3.1, Set 2). When the solution pH was ~2.0, the removal was comparatively lower, about 52%. This can be due to the competitive adsorption of hydrogen ion with Cu^{2+}. Adsorptivity of Cu^{2+} increased with increase of pH. While increasing pH from 4.0 to 5.0, a rapid decrease in remaining Cu^{2+} concentration

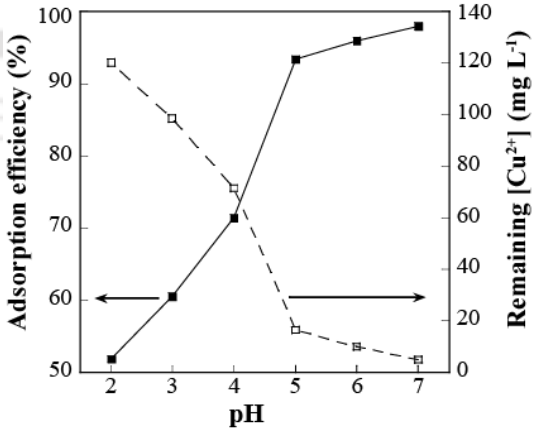

Figure 3.6. Influence of pH on interaction of Cu^{2+} on TMA coated surface

was noticed (71.5–16.5 mg L^{-1}). This indicates a sharp rise in Cu^{2+} uptake by the adsorbent at this pH range (Figure 3.6) as the removal reached to ~94% at pH 5.0. At this pH, carboxyl groups of TMA are in dissociative form and strongly chelates with positively charged Cu^{2+} ions, where the Cu^{2+} binds with each carboxylate moieties of TMA. This complexation results in crystalline structure which was observed from the SEM image (Figure 3.5b). The favourable surface complexation of Cu^{2+} with TMA functional groups also reported in other studies.[3.2,3.19] Beyond pH 5.0, Cu^{2+} adsorption increased very little, about 2–4% up to pH ~7.0. But, with the increase in pH, the degree of hydrolysis of Cu^{2+} ion increases. Baes and Mesmer reported that onset of metal hydrolysis and precipitation begins at pH ~6.0 for copper.[3.20] A blank experiment with only Cu^{2+} solution of 250 mg L^{-1} was performed which support the above report. Thus, above pH 5.0 precipitations might affect Cu^{2+} removal in addition with adsorption. Hence the pH for Cu^{2+} adsorption was set below pH 6.0 and all the further reaction was performed in pH 5.0 afterwards.

3.4.1.5. Thermodynamic study of Cu^{2+} adsorption

Temperature of adsorption is a very important regulating parameter associated with different thermodynamic aspect of this process. In this study, temperature was varied during the adsorption process to check its effect on adsorption capacity (Table 3.1, Set 3). The adsorption capacity of the adsorbent decreased from 2.37 to 1.84 mg g^{-1}, when temperature was increased from 25 to 50 °C (Figure 3.7a). This implies that the Cu^{2+} adsorption onto TMA coated alumina is an exothermic process. The adsorption efficiency decreased from 95 to 74% with the increase in temperature from 25 to 50 °C, which indicates lower adsorption efficiency at higher temperature. The standard Gibbs free energy change (ΔG^0) of Cu^{2+} adsorption was calculated for the temperature range of 25 to 50 °C. The negative values of ΔG^0 at all temperatures (Table 3.2) suggest that the adsorption process was spontaneous and thermodynamically favourable. Higher the negative value of ΔG^0, higher the driving force of adsorption. As the temperature increased from 25 to 50 °C, values of ΔG^0 value decreased from −12.88 to −8.94 kJ mol^{-1}. This indicates a lesser driving force for Cu^{2+} adsorption, and decreased sorption efficiency onto adsorbent surface at higher temperature. Moreover, the standard enthalpy (ΔH^0) and entropy (ΔS^0) change were calculated from the slope and intercept of plot between $\ln(k_c)$ vs. $(1/T)$ using Van't Hoff equation (Figure 3.7b). The ΔH^0 is calculated to be −57.71 kJ mol^{-1}, which also established the exothermic nature of the adsorption

process. The negative value of ΔS^0 (-151.7 J mol^{-1} K^{-1}) indicates the higher order reaction during adsorption of Cu^{2+} onto TMA coated alumina.

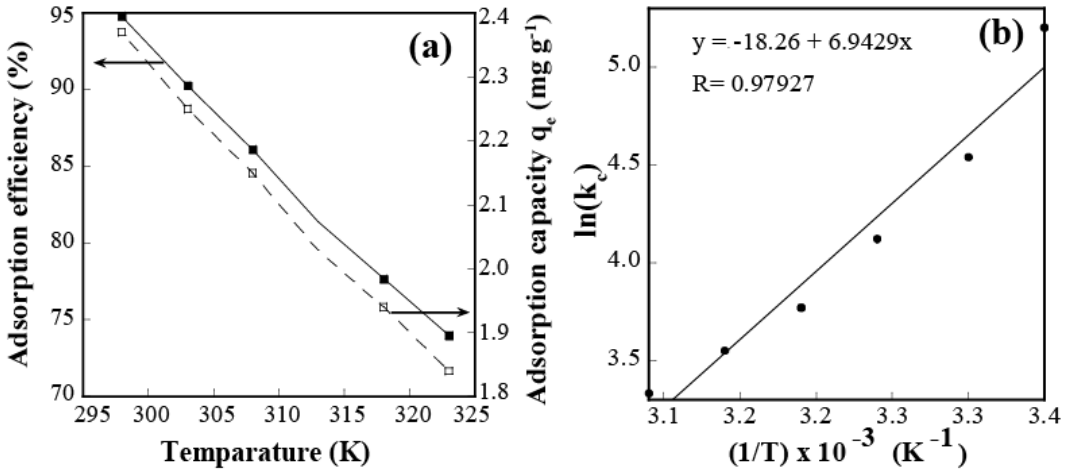

Figure 3.7. (a) Effect of temperature on Cu^{2+} adsorption and (b) Van't Hoff plot of Cu^{2+} adsorption.

Table 3.2. Values of Gibbs free energy (ΔG^o) of Cu^{2+} adsorption at various temperatures

	Temp (°C)					
	25	**30**	**35**	**40**	**45**	**50**
ΔG^o (KJ mol^{-1})	-12.88	-11.43	-10.54	-9.80	-9.38	-8.94

3.4.1.6. Effect of adsorbent dose and adsorption isotherm

Amount of TMA coated alumina was varied from 20 to 100 g L^{-1} in a set of 250 mg L^{-1} Cu^{2+} solutions, separately at pH 5.0 (Table 3.1, Set 4). The adsorption efficiency of copper in equilibrium increased from 84.32 to 95.6% when adsorbent dose increased from 20 to 100 g L^{-1}. Moreover, considerable increase in the q_e value from 2.39 to 10.54 mg g^{-1} was observed when adsorbent dose decreased from 100 to 20 g L^{-1} (Figure 3.8). From these two data it can be said that adsorption of Cu^{2+} with TMA coated alumina is also efficient in lower adsorbent dose such as 20 g L^{-1}, as found in case of higher dose. At higher adsorbent concentration, the total available surface area increases while the concentration of solute remain fixed, this results in decrease in adsorption capacity per unit surface concentration (q_e value).

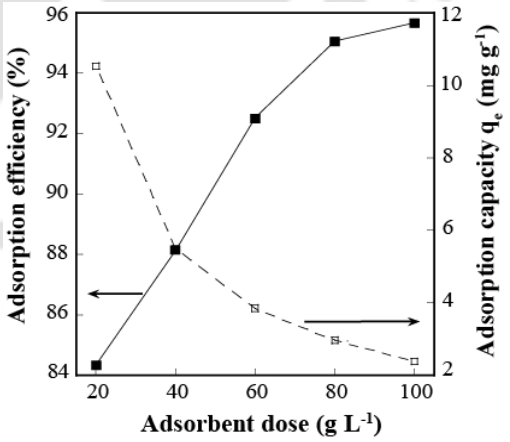

Figure 3.8. Influence of TMA coated alumina concentration on interaction of Cu^{2+}

Most widely used adsorption isotherms models *viz.* Langmuir, Freundlich, and Temkin isotherm were studied for this adsorption process (Table 3.1, Set 5). The adsorption isotherm for the Cu^{2+} is shown in Figure 3.9a. Initially the adsorption at equilibrium (q_e) increased from ~3.0 to ~9.5 mg g^{-1}, at ~9.5 mg g^{-1}. The linearized form of Langmuir adsorption isotherms are plotted in Figure 3.9b. The experimental results match well with the Langmuir isotherm pattern. This indicates a monolayer adsorption process (constant heat of adsorption for all sites) has been taken place. Based on this it is anticipated that the adsorption of each molecule has same activation energy as the curve fitting implies the homogeneity of the adsorbent. The Langmuir isotherm constants were determined from Figure 3.9b and listed in Table 3.3. The maximum Cu^{2+} uptake (Q_m) was achieved 10.80 mg g^{-1}. As described by Hall *et al.*[3.21], "constant separation factor" or "equilibrium parameter," R_L was determined. For these experiments, the value of R_L was found to be 0.054, which indicate the favourability of Langmuir model in this study. The experimental data was plotted in Freundlich isotherm shown in Figure 3.9c. It was found that the adsorption isotherm data also could be described with Freundlich isotherm model to a much lesser extent.

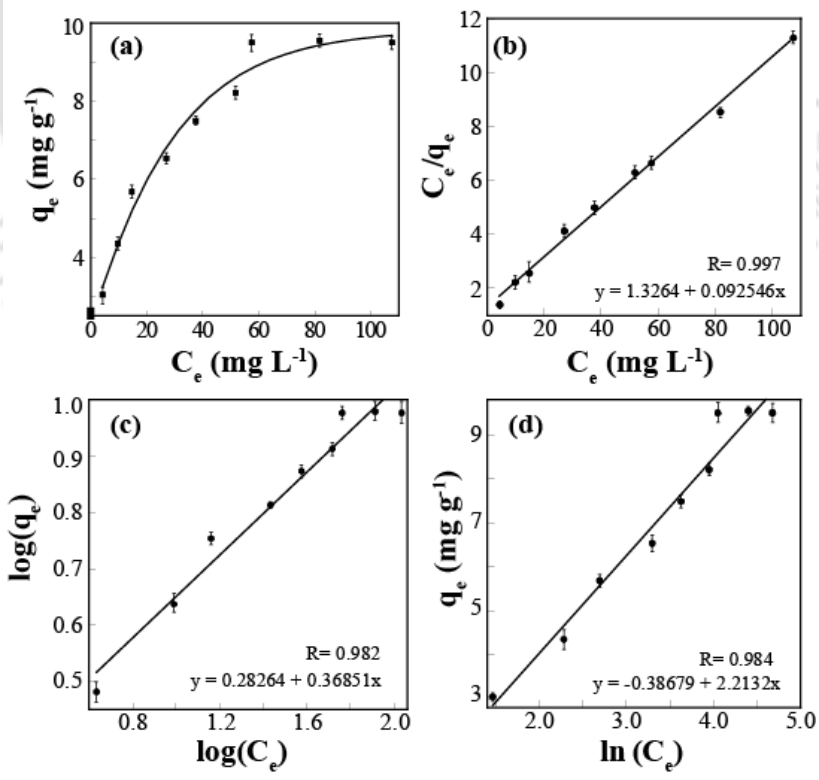

Figure 3.9. (a) Adsorption isotherm of Cu^{2+}, (b) Langmuir linear isotherm model, (c) Freundlich linear isotherm model and (d) Temkin linear isotherm model.

The Freundlich uptake factor (K_f) and intensity factor (n) was determined from the linearized Freundlich plot (Figure 3.9c). The value of intensity factor was found 2.713, which also indicates the favourability of this process.[3.22] For all cases the Langmuir equation represents a better fit of the experimental data than Freundlich equation. In case of Temkin isotherm, a factor, which considers the adsorbing species and adsorbate interaction, is taken into account. The value of Temkin binding constant A can be calculated from the Temkin plot (Figure 3.9d) and given in Table 3.3. The experimental data was better fitted with Langmuir isotherm (R^2 = 0.997) than either of Freundlich (R^2 = 0.982) or Temkin (R^2 = 0.984) isotherm. In addition, the chi-square test (χ^2) was also done to support the best fit adsorption model.[3.23] From the experimental data, the χ^2 value of Langmuir model (0.161) was found to be lower than either Freundlich (0.321) or Temkin (0.216) isotherm model. Therefore, the uptake of Cu^{2+} ion preferably follows the monolayer adsorption process, and the Coulombic interaction is the dominant driving force in this process as confirmed from Langmuir model.[3.24]

Table 3.3. Parameters of different isotherm models of Cu^{2+} adsorption.

Langmuir isotherm			**Freundlich isotherm**			**Temkin isotherm**		
Q_m (mg g^{-1})	b (L mg^{-1})	R	K_f (mg g^{-1})	n	R	A (L g^{-1})	m	R
10.80	0.0698	0.997	1.917	2.713	0.982	0.84	1119.3	0.984

3.4.1.7. Adsorption kinetics studies

The kinetics of adsorbate uptake is required for selecting optimum operating conditions for the full-scale batch process. Here the effects of initial concentration, contact time, and adsorbent dosage were analyzed from the kinetic point of view. The initial adsorption rate was rapid as more than 50% of equilibrium uptake was adsorbed within the first 10 min as discussed earlier (section 3.4.1.3). After that the adsorption proceeds at a comparatively slower rate until equilibrium reached. The adsorption kinetics was studied with respect to Lagergren first order and second order kinetic model. Validity of these two models was checked by performing kinetics under different initial metal concentration. The kinetic rate constants were calculated from the linearized kinetic plots. Lagergren first order model shown a correlation coefficient (R) of 0.988 on average, where the second-order kinetic model shown a higher R value of 0.998 on average. The χ^2 test was also done for best fit kinetic model. It has been found that χ^2 values were much

less in second-order model than that of first-order (Table 3.4). Therefore, the errors between the experimental and calculated q_t values were much less for second order kinetic model. Experimental results were also compared with the theoretical first and second order kinetic model graphically (Figure 3.10), and found to be fitted well with pseudo-second-order model. Thus, based on the high correlation coefficient (R), low χ^2 value, and well fitting of experimental data with second-order model, it can be said that Cu^{2+} adsorption onto TMA coated alumina preferably followed second order kinetic model than first order rate law.

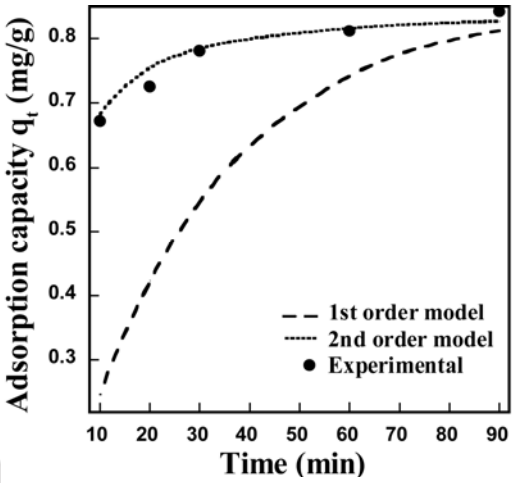

Figure 3.10. Comparison of experimental and modeled evaluation of adsorption kinetics of Cu^{2+}

Table 3.4. Comparison of first- and second-order kinetic model of Cu^{2+} adsorption

Initial concentration (mg L^{-1})	Experimental q_e value (mg g^{-1})	First order kinetics			Second order kinetics		
		k_1 (L min^{-1})	R value	χ^2	k_2 (g mg^{-1} min^{-1})	R value	χ^2
100	0.851	0.035	0.985	0.79	0.479	0.999	0.0076
150	1.23	0.029	0.982	1.78	0.250	0.999	0.0042
200	1.54	0.018	0.992	4.95	0.142	0.997	0.0190
250	1.86	0.022	0.992	4.27	0.135	0.999	0.0086

3.4.1.8. Effect of TMA concentration and comparison with uncoated alumina

The influence of TMA concentration in preparation of adsorbent and its efficiency on Cu^{2+} has also been studied in economic point of view. Three different adsorbents, containing 50 mg (I), 100 mg (II), and 200 mg (III) of TMA per 1 g of alumina were prepared and added separately in a series of 125–250 mg L^{-1} Cu^{2+} solution. A set of experiment was also done with uncoated alumina to compare the enhancement in adsorption efficiency upon TMA coating. At steady state, the adsorption efficiency decreased with increase of Cu^{2+} concentration in all of the four cases (Figure 3.11a). From the Figure 3.11a, it can be seen clearly that adsorption efficiency of uncoated alumina was much lower than that of TMA coated adsorbents (I, II, and III). Only 34.1% adsorption efficiency was achieved with uncoated alumina (in 125 mg L^{-1} of Cu^{2+}

concentration) and efficiency decreased to 9.8% upon increase in Cu^{2+} concentration to 250 mg L^{-1}. Adsorption study with three different TMA contained adsorbents revealed that, adsorption efficiency increased significantly from 71.8 to 95.0% (in 125 mg L^{-1} of Cu^{2+} solution) with adsorbents I and II, respectively. This indicates an increase in TMA concentration from 50 mg per g of alumina to 100 mg per g of alumina had a greater effect on Cu^{2+} adsorption. When the TMA concentration increased further up to 200 mg per g of alumina (adsorbent III), it showed very little increment in adsorbing capacity further compared to adsorbent II. About 96.7% adsorption was achieved with adsorbent III (in 125 mg L^{-1} of Cu^{2+} solution). Thus, only 1–2% increment in adsorption efficiency was achieved when TMA concentration onto alumina increased from 100 to 200 mg per g of alumina. Hence, the adsorbent II (100 mg TMA/g alumina) is almost saturated with TMA, and was also found to be most efficient than the other adsorbents (I, III, and uncoated alumina). Therefore, all the experiments performed with adsorbent II were efficient in commercial point of view.

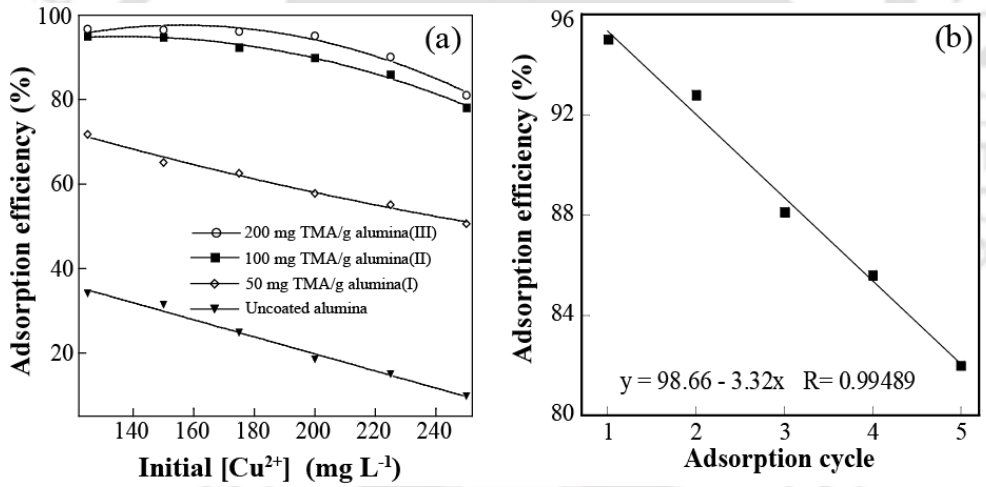

Figure 3.11. (a) Effect of different TMA concentration in preparation of adsorbent on Cu^{2+} adsorption and comparison with uncoated alumina, (b) Multi-cyclic adsorption efficiency of TMA coated alumina.

3.4.1.9. Desorption and multi-cyclic use of the adsorbent for Cu^{2+} interaction

Desorption of Cu^{2+} from the adsorbent surface were carried out in batch mode. HCl and H_2SO_4 were used to desorb the adsorbed Cu^{2+} from the surface. Concentration of the acids was varied from 0.2 to 1 M to get the optimum condition (Table 3.5). Almost ~100% recovery of the adsorbent was achieved by both HCl and H_2SO_4. The kinetics of desorption was also performed by taking out the samples after adding the desorbents, at a regular interval of time. It was found that desorption kinetics was faster than adsorption

kinetics. Maximum amount of Cu^{2+} (96–97%) was desorbed from the adsorbent within initial 5 min when mixed with 0.2 M HCl. 100% desorption obtained within 15 min. Acid treatment might displace some of the TMA molecules from the alumina surface as well. As a result decrease in adsorption efficiency of the adsorbent was noticed in further re-use. However, complete displacement of TMA from the alumina surface was not encountered. The adsorbent was air dried after desorption and re-used for the 5 continuous cycles under same conditions to check its multi-cyclic adsorption efficiency. It was found that the adsorption efficiency decreased from 95 to 82% only, after recycling of 5 times (Figure 3.11b). Well fitting of experimental data (R^2 = 0.994) confirms the linear decrease in activity of TMA coated alumina after 5 cyclic operation. Overall the adsorption efficiency remains at a considerable stage of ~82% after complete 5 cycle of adsorption–desorption process. This implies it retained a potent multi-cyclic adsorption capability in spite of acid treatment.

Table 3.5. Comparison of first- and second-order kinetic model of Cu^{2+} adsorption

Acid strength	Desorption efficiency (%)	
(M)	HCl	H_2SO_4
0.2	71.00	91.00
0.4	96.00	92.00
0.6	98.00	93.10
0.8	100.0	97.23
1.0	100.0	100.0

3.4.1.10. Summary

From the above study, we achieved the acidic 'hard' surface TMA coated alumina as a potent, cheap and water stable adsorbent for toxic Cu^{2+}. The interaction of Cu^{2+} could be controlled by controlling the solution pH which further controls the binding of carboxylic acid and Cu^{2+} ion. The carboxylic groups present on TMA can strongly bind the Cu^{2+} ions in aqueous solution. Adsorption efficiency enhanced by ~60% upon TMA coating compared to uncoated alumina. Kinetic and isotherm studies have revealed that TMA coated alumina is a potent adsorbent for divalent Cu^{2+} ion. The adsorption data fitted well in Langmuir isotherm and followed the second-order rate kinetics preferably. Maximum monolayer copper adsorption capacity (Q_m) was found 10.8 mg g^{-1}. In addition, the favourable thermodynamic properties proved this adsorption process to be spontaneous

and feasible. Moreover, multi-cyclic efficient adsorbing capability of Cu^{2+} made it a potential alternative for adsorption of toxic Cu^{2+} from wastewater.

3.4.2. Comparative interaction of Fe^{3+}, Fe^{2+} and other cationic pollutants

3.4.2.1. Background

Water pollution by toxic metals has gained relatively more significance in view of their persistence and toxicity. It has a major impact on the public health and the economy. Earlier it has been reported[3.25] that, in terms of the quantity of water needed to dilute such wastes to drinking-water standards, the annual toxicity of all metals mobilized, exceeds the combined total toxicity of the radioactive and organic wastes generated each year. The release of Fe^{3+}/Fe^{2+}, Co^{2+} and Ni^{2+} into terrestrial and aquatic ecosystems is attributed to many human activities, specially mining of ore deposits and industrial discharges. Typically, acid mine drainage (AMD), a potent threat to environment, is a rich source of dissolved iron.[3.26] AMD and most of the other contaminated surface water is highly acidic, where the Fe^{3+} is the predominant soluble species. Acute exposure to iron is characterized by vomiting, gastrointestinal bleeding, pneumonitis, convulsions, coma, and jaundice in human body.[3.27] Therefore, the removal of dissolved iron from mine drainage and industrial wastewaters is a great challenge for protection and restoration of aquatic resources. Iron can be removed from water system by simple pH adjustment, as Fe^{3+} precipitates as $Fe(OH)_3$ at pH > 4.0. Although precipitation method is cost effective and simple in use but it generates significant amount of sludge. Management of this highly insoluble hydroxide sludge is of prime concern to the environmental scientist due to its insoluble nature and difficulty in dewatering. Acid mine drainage contains high concentration of Fe^{3+} ion (100–150 mg L^{-1}). Precipitation method may not be appreciated due to high sludge generation. This generates a great need to develop remediation technologies. The adsorption phenomenon has still been found economically appealing for removal of toxic metal ions from wastewater by choosing some adsorbents under optimum operating parameters. Several studies on adsorption of Fe^{3+} by zeolite, activated carbon, tannic resins, palm fruit bunch etc.[3.28] were reported earlier. But, efficient removal of Fe^{3+} in natural high acidic condition is still a major problem. This section primarily describes adsorptive properties of Fe^{3+} from aqueous phase by TMA coated adsorbent. It also presents a comparative study of Fe^{3+} adsorption with Fe^{2+}, Co^{2+} and Ni^{2+} adsorption from aqueous solution. This study provides the insight into Fe^{3+} ion adsorption from aqueous solutions in terms of equilibrium, kinetics, isotherm and

thermodynamic parameters. Various system parameters for Fe^{3+} and Fe^{2+} adsorption such as initial ion concentration, time, pH, and temperature were optimized in this study. The acidic condition of this adsorption system closely resembles the natural polluted resources of Fe^{3+}. Hence, the practical applicability of this process can be assessed. In addition, recovery of metal ion, regeneration of adsorbent and multi-cyclic use of adsorbent was also studied.

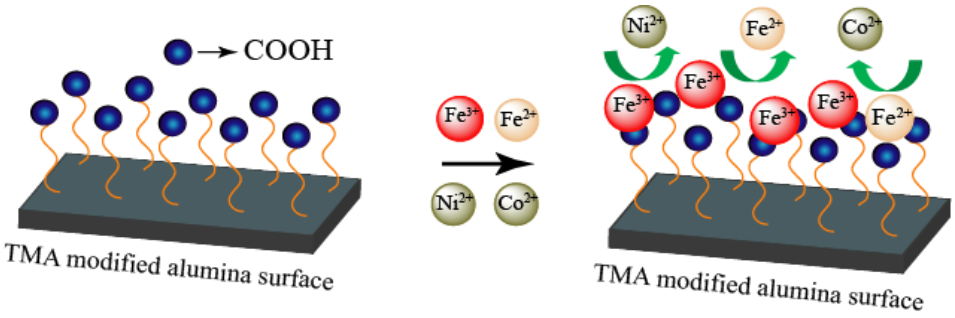

Scheme 3.2. Illustration of comparative and preferable interaction of Fe^{3+}/Fe^{2+} and other cations on TMA coated acidic 'hard' surface.

3.4.2.2. Materials and methods

Adsorption studies. A series of adsorption experiments were performed in batch mode. An amount of 50 mL aqueous solutions of metal ion of different concentrations were incubated with 5 g L^{-1} adsorbent. The adsorption kinetics were performed by withdrawing the samples at regular interval and centrifuged to obtain suitable aliquots for analysis of metal ion concentration. Rate constants of kinetic models were also calculated from the conventional rate equations. To study the influence of pH, solution pH was adjusted by adding 0.1 M NaOH and 0.1 M HCl and optimized for the highest adsorption efficiency for all metal ions. For adsorption isotherm experiments, solution pH was controlled as optimized before with different initial Fe^{3+} (20 – 200 mg L^{-1}) and Fe^{2+} (40 – 100 mg L^{-1}) concentrations. The adsorption capacity (q_e value, mg g^{-1}) for these metal ions was calculated in each case. The adsorption of Fe^{3+} and Fe^{2+} was also compared with the adsorption of other metal ions like Co^{2+} and Ni^{2+} in some cases. A couple of preliminary experiments were performed with Fe^{3+}, Fe^{2+}, Co^{2+} and Ni^{2+} under similar conditions to investigate the adsorption specificity of TMA coated alumina towards different metal ions. Control experiments were carried out in each case to validate the adsorption phenomenon. All the experiments were performed in duplicate and mean values were taken into account.

Desorption and re-adsorption study. Desorption efficiency of TMA coated alumina was studied for Fe^{3+} and Fe^{2+} adsorption. The adsorbent used for adsorption was separated from the aqueous solution by centrifugation and subsequent filtration to ensure complete separation. This adsorbent was then air dried and treated with 0.2 to 1 N HCl and H_2SO_4 solution to study the desorption phenomena of Fe^{3+}/Fe^{2+} ions. After acid treatment the adsorbent was washed multiple times with double distilled water and again air dried before reuse for three subsequent cycles. Reuse of the adsorbents was performed to study the multi-cyclic efficiency of the adsorbent.

3.4.2.3. Equilibrium studies

Adsorption equilibrium was studied with different initial concentrations of Fe^{3+} (100 – 200 mg L^{-1}) and Fe^{2+} (20 – 100 mg L^{-1}) at 25 °C separately. The adsorbent was added at a constant dose of 5 g L^{-1} separately in each sample. Initially, solution pH was found ~2.0 for Fe^{3+} and ~4.0 for Fe^{2+}, and was left uncontrolled at that value for this equilibrium study. Change in solution pH at equilibrium was insignificant (~2.5 for Fe^{3+} and ~4.2 for Fe^{2+}), which indicates little variation in solution pH throughout the adsorption process. Couple of control experiments containing only Fe^{3+} and Fe^{2+} confirmed no precipitation at this pH range respectively. Initially amount of adsorbed Fe^{3+} and Fe^{2+} increased with increase in contact time and remained nearly constant (a plateau stage) once it reached steady state (q_e) (Figure 3.13). For both Fe^{3+} and Fe^{2+}, adsorption was very fast as equilibrium reached within 60 min irrespective of initial concentration. No oxidation of Fe^{2+} was noticed during this time duration in the given condition as supported by the control experiments. At equilibrium, q_e value for Fe^{3+} was ~20 mg g^{-1} with 100 mg L^{-1} initial solution. About ~90% of the equilibrium Fe^{3+} uptake was adsorbed rapidly within first 15 min. This indicates a high adsorption rate for Fe^{3+}. The q_e value for Fe^{3+} increased from ~20 mg g^{-1} to ~26.0 mg g^{-1} with the change in initial Fe^{3+} concentration from 100 to 200 mg L^{-1} (Figure 3.13a). Adsorption process of Fe^{2+} is comparatively slower than that of Fe^{3+}. Equilibrium Fe^{2+} uptake (q_e)was only ~4.7 mg g^{-1} with an initial solution of 100 mg L^{-1}, which indicates much lower adsorption of Fe^{2+} compared to Fe^{3+} (Figure 3.13b). The equilibrium uptake (q_e) for Fe^{2+} decreased from 4.6 mg g^{-1} to 2.6 mg g^{-1} when the initial Fe^{2+} was decreased from 100 mg L^{-1} to 40 mg L^{-1}. In case of Cu^{2+} interaction, it was found that equilibrium reached within 120 min. Therefore, adsorption process of Fe^{3+} and Fe^{2+} is quite faster than Cu^{2+}. A similar set of experiment with Co^{2+} and Ni^{2+} revealed that the adsorption of was much less than all other metals (graph not

shown) as at equilibrium the q_e value was only ~1 mg g^{-1} for both Co^{2+} and Ni^{2+}, with 100 mg L^{-1} initial metal solution. It also took longer time of ~2–3 h to reach the equilibrium. From scanning electron micrograph it was found that TMA coated alumina is the aggregates of smaller crystallites with average dimension of < 1 μm (Appendix Figure A3.1). EDX spectra show the presence of Al, O and C in the adsorbent. Upon Fe^{3+} adsorption, the overall surface morphology of adsorbent was changed. It became more crystalline in nature and forms aggregates of micron size plates. The presence of iron on the surface of the adsorbent was confirmed by EDX spectrum. Powder XRD pattern of the adsorbent after Fe^{3+} adsorption is characteristic of iron deposited on the surface (Appendix, Figure A3.2).

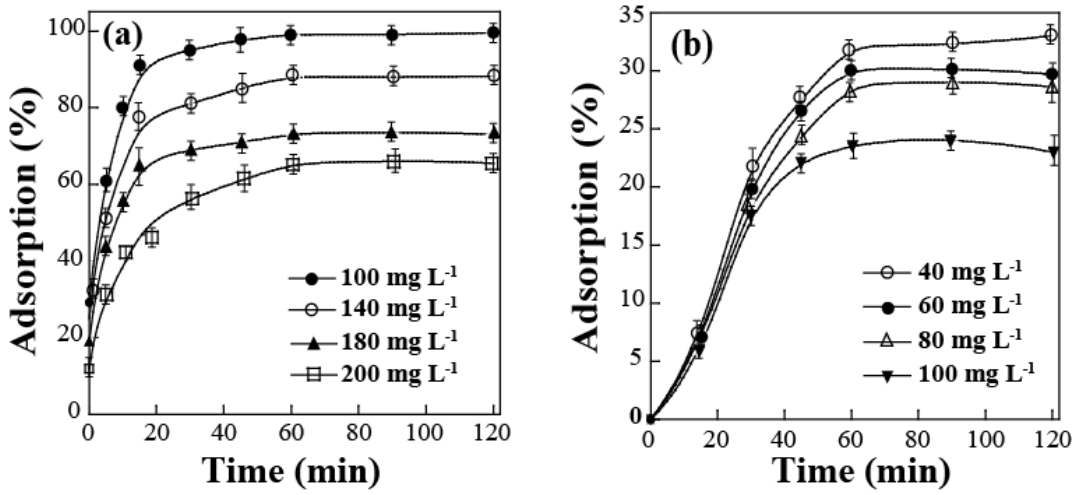

Figure 3.13. Effect of initial concentration on adsorption capacity of (a) Fe^{3+} and (b) Fe^{2+} ion onto TMA coated alumina.

3.4.2.4. Influence of solution pH

Solution pH has a significant role on adsorption as well as on precipitation for Fe^{3+} and Fe^{2+}. The adsorption experiment was carried out in a wide range of pH varied from 1 to 6. Two separate sets of Fe^{3+} and Fe^{2+} solution of 100 mg L^{-1} was taken and treated with 5 g L^{-1} adsorbent at 25 °C. At pH ~1.0, equilibrium Fe^{3+} adsorption (q_e) was much low ~3.0 mg g^{-1} (Figure 3.14a). This is might be due to the competitive adsorption of H^+ with Fe^{3+}. Amount of Fe^{3+}adsorbed (q_e) was found to increase from pH ~1.5. In the pH range of 1.5–3.0, the q_e value of Fe^{3+} was increased from ~12.6 mg g^{-1} to ~19.5 mg g^{-1}, while no precipitation took place (confirmed with blank solutions). This indicates an excellent Fe^{3+} adsorption capacity of TMA coated alumina even at pH of ~1.5, when most of the carboxyl group of TMA was in protonated condition (pK_a^1 of TMA = 2.84)[3.6]. At

pH ~3.0, some carboxyl groups of TMA are dissociated form and can strongly and preferentially bind 'hard' Fe^{3+} ions following Pearson's Hard Soft Acid Base (HSAB) principle. This reflects that Fe^{3+} can strongly binds with protonated as well as dissociated carboxyl group of TMA, which leads to high adsorption capacity of Fe^{3+} in a highly acidic pH condition. Precipitation of Fe^{3+} started beyond pH 3.0, and about 70–80% Fe^{3+} was found to be precipitated at pH ~4.0. Complete precipitation of Fe^{3+} occurred beyond pH 4.0 (Appendix Figure A3.3). Adsorption of Fe^{2+} was found to be much lower than that of Fe^{3+} (Figure 3.14b). Almost no Fe^{2+} adsorption was observed up to pH ~2.0 indicating poor adsorption efficiency at highly acidic pH. Only ~3.4 mg g^{-1} to ~5.6 mg g^{-1} Fe^{2+} was adsorbed at equilibrium (q_e) in the pH range of 3.0–5.0. Precipitation of Fe^{2+} started beyond pH 5.0 and almost ~100% Fe^{2+} precipitated at pH 6.0 (Appendix Figure A3.3).

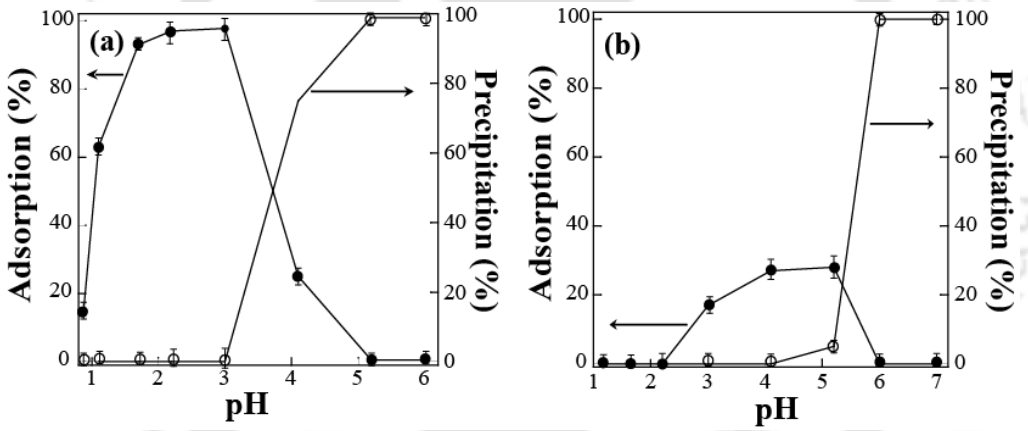

Figure 3.14. Effect of pH on adsorption and precipitation of 100 mg L^{-1} separate solution of (a) Fe^{3+} and (b) Fe^{2+} ion.

To study the competitive adsorption nature of Fe^{3+} and Fe^{2+}, another set of experiment was performed with an equi-molar mixed solution of Fe^{3+} and Fe^{2+}. Equimolar amount (0.2 moles) of Fe^{3+} and Fe^{2+} was mixed in a solution and treated with 5 g L^{-1} adsorbent. Adsorption of Fe^{3+} in a mixed solution was quite comparable with that of Fe^{3+} in a pure solution. The q_e value of Fe^{3+} in a mixed solution increased from 12.6 mg g^{-1} to 19.4 mg g^{-1} while increasing the pH from 1.5 to 2.0 (Figure 3.15a), which is quite similar of Fe^{3+} removal in pure solution. Whereas, the equilibrium uptake (q_e) of Fe^{2+} in mixed solution was found to be decreased even further than that of Fe^{2+} in pure solution. Only ~1.4 mg g^{-1} of Fe^{2+} was adsorbed in a mixed solution at pH range of 3.0–5.0 (Figure 3.15b). This indicates a much higher affinity of 'hard' base carboxylate of TMA towards

'hard' acid Fe^{3+} than border-line Fe^{2+} in mixed solution. Hence, in mixture there is a decrease in adsorption efficiency of Fe^{2+} compared to Fe^{3+}. Moreover, the precipitation nature of these ions in a mixed solution is different from the pure solutions (Appendix Figure A3.3).

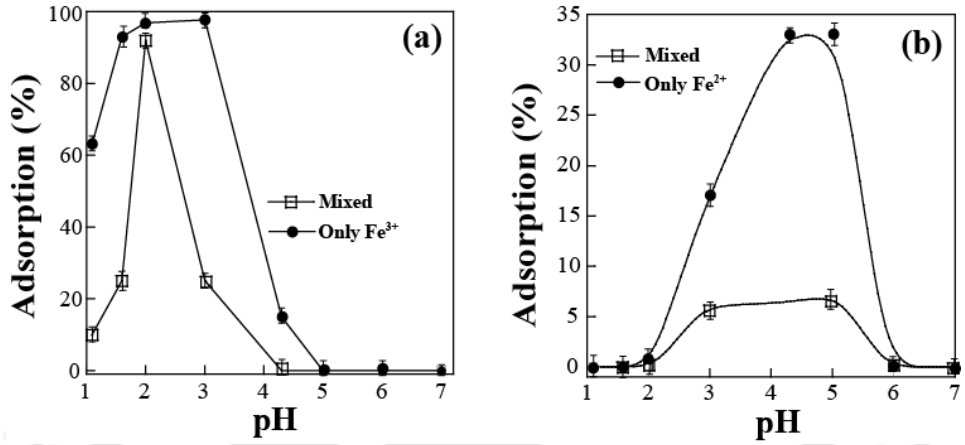

Figure 3.15. Competitive adsorption studies of (a) Fe^{3+} and (b) Fe^{2+} in an equi-molar mixed ion solution.

Precipitation of Fe^{3+} in a mixed solution started earlier at pH ~3.0; whereas, precipitation of Fe^{3+} in a pure solution was found to start beyond pH ~4.0. Similar kind of effect was observed in case of Fe^{2+} ion also. About ~70–80% of Fe^{2+} was precipitated at pH 5.0 in mixed ion solution where only ~5% precipitation was found in a pure Fe^{2+} solution at that pH. Thus, it can be said that the mixed ions has a tendency to precipitate earlier compared to each of their individual solutions. In our previous section with Cu^{2+} adsorption, maximum adsorption capacity was ~11.0 mg g^{-1} at pH 5.0, while the precipitation of Cu^{2+} started beyond pH 5.0. High removal of Fe^{3+} in highly acidic solution states its favourability in removing iron from acidic wastewaters compared to Cu^{2+}. Most importantly, by adsorption, Fe^{3+} concentration can be reduced to ~3–5 mg L^{-1} (with initial concentration up to 100 mg L^{-1}) which obeys the Best Available Technology (BAT) discharge limits for acid mine wastewater (< 7.0 mg L^{-1} daily).[3.29] This indicates a highly efficient adsorption system to meet the environmental protection requirement. The adsorption efficiency of Co^{2+} and Ni^{2+} was studied at different pH range and compared with iron and copper adsorption. Removal efficiency of Co^{2+} and Ni^{2+} remained almost constant ~5% with 100 mg L^{-1} solution in a pH range of 2.0–5.0. At a higher pH of ~6.0 or beyond, precipitation of Co^{2+} and Ni^{2+} started. This indicates a much lower adsorption efficiency of Co^{2+} and Ni^{2+} than either of Fe^{3+}/Fe^{2+} or Cu^{2+} by this adsorbent.

3.4.2.5. Influence of temperature

Temperature of this adsorption experiment was varied to study thermodynamic feasibility of adsorption process. Adsorption of 100 mg L^{-1} of both Fe^{3+} and Fe^{2+} was performed (with 5 g L^{-1} adsorbent dose) at 25 °C and 50 °C separately. Solution pH was maintained at ~2.0 for Fe^{3+} and ~4.0 for Fe^{2+}. At equilibrium, q_e value was found to be almost same at both 25 °C and 50 °C in both cases. This indicates that temperature did not have much effect on adsorption efficiency of Fe^{3+} and Fe^{2+} (Figure 3.16). Standard Gibbs free energy change (ΔG^0) of adsorption was calculated for both temperatures.

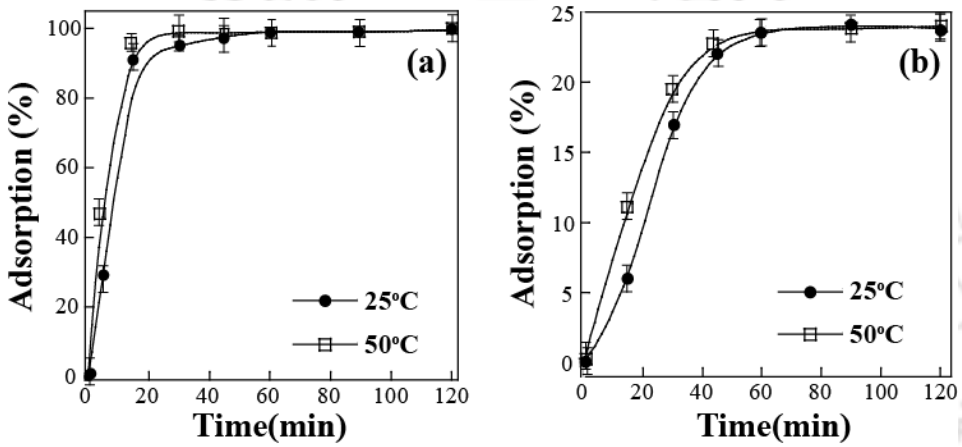

Figure 3.16. Effect of temperature on amount adsorbed of (a) Fe^{3+} and (b) Fe^{2+} ion on TMA coated alumina surface.

The ΔG^0 values at 25 °C were found to be −24.5 kJ mol^{-1} and −14.1 kJ mol^{-1} for Fe^{3+} and Fe^{2+}, respectively. Again, at 50 °C the ΔG^0 values were almost same as found at 25 °C for both Fe^{3+} and Fe^{2+}. Thus, ΔG^0 of the adsorption remain invariant with temperature. The negative values of ΔG^0 at both temperatures suggest that the adsorption process was spontaneous and thermodynamically favourable. Higher negative value of ΔG^0 for Fe^{3+} indicates a higher driving force compared to Fe^{2+}. Adsorption of Cu^{2+} onto TMA coated alumina had an driving force of −12.8 kJ mol^{-1} at 25 °C, which is almost similar to Fe^{2+} but much less than Fe^{3+}. Moreover the Cu^{2+} adsorption was found to be an exothermic process as the ΔG^0 value decreased from −12.8 kJ mol^{-1} to −8.9 kJ mol^{-1} when the temperature increased from 25 °C to 50 °C.

3.4.2.6. Initial metal ion concentration and adsorption isotherm

Initial metal ion concentration plays an important role in affecting the adsorption capacity (q_e) of the adsorbent. In this adsorption process, experimental data were fitted in

Langmuir, Freundlich and Temkin isotherm model. About 5 g L^{-1} adsorbent was added in a series of 20–200 mg L^{-1} Fe^{3+} and 20–100 mg L^{-1} Fe^{2+} solution separately. The adsorption isotherm plots for Fe^{3+} and Fe^{2+} are shown in Figure 3.17. High affinity for adsorption of Fe^{3+} and Fe^{2+} on TMA coated surface was observed at low metal ion concentration. In case of Fe^{3+}, initially q_e value increased from ~3.98 mg g^{-1} to ~26.0 mg g^{-1} when the C_e value increases from ~0.06 mg L^{-1} to ~30.5 mg L^{-1}. Beyond this C_e value, q_e almost became constant at ~26.0 mg g^{-1} for Fe^{3+} (Figure 3.17a). Whereas for Fe^{2+}, q_e increased from ~0.4 mg g^{-1} to ~4.7 mg g^{-1} with the increase in equilibrium Fe^{2+} concentration from ~18.0 mg L^{-1} to ~76.5 mg L^{-1} (Figure 3.17b). The experimental results were found to match well with the linearized Langmuir isotherm plot for both the cases ($R_{Fe(III)} = 0.999$, $R_{Fe(II)} = 0.973$). This indicates a monolayer adsorption process (constant heat of adsorption for all sites) which needs same activation energy for each molecule to adsorb. The Langmuir isotherm constants for $Fe^{3+}$and Fe^{2+} were determined from linearized Langmuir plot and listed in Table 3.5. Langmuir binding constant for Fe^{3+} was much higher (~1.05 L mg^{-1}) than that of Fe^{2+} (~0.018 L mg^{-1}). Maximum metal uptake (Q_m) for Fe^{3+} and Fe^{2+} calculated from the Langmuir model was 26.6 mg g^{-1} and 8.4 mg g^{-1}, respectively. Other isotherm models like Freundlich and Temkin showed a less correlation coefficient compared to Langmuir model for both Fe^{3+} and Fe^{2+}. The isotherm model constants for these models are given in Table 3.5. This indicates a higher adsorption capacity for Fe^{3+} compared to Fe^{2+}. Whereas, in our previous study, Q_m for Cu^{2+} was found to be ~10.8 mg g^{-1}, which is also lower than that of Fe^{3+}. As described by Hall *et al.*,[3.21] "constant separation factor" or "equilibrium parameter", R_L for these experiments, was found to be 0.009 for Fe^{3+} and 0.357 for Fe^{2+}. This reflects the favourability of Langmuir model for both the ions. In case Cu^{2+} adsorption studied previously, isotherm data was also found to be fitted well with Langmuir model. In addition, the Chi-square test was also done for error analysis.[3.23] From the experimental data, the χ^2 value of Langmuir model (0.42 for Fe^{3+} and 0.026 for Fe^{2+}) was found very low compared to other isotherm model, which indicates small deviation between experimental data and Langmuir model. Moreover, for Cu^{2+} also the χ^2 value was also found to be low in case of Langmuir model. Therefore, the uptake of all the three metal ions (Fe^{3+}, Fe^{2+} and Cu^{2+}) preferably follows the monolayer adsorption process, where coulombic interaction is the dominant driving force.[3.24]

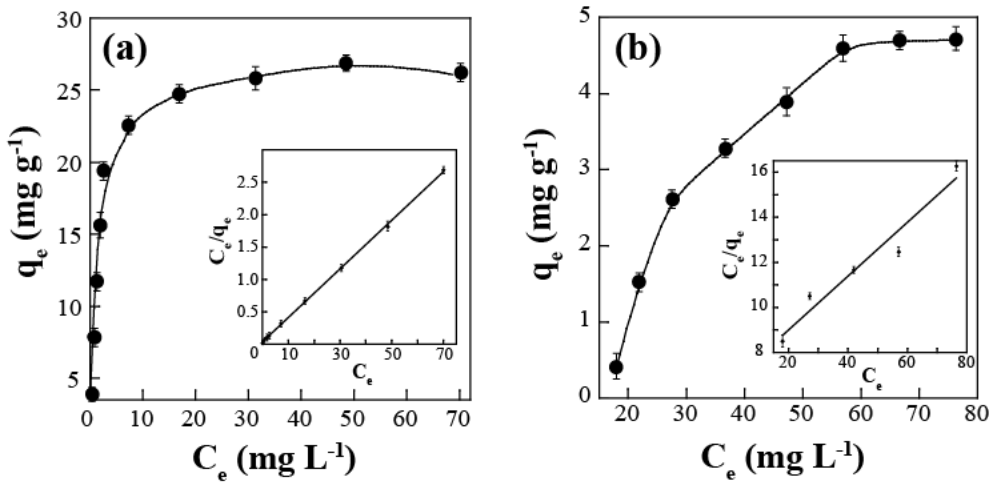

Figure 3.17. Adsorption isotherm of (a) Fe^{3+} and (b) Fe^{2+} ion adsorption, and linearized Langmuir model for Fe^{3+} and Fe^{2+} ion adsorption (*inset*).

Table 3.5. Parameters of different adsorption isotherm model for Fe^{3+} and Fe^{2+} adsorption

Ions	Langmuir isotherm			Freundlich isotherm				Temkin isotherm	
	Q_m (mg g^{-1})	b (L mg^{-1})	R	K_f (mg g^{-1})	n	R	A (L g^{-1})	m	R
Fe^{3+}	26.6	1.05	0.999	11.09	3.83	0.944	45.33	697.9	0.978
Fe^{2+}	8.4	0.018	0.973	0.353	1.62	0.971	0.127	1143.8	0.975

3.4.2.7. Adsorption kinetics

Initial adsorption was found rapid for Fe^{3+} but comparatively slower in case of Fe^{2+} as described previously. The adsorption kinetics was studied with respect to first order and second order kinetic model. Adsorption kinetics experiments were carried out with different initial metal concentration to validate these models. Pseudo second order kinetic model has shown high correlation coefficient (R) value for both Fe^{3+} and Fe^{2+} compared to first order model, in all the cases (Table 3.6). It has been found that χ^2 values were very small in second order model for both of Fe^{3+} and Fe^{2+} (Table 3.6). Therefore, the errors between the experimental and calculated q_t values were very less for second order kinetic model. A graphical comparison of experimental results with the theoretical second order kinetic model with different metal concentration was also done (Figure 3.18), and found to be fitted well with second order model for all the concentrations. Thus, based on the high correlation coefficient (R), low χ^2 values, and well fitting of experimental data with second order model, it can be anticipated that Fe^{3+} and Fe^{2+} adsorption onto TMA coated

alumina followed second order adsorption model preferably. Similar nature was observed in case of Cu^{2+} adsorption which was also fitted well in second order model.

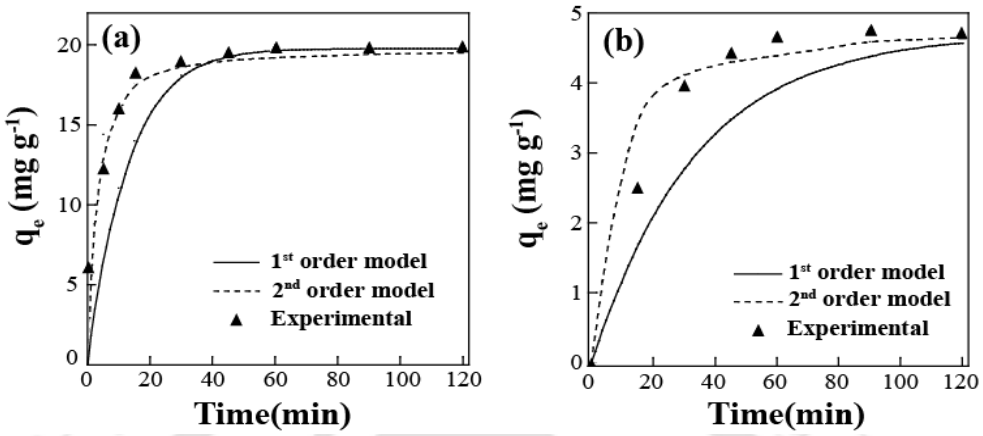

Figure 3.18. Comparison of experimental data and second order kinetics with 100 mg L^{-1} solution of (a) Fe^{3+} and (b) Fe^{2+} ion.

Table 3.6. Comparison of first and second order kinetic model for Fe^{3+}/Fe^{2+} adsorption.

Ionic Species	Initial conc. (mg L^{-1})	Experi-mental q_e (mg g^{-1})	First order kinetics			Second order kinetics		
			k_1 (L min^{-})	R value	χ^2	k_2 (g mg^{-1} min^{-1})	R value	χ^2
Fe^{3+}	100	19.8	0.082	0.976	8.121	0.027	0.998	0.438
	140	24.64	0.062	0.970	18.06	0.016	0.998	0.300
	180	26.2	0.069	0.969	16.65	0.0169	0.999	0.406
	200	26.0	0.055	0.994	9.70	0.008	0.995	0.638
Fe^{2+}	40	2.56	0.025	0.730	0.513	0.056	0.990	0.085
	60	3.60	0.023	0.574	1.025	0.043	0.989	0.064
	80	4.56	0.012	0.355	7.390	0.029	0.987	0.162
	100	4.70	0.030	0.597	0.735	0.051	0.994	0.044

3.4.2.8. Adsorption mechanism of Fe^{3+} and Fe^{2+}

The selective adsorption of Fe^{3+} by TMA coated alumina can be explained by the coordination chemistry of the TMA. Formation and stability of metal–ligand complexes depended on several factors such as size and charge of metal ions, ligand field effect, etc. According to their preferential bonding, ligand and metal ions were classified in two different classes.[3.30,3.31] Pearson[3.32] introduced the term 'hard' and 'soft' to describe these two classes of metals and ligands. In addition to these fundamental 'hard' and 'soft'

categories, "borderline acids and bases" are useful which are having intermediate properties of 'hard' and 'soft' categories. Pearson also proposed a rule to predict the formation and stability of the metal–ligand complexes. According to Pearson's rule, 'hard' acids prefer to bind to 'hard' bases and soft acids prefer to bind to soft bases. Our study of Fe^{3+} and Fe^{2+} adsorption by TMA coated alumina could be well described with this HSAB principle. According to the classification of the metal ions ('hard' or 'soft' acids), Fe^{3+} is 'hard' acid because of its small size and high charge whereas Fe^{2+} resides in "borderline acid" group because of its relatively larger size and lower charge. Hence 'hard' base TMA forms a stronger and stable complex with 'hard' acid Fe^{3+} compared to borderline acid Fe^{2+}, according to Pearson's rule. Same explanation is valid for other two borderline metal ions Co^{2+} and Ni^{2+}. In addition, species having high electronegativities (Fe^{3+}, $\chi = 1.96$) are 'hard' and those having low electronegativities (Fe^{2+}, $\chi = 1.8$)[3.31] are soft. Therefore TMA, which contains multiple carboxylate groups (a 'hard' base), is selective towards 'hard' acid Fe^{3+} than the borderline acid $Fe^{2+}/Co^{2+}/Ni^{2+}$. From our experimental data we found that, the ΔG^0 value for Fe^{3+}adsorption with TMA (~25.0 kJ mol^{-1}) was higher than that of Fe^{2+} (~14.0 kJ mol^{-1}). Also the binding constant for Fe^{3+} was much higher (~1.05 L mg^{-1}) compared to the binding constant for Fe^{2+} adsorption (~0.018 L mg^{-1}).

3.4.2.9. Comparison of TMA coating with uncoated alumina

A set of experiment was done with uncoated alumina to compare the enhancement in adsorption efficiency upon TMA coating. In this study, solution pH was kept at their optimized value of ~2.0 for Fe^{3+} and ~5.0 for Fe^{2+} to compare the adsorption efficiency of TMA coated alumina with uncoated alumina under similar condition. From Figure 3.19a, it can be seen clearly that adsorption efficiency of uncoated alumina was much lower than the TMA coated adsorbents for both Fe^{3+} and Fe^{2+}. Adsorption capacity by TMA coated alumina was ~20.0 mg g^{-1} for Fe^{3+} (with 100 mg L^{-1} solution), while with uncoated alumina it was only ~6.2 mg g^{-1} for the same. Similar observation was also made for Fe^{2+} (Figure 3.19b). Only ~1 mg g^{-1} of Fe^{2+} was adsorbed with uncoated alumina (with 100 mg L^{-1} of Fe^{2+} solution) and it increased up to ~5.4 mg g^{-1} upon TMA coating. Moreover, from our previous study we found that synthesized adsorbent was saturated with TMA and shown high adsorption capacity for Cu^{2+} compared to uncoated one as well.

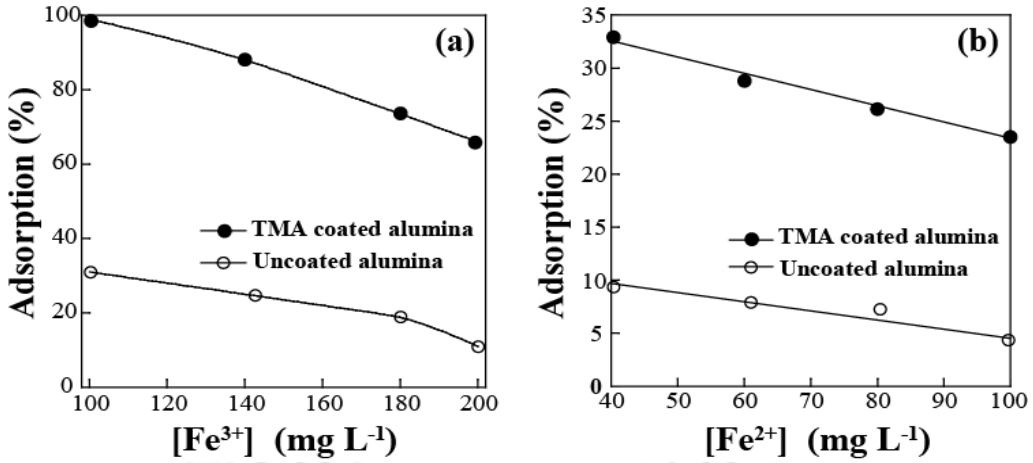

Figure 3.19. Comparison of TMA coated alumina with uncoated alumina for the enhancement in adsorption of (a) Fe^{3+} and (b) Fe^{2+} upon TMA coating.

3.4.2.10. Summary

We have used TMA coated alumina for adsorption of Fe^{3+}, Fe^{2+}, Co^{2+} and Ni^{2+} ions from aqueous solution successfully. The interaction of these cationic species could be controlled and preferential binding of Fe^{3+} was observed from a competitive solution. A detailed comparative study has been performed to evaluate the specificity of the adsorbent towards a particular metal ion. Kinetic studies revealed that it is a highly efficient adsorbent for Fe^{3+} (~20 mg g^{-1}), even at high acidic pH ~1.5–2.0. Thus, it can be a good choice for Fe^{3+} removal from acidic wastewaters such as mine drainages. Adsorption efficiency increased significantly (~68%) upon TMA coating than uncoated alumina. Comparison among different metal ions revealed that, TMA coated alumina has much higher adsorption affinity towards Fe^{3+} (~20.0 mg g^{-1}) compared to Fe^{2+} (~5.4 mg g^{-1}), Co^{2+} (~1 mg g^{-1}) and Ni^{2+} (~1 mg g^{-1}). The comparison has been explained on the basis of coordination chemistry of the TMA, the active adsorbent. Adsorption process of both Fe^{3+} and Fe^{2+} fitted well in Langmuir model and followed the second order rate kinetics preferably. Maximum monolayer adsorption capacity (Q_m) was found 26.6 mg g^{-1} for Fe^{3+} and 8.4 mg g^{-1} for Fe^{2+}. Negative values of ΔG^0 (−24.5 kJ mol^{-1} for Fe^{3+} and −14.1 kJ mol^{-1} for Fe^{2+}) proved this process to be spontaneous and feasible even at 50 °C. Reasonable adsorption capacity in subsequent adsorption cycles can assess the applicability of this adsorbent for reuse. Moreover, removal of Fe^{3+} by TMA coated alumina meets the criteria of Best Available Technology (BAT) discharge limits for acid mine wastewater (less than ~7.0 mg L^{-1} daily) with initial concentration up to 100 mg L^{-1}.

Hence, TMA coated basic alumina is found to be a potent adsorbent for metal ions with a very high adsorbing capacity for Fe^{3+} from aqueous solution.

3.4.3. Selective interaction of phosphate (PO_4^{3-}) and other anions

3.4.3.1. Background

Phosphate is essential for the growth of photosynthetic algae and cyanobacteria. Thus excessive supply of phosphorus from runoff into water bodies (e.g. lakes, rivers, creeks etc.) causes eutrophication, which is the abundance of aquatic plants, growth of algae, and depletion of dissolved oxygen. Another important environmental setback is the red tide found in lake and sea which caused by eutrophication. Therefore, the removal of phosphate from wastewater before discharge is important. To meet the maximum phosphate discharge limits, treated wastewaters from municipalities and industrial effluents with phosphorous content less than 2.0 mg L^{-1},[3.33] but still it may responsible for eutrophication, which leads to short and long-term environmental and aesthetic problems in lakes, coastal areas, and other confined water bodies. In recent past variety of methods has been employed to remove phosphate, but most of them are dealt with relatively higher concentration of phosphate which left the effluent P concentration well above 2 mg L^{-1} in most of the cases. Typical removal methods for high concentration of phosphate consist of biological treatments such as the conventional activated-sludge process, chemical treatments such as flocculation with Al, Fe, and Ca components. However, in the case of a lower concentration of phosphate, bio-treatment and precipitation are not much effective. Instead, adsorption methods can show effective removal efficiency in lower phosphate concentration. Diverse solid materials, including fly ash,[3.34] activated alumina, natural adsorbent, goethite and polymeric ligand exchanger[3.35] have been applied as adsorbent for phosphate. But most of them work well in a selective acidic or neutral range of pH[3.36] not in a broad pH range. Moreover, selectivity of a desired ion from a multiple component system is an important aspect in adsorption process. Based on the risk of very dilute contaminants in water and more stringent standards imposed as discussed earlier, it is important to develop new kinds of selective and efficient adsorbents. However, no such studies were found to be reported which could selectively uptake phosphate from an aqueous solution in a wide pH range.

In this section the enhanced and selective adsorption of phosphate from aqueous solution throughout a broad pH range (pH ~1.0 – 8.0) has been studied. The efficiency of this system in low phosphate concentration solution such as 1 mg L^{-1} has also been studied.

These constraints of phosphate removal were never encountered before. The probable mechanism of phosphate adsorption on carboxylic functional groups in different pH has been explained. Moreover, complete desorption of phosphate and regeneration of adsorbent after adsorption was studied. This study provides the insight into selective phosphate interaction from aqueous solutions in terms of equilibrium, kinetics, isotherm and thermodynamic parameters.

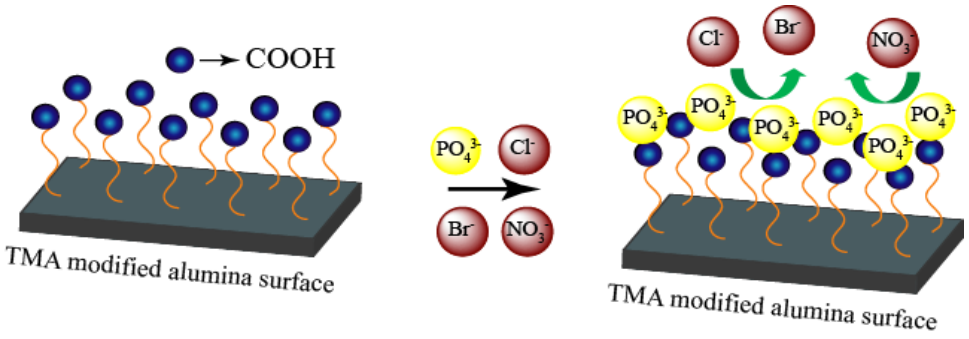

Scheme 3.3. Schematic illustration of controlled interaction of phosphate and other anion on TMA coated alumina surface.

3.4.3.2. Materials and methods

Adsorption studies. Adsorption experiments were conducted in batch technique to obtain kinetic and equilibrium data. The experiments were carried out in 100 mL screw capped vials containing 50 mL of phosphate solutions of different concentrations (1 - 100 mg L^{-1}) with 20 g L^{-1} adsorbent. The pH of the adsorption experiments was varied (by 0.1 M HCl and NaOH) from 1.0 to 14.0 to check the adsorption efficiency of TMA modified alumina from higher acidic to basic region. Kinetics experiments were carried out at different time interval by withdrawing the aliquot of supernatant from the adsorption mixture. The sample withdrawn from solution at regular time interval was immediately filtered through 0.2 µm Millipore filter paper to stop further reaction. Analysis of phosphate was done spectrophotometrically by stannous chloride method.[3.37] Adsorption isotherms were studied with varying concentrations of phosphate (1 - 100 mg L^{-1}) with fixed amount of adsorbent (20 g L^{-1}) at high acidic pH (~1.0). FT-IR characterization (4000 - 450 cm^{-1}) of the adsorbent before and after phosphate adsorption was done. After adsorption, the adsorbent was treated with 0.1-0.5 M NaOH solution for phosphate desorption. Samples were withdrawn at regular time interval and subsequently filtered to separate the desorbed phosphate solution from the adsorbent. Amount of phosphate desorbed in solution was measured in a fixed time interval by stannous chloride method. Control was taken in each case and all experiments were performed in duplicate for data consistency.

Selectivity of phosphate adsorption. A competitive adsorption experiments were performed with different anions to find out the selectivity of phosphate adsorption. A mixture of solution was prepared in distilled water containing chloride, nitrate, bromide and phosphate ion of individual concentration of 0.05 mM each. About 20 g L^{-1} adsorbent was added in this mixed solution (pH ~1.0) and left on constant stirring up to 400 min which was found sufficient to reach equilibrium for all the ionic species as studied individually in preliminary experiments. The individual anion concentration in the mixed solution, before and after adsorption was measured by ion chromatography.

3.4.3.3. Adsorption steady state and kinetic model.

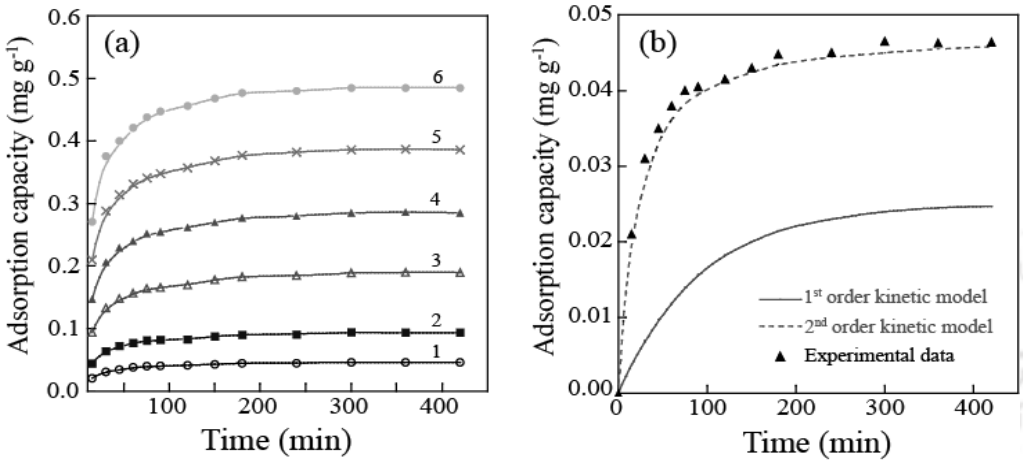

Figure 3.20. (a) Kinetics of adsorption for different initial phosphate concentration, and (b) Comparison of experimental data with first and second order kinetic model.

Adsorption capacity of this adsorbent as a function of time with varying phosphate concentrations (1 – 10 mg L^{-1}) are shown in Figure 3.20a. The phosphate solutions were equilibrated with 20 g L^{-1} adsorbent at pH ~1.0. In this pH aqueous phosphoric acid (H_3PO_4) is the predominant ionic species which can bind with TMA via hydrogen bonding. Initially adsorption is fast leading to almost equilibrium conditions after which the steady state reached within 180 min. Although steady state reached after same time duration, an increase in adsorption capacity (q_e, mg g^{-1}) was observed with the increase of initial phosphate concentration. Increase in phosphate concentration accelerates the diffusion of phosphate from the bulk solution onto adsorbent due to high concentration gradient.[3.38] Therefore, the q_e value increased from 0.046 mg g^{-1} to 0.48 mg g^{-1} while the initial phosphate concentration was increased from 1 mg L^{-1} to 10 mg L^{-1}. Almost 93% adsorption of phosphate was achieved with initial P concentration as low as 1 mg L^{-1}. To

evaluate the differences in adsorption kinetic rates with different initial phosphate concentration, the kinetics of phosphate adsorption is described with first order and second order kinetic model.

The linearized curve fits (Appendix, Figure A3.8) were plotted from the first and second order model. The kinetic rate constants and correlation coefficients values were then calculated and listed in Table 3.7. However, the adsorption of phosphate on TMA coated alumina seemed to be described better by pseudo second order equation. Second order model showed a higher correlation coefficient (R) than that of first order model irrespective of initial phosphate concentration. The initial sorption rate (h) for second order model was raised from 0.002 to 0.039 mg g^{-1} min^{-1} with increase in initial phosphate concentration from 1 to 10 mg L^{-1}. Moreover, the experimental data were compared together with pseudo first and second order models (Figure 3.20b). The second order model matches well with the experimental data, as first order model was far underestimated the actual amount of phosphate adsorbed. The χ^2 tests were also performed for error analysis between experimental and modeled kinetic equations.

Table 3.7. Kinetic parameters of phosphate adsorption on trimesic acid coated alumina.

Initial phosphate (mg L^{-1})	Experimental q_e (mg/g)	First order kinetic model			Second order kinetic model			
		R	k_1 (min^{-1})	χ^2	R	k_2 (g mg^{-1} min^{-1})	h (mg g^{-1} min^{-1})	χ^2
1	0.046	0.970	0.011	0.083	0.999	1.190	0.002	$5x10^{-5}$
4	0.190	0.979	0.013	0.125	0.999	0.322	0.011	$7x10^{-4}$
8	0.386	0.991	0.015	0.281	0.999	0.187	0.027	0.001
10	0.485	0.985	0.016	0.459	0.999	0.169	0.039	0.001

3.4.3.4. Influence of pH and interaction mechanism

The pH of the adsorption system was varied from 1.0 to 14.0 to study its effect on phosphate adsorption. Adsorption capacity at different pH with two different initial phosphate concentrations is shown in Figure 3.21. Special focus has been given on the highly acidic region where we found a significant phosphate removal. Steady and high removal efficiency (~93 – 96%) of phosphate was observed over a broad pH range of ~1.0 – 8.0 and adsorption efficiency decreases drastically beyond pH ~8.0 and reaches

almost zero at pH ~14.0 (Figure 3.21). It is expected that the adsorption of phosphate (at different ionic forms) on TMA occurs through the formation of strong intermolecular O–H···O hydrogen bonding between phosphate and carboxyl moieties (Figure 3.22). Depending upon the pH and dissociation constant of the phosphate and carboxyl groups, number of hydrogen bond varied which results in the alteration of adsorption capacity. At pH < 2.0 (pK_a^1 of TMA is ~2.8 and phosphate is ~2.2) both the adsorbate and adsorbent are fully protonated. Hence, it is anticipated that –P–OH and –P=O groups of phosphate can form one or two H-bonds with –C=O and –OH groups of TMA respectively as shown in Figure 3.22a. The pK_a^2 value of phosphoric acid is ~7.2.

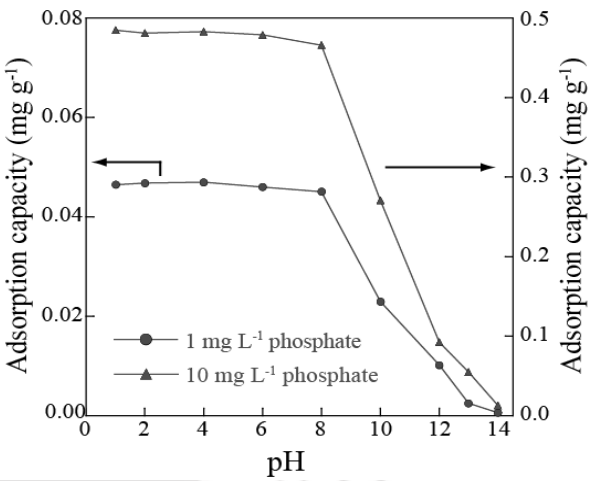

Figure 3.21. Influence of pH on phosphate adsorption on trimesic coated alumina.

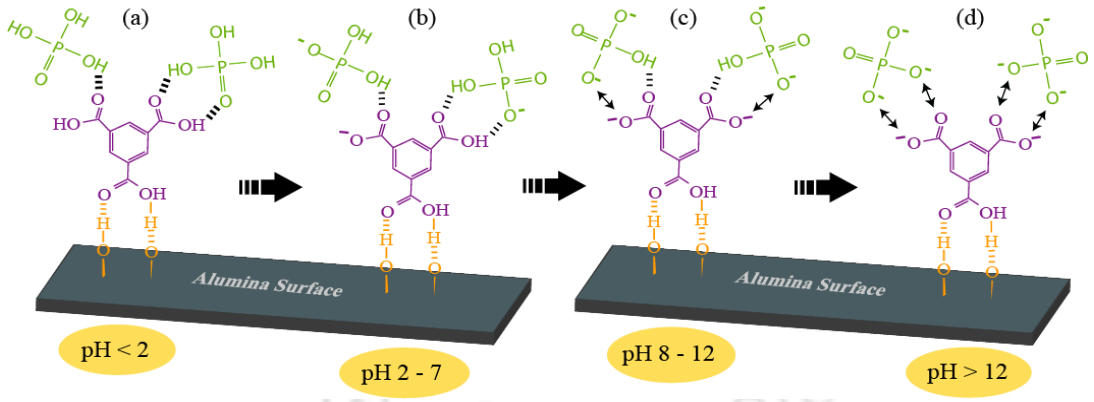

Figure 3.22. Schematic representation of probable surface complexes between phosphate and trimesic acid attached on alumina surface at different pH.

Hence, at pH range 2.0 to 7.0 the predominant species is $H_2PO_4^-$, which acts as two hydrogen bond donors as well as two hydrogen bond acceptors. In this pH range also it forms strong intermolecular –O–H···O type hydrogen bond with already deprotonated TMA (pK_a^2 = 3.7 and pK_a^3 = 4.8) attached to the solid surface (Figure 3.22b). However, at pH > 8.0 the predominant species is HPO_4^{2-}, which is having only one hydrogen bond donor group. Moreover, the repulsion between the two negatively charged species

become dominant (Figure 3.22c) and the adsorption capacity started to decrease. Beyond the third dissociation constant of phosphate (pH > 12.0) strong electrostatic repulsion between the fully deprotonated carboxylic group and PO_4^{3-} leads to a complete reduction in adsorption (Figure 3.22d). FT-IR spectra of the adsorbent were taken before and after the adsorption process (Appendix, Figure A3.10). The broad peak centered on 3400 cm^{-1} is attributed to stretching frequency of H-bonded –O–H group.[3.11,3.39] The –C=O stretching gives rise to absorption at ~1630 cm^{-1} in both the cases. At ~1450 cm^{-1}, a shoulder of –O–H stretching is found. The new peaks at ~1250 and ~1100 cm^{-1} found after adsorption of phosphate are characteristic stretching frequencies of P=O vibration.

3.4.3.5. Isotherm studies of phosphate adsorption

The equilibrium adsorption isotherm of phosphate removal is presented in Figure 3.23a. The initial phosphate concentration was varied from 1 to 100 mg L^{-1} and stirred with 20 g L^{-1} of adsorbent at pH ~1.0. The mixed solution was stirred up to 200 min at 25 °C to ensure steady state. According to the slope of initial portion of the curve, as seen from Figure 3.23a, the adsorption isotherm may be classified as H-type of the Giles' classification.[3.40] The H-type isotherms are the most common and correspond to high affinity of adsorbate for a given adsorbent. Hence, competition from the solvent for adsorption sites was not observed. As the isotherm tends to plateau, it seems reasonable to assume that complete coverage of the adsorbent surface occurs and steady state is reached. The adsorption isotherm of phosphate (predominate as H_3PO_4 in pH ~1.0) onto TMA coated alumina was analyzed by Langmuir and Freundlich isotherm models.

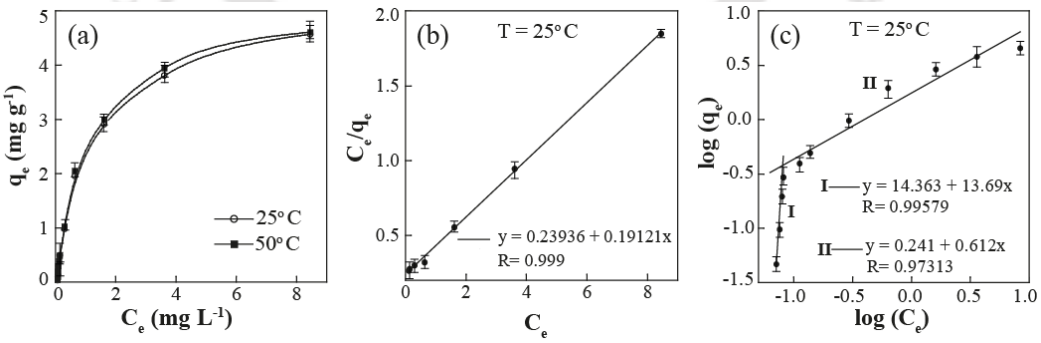

Figure 3.23. (a) Adsorption isotherms at 25°C and 50°C. (b) Langmuir isotherm model and (c) Freundlich isotherm model.

The Langmuir plot (Figure 3.23b) represented a good agreement with the experimental data. This suggests a monolayer coverage of phosphate on adsorbent surface. The

maximum uptake capacity (Q_m) and Langmuir binding constant (*b*) at 25 °C were calculated from this linearized plots and listed in Table 3.8. Maximum uptake capacity (Q_m) was 5.2 mg g^{-1}. The "constant separation factor" or "equilibrium parameter," R_L, was also calculated to evaluate the favorability of Langmuir adsorption process. The value of R_L was 0.05 which is consistent with the favorability of the adsorption process. The experimental data could be described with Freundlich model to lesser extent as seen from Figure 3.23c. The Freundlich uptake factor K_f and intensity factor *n*, with the respective determination coefficients R, are also calculated and presented in Table 3.8. Instead of continuous linearity, Freundlich pattern exhibited a two segment linear relationship of log (q_e) and log (C_e). The initial segment has a very high uptake factor (K_f = 2.3 × 10^{14} L g^{-1}) than the latter one. Again, the Freundlich exponent factor *n* of the initial segment is lower than the latter one, which probably indicates the highly increased adsorption capacity of phosphate on TMA coated alumina at higher concentration. More generally, the application of the Langmuir model seemed to be more appropriate than that of Freundlich model. The χ^2 tests of error analysis also established the better agreement of Langmuir model with experimental data than Freundlich model.

Table 3.8. Parameters of Langmuir and Freundlich isotherm model of phosphate adsorption.

Langmuir isotherm				Freundlich isotherm				
Q_m (mg g^{-1})	b (L mg^{-1})	R	χ^2	K_f (L g^{-1})	n	R	χ^2	
5.23	0.80	0.999	0.233	2.3x10^{14}	0.073	0.995	0.412	Initial segment
				1.786	1.727	0.969	0.551	Final segment

3.4.3.6. Thermodynamic studies of phosphate adsorption

Thermodynamic aspect of phosphate adsorption was studied by performing the experiments at 25°C and 50°C by keeping other parameters constant. As shown in Figure 3.23a, adsorption capacity is almost the same in both temperatures, indicating no significant effect of temperature variation on adsorption capacity. Standard Gibbs free energy change (ΔG°) of phosphate adsorption was calculated for both the temperature. High negative ΔG° values were obtained at both temperatures, which suggest the favorability of this adsorption process. ΔG° value at 25°C was −15.6 kJ mol^{-1} and at 50°C was −16.8 kJ mol^{-1}. Moreover, the maximum adsorption capacity (Q_m) also remains almost the same at a high temperature of 50°C. Thus, adsorption of phosphate has a high

driving force toward TMA coated alumina which is consistent with our previous kinetic discussion.

3.4.3.7. Selective interaction of phosphate

From the chromatogram of competitive study it is clear that adsorption of phosphate is much more selective than Cl^-, Br^- and NO^-_3 (Figure 3.24a). The results obtained from chromatogram clearly indicate that more than 90% of initial phosphate was adsorbed on TMA coated alumina while adsorption of other anions was almost insignificant (see Appendix). Selective adsorption of phosphate over other anions can be described on the basis of the charge density of these anions. Previously we proposed that phosphate group at different form (H_3PO_4, $H_2PO_4^-$, HPO_4^{2-} or PO_4^{3-}) interact differently with TMA coated alumina at different pH. At pH ~1.0–2.0 phosphate remain as phosphoric acid (H_3PO_4) and acts as a three site hydrogen bond donor and one site hydrogen bond acceptor. Whereas, Cl^-, Br^- and NO^-_3 are dissociated at pH ~1.0–2.0 ($pK_a^1 < 0$) and can act as only single site hydrogen bond acceptor. On the other hand, carboxyl group of TMA acts as single site hydrogen bond donor and acceptor, and can form hydrogen bonds with proton donor or acceptor groups. Because of the tri-protic dissociation of ortho-phosphoric acid, its conjugate bases ($H_2PO_4^-$, HPO_4^{2-} and PO_4^{3-}) cover a wide pH range of pH 1.0–8.0 (Scheme X). Hence through a wide pH range, ortho-phosphoric acid and its conjugate bases possess higher charge density and thereby a greater affinity toward the carboxyl group of TMA over the other anions. Therefore, H_3PO_4 can form hydrogen bonding with carboxyl group of TMA more easily. As a result, we have observed a highly selective phosphate adsorption compared to other anions (Figure 3.24b).

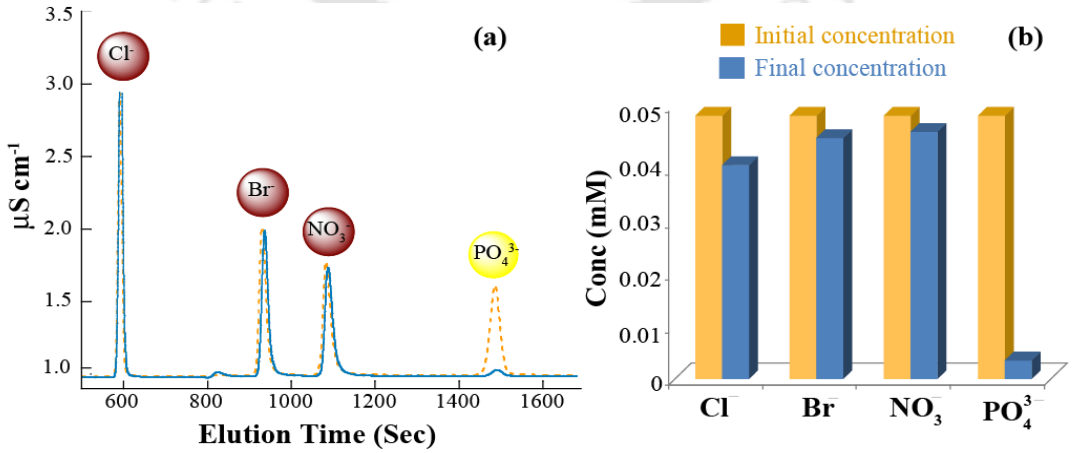

Figure 3.24. (a) Ion chromatogram of competitive phosphate adsorption study with other anions (Cl^-, Br^- and NO^-_3) and (b) selective binding of phosphate on TMA coated surface.

3.4.3.8. Desorption of phosphate from the surface

Desorption of phosphate is an important step in order to regenerate the adsorbent and recovery of phosphate.[3.41] Once adsorbed, the adsorbent was treated with a series of 0.1 to 0.5 M NaOH solution for desorption of phosphate. The amount of phosphate desorption increased from ~80% to ~100% with the increase of alkali strength from 0.1 to 0.5 M. Desorption kinetics was faster than adsorption process. About 100% phosphate was desorbed within 30 min as the estimation of filtered supernatant by stannous chloride method (Figure 3.25). Enriched phosphate in desorbed solution can be recovered as calcium phosphate precipitation by addition of $CaCl_2$ as described elsewhere.[3.41]

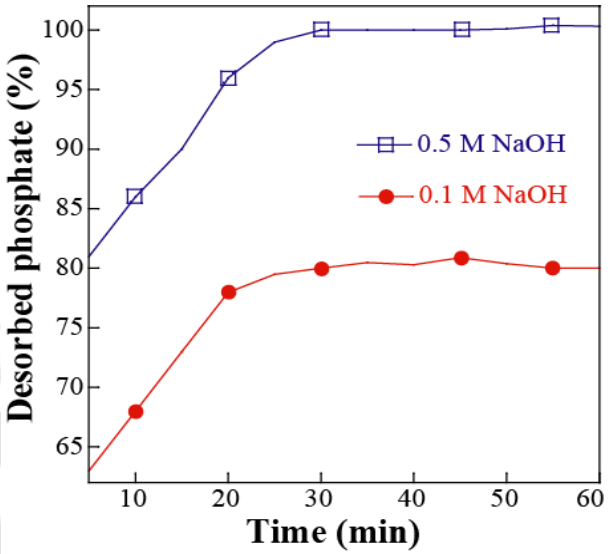

Figure 3.25. Desorption kinetics of phosphate with 0.1 M and 0.5 M NaOH solution.

3.4.3.9. Summary

The interaction of phosphate on TMA coated surface could be controlled by controlling pH and selectivity was achieved in presence of other anions. The adsorption capacity increases with the increase in initial phosphate concentration, while having significant adsorption efficiency even from low concentration (~1.0 mg L^{-1}) solution. High and consistent binding capacity was found throughout a wide range of pH (1.0 – 8.0). Significant phosphate removal efficiency at high acidic range (pH ~1.0) should be noticed. Most significantly, highly selective and efficient adsorption of phosphate was observed from the competitive adsorption experiments with other anions like chloride, bromide and nitrate. A good agreement between Langmuir isotherm and experimental data suggest monolayer coverage of phosphate upon adsorption. The maximum adsorption capacity (Q_m) was ~5.2 mg g^{-1} as calculated from Langmuir model. The phosphate adsorption has been found to be thermodynamically favorable without any significant change in adsorption capacity with variation in temperature. Recovery of phosphate and regeneration of the adsorbent was possible by complete desorption of phosphate loaded adsorbent.

Part 2:

3.5. Interaction of proteins on trimesic acid coated acidic 'hard' surface

This section describes the interaction of two different proteins namely, bovine serum albumin (BSA) and hen egg white lysozyme (HEWL) on trimesic acid coated acidic 'hard' surface. Trimesic acid coated alumina surface prepared by simple surface modification technique and it has been used for the first time in protein interaction studies. The different properties of BSA and HEWL are shown in Figure 3.26.

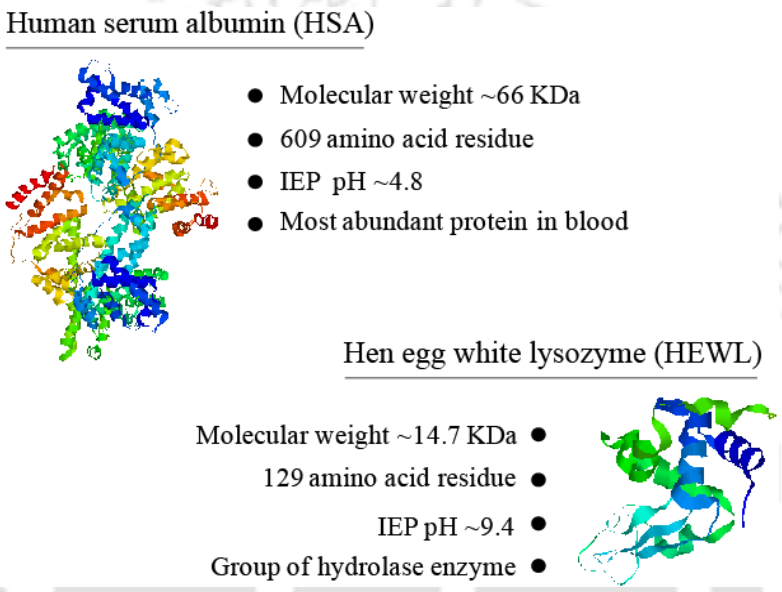

Figure 3.26. Physicochemical properties of bovine serum albumin (BSA) analogue human serum albumin (PDB ID:1bm0) and hen egg white lysozyme (HEWL, PDB ID:3iju). Structures obtained from PDB (www.rcsb.org).

3.5.1. Background

Interactions of biomolecules at various micro- to nano-scale organized surfaces are receiving considerable interest as it can induce interaction specificity depending upon various surface properties. The surface specific interaction of proteins is a key fundamental process associated with many budding scientific and industrial fields including biomaterials, bioseparation technology, and bio-nanotechnology. In this regard, the adsorption selectivity of proteins on different solid surfaces is pivotal for the construct of interfacial assemblies like biosensors, actuators and separators for higher scale application. Selectivity at different modified interfaces helps to predict how and which protein and other biologically important species are adsorbed on specific surfaces.

Moreover, the detailed structure-function analysis of a selectively adsorbed protein at interface can be very much useful in understanding the primary interaction of biomolecules with other specific receptors.

Adsorption selectivity of proteins based on electrostatic means can be controlled by specific surface modification. Tailored made charged surfaces can be tuned up for selective adsorption of protein of interest and separation from biological system based on their surface charge, specific area and hydrophobicity. Various types of coating with different functional groups[3.42] and polymers[3.43] were used to control (enhance/reduce) the protein adsorption on different solid surfaces. The adsorption of proteins on modified surfaces is mostly influenced by charged molecules.[3.44] Though the retaining of native-like structure of proteins on some charged surfaces have been reported, it can bind proteins regardless of the protein net charge.[3.45] This indicates a lack of selectivity in adsorption behavior when more than one type of protein is present. In this regard, introducing small charged functional groups with specific ionization properties on solid surfaces can be useful for controlled adsorption of proteins. Apart from the average characteristics of engineered surfaces, the 3-D structure, conformational rigidity, iso-electric point and distribution of charged/hydrophobic patches on the surface of a protein also governs the adsorption pattern.[3.46] The interaction of proteins with charged solid surfaces governs through the side chain groups of amino acid residues on protein surface through electrostatic interaction. Therefore the specific functional group on the surface is very crucial for controlled interaction with the specific amino acid side chain residues. Moreover, retaining the original activity of selectively adsorbed enzyme on a solid surface is a major challenge in protein-surface interaction. Occasionally the activity of enzymes reduces significantly upon adsorption on a surface,[3.47] and hence their usability in biomedical or biotechnological fields reduces. Therefore, a specifically immobilized enzyme at solid-liquid interface with a high retention of activity is in high demand.

Herein, for the first time we have studied the selective interaction of lysozyme from a mixed solution (with BSA) along with the enzymatic activity on TMA modified surface. Control over protein interaction was achieved through the same functional groups (of TMA) introduced on the alumina surface by changing specific conditions. These charged carboxylic groups of TMA, which can interact with the positively charged amino acid side chains of proteins, can regulate the attachment of different proteins based on its dissociation constant and iso-electric points of different proteins. Previous reports also suggested the binding of proteins with terminal carboxylate functional groups on the

surface.[3.48] Herein, a new insight of controlled protein-surface interaction on TMA coated surface has been provided in terms of adsorption kinetics, thermodynamics and structural point of view and with a high retention of immobilized enzyme activity. In this section, two different proteins were chosen as model proteins that vary in protein net charge and thermodynamic stability against unfolding namely, hen egg white lysozyme (pH_{IEP} ~11, ΔG ~63 KJ mol^{-1})[3.49] and bovine serum albumin (pH_{IEP} ~4.8, ΔG ~18 KJ mol^{-1}).[3.50] Therefore, the strength of interaction of these proteins with negatively charged TMA coated surface would be different which can lead to a different adsorption pattern on TMA modified surface. Selectivity of protein adsorption was studied in a wide pH range. Detail adsorption kinetics and isotherm studies have been done for in-depth analysis of adsorption phenomena. The tertiary and secondary structure of selectively adsorbed lysozyme was analyzed with fluorescence and FT-IR spectra. Moreover, the detail enzyme kinetics study has been performed to analyze the retention of activity of the adsorbed enzyme on TMA coated surface.

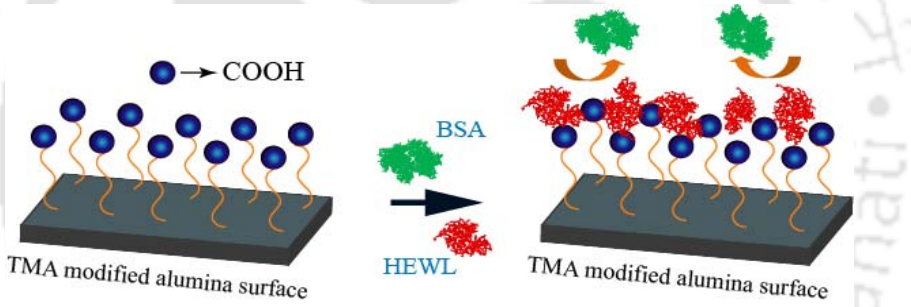

Scheme 3.4. Schematic illustration of controlled interaction of BSA and lysozyme on TMA modified surface.

3.5.2. Materials and methods

Adsorption of proteins. Protein adsorption experiments were carried out in batch mode to obtain kinetic and steady state data with both individual and mixed protein solution. Batch adsorption studies was performed in 2 mL sample vials by adding desired concentration of BSA and lysozyme solution to a different proportion of TMA coated alumina particles. Protein solutions were prepared in 50 mM acetate and phosphate buffer at different pH. Solution pH was varied from 3.0 to 8.0 to study the adsorption selectivity of both BSA and lysozyme on carboxylated surface. Adsorption kinetics was studied by withdrawing the samples at regular interval and subsequent centrifugation to obtain suitable aliquots for analysis of protein concentration. The amount of adsorbed proteins (Γ_{BSA} and Γ_{Lys}, µg m^{-2}) on TMA coated surface was calculated from initial (C_0, mg L^{-1})

(C_e, mg L^{-1}) and final protein concentration and specific surface area (m^2 g^{-1}) of TMA coated alumina. The initial and final protein concentration of individual BSA and lysozyme was determined by Bradford assay procedure measuring at 595 nm. Binding stoichiometry and isotherm experiments were performed with different ratio of protein concentration and surface area. The thermodynamic aspects of adsorption of protein adsorption have also been analyzed in a wide temperature range from 5°C to 40°C. For selectivity study of protein adsorption, equal amount of BSA and lysozyme in a mixed solution was added to a fix amount of TMA coated particles at pH 7.4. Fresh protein solution was made prior to each experiment with 50 mM phosphate buffer and acetate buffer solution at different pH for adsorption studies. The residual amount of both BSA and lysozyme after competitive adsorption was determined by Bradford assay method and specific activity of lysozyme in the mixed solution.

Fluorescence spectra for tertiary structure. The tertiary structure of lysozyme in solution and in adsorbed state was measured at 25°C using tryptophan fluorescence emission technique in a steady-state spectrofluorimeter.

FT-IR spectroscopy for secondary structure. The secondary structure of lysozyme in native solution and adsorbed on TMA coated surface has been studied with the FT-IR spectrum. The amide I (1700-1600 cm^{-1}) region has been widely used to quantify the individual elements of secondary structural elements of a protein in solution as well as in lyophilized state.[3.51] FT-IR spectra of lyophilized native lysozyme and immobilized on TMA coated surface at different temperature, pH and surface coverage, were taken for secondary structural analysis. A total of 60 scan at 4 cm^{-1} resolution (with 1 mg samples in 100 mg KBr) were performed and averaged to obtain each spectrum. The FT-IR spectrum of adsorbed proteins on TMA-coated surface was obtained by subtracting the spectrum of TMA coated alumina in a *Spectrum-One* (v 5.3.1) software. Fourier self-deconvolution (FSD) was applied to the unsmoothed spectra in each case for band narrowing (full width half-maxima, fwhm = 16 cm^{-1} and enhancement factor, k = 2.0).[3.52] Gaussian curve-fitting was then performed using *GRAMS/AI* software (Thermo Fisher Scientific, Massachusetts) on the Fourier self-deconvoluted amide I band region. The secondary structural element (%) was calculated from the areas of the individual assigned bands and their fraction of the total area in the amide I region with a linear baseline fitting, as described in literature.[3.51,3.53] In each case, the secondary structural content was determined from two independently obtained spectra, the values were averaged, and the standard deviations were calculated.

Determination of enzymatic activity. The enzymatic activity of lysozyme in native solution and in adsorbed state was measured at 25°C in 50 mM phosphate buffer at pH 7.4. The rate of lysis of *Micrococcus lysodeikticus* (*M. luteus*) was measured to determine the lysozyme activity. A stock solution of *M. lysodeikticus* (2 mg mL^{-1}) was freshly prepared and diluted to different desired concentration (100-800 μg mL^{-1}) in final enzyme assay buffer (50 mM phosphate buffer, pH 7.4 and ionic strength 0.05 M). The rate of lysozyme activity *v* was determined by measuring the initial rate of decrease (for first 5 min) in the absorbance at 450 nm. In case of adsorbed lysozyme, the turbidity due to only TMA coated particles were subtracted in each case to get the lytic decrease of *M. lysodeikticus* in a 3 mL cuvette. The absorbance of reducing turbidity of *M. lysodeikticus* solution was measured in every 1 min for a time period of 5 min and mechanically stirred during the time lags between the spectroscopic measurements. The enzyme kinetic study for free and adsorbed lysozyme was performed at 25°C with a *M. lysodeikticus* concentration range of 0.1−1.0 mg mL^{-1}. The final concentration of enzyme was adjusted to 0.35 μg μL^{-1} for the kinetic study. For comparison of specific enzymatic activity of free and adsorbed lysozyme, an equal amount of enzyme was added in each case.

3.5.3. Selective interaction of lysozyme and influence of pH

Coating of TMA on alumina surface introduces carboxylate groups on alumina surface. Binding of TMA mainly facilitates through the carboxylate moieties of TMA and surface hydroxyl groups of alumina. Previous reports suggest that organic acids adsorbs onto alumina surface through hydrogen bonding[3.7] between the carboxylate moiety of TMA and surface hydroxyl group of alumina. TMA have three pK_a values likely 2.5, 3.2 and 4.5 respectively. Therefore, at pH < pK_a of the organic acid, a hydrogen bond may established between each oxygen atom in the carboxylic group of TMA and the oxygen atom on the alumina surface. Again, at higher pH > pK_a of organic acid, the adsorption of TMA on metal oxide surfaces like alumina, is largely affected by electrostatic interactions. At pH < pH_{pzc} (point of zero charge), the alumina surface remains positively charged and a strong electrostatic bond can form between the dissociated carboxylate moieties of TMA (pH > pK_a of TMA) and surface hydroxyl groups of alumina. Therefore, TMA coated alumina surface generates a carboxylated surface which is fully protonated at pH < 2.5, dissociates at higher pH and become fully deprotonated (negatively charged) at pH > ~5.0.

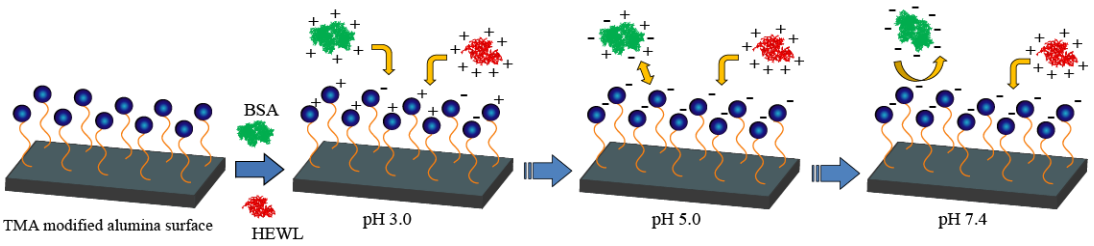

Scheme 3.5. Schematic representation of competitive adsorption of BSA and hen egg white lysozyme (HEWL) on TMA coated surface. At pH ~3.0 both the positively charged proteins can adsorbed on the partially deprotonated TMA coated surface via electrostatic and/or hydrogen bonding. At higher pH ~7.4 electrostatic repulsion between the negatively charged BSA and TMA coated surface reduce the adsorption of BSA drastically; however, the positive charged lysozyme at this pH can still bind with the fully deprotonated surface.

The selectivity of lysozyme adsorption was tested in a broad pH range (Scheme 3.5). The adsorption phenomena of BSA and HEWL (0.5 mg mL^{-1} of each protein) on TMA coated surface at three different pH is shown in Figure 3.27. As seen both from the individual (Figure 3.27a) and competitive (Figure 3.27b) adsorption results on TMA coated surface, it is clear that with the increase of pH, the adsorption of BSA reduces on the carboxylated surface. At physiological pH ~7.4, lysozyme was almost selectively adsorbed on the carboxylated surface with a high adsorption capacity of ~641 µg m^{-2}, whereas adsorption of BSA was almost negligible (Γ_{BSA} ~0.8 µg m^{-2}). This can be explained from the isoelectric point (IEP) of the proteins and their interaction with TMA coated surface at respective pH. BSA has an IEP at pH ~4.8-5.0 and therefore contains a net positive charge in the pH range of 3.0-5.0. The comparatively higher adsorption of BSA at acidic pH (3.0-5.0) mainly governs through the electrostatic interaction. The carboxylated surface has a partial negative charge beyond its first dissociation constant (pK_a^1 ~2.5) and can form an electrostatic bond with then positively charged BSA in this pH range of 3.0-5.0. Adsorption capacity of BSA reduces at higher pH (pH > 5.0) and become almost zero at physiological pH (pH ~7.4) in a mixed protein solution. However, the small amount of adsorption of BSA (Γ_{BSA} = ~45 µg m^{-2}) at higher pH (pH > 5.0) from individual solution (Figure 3.27a) can be attributed to the hydrophobic interaction with the 'soft' BSA and carboxylated surface, however this adsorption capacity also nullified in case of the mixed protein solution (Figure 3.27b) mainly due to the competitive binding of lysoyme present in the solution. The drastic reduction in adsorption of BSA at higher pH (pH > 5.0) is mainly because of the electrostatic repulsion between the negatively charged TMA surface (pK_a^3 ~4.5) and BSA. On the other hand, having an IEP value at pH ~9.4,

lysozyme has a net positive charge throughout the pH range studied here and can bind easily with the negatively charged TMA surface. The adsorption capacity of lysozyme at acidic pH (pH ~3.0) is comparatively less (Γ_{Lys} = ~365 µg m^{-2}) due to protonated TMA surface which reduces electrostatic interaction with lysozyme, but still adsorption may facilitates through hydrogen bonding. At higher pH, deprotonation of TMA surface enhances the electrostatic interaction with lysozyme in addition with hydrogen bonding, which lead to a high and selective adsorption of lysozyme (Γ_{Lys} = ~641 µg m^{-2}) over BSA at physiological pH (~7.4).

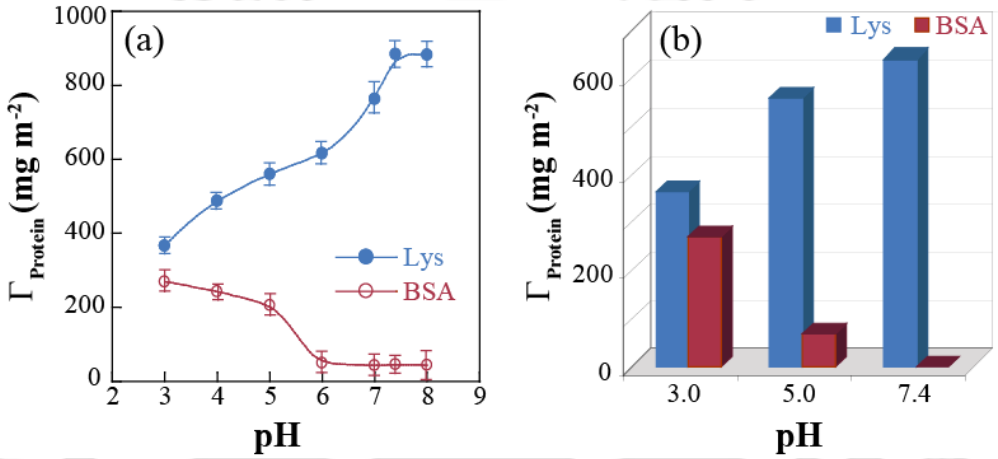

Figure 3.27. (a) Adsorption profile of BSA and lysozyme at different pH on TMA coated alumina surface from individual solution; (b) Competitive adsorption capacity of BSA and lysozyme on TMA coated surface at different pH from an equi-molar mixed solution.

Lysozyme, a small sized ellipsoid protein[3.54] is believed to bind with hydrophilic/charged surface through its charged polar amino acid residues. In the first report, Blake *et al.*[3.54] illustrated that the amino (N)- and carboxyl (C)-termini of the lysozyme molecule located at the opposite end of the active site. Later on, several works have indicated that lysozyme do adsorb on a charged surface in a preferable side-on mode through its N, C-terminal face residues.[3.55] Therefore it is most likely that, lysozyme adsorb on TMA coated surface (negatively charged) through its most positively charged patch (mostly contain Lysine and Arginine) lies on the N, C-terminal of the protein, in the pH range studied here. Similar mechanism of interaction of lysozyme with negatively charged surface also reported by Haggerty and Lenhoff.[3.56] They suggested that orientation of interaction of lysozyme molecule with negatively charged surface is a crucial parameter in adsorption energy and the electrostatic energy is minimized when the lysozyme molecule interact with a negatively charged surface through its most positively charged

patch located opposite side of the active site of the enzyme. Moreover, the preferred orientation of lysozyme on a surface at low surface coverage is likely to be 'side-on' mode,[3.57] which also involves an re-orientation of the protein after preliminary adsorption on the surface to optimize the interaction.[3.55c] Daly *et al.* reported that at low surface coverage of lysozyme preferred re-orientation on a charged surface through the N, C terminal residues places the active site of lysozyme towards the solution. As surface saturation reaches at higher protein concentration, these adsorbed protein layers restructured along with the adjacent protein solution from the bulk solution to fill up the free surface area available. On a charged surface, protein structure altered very often to minimize its adsorption energy. The electrostatic interaction with the surface and the internal interaction between the neighboring proteins on the surface have a major impact on the adsorbed protein structure. In most of the cases the tertiary structure unfolded partially and the charged residues interacted with the surface exposed and oriented towards the surface. Therefore it is quite likely that, the α-helices at the most positive patch of lysozyme (opposite end of the active site) are unfolded upon adsorption on TMA coated surface and the polar residues are exposed towards the surface.

3.5.4. Adsorption equilibrium and kinetic analysis

Adsorption kinetics of both BSA and lysozyme (individual 0.5 mg mL^{-1} each) was studied at a 5 min time interval up to 1 h of time duration at pH 7.4. Initially adsorption of both the proteins on TMA modified surface is fast leading to almost steady state conditions after which adsorption capacity was linear and reached steady state within 15 min (Figure 3.28). Although steady state reaches in almost same time, the steady state adsorption capacity of BSA (from individual solution) was very less (Γ_{BSA} = ~45 μg m^{-2}) compared to that of lysozyme (Γ_{Lys} = ~890 μg m^{-2}) at pH 7.4. The kinetic rate of lysozyme adsorption on TMA coated surface was evaluated by first order and second order model. The linearized graph of first and second order model was plotted and the

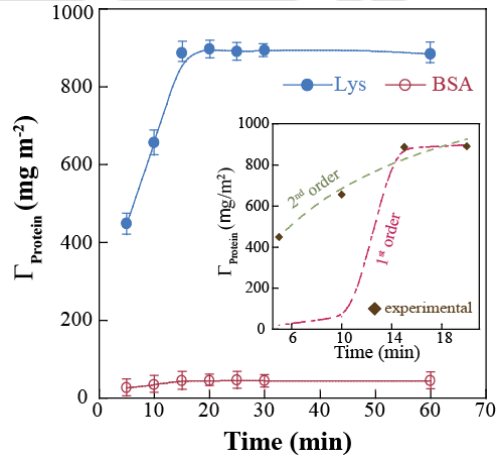

Figure 3.28. Adsorption kinetics of lysozyme and BSA from individual solutions at pH ~7.4. (*Inset*) Comparison of first and second order kinetic model with experimental and calculated data.

rate constant values were calculated (Appendix Figure A3.11). However, the adsorption of lysozyme on TMA coated alumina seemed to be described better by second order equation. Second order model showed a higher correlation coefficient (R^2) of 0.989 than that of first order model ($R^2 = 0.974$), which can be attributed to the actual heterogeneous nature of the TMA coated surface. The first and second order rate constants were 0.85 L min^{-1} (k_1) and 6.4×10^{-5} g mg^{-1} per minute (k_2) respectively. Moreover, the experimental data were compared together with pseudo first and second order models (Figure 3.28, inset). The second order model matches well with the experimental data, as the first order model was far underestimated the actual amount of lysozyme adsorbed.

3.5.5. Adsorption isotherm and binding stoichiometry

Adsorption isotherm experiments were performed by adding a fix amount of TMA coated alumina (2 g L^{-1}) to different concentration of lysozyme (0.1 - 0.5 mg mL^{-1}) at pH 7.4 in room temperature. The steady state adsorption isotherm with different lysozyme concentration on TMA coated surface is shown in Figure 3.29a. The initial slope in the isotherm plot indicates high affinity of lysozyme for TMA coated surface, which approaches a plateau indicating the steady state surface coverage of lysozyme. The steady state surface coverage approaching plateau of lysozyme (Γ_{Lys}) on TMA coated surface was found to be ~890 µg m^{-2}; whereas, the steady state surface coverage of BSA from mixed solution was not significant compared to lysozyme at pH 7.4 (isotherm plot not shown). The steady state adsorption isotherm of lysozyme on TMA coated surface has been analyzed with Langmuir and Freundlich models.

Langmuir model showed a good agreement with the experimental data compared to Freundlich model (Figure 3.29a, inset). This indicates a monolayer coverage of lysozyme upon adsorption on TMA coated surface which can be facilitate through the interaction between positively charged patch of lysozyme and TMA coated surface as discussed before. The constant values of both the isotherms were calculated from the linearized plots (Appendix, Table A3.3). The maximum adsorption capacity ($\Gamma_{Lys,m}$) of lysozyme on TMA coated surface was ~2.17 mg m^{-2} as obtained from Langmuir model. The Langmuir binding constant for lysozyme with TMA coated surface was found to be 0.0021 L mg^{-1}. Moreover, the favourability of Langmuir model was analyzed with a 'constant separation factor' or 'equilibrium parameter', R_L, was also calculated. The value of R_L was found 0.86 which is consistent with the favorability of the adsorption process (for a favorable process $0 < R_L < 1$).

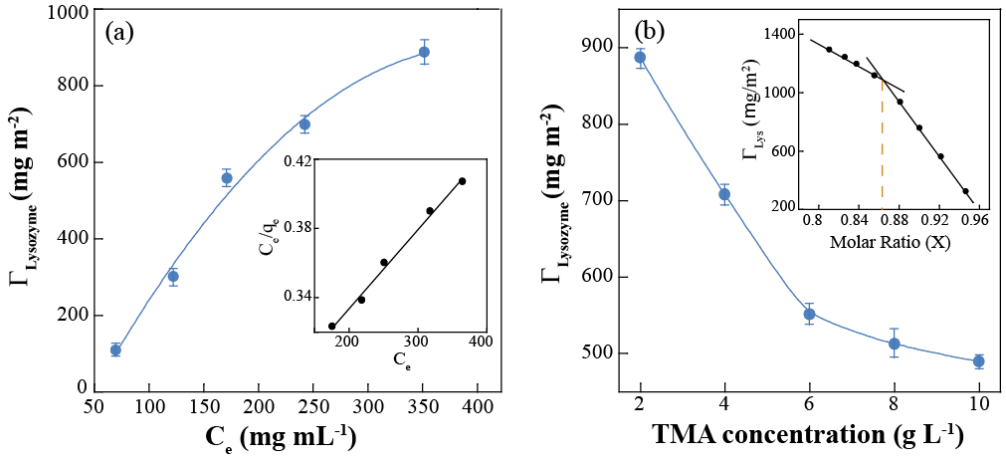

Figure 3.29. (a) Adsorption isotherm of lysozyme on TMA coated surface at pH 7.4. (*Inset*) Langmuir isotherm model fitting for lysozyme adsorption. (b) Influence of available surface concentration on adsorption capacity of lysozyme at pH 7.4. (*Inset*) the Job's plot for determining the binding stoichiometry of lysozyme and TMA coated surface. The molar ratio (X) calculated from the relation, X = [TMA coated alumina] / [[TMA coated alumina] + [Lysozyme]].

However, upon increasing the available surface area by adding increasing amount of TMA coated alumina (2 to 10 g L^{-1}), the adsorption capacity of lysozyme (Γ_{Lys}) decreases from ~890 µg m^{-2} to ~490 µg m^{-2} as shown in Figure 3.29b. The binding stoichiometry of lysozyme with TMA coated surface was determined from the molar ratio of TMA coated alumina and lysozyme concentration using Job's plot. The breakpoint of the plot gives the corresponding mole fraction which indicates the binding stoichiometry.[3.58] The binding isotherm plot (Figure 3.29, inset) of lysozyme shows a breakpoint at the molar ratio of 0.86 of TMA coated alumina and lysozyme concentration. This indicates a binding stoichiometry of 0.86 for TMA coated surface with lysozyme in this case.

3.5.6. Thermodynamics studies of lysozyme adsorption

The thermodynamics parameter of selective adsorption of lysozyme on TMA coated surface has been studied in a wide temperature range of 5°C to 40°C. The surface coverage of lysozyme decreases from ~590 µg m^{-2} to ~350 µg m^{-2} with the increase in temperature. The decrease in surface coverage at higher temperature indicates the adsorption process is exothermic in nature. The standard Gibb's free energy (ΔG^o) of lysozyme adsorption on TMA coated surface was calculated. The standard Gibb's free

energy (ΔG^o) values were found to be negative in the whole temperature range which indicates the favourability of the process. The negative value of ΔG^o of adsorption of lysozyme indicates that adsorption process is spontaneous and thermodynamically favourable. However, the ΔG^o values was not changed much (-13.0 to -12.6 KJ mol^{-1}) in this temperature range (Figure 3.30). Moreover, the standard average enthalpy change (ΔH^o) and entropy change (ΔS^o) can be calculated from the Van't Hoff equation. A linearized plot between ln(K_c) and 1/T was used to calculate the values of ΔH^o and ΔS^o (Appendix, Figure A3.13). The average change in entropy (ΔS^o) for lysozyme adsorption was found to be -7.3 J K^{-1} mol^{-1}. The negative value of ΔH^o (-14.9 KJ mol^{-1}) also supports the exothermic nature of the adsorption process. Therefore, the selective adsorption of lysozyme on TMA coated surface was found to be thermodynamically favourable and exothermic in nature in this temperature range at pH 7.4.

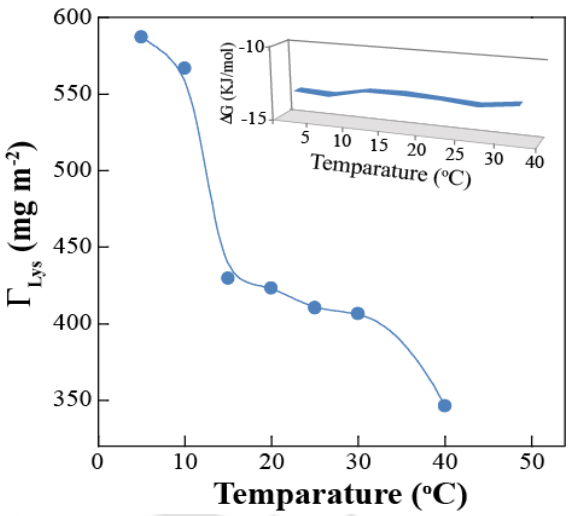

Figure 3.30. Influence of system temperature on the adsorption capacity of lysozyme. (*Inset*) Gibbs free energy change (ΔG^o) profile of lysozyme adsorption in the temperature range of 5-40°C.

3.5.7. Structural studies of adsorbed enzyme

The steady state fluorescence spectroscopy of lysozyme in solution (native) and after adsorption on TMA coated surface is shown in Figure 3.31. Lysozyme is a 129 residue (including 6 tryptophan)[3.54] containing globular protein comprises of mostly α-helices. The native lysozyme in solution has an emission maxima at ~345 nm (Figure 3.31) indicate that tryptophan molecule exposed to the water environment. The emission at ~345 nm is solely for the tryptophan molecule in lysozyme. After adsorption on the TMA coated surface, the fluorescence spectra of lysozyme partially quenched without any shifting in the λ_{max}, which can be due to the change in polarity of the surrounding environment of tryptophan after adsorption. The quenching in emission spectra indicates a partially unfolded tertiary structure, possibly in a molten-globule like intermediate stage of lysozyme on TMA coated surface. The quenching of fluorescence intensity of lysozyme upon adsorption on TMA coated surface might be due to the presence of a

strong tryptophan quenching groups in proteins like cysteine.[3.59] This could be possible when the tertiary structure of lysozyme gets changed and unfolded upon adsorption in such a way that the tryptophan occupies a position with spatial proximity to cysteine. The fluorescence anisotropy of lysozyme has been measured in free and adsorbed state to ensure its binding with TMA coated surface. The native lysozyme anisotropy in solution was 0.065 (Figure 3.31, inset), which increased to 0.114 after adsorption. This indicates an increased rigidity in the surrounding environment of the fluorophores upon binding on TMA coated surface. The increased anisotropy value can be attributed to the imposed motional restriction on the fluorophore of lysozyme, due to the adsorption on TMA coated surface.

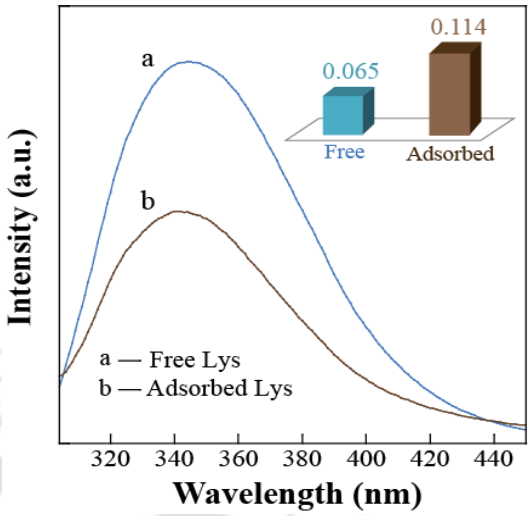

Figure 3.31. Steady state fluorescence emission spectra of free lysozyme in solution and adsorbed on TMA coated surface. (Inset) The anisotropy values of free and adsorbed lysozyme at pH 7.4 and 25°C.

The FT-IR spectra of native and adsorbed lysozyme under three different condition, such as in different surface coverage, pH and temperature, were taken from 4000 to 450 cm^{-1}. For structural analysis, the FT-IR spectra of all adsorbed lysozyme were subtracted from the FT-IR spectra of TMA coated lysozyme as discussed above. In all cases, the broad band at 1700-1600 cm^{-1} is attributed to the amide I, mainly due to the –C=O and –N-H bending vibration of amino acid side chains of lysozyme. The individual secondary structural elements of lysozyme at different state were quantified by Gaussian deconvolution analysis of the amide I region in each case (Figure 3.32).[3.52,3.60] The Gaussian peak at 1657 ± 2 cm^{-1} was assigned to α-helix, bands at 1694 ± 2, 1640 ± 1, and 1632 ± 2 cm^{-1} were assigned to β-sheet, and all other peaks were assigned to unordered structural elements including β-turns, random coils, and extended chains.[3.51a] The Gaussian analysis reveals the α-helical content of ~24% along with ~32% of β-sheets and ~43% of unordered elements of native lysozyme, similar with previous reports.[3.51a,3.53] The helical content of lysozyme varies upon adsorption on TMA coated surface at different conditions. Helical structures of adsorbed lysozyme remain almost similar to that of native one, at a lower surface coverage of ~490 μg m^{-2} (Figure 3.32a), as merely ~1% decrease in α-helix content was observed (Table 3.9). However, upon increasing the

surface coverage of adsorbed lysozyme to ~890 µg m^{-2}, the helical content reduces more to ~22% (Table 3.9).

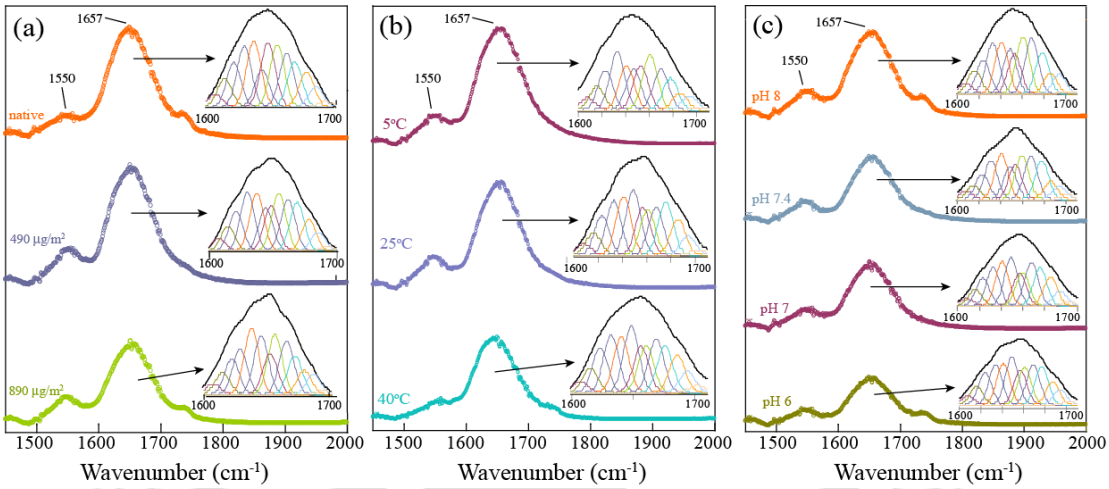

Figure 3.32. The amide I region (1700-1600 cm^{-1}) of the FT-IR spectra of native and adsorbed lysozyme (lyophilized) at different surface coverage (a), temperature (b) and pH (c). (*Inset*)The corresponding Gaussian distribution analysis were performed to get the individual secondary structural content of native and adsorbed lysozyme in each case.

This indicates that higher surface coverage of lysozyme at room temperature (pH ~7.4) imposes some spatial restriction of adsorbed lysozyme, which resulted in a loss of secondary structural content to some extent. Adsorption experiments of lysozyme at different pH from 6.0-8.0 did not have significant effect on the secondary structure of adsorbed lysozyme. As obtained from Gaussian analysis, the α-helical content remains in between ~21-22% in the whole pH range of 6.0-8.0 (Figure 3.32c). Though the surface coverage of lysozyme increases in this pH range (from 600-800 µg m^{-2}) it does not have much effect on the secondary structure of adsorbed enzyme. We have also analyzed the secondary structure of lysozyme adsorbed at different temperature (Figure 3.32b). The α-helical content of adsorbed lysozyme remains ~23-24% in the temperature range of 5-25°C, which indicates a minor structural change in this temperature range. However, at 40°C, the α-helical content of adsorbed enzyme reduced to ~19-20% reveals a comparatively more loss of secondary structures at higher temperature. Therefore, from all these analysis it has been found that the secondary structural content of adsorbed lysozyme at different pH and temperature did not alter much from its native structure; which depicts a partially unfolded in tertiary structure of lysozyme with mostly retention of secondary structures on TMA coated surface.

Table 3.9. Individual secondary structural elements (%) of native and adsorbed lysozyme at different condition as calculated from Gaussian peak fitting of amide I band of each spectrum.

	α-Helix (%)	β-Sheet (%)	Unordered (%)
Native Lysozyme (lyophilized)	~25	~32	~43
At different surface coverage			
Γ_{Lys} ~490 μg m^{-2}	~24	~26	~50
Γ_{Lys} ~890 μg m^{-2}	~22	~27	~51
Adsorbed lysozyme at different pH			
pH 6.0	~21	~26	~53
pH 7.0	~21	~37	~42
pH 7.4	~22	~28	~50
pH 8.0	~22	~27	~51
Adsorbed lysozyme at different temp.			
5°C	~24	~26	~50
25°C	~23	~26	~51
40°C	~19	~27	~54

3.5.8. Activity of immobilized enzyme

The activity of lysozyme adsorbed on TMA coated surface relative to that of free protein was analyzed during a period of 7 min with 0.2 - 0.5 mg mL^{-1} of *M. lysodeikticus* solution (Appendix, Figure A3.14). The rate of lysis of *M. lysodeikticus* by free and adsorbed lysozyme with 0.2 mg mL^{-1} substrate concentration is shown in Figure 3.33a. Adsorbed lysozyme retained its activity up to ~98% compared to that of free protein with 0.2 mg mL^{-1} of *M. lysodeikticus* solution. In each case, the activity of free lysozyme with same *M. lysodeikticus* solution was taken as 100%. However, at higher substrate concentration (~0.5 mg mL^{-1}) the relative activity of adsorbed enzyme reduced a bit to ~91% (Figure 3.33a, inset). This retention of high enzymatic activity may be explained from the plausible adsorption pattern of lysozyme molecule. Adsorption of lysozyme on TMA coated surface mainly facilitated through the most positively charged patch of the molecule located opposite to the active site, as discussed above. This can lead to an orientation of adsorbed lysozyme, where the active site is away from the surface towards the bulk solution, which can be a major breakthrough for retention of high enzymatic activity. We have also studied the effect of only TMA coated alumina alone on the lysis of *M. lysodeikticus*, which did not reflect any positive result with the substrate

concentration range studied here. Moreover, the rate of enzymatic activity, v (mg mL^{-1} min^{-1}) is calculated following the Michaelis-Menten kinetics[3.61] given by,

$$v = \frac{v_{\max}.[S]}{K_m + [S]} = \frac{k_{cat}.[E]_T.[S]}{K_m + [S]} \quad (3.1)$$

Where, [S] is substrate concentration (mg mL^{-1}), v_{max} is the maximum rate attained at infinite concentration of substrate, K_m is the Michaelis-Menten constant. The term v_{max} can be further expressed by k_{cat} and $[E]_T$, which is turn over number and total enzyme concentration used for kinetics study, respectively. The enzyme kinetic studies was performed with ~35 µg of adsorbed lysozyme per mg of TMA coated alumina and relatively equal amount of free enzyme was added for sake of comparison in each case. Figure 3.33b shows the Michaelis-Menten plot for the hydrolysis of *M. lysodeikticus* by free and adsorbed enzyme at pH 7.4 and 25°C. The values of maximum rate (v_{max}) and Michaelis-Menten constant (K_m) were calculated from a linearized Lineweaver-Burk plot for both free and adsorbed enzyme (Figure 3.33b, inset). The kinetic parameters were calculated and given in Table 3.10.

Table 3.10. Kinetic constants of enzyme activity study of free and adsorbed lysozyme on TMA coated surface as calculated from Lineweaver-Burk plot.

	v_{max} ($mgmL^{-1}$ min^{-1})	K_m (mg)	k_{cat} (sec^{-1})
Free Lysozyme	1.75	8.9	4.8
Adsorbed Lysozyme	1.79	13.7	5.1

The maximum velocity (v_{max}) of free lysozyme activity was almost same after adsorption on TMA coated surface (1.75 and 1.79 mg mL^{-1} per minute respectively); *i.e.* adsorption of lysozyme has a little influence on the release of product (here in terms of lysis of *M. lysodeikticus*) in the rate limiting step. The K_m value of lysozyme increases from 8.9 to 13.7 mg after adsorption TMA coated surface. The increase in K_m value indicates a reduced binding affinity of the adsorbed enzyme towards the lysis of *M. lysodeikticus*. However, the change in K_m value has a comparatively lesser effect on the turn-over number (k_{cat}) of the enzyme. The k_{cat} value of lysozyme in adsorbed state on TMA coated surface is slightly higher than that of free enzyme (4.8 and 5.1 per second respectively for free and adsorbed) as obtained from Michaelis-Menten kinetics. Hence, the binding of lysozyme has affected the K_m value most, and has a little effect on the kinetic velocity (v). Therefore, it can be an efficient means of tuning surface immobilization of enzyme which

significantly included the selectivity of enzyme adsorption from a mixed protein solution with high retention of activity.

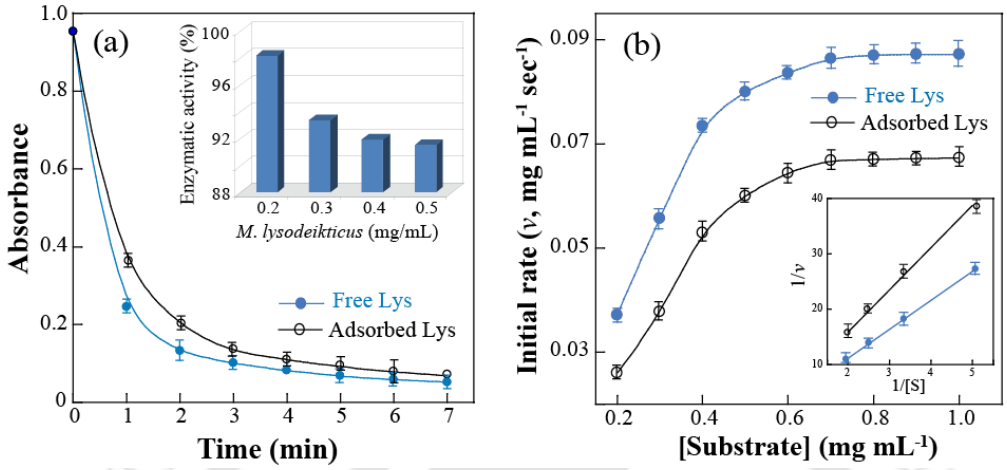

Figure 3.33. (a) Enzyme activity study of free and adsorbed lysozyme with 0.2 mg mL^{-1} initial substrate (*M. lysodeikticus*) concentration solution, (*Inset*) relative activity (%) of adsorbed lysozyme on TMA coated surface with different initial *M. lysodeikticus* concentration solution. In each case, the activity of free enzyme is taken as 100% respectively. (b) Michalelis-Menten enzyme kinetics of free and adsorbed lysozyme, (*Inset*) double reciprocal Lineweaver-Burk plot of free and adsorbed lysozyme.

3.5.9. Summary

In the above section, we have shown an effective approach for selective interaction of lysozyme on a carboxylated coated surface at physiological pH (7.4). Hen egg white lysozyme selectively adsorbed from a mixed solution with BSA on TMA coated alumina particles. The selectivity of lysozyme adsorption at physiological pH can be attributed to the electrostatic interaction between surface TMA and proteins in this pH range which is affected by and iso-electric point and pK_a value of proteins and TMA molecule respectively. Detail studies reveal that adsorption of lysozyme over BSA was first and followed second order kinetics preferably. Isotherm studies indicate a maximum monolayer coverage of lysozyme which can be expressed better by Langmuir isotherm model. A binding stoichiometry of 0.86 for surface to lysozyme was obtained following the Job's plot. Selective adsorption of lysozyme was thermodynamically favourable and exothermic in nature. The adsorbed lysozyme was partially unfolded and remains in a molten-globule like structure as obtained from fluorescence spectra. However, the secondary helical structures of adsorbed lysozyme were almost retained (only ~2-3% loss in α-helical content) compared to native enzyme as analyzed from FT-IR study. Moreover, the adsorbed lysozyme was found to retain very high activity (~98%) relative

to its native protein in solution. An enzymatic kinetic analysis revealed that adsorption phenomena did not affect the rate of enzymatic activity (v), though the binding affinity of lysozyme (K_m) reduced. Therefore adsorption studies on TMA coated alumina surface can be an effective approach in tuning protein-surface interaction, where the selectivity of protein adsorption can meet with the retention of high enzymatic activity.

References

[3.1] Ying, S. M.; Mao, J. G. *J. Mol. Struct.* 2005, 748, 63.

[3.2] Zhang, W.; Bruda, S.; Landee, C. P.; Parent, J.; Turnbull, M.M. *Inorg. Chim. Acta* 2003, 342, 193.

[3.3] Holmes, K. E.; Kelly, P. K.; Elsegood, M. *Dalton Trans*. 2004, 21, 3488.

[3.4] Snyder, L. R. *J. Chromatogr. A* 1966, 23, 388.

[3.5] Mao, Y.; Fung, B. M. *Chem. Mater*. 1998, 10, 509.

[3.6] Guan, X. H.; Chen, G. H.; Shang, C. *J. Colloid Interface Sci*. 2006, 301, 419.

[3.7] Mao, Y.; Fung, B. M. *J. Colloid Interface Sci*. 1997, 191, 216.

[3.8] Evanko, C. R.; Dzombak, D. A. *Environ. Sci. Technol*. 1999, 32, 2846.

[3.9] Evans, H. E.; Weinberg, W. H. *J. Chem. Phys*. 1979, 71, 4789.

[3.10] Edwards, M.; Benjamin, M. M.; Ryan, J. N. *Colloids Surf. A* 1996, 107, 297.

[3.11] Silverstein, R. M.; Bassler, G. C.; Morrill, T. C. *Spectrometric Identification of Organic Compound* (fifth ed.), 1991, Wiley, New York.

[3.12] Molinari, R.; Poerio, T.; Cassano, R.; Picci, N.; Argurio, P. *Ind. Eng. Chem. Res*. 2004, 43, 623.

[3.13] Gündoğan, R.; Acemioğlu, B.; Alma, M. H. *J. Colloid Interface Sci*. 2004, 269, 303.

[3.14] Flemming, C. A.; Trevors, J. T. *Water Air Soil Pollut*. 1989, 44, 143.

[3.15] Rengaraj, S.; Kim, Y.; Joo, C. K.; Yi, J. *J. Colloid Interface Sci*. 2004, 273, 14.

[3.16] Aaseth, J.; Norseth, T. *Handbook on the Toxicity of Metals*, 1986, Elsevier, Amsterdam.

[3.17] (a) Kumar, G. P.; Kumar, P. A.; Chakraborty, S.; Ray, M. *Sep. Purif. Technol*. 2007, 57, 47. (b) Bailey, S. E.; Olin, T. J.; Bricka, R. M.; Adrian, D. D. *Water Res*. 1999, 33, 2469.

[3.18] (a) Goyal, M.; Rattan, V. K.; Aggarwal, D.; Bansal, R. C. *Colloids Surf. A* 2001, 190, 229. (b) Subramaniam, K.; Yiacoumi, S. *Colloids Surf. A* 2001, 191, 145. (c) Bois, L.; Bonhommé, A.; Ribes, A.; Pais, B.; Raffin, G.; Tessier, F. *Colloids Surf. A* 2003, 221, 221. (d) Cassella, R. J.; Bitencourt, D. T.; Branco, A. G.; Costa Ferreira, S. L.; de Jesus, D. S.; de Carvalho, M. S.; Santelli, R. E. *J. Anal. Atomic Spectrometry* 1999, 14, 1749. (e) Tseng, R. L.; Wu, F. C.; Juang, R. S. *J. Chem. Tech. Biotechnol.* 1999, 74, 533. (f) Kim, M. S.; Hong, K. M.; Chung, J. G. *Water Res.* 2003, 37, 3524. (g) Huang, Y. H.; Hsueh, C. L.; Cheng, H. P.; Su, L. C.; Chen, C. Y. *J. Haz. Mat.* 2007, 144, 406.

[3.19] Chen, J.P.; Wu, S. *Langmuir* 2004, 20, 2233.

[3.20] Baes, C. F.; Messmer, R. E. *The Hydrolysis of Cations*, 1976, Wiley, New York.

[3.21] Hall, K. R.; Eagleton, L. C.; Acrivos, A.; Vermeulen, T. *Ind. Eng. Chem. Fund*. 1966, 5, 212.

[3.22] Voice, T. C.; Weber, W. J. *Water Res*. 1983, 17, 1433.

[3.23] Ho, Y. S.; Chiu, W.; Wang, C. *Bioresour. Technol*. 2005, 96, 1285.

[3.24] Sun, G.; Shi, W. *Ind. Eng. Chem. Res*. 1998, 37, 1324.

[3.25] Nriagu, J. O.; Pacyna, J. M. *Nature* 1988, 333, 134.

[3.26] Wingenfelder, U.; Hansen, C.; Furrer, G.; Schulin, R. *Environ. Sci. Technol*. 2005, 39, 4606.

[3.27] Moore, J. W. *Inorganic Contaminants of Surface Water,* 1999, Springer-Verlag, New York.

[3.28] (a) Aksu, Z. ; Calik, A. *J. Environ. Sci. Health Part A – Toxic Hazard. Substances Environ. Eng.* 1999, 34, 2087. (b) Santana, J. L.; Lima, L.; Torres, J.; Martinez, F.; Olivares, S. *J. Radioanal*. *Nucl. Chem.* 2002, 251, 467. (c) Nassar, M. M.; Ewida, K. T.; Ebrahiem, E. E.; Magdy, Y. H.; Mheaedi, M. H. *J. Environ. Sci. Health Part A – Toxic Hazard. Substances Environ. Eng.* 2004, 39, 421.

[3.29] (a) Mohan, D.; Chander, S. *J. Hazard. Mater.* 2006, 137, 1545. (b) Hellier, W. W.; In: Azcue, J. M. (Ed.), *Environmental Impacts of Mining Activities*, 1999, Springer-Verlag, Berlin.

[3.30] Ahrland, S.; Chatt, J.; Davies, N. R. *Quart. Rev. Chem. Soc.* 1958, 72, 265.

[3.31] Huheey, J. E.; Keiter, E. A.; Keiter, R. L.; Medhi, O. K. *Inorganic Chemistry: Principles of Structure and Reactivity* (fourth ed.), 2007, Harper Collins, New York.

[3.32] Pearson, R. G. *J. Am. Chem. Soc.* 1963, 85, 3533.

[3.33] Chen, J.; Kong, H.; Wu, D.; Hu, Z.; Wang, Z.; Wang, Y. *J. Colloid Interface Sci.* 2006, 300, 491.

[3.34] (a) Grubb, D. G.; Guimaraes, M. S.; Valencia, R. *J. Hazard. Mater.* 2000, 76, 217. (b) Oguz, E. *Colloids Surf. A*. 2005, 262, 113. (c) Pengthamkeerati, P.; Satapanajaru T.; Chularuengoaksorn, P. *Fuel* 2008, 87, 2469.

[3.35] (a) Genz, A.; Kornmuller, A.; Jekel, M. *Water Res.* 2004, 38 3523. (b) Zhao, D.; Sengupta, A. K. *Water Res*. 1998, 32, 1613. (c) Karageorgiou, K.; Paschalis, M.; Anastassakis, G. N. *J. Hazard. Mater*. 2007, 139, 447. (d) Nowack, B.; Stone, A. T. *Water Res.* 2006, 40, 2201.

[3.36] (a) Urano K.; Tachikawa, H. *Ind. Eng. Chem. Res*. 1991, 30, 1893. (b) Hano, T.; Takanashi, H.; Hirata, M.; Urano, K.; Eto, S. *Water Sci. Technol.* 1997, 35, 39. (c) Ookubo, A.; Ooi, K.; Hayashi, H. *J. Pharm. Sci.* 1992, 81, 1139.

[3.37] APHA, WEF, AWWA. In: Clesceri, L. S.; Greenberg, A. E.; Eaton, A. D. (Eds.), *Standard Methods for the Examination of Water and Wastewater* (20th ed.), 1998, American Public Health Association, Washington, DC.

[3.38] Ozcar, M. *Cem. Concr. Res.* 2003, 33, 1583.

[3.39] Joshi, V. S.; Joshi, M. J. *Cryst. Res. Technol.* 2003, 38, 817.

[3.40] Giles, C. H.; McEvan, T. H.; Nakhwa, S. N.; Smith, D. *J. Chem. Soc.* 1960, 4, 3973.

[3.41] (a) Kuzawa, K.; Jung, Y. J.; Kiso, Y.; Yamada, T.; Nagai, M.; Lee, T. G. *Chemosphere* 2006, 62, 45. (b) Kim, E. H.; Lee, D. W.; Hwang, H. K.; Yim, S. *Chemosphere* 2006, 63, 192.

[3.42] (a) Deng, L.; Mrksich, M.; Whitesides, G. M. *J. Am. Chem. Soc.* 1996, 118, 5136. (b) Chapman, R. G.; Ostuni, E.; Takayama, S.; Holmlin, R. E.; Yan, L.; Whitesides, G. M. *J. Am. Chem. Soc.* 2000, 122, 8303. (c) Silin, V.; Weetall, H.; Vanderah, D. J. *J. Colloid Interface Sci.* 1997, 185, 94.

[3.43] (a) Ogawa, R.; Nagasaki, Y.; Shibata, N.; Otsuka, H.; Kataoka, K. *Polym. J.* 2002, 34, 868. (b) Bearinger, J. P.; Terrettaz, S.; Michel, R.; Tirelli, N.; Vogel, H.; Textor, M.; Hubbell, J. A. *Nat. Mater.* 2003, 2, 259.

[3.44] (a) Kusumo, A., Bombalski, L., Lin, Q., Matyjaszewski, K., Schneider, J. W., and Tilton, R. D. *Langmuir* 2007, 23, 4448. (b) Schwint, P., Voegel, J.-C., Picart, C., Haikel, Y., Schaaf, P., and Szalontai, B. *J. Phys. Chem. B* 2001, 105, 11906-11916.

[3.45] (a) Wittemann, A., Haupt, B., and Ballauff, M. *Phys. Chem. Chem. Phys.* 2003, 5, 1671. (b) Anikin, K., Rcker, C., Wittemann, A., Wiedenmann, J., Ballauff, M., and Nienhaus, G. U. *J. Phys. Chem. B* 2005, 109, 5418. (c) Hollmann, O., and Czeslik, C. *Langmuir* 2006, 22, 3300.

[3.46] Andrade, J. D. *Surface and Interfacial Aspects of Biomedical Polymers*; Plenum Press: New York, 1985; Vol. 2.

[3.47] (a) Lensun, L., Smith, T. A., and Gee, M. L. *Langmuir* 2002, 18, 9924. (b) Vermonden, T., Giacomelli, C. E., and Norde, W. *Langmuir* 2001, 17, 3734. (c) Maste, M. C. L., Norde, W., and Visser, A. J. W. G. *J. Colloid Interface Sci.* 1997, 196, 224.

[3.48] (a) Sivaraman, B.; Fears, K. P.; Latour, R. A. *Langmuir*, 2009, 25, 3050. (b) Veiseh, M.; Zareie, M.H.; Zhang, M. *Langmuir*, 2002, 18, 6671. (c) Ajikumar, P. K.; Ng, J. K.; Tang, Y. C.; Lee, J. Y.; Stephanopoulos, G.; Too, H. *Langmuir*, 2007, 23, 5670.

[3.49] (a) Tanford, C., and Roxby, R. *Biochemistry* 1972, 11, 2192. (b) Privalov, P. L., and Khechinashvili, N. N. *J. Mol. Biol.* 1974, 86, 665.

[3.50] (a) Carter, D. C., and Ho, J. X. *Adv. Protein Chem.* 1994, 45, 153203. (b) La Rosa, C., Milardi, D., Fasone, S., and Grasso, D. *Thermochim. Acta* 1994, 235, 231.

[3.51] (a) Griebenow, K.; Klibanov, A. M. *J. Am. Chem. Soc.*1996, 118, 11695. (b) Griebenow, K.; Klibanov, A. M. *Proc. Natl. Acad. Sci. U.S.A.* 1995, 92, 10969. (c) Fu, F.-N.; DeOliveira, D. B.; Trumple, W. R.; Sakar, H. K.; Singh, B. R. *Appl. Spectrosc.* 1994, 48, 1432.

[3.52] Fu, K.; Griebenow, K.; Hsieh, L.; Klibnov, A. M.; Langer, R. *J. Controlled Release* 1999, 58, 357.

[3.53] Costantino, H. R.; Griebenow, K., Mishra, P.; Langer, R.; Klibanov, A. M. *Biochim. Biophys. Acta* 1995, 1253, 69.

[3.54] Blake, C. C. F.; Koenig, D. F.; Mair, G. A.; North, A. C. T.; Phillips, D. C.; Sarma, V. R. *Nature* 1965, 206, 757.

[3.55] (a) Su, T. J.; Lu, J. R.; Thomas, R. K.; Cui, Z. F.; Penfold, J. *J. Colloid Interface Sci.* 1998, 203, 419. (b) Wertz, C. F.; Santore, M. M. *Langmuir* 2002, 18, 1190. (c) Daly, S. M.; Przybycien, T. M.; Tilton, R. D. *Langmuir* 2003, 19, 3848. (d) Aizawa, T.; Koganesawa, N.; Kamakura, A.; Masaki, K.; Matsuura, A.; Nagadome, H.; Terada, Y.; Kawano, K.; Nitta, K. *FEBS Lett.* 1998, 422, 175.

[3.56] Haggerty, L.; Lenhoff, A. M. *Biophys. J.* 1993, 64, 886.

[3.57] Pellenc, D.; Bennett, R. A.; Green, R. J.; Sperrin, M; Mulheran, P. A. *Langmuir* 2008, 24, 9648.

[3.58] Goobes, G., Goobes, R., Shaw, J. W., Gibson, M. J., Long, R. J., Raghunathan, V., Schueler-Furman, O., Popham, M. J., Baker, D., Campbell, T. C., Stayton, S. P. and Drobny, G. P. *Magn. Reson. Chem.* 2007, 45, S32– S47.

[3.59] (a) Koutsopoulos, S.; Patzsch, K.; Bosker, W. T. E.; Norde, W. *Langmuir* 2007, 23, 2000. (b) Lakowicz, J. R. Principles of Fluorescence Spectroscopy, 2nd ed.; Springer: New York, 2006.

[3.60] Murayama, K.; Tomida, M. *Biochemistry* 2004, 43, 11526.

[3.61] Copeland, R.A. Enzymes-A practical introduction to structure, mechanism and data analysis, 2nd ed.; Wiley-VCH: New York, 2000.

Appendix

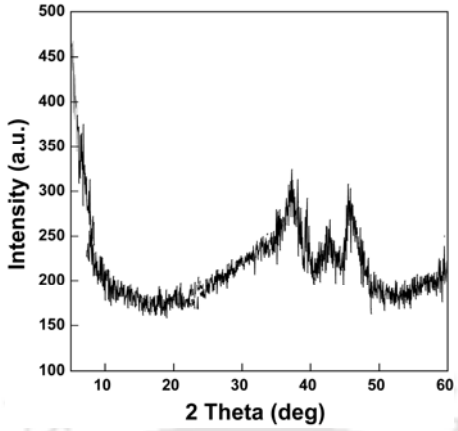

Figure A3.1. PXRD spectra of Fe^{3+} adsorbed TMA coated alumina.

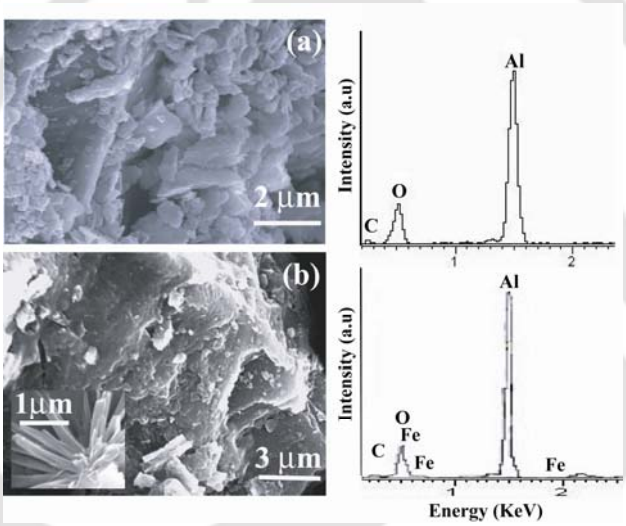

Figure A3.2. SEM pictures and EDX spectrum of TMA coated alumina (a) before adsorption, (b) after Fe^{3+} adsorption.

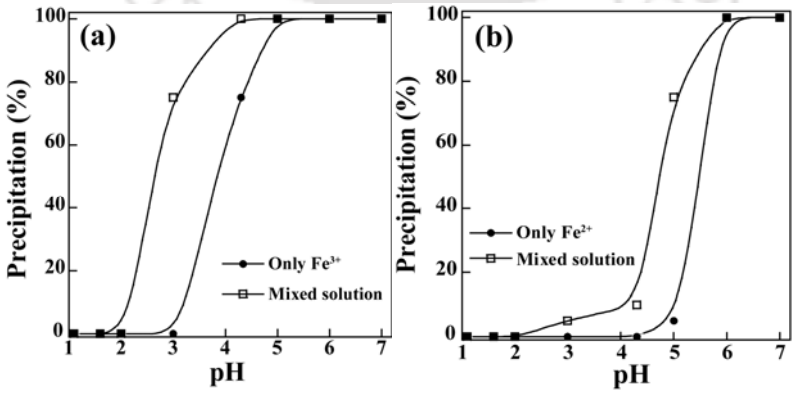

Figure A3.3. Comparison of precipitation of (a) Fe^{3+} and (b) Fe^{2+} ion in equi-molar mixed ion solution with each of their individual solution.

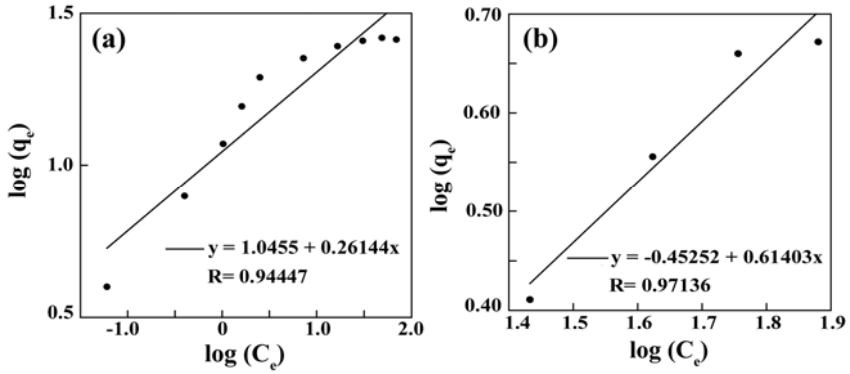

Figure A3.4. Linearized plot of Freundlich adsorption isotherm model for (a) Fe^{3+} and (b) Fe^{2+} ion on TMA coated alumina.

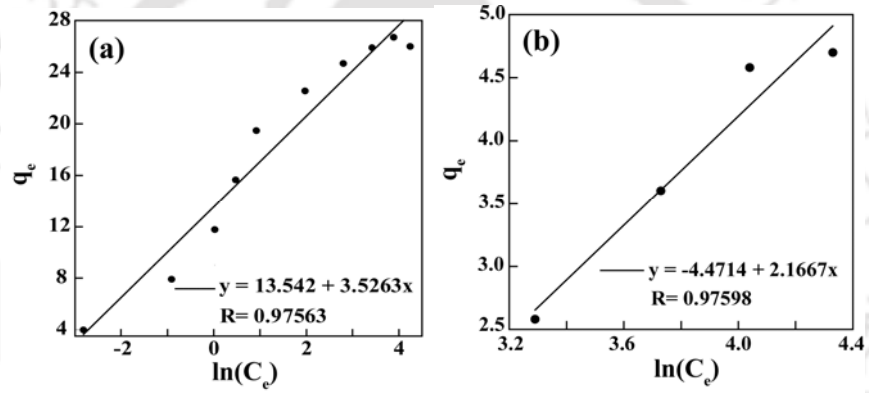

Figure A3.5. Linearized plot of Temkin adsorption isotherm model for (a) Fe^{3+} and (b) Fe^{2+} ion.

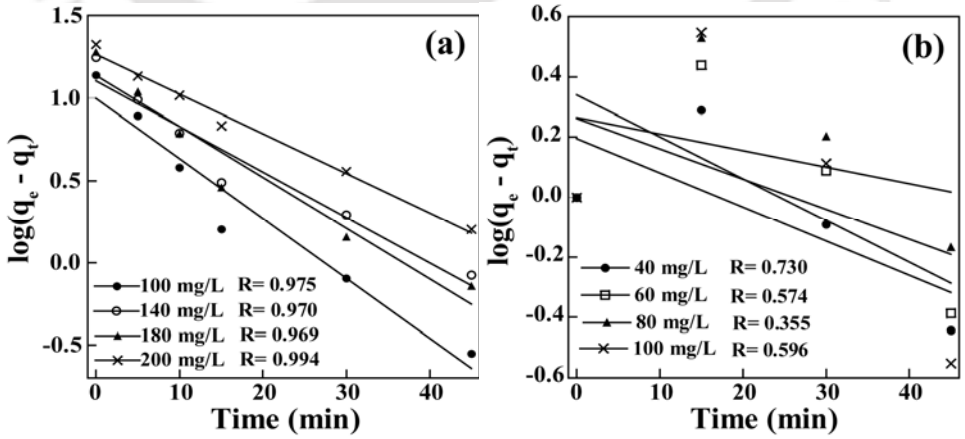

Figure A3.6. Linearized form of first order kinetic model plots for (a) Fe^{3+} and (b) Fe^{2+} ion adsorption.

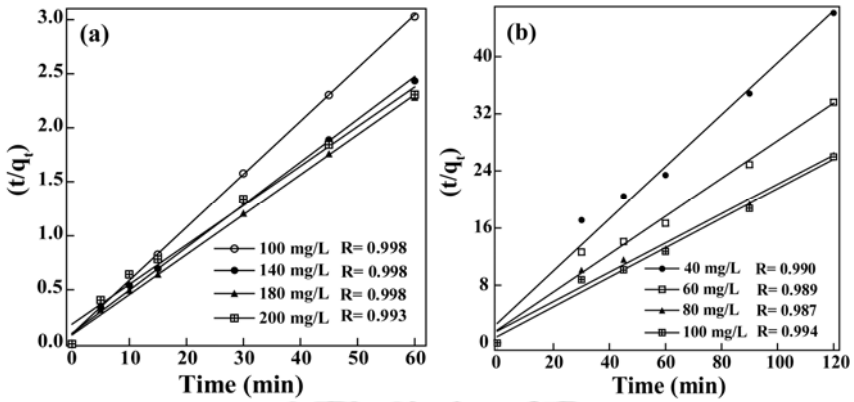

Figure A3.7. Linearized form of second order kinetic model plots for (a) Fe^{3+} and (b) Fe^{2+} ion adsorption.

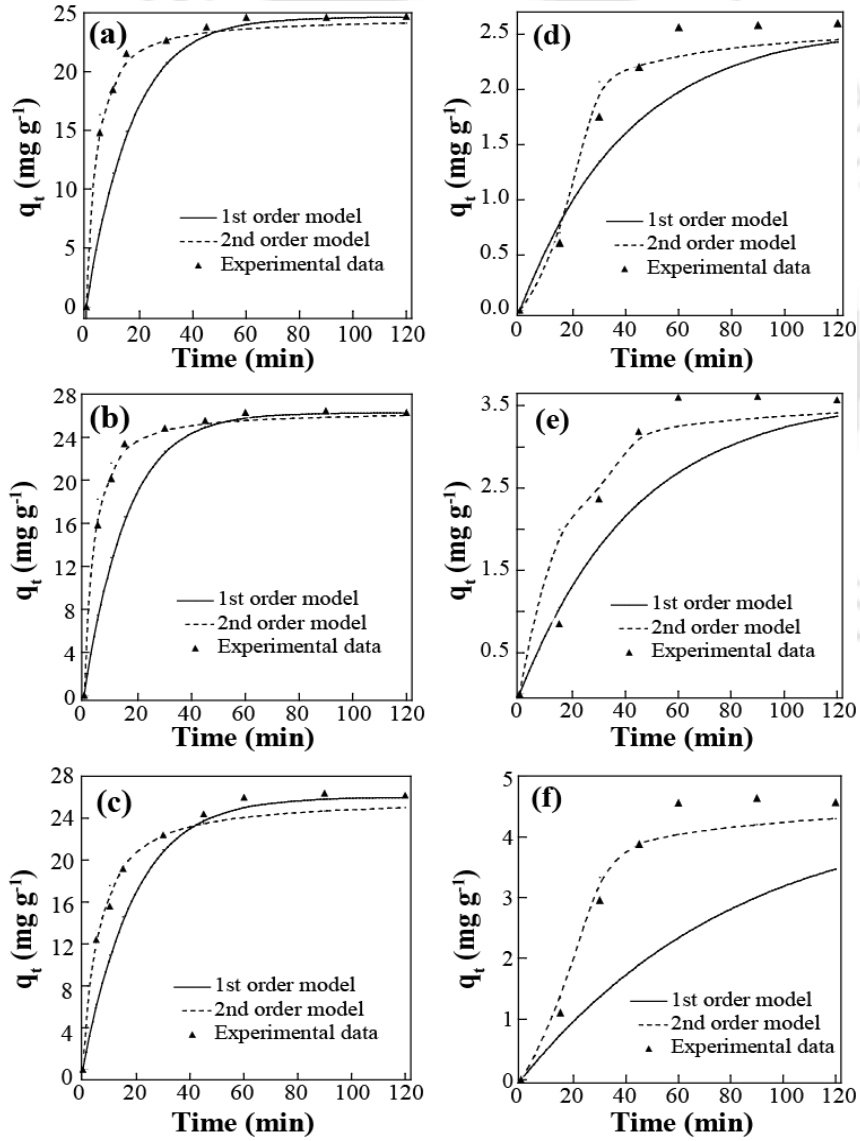

Figure A3.8. Experimental and modelled kinetics comparison studies of Fe^{2+} adsorption with 40 mg L^{-1}, 60 mg L^{-1} and 80 mg L^{-1} initial concentration solution of Fe^{3+} (a, b, c respectively) and Fe^{2+} (d, e, f respectively) ions.

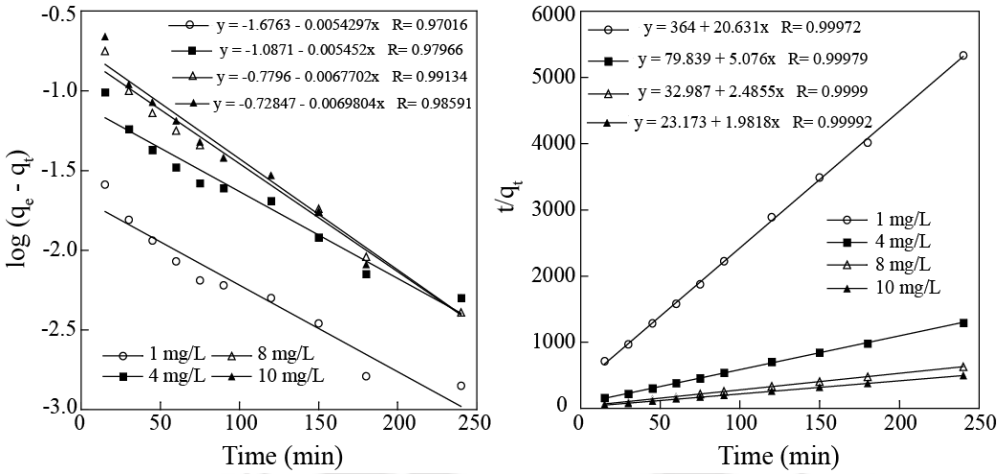

Figure A3.9. Linearized form of (a) first order and (b) second order kinetic plot of phosphate immobilization. Initial phosphate concentration was varied from 1 mg L^{-1} to 10 mg L^{-1} with adsorbent dose of 20 g L^{-1} at pH ~1.0.

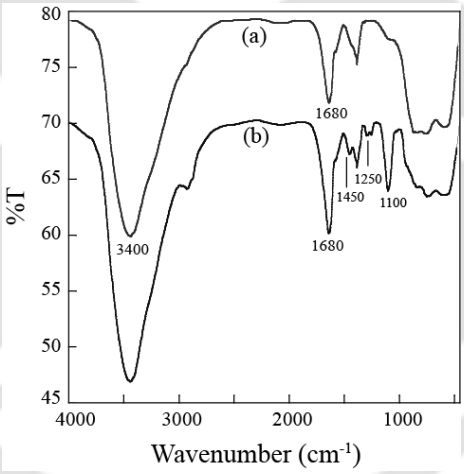

Figure A3.10. FT-IR spectra of TMA coated alumina (a) before and (b) after phosphate adsorption

Table A3.1. Area under curve and concentration of phosphate from ion chromatogram of competitive anion adsorption study (with 0.05 mM concentration solution) to evaluate selectivity of phosphate.

	Area (μS cm^{-1}) × sec				Concentration (mg L^{-1})			
	Cl^-	Br^-	NO_3^-	PO_4^{3-}	Cl^-	Br^-	NO_3^-	PO_4^{3-}
Before adsorption	27.8	20.1	18.4	17.7	1.99	3.62	2.62	4.71
After adsorption	25.5	19.8	17.1	1.3	1.62	3.33	2.46	0.33

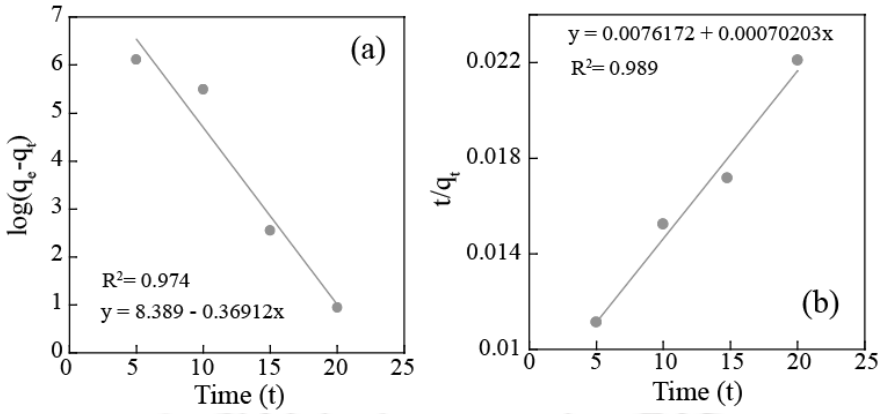

Figure A3.11. (a) First order and (b) second order kinetic model analysis of lysozyme adsorption on TMA coated surface at pH 7.4 and 25oC. Adsorption kinetics could be better described with second order model.

Table A3.2. Kinetic rate constants and correlation coefficient of lysozyme adsorption on TMA coated surface.

	First order kinetics		Second order kinetics	
	k_1 (L min^{-1})	R^2	k_2 (g mg^{-1} min^{-1})	R^2
Lysozyme	0.850	0.974	6.4×10^{-5}	0.983

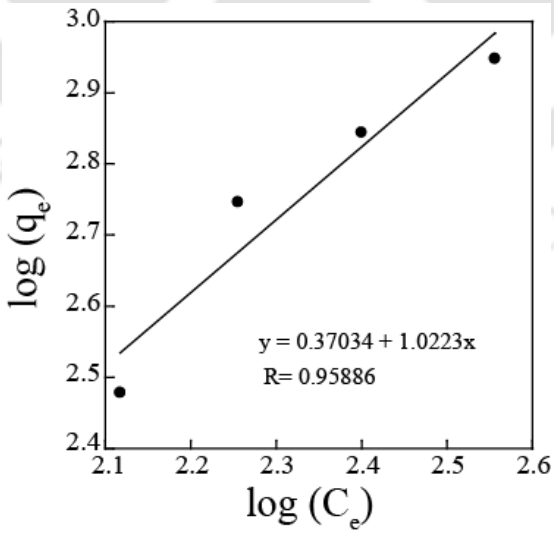

Figure A3.12. Freundlich adsorption isotherm model of lysozyme adsorption on TMA coated surface. However, the isotherm data fitted better in Langmuir model as discussed in the main text.

Table A3.3. Langmuir and Freundlich isotherm parameters of lysozyme adsorption on TMA coated surface.

	Langmuir isotherm				Freundlich isotherm		
	$\Gamma_{Lys,m}$ (mg m^{-2})	b (L mg^{-1})	R^2	R_L	K_f (mg m^{-2})	n	R^2
Lysozyme	2.17	0.0021	0.998	0.86	2.344	0.980	0.958

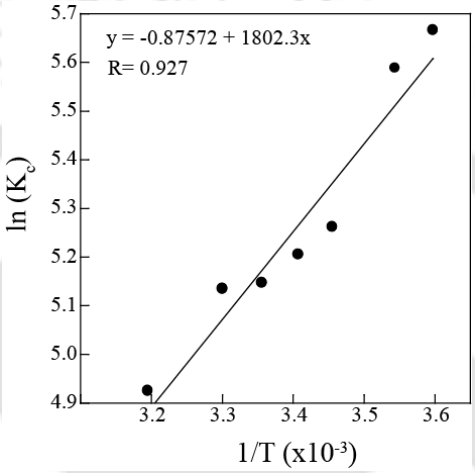

Figure A3.13. Van't Hoff plot of lysozyme adsorption on TMA coated surface at pH 7.4.

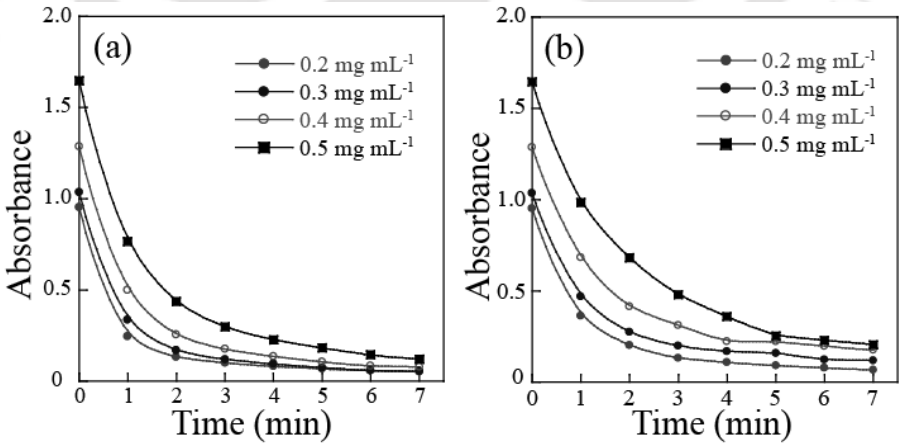

Figure A3.14. Activity of (a) free and (b) adsorbed lysozyme with different concentration of *M. lysodeikticus* (substrate) solution (0.2-0.5 mg mL^{-1}). The ordinate represents the decay in absorbance due to the lysis of *M. lysodeikticus* by free and adsorbed lysozyme measured for 7 min.

Chapter 4

Interaction of Proteins and Ions on a Basic 'Hard' Nanoparticle Surface

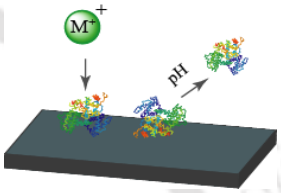

Chapter 4

4.1. Introduction

Progressing from the interaction of proteins and ions on acidic hard surface, as described in previous chapter, this chapter describes the interaction of bovine serum albumin (BSA) and several toxic metal ions with a basic 'hard' nanoparticle surface. Basic copper carbonate, which naturally occurs as malachite, is a secondary copper mineral with the composition of $Cu_2(OH)_2CO_3$. The presence of $-CO_3$ and $-OH$ groups on the surface of malachite makes it a 'hard' surface which can bind strongly with the 'hard' metal ions from aqueous solution. It has been used extensively as catalyst, fertilizer, antimicrobial agent, wood preservative, sensor development, and in fabricating electronic devices.[4.1] There are very few reports on synthesis of malachite nanoparticles. Recently, Molchan *et al*.[4.2] reported a polyol-mediated synthesis of malachite nanoparticle (NP) which involves the reaction in non aqueous ethylene glycol media. Hydrophilic malachite nanoparticles have been synthesized and used as a basic 'hard' surface for interaction of proteins and metal ions in this section.

4.2. Synthesis of basic 'hard' malachite nanoparticles

An amount of 200 mg of $CuSO_4 \cdot 5H_2O$ was added to 100 mL of 4 mM aqueous solution of SDS in a 250 mL round-bottom flask with stirring for 30 min. After that, 10 mM Na_2CO_3 solution was added drop wise with constant stirring at room temperature for an additional 2 h. This resulted in the formation of a green suspension which was stable as no sedimentation was observed for more than 24 h. The reaction product was centrifuged at 15000 rpm. Two-step washing was undertaken; first the precipitate was resuspended by sonication in distilled water several times to remove soluble impurity, followed by several times washing with ethanol. The final product was centrifuged and vacuum-dried for overnight. The malachite nanoparticles were characterized by a transmission electron micrograph (TEM). The malachite NPs were also characterized by scanning electron micrograph (SEM) images, Powder X-ray diffraction (PXRD), FT-IR spectroscopy TGA Specific surface area, pore volume and the surface charge of malachite NPs were also determined.

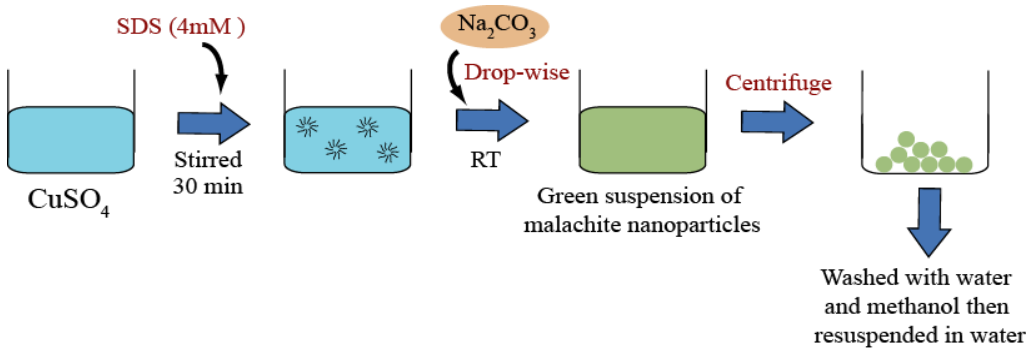

Scheme 4.1. Illustration of synthesis procedure of malachite nanoparticles

4.3. Characterization of malachite nanoparticles

Malachite nanoparticles have been synthesized via a simple one-step method in aqueous solution. TEM images (Figure 4.1a) and corresponding particle size distribution analysis (Figure 4.1b) revealed the spherical shape of malachite NPs which are fairly polydisperse having a size distribution in the range of 100−150 nm. Energy-dispersive X-ray (EDX) analysis of the SEM images reflects the presence of Cu, C, and O only (Appendix, Figure A4.1). Powder X-ray diffraction data (Figure 4.1c) shows the formation of crystalline malachite mineral, and the peaks are matching well with malachite phases (JCPDS file no. 01-076-0660). The average crystallite size calculated, ~130 nm using the Debye−Scherrer equation from the fwhm of the strongest peak, is consistent with the TEM and size distribution analysis. The N_2 adsorption isotherm of the BET analysis represents the type II isotherm according to Brunauer's classification (Appendix, Figure A4.2). From analysis, we found that malachite NPs have a specific surface area of 20.5 ± 0.2 $m^2 g^{-1}$ and pore volume of 0.060 $cm^3 g^{-1}$.

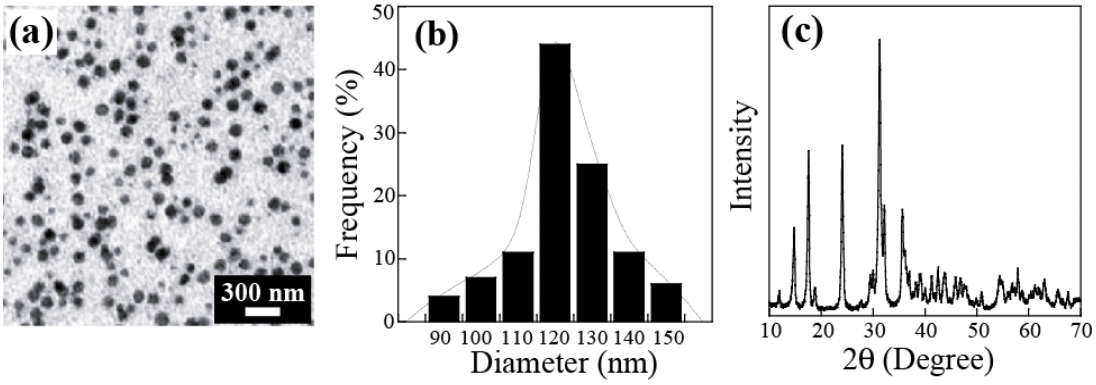

Figure 4.1. (a) TEM images (~100−150 nm), (b) particle size distribution, and (c) powder XRD pattern of malachite nanoparticles.

FT-IR spectra (Appendix, Figure 4.3) show few characteristic peaks of malachite minerals. The sharp peaks at 3410 and 3320 cm^{-1} are due to stretching vibration of −O−H. Peaks at 1505 and 1396 cm^{-1} are attributed to the ν_3 antisymmetric $(CO_3)^{2-}$ stretching modes.[4.3] The intensive band at 1096 cm^{-1} is assigned to the ν_1 $(CO_3)^{2-}$ symmetric stretching vibration. The bands at 810 and 748 (ν_4 of CO_3) cm^{-1} are due to ν_2 and ν_4 bending modes, respectively.[4.4] Thermogravimetric analysis reveals a sharp decomposition of malachite NPs in the temperature range of ~250−330°C as can be seen from the TGA and differential thermal analysis (DTA) curves (Figure 4.2a), which is in good agreement with the previous reports.[4.5,4.6] Tanaka and Yamane[4.5] and Brown *et al*.[4.6] reported a single-step decomposition of malachite as follows:

$$CuCO_3.Cu(OH)_2 \rightarrow 2CuO + CO_2 + H_2O \qquad (4.1)$$

A similar decomposition pattern was also found in our study. The theoretical weight loss of malachite based upon the above-discussed equation is ~28.0%, whereas the measured weight loss from the TGA curve (Figure 4.2a) is about ~28.6%. Therefore, the theoretical and experimental weight losses were found to be close together. The DTA curve shows a sharp endothermic peak at temperature of ~300 °C, which corresponds to the decomposition to CuO. The measured ζ-potential of malachite NPs is shown in Figure 4.2b. From ζ-potential measurement it has been found that malachite NPs have a high positive charge (~15−20 mV) on their surface in the pH range of 5−7. The point of zero charge (pzc) of malachite NPs is around pH ~7.6 which is similar to previously reported results by Gonzaletz and Laskowski.[4.7]

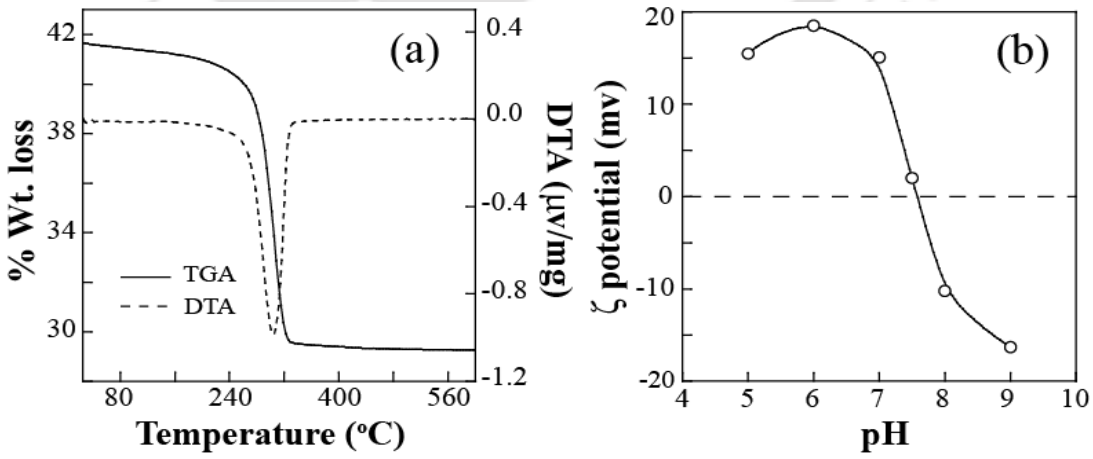

Figure 4.2. (a) Thermogravimetric analysis and (b) ζ-potential measurement of malachite nanoparticles.

This chapter has been divided into two sections:

Part 1: pH controlled interaction of BSA on basic hydrophilic malachite nanoparticles surface.

Part 2: Controlled interaction of toxic and precious metal ions on BSA−malachite nanocomposites.

Part 1:

4.4. pH controlled interaction of BSA on basic hydrophilic malachite nanoparticles surface.

4.4.1. Background

The interaction of proteins with inorganic mineral nanoparticles and nanoparticle-based materials is a fundamental phenomenon which has broad and emerging fields of applications like biomaterials, bioseparation technology, and bio-nanotechnology.[4.8] Moreover, in nanotechnology, protein−surface interactions are crucial for assembly of interfacial protein constructs, such as sensors and activators. Though the adsorption phenomenon of proteins on different solid substrates is widely studied, its mechanism is not fully understood. When protein solution is exposed to solid surface, it often leads to adsorption. The adsorption process comprises many steps, starting with the transport of the protein from the solution to the surface, attachment and relaxation at the adsorbent surface, and release of the protein from the surface back into the solution. Depending upon the nature of the surface and pH, the protein molecule gets adsorbed on the surface through different types of interactions like van der Waals, electrostatic, or hydrogen bonding.[4.9] On hydrophilic surfaces, 'hard' proteins adsorb mainly due to electrostatic attraction, whereas 'soft' proteins often gain in entropy from unfolding at solid surfaces, which is one of the driving forces of adsorption.[4.10,4.11] Therefore, to a large extent the adsorption phenomenon is dependent upon the surface properties. In addition with the hydrophilic and hydrophobic nature of the solid−liquid interface, the acidic or basic nature of the solid interface and proteins may have an effect on the protein adsorption behavior. In this regard, an acidic or basic surface would interact differently with acidic or basic proteins. The adsorption of protein on malachite NPs can be of interest in several ways. The influence of the basic nature of malachite NP on protein adsorption behavior (in terms of solution pH) can be compared to studies of known acidic NP like silica. The different adsorption behavior of a protein on acidic and basic surfaces can be utilized in many applications like in bioseparation, bio-nanotechnologies, and in

development of biochemical sensors. Previous studies on BSA adsorption on acidic silica and other hydrophilic surfaces reported the adsorption maxima around the isoelectric point (IEP) of BSA (~pH 4.7) and significant decrease in adsorption with increasing the pH beyond IEP_{BSA}.[4.12-4.16] BSA primarily interacts with the surface hydroxyl group of silica through the hydrogen bonding and electrostatic interaction.[4.17-4.19] While increasing the pH away from the IEP of the proteins, the electrostatic repulsion between the proteins and the negatively charged silica surface (pH_0 at ~2.7−3.0)[4.20] increases. Though the affinity is reduced, still negatively charged proteins (at pH > IEP) can adsorb on the negatively charged silica surface, by compensating the electric repulsion through its conformational alteration. In other studies also, reduced surface coverage of BSA on hydrophilic inorganic oxide nanoparticles like magnetite and TiO_2 upon immediate increase of pH > IEP_{BSA} was reported.[4.21-4.24] Similar adsorption behavior was also found on several hydrophilic inorganic minerals.[4.25,4.26] In these cases also a significant decrease in surface coverage of protein was observed just above the IEP of the protein. However, with malachite NPs, we expected to have an additional acid−base interaction at pH > IEP of protein due to the basic nature of malachite surface, which may affect the adsorption behavior of acidic BSA.

In addition with the surface−protein interaction, different surface modifications have an interesting impact on the protein adsorption phenomenon. Incorporating a hydrophilic/hydrophobic functional group on a solid surface can result in different adsorption behaviors of proteins. This can be useful in bioseparation technologies and sensor surface development. Stearic acid is a natural, biomimetic saturated fatty acid with a long (C_{18}) flexible hydrocarbon chain. The carboxyl group in stearic acid is reactive and can easily form a hydrogen bond to a hydrophilic surface. Hence, on a hydrophilic surface like malachite, stearic acid is expected to interact through carboxylate groups with the hydroxyl groups of malachite surface. Therefore, the adsorption behavior of BSA on these stearic acid modified NPs (SA−malachite NPs) will be affected and is of interest on the basis of surface modification.

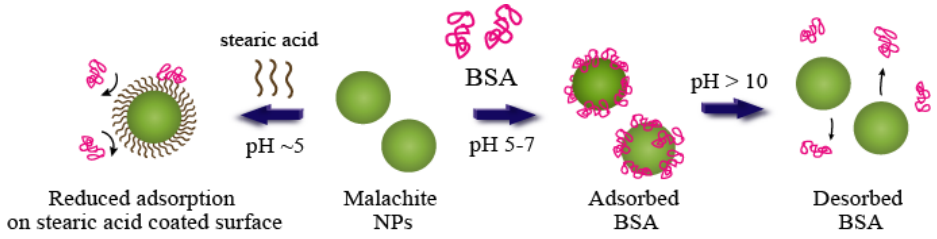

Scheme 4.2. pH controlled interaction of BSA on malachite nanoparticles and stearic acid modified malachite nanoparticles.

This section describes a highly pH-controlled adsorption−desorption behavior of BSA on malachite nanoparticle surface (Scheme 4.2). Malachite nanoparticles have been synthesized in a simple and new sodium dodecyl sulfate (SDS)-mediated method in aqueous media and for the first time have been used as a model basic−hydrophilic surface for protein adsorption. Bovine serum albumin (BSA), which is the most abundant protein in plasma, was taken as a model protein for adsorption studies. Well-known structural features of BSA[4.27,4.28] help in investigation of protein conformational changes on malachite and SA−malachite NPs. A dissimilar adsorption phenomenon of BSA on basic malachite NPs has been observed compared to other nanoparticles like acidic silica, magnetite, or TiO_2 in the context of solution pH, which can be useful in bioseparation, bionanotechnology, and in developing biochemical sensors. We have also investigated the influence of stearic acid coating on malachite NPs on BSA adsorption. In situ analysis of conformational characteristics of BSA by standard spectroscopic techniques like circular dichroism and fluorescence spectroscopy was feasible due to the small size (~100−150 nm) of malachite NPs. Steady-state and time-resolved fluorescence spectroscopies were employed to monitor the change in tertiary conformation and binding of BSA with malachite NPs. Fourier transform infrared spectroscopy (FT-IR) and circular dichroism (CD) were used to monitor the secondary structural changes of BSA in the adsorbed state and after desorption. Atomic force microscopy (AFM) has also been used for the direct visualization and analysis of the adsorbed protein layers onto the malachite NP surface. These techniques together provide information on both the macroscopic scale as well as the molecular level of the BSA−malachite NP interaction.

4.4.2. Materials and methods

Materials. Prior to each experiment, fresh aqueous protein solutions of different concentrations (1−5 mg mL^{-1}) with Milli-Q water (18.2 MΩ) were prepared. Stearic acid dissolved in methanol and used for surface modification of malachite nanoparticles.

Coating of malachite nanoparticles with stearic acid. A 20 mL aliquot of stearic acid solution (5 mg mL^{-1} in methanol) was added to 100 mg of malachite NPs in a conical flask. This mixture was stirred continuously for 5 h. The adsorption profile of stearic acid was determined by measuring the concentration of stearic acid remaining in the supernatant by base titration as a function of time. Once steady state has been reached, the aliquots were separated from the solid phase by 15 min of centrifugation at 15000 rpm in a *REMI-2000* (India) centrifuge. The precipitate was further resuspended by sonication

and washed with deionized Milli-Q water and thereafter vacuum-dried before adsorption studies.

Adsorption experiment of BSA. Batch adsorption experiments were performed in 2 mL vials by adding 100 mg (20 g L^{-1}) of malachite NPs to BSA aqueous solution of different concentrations (1−5 mg L^{-1}). These vials were stirred in an incubator shaker for 5 h at 20°C. The adsorption kinetics was studied (with 1 mg mL^{-1} BSA and 20 g L^{-1} malachite) by withdrawing the samples at regular intervals and subsequent centrifugation to obtain suitable aliquots for analysis of protein concentration. Preliminary studies showed that this period of time is sufficient to ensure steady state. Solution pH was varied from 4.0 to 12.0 in different sets of experiments to study its effect on the adsorption and release of BSA from malachite surface. Once the steady state was reached, the protein-adsorbed NPs were separated from unbound proteins in solutions by centrifugation at 15000 rpm for 15 min. The supernatant was measured for residual BSA concentration in UV spectrophotometer from the absorbance at 280 nm. The amount of BSA adsorbed per unit weight of malachite (q_e, mg of BSA/g of malachite) can be calculated from the initial (C_0, mg L^{-1}) and final (C_e, mg L^{-1}) protein concentration and malachite concentration (g L^{-1}) in the solution. Surface coverage of BSA, Γ_{BSA} (mg m^{-2}), was calculated at different adsorption conditions from the mass balance and specific surface area of malachite NPs. The adsorption behavior of BSA on SA−malachite NPs has been studied and the influence of surface modification on protein adsorption was monitored in a similar way described above. This study with SA−malachite NPs was performed at the pH where high Γ_{BSA} was achieved for BSA adsorption on bare malachite NPs from previous experiments. The isotherm experiment with different initial protein solutions (0.1−1.0 mg L^{-1}) was also performed to get the maximum adsorption capacity on SA−malachite NPs. Protein-loaded NPs were resuspended by sonication in a protein-free aqueous solution for desorption study. Solution pH was raised with 0.1 M NaOH to study desorption of BSA as a function of pH. Samples were taken out at regular intervals and centrifuged to separate desorbed BSA from malachite NPs. Concentration of the desorbed BSA at different pH was measured by a UV spectrophotometer.

Fluorescence emission spectroscopy. Tertiary structural changes of BSA in native, adsorbed, and desorbed states were measured using a tryptophan fluorescence emission technique in a steady-state spectrofluorimeter. The excitation wavelength at 290 nm was chosen because almost all the fluorescence emission signal excited at this wavelength is derived from tryptophan. The tryptophan emission fluorescence spectrum was collected

in the wavelength range of 320−500 nm at 20 °C. The emission spectra of protein samples containing malachite NPs were corrected using the baseline acquired from suspension of the same concentration of malachite NPs without BSA. Steady-state anisotropy measurement was performed in all the cases. Time-resolved intensity decays of the proteins in different state were measured. The sample was excited by Pico-quant 290 nm laser source, and the decay was measured in a time scale of 0.0488 ns/channel. The decay curves were analyzed by FAST software using the discrete exponential method, and the mean lifetime (τ_m) of BSA in different experimental conditions was also calculated.

Circular dichroism. The secondary conformational characteristics of BSA in native solution, in adsorbed state, in solution after being desorbed from malachite NPs, and after interaction with SA−malachite NPs were investigated by far-UV CD spectra in a spectropolarimeter. The concentration of BSA was ~0.1 mg mL^{-1}. Spectra were recorded in a 0.1 cm path length quartz cuvette for acquisition in the far-UV region of 180−240 nm. For all the samples data was collected by averaging three scans with the scan rate of 50 nm min^{-1} at 20 °C. Blank spectra of the solution and of the particle suspension without protein were obtained at identical conditions to correct the albumin spectra at the adsorbed state. Spectra were analyzed for secondary structure content by a curve-fitting method described by Yang *et al.*[4.29] All fittings had normalized root-mean-square (rms) error less than 10 as described by Brahms and Brahms[4.30] for best quality fit.

Fourier transform infrared spectra. FT-IR spectra of lyophilized BSA samples of native, adsorbed, and desorbed states and after interaction with SA−malachite NPs were taken. All the spectra of lyophilized samples were measured with 1 mg samples in 200 mg of KBr as a pellet on the range of 2500−500 cm^{-1}. After background correction, Fourier self-deconvolution (FSD) was applied to the unsmoothed spectra for band narrowing (full width half-maxima, fwhm = 16 cm^{-1} and enhancement factor, k = 2.0).[4.31] Gaussian curve-fitting was then performed using GRAMS/AI software (Thermo Fisher Scientific, Massachusetts) on the Fourier self-deconvoluted amide I band region. The secondary structural content was calculated from the areas of the individual assigned bands and their fraction of the total area in the amide I region. In each case a linear baseline was fitted in addition to the Gaussian bands.

Atomic force microscopic studies. AFM studies of BSA adsorbed on malachite surfaces were performed in room temperature. The malachite layer was prepared on mica wafers by spin-coating and thereafter incubated in the protein solution (1 mg mL^{-1}) at room

temperature for 5−6 h to ensure steady-state protein adsorption. Then the wafers were washed with ultrapure water to remove the unbound proteins. The images were reproducible. For the determination of adsorbed BSA molecules, the horizontal peak-to-valley distances were calculated.

4.4.3. pH controlled interaction of BSA on malachite nanoparticles

The adsorption and release of BSA onto malachite nanoparticle surface was found to be highly pH-controlled (Figure 4.3). The dehydration of the surface is an entropic driving force due to which proteins do adsorb on the solid surface upon exposure. On a hydrophilic surface like malachite, proteins adsorb mainly through electrostatic interaction. Adsorption could also be favored by entropic gain of BSA due to alteration in native conformation at the malachite interface. Gain in entropy by decrease in protein secondary structure upon adsorption on hydrophilic surfaces has also been reported in several studies previously.[4.12,4.14,4.32,4.33] Uptake of BSA on malachite surface was quite fast as the steady state reaches within 5 h (Appendix, Figure 4.4). The adsorption kinetics was analyzed in the light of first-order and second-order model. It has been found that the second-order model showed a better correlation coefficient (R = 0.997) than the first-order model (R = 0.962) (Appendix, Figure A4.5), which indicates the adsorption kinetics preferably follows the second-order kinetic model. Previous studies anticipated that the reason behind the second-order kinetics is the heterogeneity of the active sites on the surface.[4.34] Therefore, it can be speculated that the heterogeneous nature of the active site on malachite surface is responsible for second-order adsorption kinetics. We got a high surface loading capacity of BSA on malachite NPs in the pH range of ~4.5−7. Surface coverage (Γ_{BSA}) increases from 1.65 to 1.7 mg m^{-2} while increasing the pH from 4.5 to 5.0 and thereafter remains almost invariable throughout the pH range of 5−7. This observation is quite dissimilar compared to other hydrophilic surfaces like silica, magnetite, or TiO_2[4.21-4.24,4.35] as in those cases adsorption capacity decreases significantly while increasing the pH from 5 to 7. Silica is having a point of zero surface charge (pzc) at around pH ~2.0−3.0.[4.20] Adsorption of BSA on silica reduces significantly while increasing the pH just above the IEP_{BSA} mainly due to the electrostatic repulsion between the negatively charged BSA and negatively charged silica surface. On other hydrophilic surfaces, like magnetite, TiO_2, and several other inorganic minerals, electrostatic repulsion among the protein molecules as well as between the surface and protein appear as a predominant force at pH > $IEP_{protein}$, leading to significant reduction in protein

adsorption while increasing the pH from 5.0 to 7.0. [4.21-4.24,4.35] Around the pI value of BSA (pI = 4.8−5.0) protein molecules are in neutral form,[4.36] which reduces the potential electrostatic repulsion forces between them, and they can assume a more condensed conformation. Therefore in this case, the electrostatic repulsion between the malachite surface and BSA is less around IEP_{BSA}. While increasing the pH from 5.0 up to 7.0, the electrostatic interaction might play an additional role for BSA adsorption on malachite surface. From the ζ-potential analysis it was found that pzc of malachite NPs was around pH ~7.6 while having a high positive charge (~15−20 mV) on their surface in the pH range of 5.0−7.0. Due to this reason, probably the electrostatic attraction between negatively charged BSA and positively charged malachite NPs remains predominant over the electrostatic repulsion between the protein molecules in the pH range of 5.0−7.0. Therefore, unlike silica, the strong interaction between acidic BSA and basic malachite surface leads to a high and invariable surface coverage in this pH region. Moreover, entropic gain due to alteration in BSA structure also favors the adsorption of BSA on malachite surface at pH > IEP_{BSA}. The rapid decrease in adsorption capacity beyond pH 7.0 (Figure 4.3) can be attributed to predominant electrostatic repulsion between protein molecules and malachite surface. At pH > 7.6, malachite surface become negatively charged (Figure 4.3), which initiates the electrostatic repulsion between malachite and BSA resulting in reduced surface coverage. At higher pH (~10.0) this electrostatic repulsion becomes predominant between negatively charged BSA and malachite surface as well as in between the negatively charged BSA molecules, which leads to the desorption of BSA molecules from the malachite surface beyond pH 10.0.

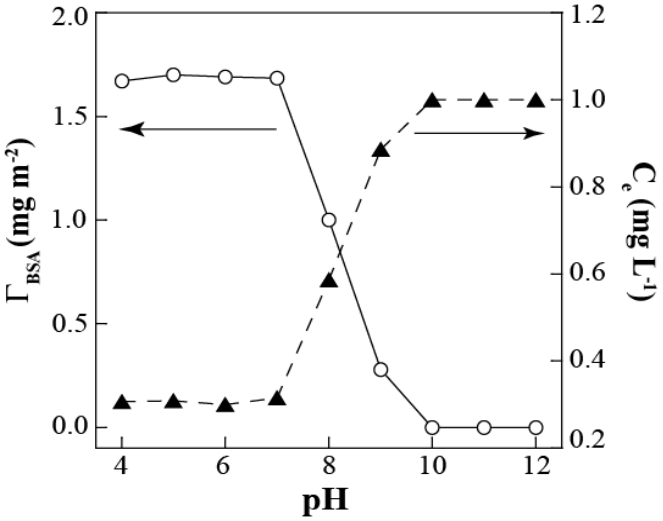

Figure 4.3. pH-dependent adsorption capacity (Γ) of BSA on malachite NPs and corresponding residual protein concentration (C_e) at steady state.

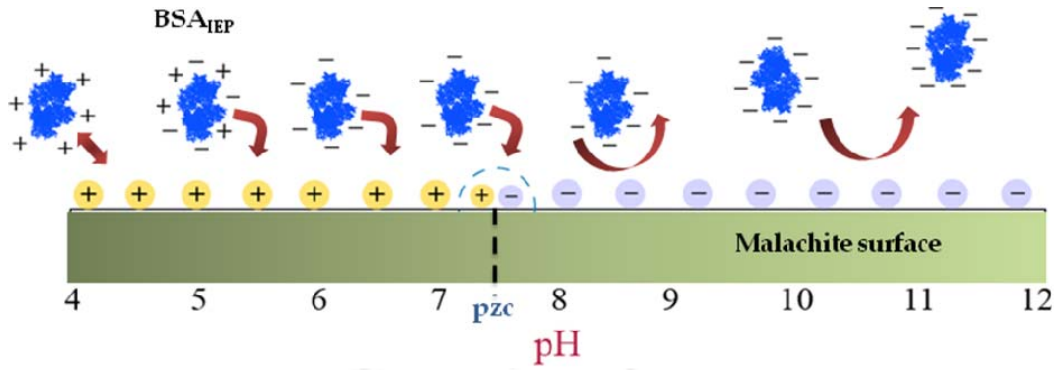

Scheme 4.3. Types of interaction between BSA molecule and malachite surface at different pH. Upto pH ~7.5, BSA get adsorbed on malachite surface, beyond pzc of malachite nanoparticles, electrostatic repulsion reduce the BSA adsorption.

Steady state surface coverage. The steady-state adsorption isotherm with different BSA concentrations on malachite surface at different pH is plotted in Figure 4.4. The isotherm plot is characterized by an initial slope indicating high protein affinity for malachite surface, and the adsorption saturation yields a plateau value ($\Gamma_{Plateau}$) corresponding to maximum amount of BSA adsorption onto malachite surface. $\Gamma_{Plateau}$ in the adsorption isotherm plot indicates the steady-state surface coverage of BSA. From the isotherm curve it can be found that surface coverage of BSA at steady state remains almost invariant in the pH range of 5.0−7.0, indicating the presence of strong interaction between BSA and malachite beyond the IEP of the protein. Heart-shaped BSA molecule can adsorb onto malachite surface in *side-on* mode or *end-on* mode, generating two different surface coverage areas for the same protein.[4.37,4.38] Two dotted horizontal lines in Figure 4.4 represent the calculated amount of surface coverage for two different adsorption patterns. As described by Rezwan *et al.*[4.28] the areas required for these two types of adsorption modes were calculated from the three-dimensional structure of highly homologous human serum albumin (HSA) monomer[4.27] and molecular weight of ~67000 g mol^{-1} of BSA. From Figure 4.4 it can be seen that at low protein concentration, Γ_{BSA} was lower than both types of theoretical monolayer surface coverage. While increasing the protein concentration, the maximum surface coverage reaches the amount that would be needed for a theoretical side-on monolayer (~2.2 mg m^{-2}). At steady state, with higher BSA concentration at the pH range of 4.0−7.0, the amount of BSA adsorbed exceeds the side-on monolayer coverage ($\Gamma_{Plateau}$ ~2.6 mg m^{-2}) but stays below the complete end-on monolayer coverage (~3.6 mg m^{-2}). From this we anticipate a mixed side-on and end-on surface coverage of BSA in the pH range of 4.0−7.0. At higher pH

(from pH ~8.0) due to electrostatic repulsion the adsorption gets hindered, which results in low surface coverage of BSA. This can be clearly seen in the graph (Figure 4.4), which shows the steady-state surface coverage stays below the theoretical side-on monolayer at higher pH. The Scatchard test[4.39] was performed to observe the presence or absence of any cooperative effects in BSA adsorption on malachite surface. Linear shape (R = 0.998) of the Scatchard plot (Appendix, Figure A4.6) implies no significant cooperative effect. Therefore, pH-controlled and non interacting adsorption−desorption behavior of BSA on malachite NPs with high loading capacity was observed. However, the UV spectra of desorbed BSA solution showed a shift of ~10 nm from that of native BSA solution (Appendix, Figure A4.7). This indicates the possibilities of conformational changes of BSA during the adsorption−desorption cycle, which was further studied in detail by other methods as discussed later.

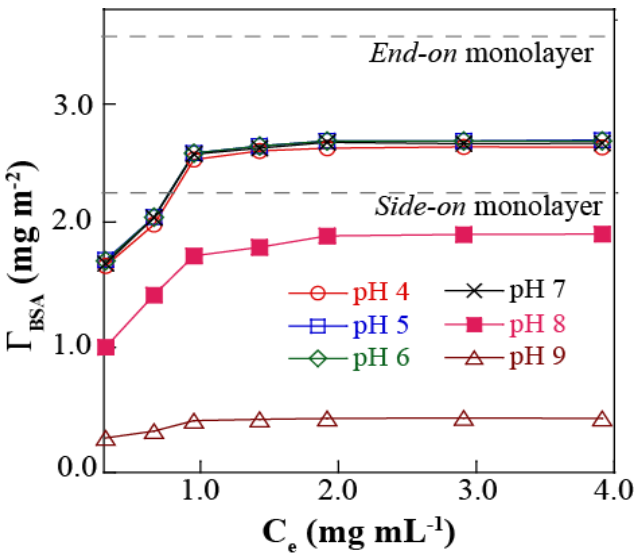

Figure 4.4. Steady-state adsorption isotherm of BSA on malachite NPs in the pH range of 4−9.

4.4.4. Interaction of BSA on stearic acid modified malachite NPs

Interaction between stearic acid solution and malachite NPs was performed for 5 h. The adsorption kinetics of stearic acid was fast, reaching a maximum value within 2 h. Solution pH was less than the pK_a value of stearic acid (pK_a = 10.1).[4.40] Again, while incubating the SA−malachite NPs with aqueous solution, no significant release of acid molecules from the malachite surface was observed as confirmed by base titration, indicating the stability of SA−malachite NPs. BSA adsorption studies with SA−malachite NPs were performed at pH ~5.0, which showed a high amount of surface coverage on bare malachite NPs. The adsorption of BSA was significantly reduced by the stearic acid modification. Only 8−10% of initial BSA concentration (at a given concentration) was adsorbed on the modified surface against that of ~75% on the bare malachite NPs as confirmed from the UV spectra of supernatant protein solution. An isotherm experiment

has been performed with different concentrations (0.1−1.0 mg mL^{-1}) of protein solution to find the maximum adsorption capacity on SA−malachite NPs (Appendix, Figure A4.8). The adsorption capacity reached almost a plateau value of ~5 mg g^{-1} on the SA−malachite surface, which was much lower than the maximum capacity on bare malachite surface (~52 mg g^{-1}). This reduction in albumin adsorption on stearic acid modified malachite surface could be due to formation of a dense and flexible coating of stearic acid layers. Malmsten *et al*.[4.41] reported that, once sufficient interfacial density is achieved among the long-chain molecules adsorbed on a solid support, van der Waals interaction between protein and coated molecules masked at the distance of separation where the steric repulsion sets in, thus reducing the diffusion of proteins through the coated layers. Moreover, Bosker *et al*.[4.42] reported that the flexible molecules have greater resistance to protein adsorption compared to the rigid moieties. In the hydrocarbon chain of fully saturated stearic acid, free rotation around each carbon−carbon bond gives the great flexibility.[4.43] Therefore being saturated; the flexibility of stearic acid coating might further help to reduce the BSA adsorption. In other words, BSA adsorption capacity is much higher on bare malachite NP surface compared to the SA−malachite NPs. However, the protein solution interacted with SA−malachite NPs was further analyzed for any conformational changes induced by the stearic acid coating.

4.4.5. Fluorescence emission spectroscopy for BSA tertiary structure

The steady-state fluorescence emission of BSA at native solution, adsorbed state, and after desorption was taken at 20 °C upon excitation at 290 nm (Figure 4.5). The adsorption experiments for spectral analysis were performed at pH ~5.0, as found to have high surface coverage at this pH from previous studies. BSA possesses two tryptophan residues. One of them is located on the bottom of a hydrophobic pocket in subdomain IIA (Trp_{213}), whereas the other is on the surface of the molecule in subdomain IB (Trp_{134}).[4.44] The characteristic emission maximum of BSA in native solution is at ~343 nm, and it indicates that the Trp_{134} is fully exposed to aqueous solvent and bound with a water molecule.[4.45] The fluorescence spectra of BSA adsorbed on malachite was shifted to ~386 nm (red shift), and the fluorescence intensity was mostly quenched. This red shift in proteins indicates the exposure of the tryptophan molecules toward a more hydrophilic atmosphere from hydrophobic or less hydrophilic environment.[4.46] BSA molecules on malachite surface are therefore in a partly unfolded state where Trp_{213} might be more exposed to the hydrophilic aqueous solution which caused the red shift in fluorescence

emission. The quenching of fluorescence intensity might be due to the strong tryptophan quenching groups in proteins like cysteine.[4.10, 4.46] This could be possible if the tertiary structure of BSA gets changed upon adsorption in such a way that the tryptophan occupies a position with spatial proximity to cysteine. Upon desorption of BSA from malachite surface (at pH ~11.0) the fluorescence spectra of the desorbed protein solution shifted to ~395 nm with a little increase in fluorescence emission intensity compared to its adsorbed state. This reflects a more unfolded state of tertiary structure where the tryptophan is exposed to the hydrophilic solvent and there is rearrangement of secondary and tertiary elements. Moreover, BSA undergoes expansion above pH 8.0, and at pH 9.0 it changes conformation to the basic form. This is due to the breaking of salt bridges between domain I and domain III.[4.47] This might favors the availability of exposed Trp_{213} residue to hydrophilic solution explaining the red shift of the desorbed protein. The fluorescence spectra of BSA solution interacted with SA−malachite NPs showed almost similar fluorescence intensity with little quenching, indicating slight alteration in the native tertiary conformation.

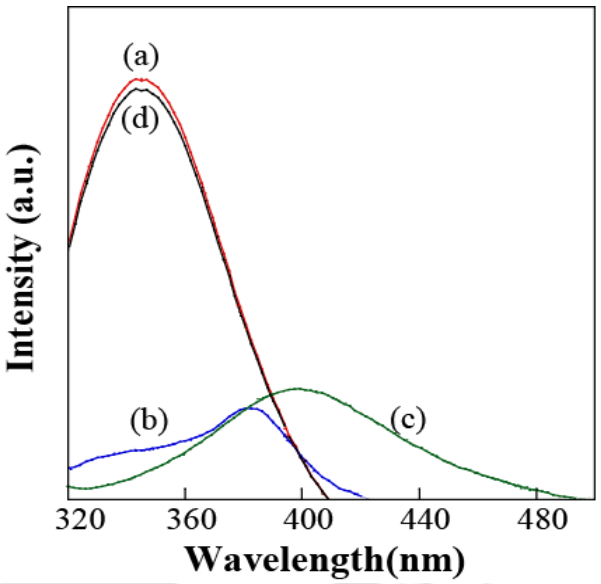

Figure 4.5. Steady-state fluorescence emission spectroscopy of BSA at (a) native state, (b) adsorbed on malachite NPs (at pH ~ 5), (c) desorbed from malachite NPs, and (d) after interaction with SA−malachite NPs.

To ascertain the binding of BSA with malachite, we measured the fluorescence anisotropy and time-resolved decay of BSA at different experimental conditions. Table 4.1 presents the variation of the fluorescence anisotropy value of BSA upon interaction with malachite NPs. The anisotropy of BSA increases from 0.099 in native solution to 0.303 upon adsorption, which suggests the increased rigidity of the surrounding environment of the fluorophore upon binding on the malachite surface. Adsorption of BSA on malachite surface implies an imposed motional restriction on the fluorophore (tryptophan) in the proteinous microenvironment. After desorption, the

anisotropy value of BSA reduces to 0.171 indicating a less restricted environment after desorption.

Table 4.1. Anisotropy and time-resolved fluorescence spectroscopic parameters of BSA in adsorption-desorption cycle on malachite NPs.

BSA	λ_{em} *(nm)*	*Aniso tropy (r)*	τ_1 *(ns)*	τ_2 *(ns)*	α_1	α_2	τ_m *(ns)*	χ^2
Native	343	0.099	0.68	5.66	0.017	0.070	4.630	1.008
Adsorbed	386	0.301	0.19	1.63	0.611	0.002	0.194	1.003
Desorbed	395	0.171	0.41	2.78	0.040	0.005	0.673	1.000

The time-resolved decay of BSA at different experimental conditions was taken at their respective emission wavelength. The data fitted well with the sums of two exponential decays with a χ^2 value close to 1.00. The decay profile of BSA at adsorbed and desorbed states was different from native solution (Figure 4.6). The individual lifetime values (τ_1 and τ_2) and amplitudes (α_1 and α_2) were calculated from the bi-exponential fit and are given in Table 4.1. The τ value with a longer lifetime was assigned to the Trp_{134} residue as it contributes most of the total fluorescence of BSA.[4.48] There is a large decrease in the τ_1 and τ_2 value (~70%) of the fluorophore upon adsorption on malachite surface. The mean lifetime (τ_m) was calculated and is given in Table 4.1. The mean fluorescent lifetime values clearly show the alteration of lifetime values in the adsorption−desorption cycle. The reduced mean lifetime (τ_m) is due to the alteration of polarity of the environment surrounding the fluorophores, which indicates partial unfolding and exposure of the fluorophore to the aqueous solvent upon binding on malachite surface. The mean lifetime value (τ_m) increased upon desorption from malachite surface but much less than the native lifetime. This can be possible due to the decrease in polarity surrounding the fluorophore, which indicates that BSA gains its structural module to some extent after desorption but does not regain the complete native conformation.

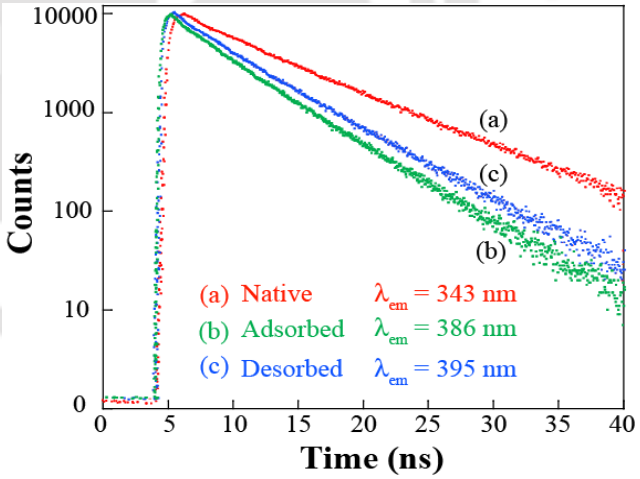

Figure 4.6. Time-resolved fluorescence decay of BSA in (a) native, (b) adsorbed on malachite surface (at pH ~5.0), and (c) after desorption from malachite surface into solution.

4.4.6. Circular Dichroism for BSA secondary structure

Far-UV CD spectra of BSA in native, adsorbed (at pH ~5.0), and desorbed states along with the protein solution incubated with SA−malachite NPs are shown in Figure 4.7. The CD spectrum of native BSA solution showed the strong negative ellipticity with the minimum ellipticity at 222 and 208 nm and a positive ellipticity at 195 nm, typical of proteins with high α-helix content.[4.18] The relative proportions of secondary structures were calculated according to the curve-fitting method described by Yang *et al*.[4.29] The secondary structural elements of BSA at different states as analyzed from the CD spectrum are given in Table 4.2. The negative band in the far CD spectra of adsorbed BSA almost collapsed to baseline, indicating a rapid decrease in helix content of adsorbed protein. Formation of unordered structure from α-helical and β-structure of proteins upon adsorption on hydrophilic surfaces is also supported elsewhere.[4.10,4.18,4.32] After desorption from the malachite surface at pH ~11.0, BSA regains the secondary structural element to some extent but not its native form entirely. Notably, the secondary structural element content of desorbed BSA (at pH ~11.0) from malachite surface was quite different from that of alkaline denaturation of BSA at pH ~11.0 as reported.[4.49]

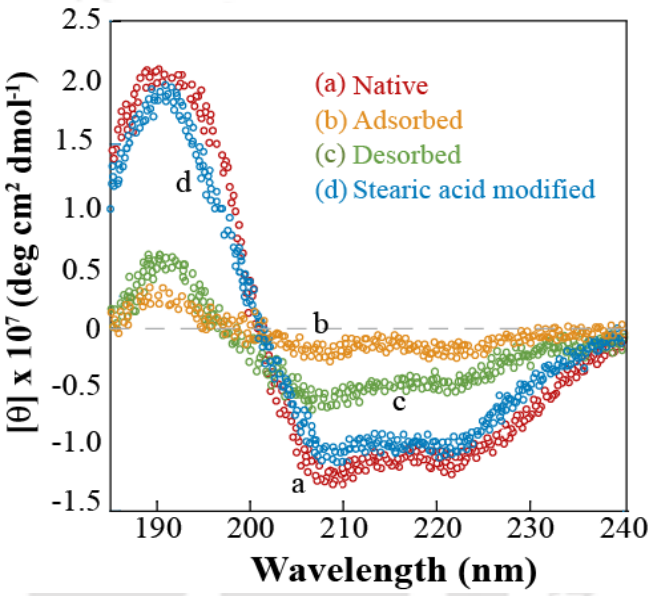

Figure 4.7. Circular dichroism spectra of BSA in solution at (a) native, (b) adsorbed on malachite NPs (at pH ~5.0), (c) desorbed from malachite surface, and (d) upon interaction with SA−malachite NPs.

Table 4.2. Secondary structural components of BSA solution in various stages of adsorption-desorption cycle on malachite NPs as analyzed from CD spectra.

	native BSA solution	adsorbed on malachite NPs	desorbed from malachite NPs	interacted with SA-malachite NPs
α-helix (%)	56 ± 2	23 ± 1	35 ± 1	53 ± 2
β-sheet (%)	21 ± 2	17 ± 2	27 ± 2	20 ± 2
Others (%)	23 ± 1	60 ± 2	38 ± 3	27 ± 1

On the other hand, upon interaction with SA−malachite NPs, BSA molecules almost retained their secondary structural element as its native form (Table 4.2). However, a small decrease (~2−3%) in α-helix content was observed upon interaction with stearic acid modified malachite nanoparticles.

4.4.7. FT-IR analysis for BSA secondary structure

The FT-IR spectra of lyophilized BSA in native, adsorbed, and desorbed states and after interaction with SA−malachite NPs were taken from 2500 to 500 cm^{-1} (Appendix, Figure A4.9). The 1700−1600 cm^{-1} region (amide I) band is mainly due to the C═O stretching and N−H bending vibration. The band at ~1540−1500 cm^{-1} corresponds to amide II, representing mainly the C−N stretch vibration.[4.50,4.51] The IR spectrum of BSA adsorbed onto malachite surface is shown after subtracting the malachite spectrum. The intensity of the amide I band decreased upon adsorption, suggesting a decrease in α-helix upon adsorption.[4.52] Further, the individual secondary structural elements of BSA at different states were quantified by Gaussian deconvolution analysis of the amide I region (1700−1600 cm^{-1}) of the FT-IR spectra (Figure 4.8).[4.31,4.53,4.54] The Gaussian distribution peak at 1656 ± 2 cm^{-1} was assigned to α-helix, bands at 1689 ± 1, 1640 ± 1, and 1630 ± 1 cm^{-1} were assigned to β-sheet, and all other peaks were assigned to unordered structural elements which included β-turns, random coils, and extended chains.[4.55] The Gaussian analysis depicts the α-helix content of 31% ± 2%, β-sheet of 21% ± 2% (rest 48% ± 2% was unordered elements) in BSA native state (Table 4.3). The difference in helix content (%) in native BSA as found from FT-IR (lyophilized) and CD analysis (solution) was mainly due to the dehydration-induced denaturation caused by lyophilization of the protein sample as described by Griebenow and Klibnov.[4.56] Upon adsorption, the α-helix content reduced to 15% ± 1%, whereas the unordered element increased to 70% ± 1% indicating a major decrease in secondary structural elements. Reduced secondary structure can provide an entropic gain which could support the adsorption of BSA on malachite NP surface at pH > IEP_{BSA}, when at the same time electrostatic repulsion between the negatively charged BSA molecules initiates. This entropic gain, together with the electrostatic attraction between malachite−BSA, can help the invariable surface coverage of BSA in the pH range of 5−7. The desorbed BSA regains some amount of helix content (23% ± 2%) as observed from curve-fitting analysis. Secondary structural element of the protein interacting with SA−malachite NPs almost retained its native structure as only 2−3% decrease in α-helix content was observed. All these structural

changes (%) analyzed by FT-IR were in good agreement with the CD spectra data as discussed before.

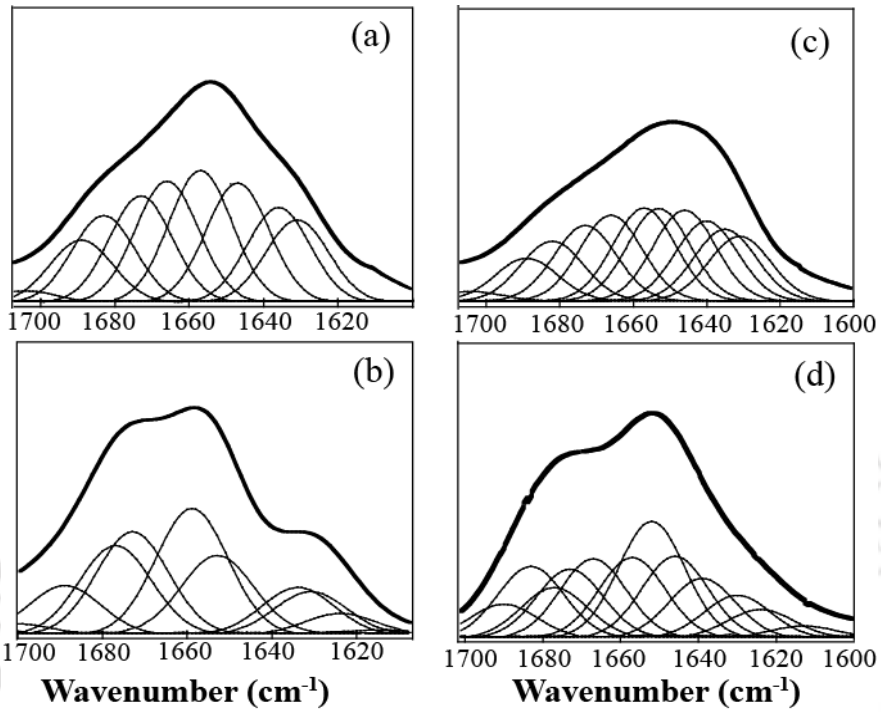

Figure 4.8. Gaussian distribution plot of amide I peak of FT-IR spectra of lyophilized BSA at (a) native, (b) adsorbed, (c) desorbed and (d) after interaction with SA-malachite NPs.

Table 4.3. Secondary structural elements of lyophilized BSA at different stages as calculated from Gaussian distribution of amide I peak of FT-IR spectra.

band position (cm^{-1}) Gaussian curve fit	Area (%) of Gaussian bands of BSA				Assignment
	native state	adsorbed on malachite NPs	after desorption	interacted with SA-malachite NPs	
1704 ± 2	1 ± 1	2 ± 1	4 ± 1	3 ± 1	Un-ordered
1689 ± 1	6 ± 1	7 ± 2	12 ± 2	6 ± 1	β-sheet
1683 ± 2	8 ± 2	15 ± 1	4 ± 1	12 ± 2	Un-ordered
1673 ± 1	11 ± 1	17 ± 1	8 ± 2	10 ± 1	Un-ordered
1666 ± 2	8 ± 2	21 ± 2	8 ± 1	6 ± 2	Un-ordered
1656 ± 2	31 ± 2	15 ± 1	23 ± 2	30 ± 1	α-helix
1647 ± 1	7 ± 1	4 ± 1	8 ± 2	8 ± 2	Un-ordered
1640 ± 1	5 ± 1	2 ± 1	11 ± 2	6 ± 1	β-sheet
1635 ± 2	10 ± 1	8 ± 2	9 ± 1	6 ± 1	Un-ordered
1630 ± 1	8 ± 2	6 ± 1	9 ± 2	9 ± 1	β-sheet
1624 ± 2	5 ± 1	3 ± 1	4 ± 1	4 ± 1	Un-ordered

4.4.8. Atomic Force Microscopy

Direct visualization of BSA adsorbed on the malachite NPs was analyzed by tapping mode AFM. The surface topology of adsorbed protein layers onto malachite surface showed adsorbed individual protein patches (Figure 4.9a). Cross-sectional analysis of the surface morphology showed that the BSA adsorbed on the surface of malachite features a step height between ~4 nm and 8 nm (Figure 4.9b). Comparison of the vertical height of the monolayer with the three-dimensional structure of BSA (~9 nm × 5 nm × 5 nm)[4.28] indicates that the BSA molecule might be adsorbed in a mixed side-on and end-on mode (Figure 4.9c) with some changes in their native dimension, which further substantiates the previous discussion. Deviation from the actual height of the native protein dimension is due to the unfolding of tertiary structure upon adsorption on the malachite surface.

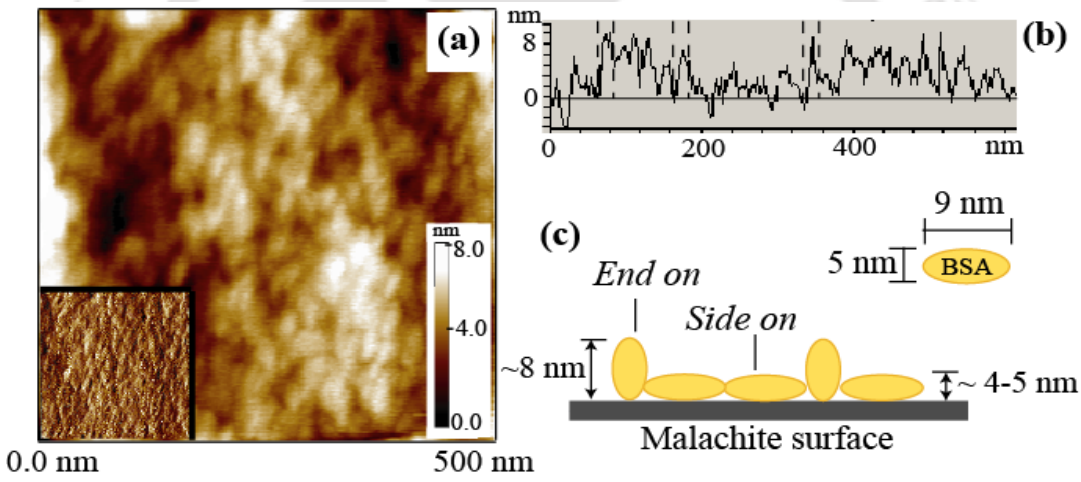

Figure 4.9. AFM imaging of (a) surface topology and amplitude (inset) of adsorbed BSA on malachite surface, (b) horizontal cross-sectional height after adsorption, and (c) schematic presentation of probable mixed end-on and side-on adsorption of BSA on malachite surface as estimated from AFM analysis.

4.4.9. Summary

In this section, a facile single-step synthesis of hydrophilic malachite nanoparticles with an average size range of 100−150 nm was demonstrated. A pH-controlled adsorption−desorption phenomenon along with a high loading capacity of BSA on malachite NPs has been acquired. The surface coverage (Γ_{BSA}) remains almost similar in the pH range of 5.0−7.0. This is quite different from other hydrophilic surfaces like silica, magnetite, or TiO_2 surfaces where adsorption significantly decreases with increase in the pH just above $IEP_{protein}$. An additional strong acid−base interaction between acidic BSA

and basic malachite surface was proposed behind the high and consistent adsorption behavior in the pH range of 5.0−7.0. The decreased secondary structural component of BSA on the malachite surface leads to a gain in entropy and further helps to maintain the high surface coverage in the range of pH 5.0−7.0. Beyond the pzc value of malachite (pH ~7.6) BSA adsorption reduces, and it desorbs completely at pH ~11.0. The malachite−BSA interaction mechanism has been elucidated; pointing out that the maximum surface coverage $\Gamma_{Plateau}$ ~2.6 mg m^{-2} is due to the mixed side-on and end-on mode adsorption, as supported by AFM data. With the use of a combinatorial analysis including CD, fluorescence spectroscopy, FT-IR, and AFM imaging it has been shown that BSA acquires conformational changes during the adsorption−desorption cycle. CD and FT-IR spectra confirm the loss of helical structure upon adsorption on the NP surface. Unfolding of native BSA tertiary structure and reduction in lifetime of the fluorophore were observed by steady-state and time-resolved fluorescence spectroscopy in the adsorbed and subsequent desorbed states. Stearic acid coating changes the adsorption behavior as only 8−10% BSA was adsorbed on SA-modified malachite NPs. In other words, BSA has a greater adsorption affinity toward the bare malachite nanoparticle surface than the stearic acid coated one. Moreover, SA−malachite NPs also have little effect on the native conformation of BSA, as 2−3% reduction in α-helix content was observed. This pH-specific adsorption behavior and high adsorption capacity beyond the $IEP_{protein}$ can be of great importance in bioseparation technology and biochemical sensor development as well as in the fabrication of controlled release devices.

Part 2:

4.5. Controlled and reversible interaction of metal ions on malachite nanoparticles and BSA−malachite nanocomposites.

4.5.1. Background

In recent years, bionano assemblies have emerged as excellent tools for various promising applications in biotechnology, material science, medical therapy, biochemical sensor design, and so forth.[4.57] On the basis of surface modification with different biomolecules, these nano-assemblies can be employed to modulate the interaction with other molecules. Selective adsorption of targeted metal ions on different modified surfaces is an important and challenging task. Metal-contaminated wastewater is a major problem in mining, electroplating, and electronic industries.[4.58] Health and ecological impact of toxic heavy metals has been extensively reported. Besides the environmental issue, there is a strong

economic incentive to remove precious metal ions from process water for reuse. Adsorption features of metal ions on a nanoparticle surface can be directed and specified with different surface modifications.[4.59,4.60] The adsorption of toxic heavy metals on various modified surfaces has been extensively studied already.[4.61] In this regard, different bionanocomposites can be a nontoxic, effective tool for selective adsorption of various toxic and precious metal ions from aqueous solution. Protein-functionalized nanoparticles can provide a tunable surface for binding with targeted metal ions. The effectiveness of such composites in adsorbing metal ions can be attributed to the preferential coordination of the metal ions with the coordinating side chain of amino acids in proteins. Significantly, proteins were found to strongly bind with precious metal ions (e.g., Au^{3+}, Pd^{2+}, etc.) mainly through its nitrogen-(imidazole) and thiol-containing amino acids.[4.62] Selective adsorption of 'soft' and precious metal ions compared to 'harder' metal ions (according to HSAB principle)[4.63] on proteins, protein-based biomass, or well-defined surface functional groups has been reported previously.[4.62,4.64-4.66] Maruyama *et al*.[4.62] reported selective adsorption of Au^{3+} and Pd^{2+} on BSA, ovalbumin, and lysozyme in solution over other ions such as Cu^{2+}, Zn^{2+}, and Ni^{2+}. Brown *et al*.[4.59] reported the selective adsorption of Hg^{2+} on a thiolated adsorbent from a multi-component solution. In another report, Ishikawa *et al*.[4.66] reported the preferable adsorption of Au^{3+} on eggshell membrane from a mixed solution containing the 'harder' ions (*viz*., Cu^{2+}, Zn^{2+}, Ni^{2+}, and Co^{2+}). These reports mainly focus on the selective adsorption of only precious metal ions from a mixed solution. However, the selective adsorption of both 'soft' and 'harder' metal ions from a multi-component solution has not been explored very much.

To investigate the controlled adsorption of selective metal ions from a mixed solution, the adsorption behavior of several metal ions on bare malachite nanoparticles and BSA-modified malachite nanoparticle surfaces have been studied. In addition, upon coating the malachite nanoparticle with the BSA molecule, the surface properties can change significantly. Introduction of thiol- and imidazole-based amino acids of BSA onto the malachite surface should provide an excellent binding affinity toward the precious metal ions. Moreover, the surface modification of malachite nanoparticles with BSA was very simple, rather than introducing well-defined functional groups to adsorb targeted metal ions. Synthesis of malachite nanoparticles was simple, and malachite was found to have a high adsorption capacity for BSA throughout the pH range 5.0−7.0. Therefore, the BSA−malachite nanocomposite can be a good surface for adsorption of precious and 'soft' metal ions.

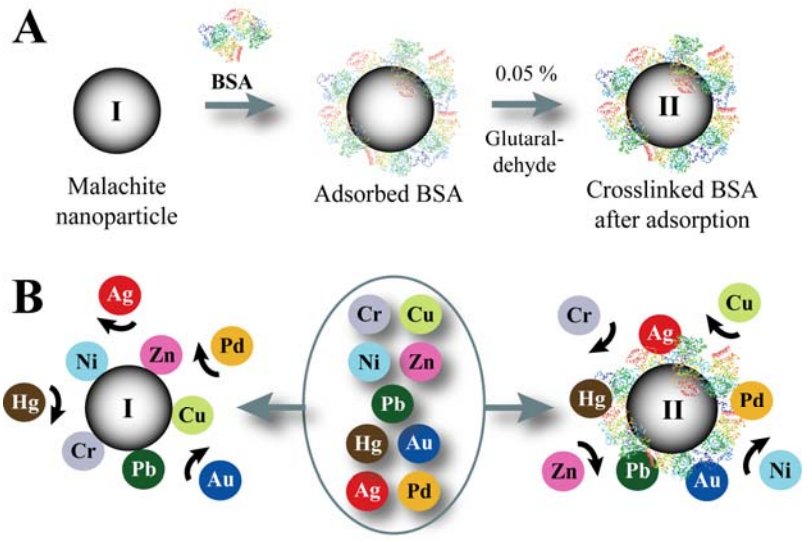

Scheme 4.4. Illustration of surface modification controlled interaction behavior of metal ions on bare malachite nanoparticles and BSA-malachite nanocomposites.

In this section, effort was given into rationalizing a design for controlled adsorption of selected metal ions by a simple surface modification technique. BSA−malachite nanocomposite has been prepared using the malachite nanoparticles synthesized previously. For the first time, malachite nanoparticles and BSA−malachite nanocomposite have been used for the adsorption studies of a series of metal ions. Herein, a simple surface modification directed reversal adsorption behavior of both 'soft' and 'harder' metal ions from a multi-component solution has been reported. On malachite nanoparticles, the adsorption of 'harder' ions is much higher compared to that of 'soft' metal ions, while after coating with BSA (in BSA−malachite nanocomposite) the adsorption of 'soft' metal ions increases significantly compared to that of 'harder' metal ions. Detail adsorption kinetics and isotherm studies have been done for in-depth analysis of adsorption phenomena. Selectivity of different metal ions adsorbing on both surfaces has been analyzed with the selectivity coefficient calculation for both single and equimolar multi-component solutions. Moreover, the adsorption behavior of metal ions on these two surfaces has been studied with a synthetic wastewater solution containing unequal amounts of different metal ions.

4.5.2. Materials and methods

Preparation of BSA−malachite nanocomposite. Malachite nanoparticles with an average size of 100−150 nm have been synthesized and characterized as described previously. Adsorption of BSA on malachite nanoparticle was found to be pH-controlled

with high adsorption capacity (Γ_{max} ~2.6 mg m^{-2}) for protein in the pH range 5−7 and complete desorption beyond pH ~10. After adsorption, protein-loaded malachite nanoparticles were further resuspended by sonication and incubated with a series of 0.01−10.0% glutaraldehyde solutions overnight for cross-linking (at pH ~5.0) (Scheme 4.4) of adsorbed BSA. The cross-linked BSA−malachite nanocomposites were then separated by centrifugation at 15000 rpm and subsequently washed several times with Milli-Q water to remove unreacted glutaraldehyde solution. To check the release of protein molecules from malachite surface, the cross-linked BSA−malachite nanocomposites were resuspended in a series of aqueous solution with a pH range 4−12 adjusted by 0.1 M NaOH. For each case, the supernatant was separated by centrifugation at regular intervals and analyzed for desorbed BSA concentration in a UV spectrophotometer.

Structural analysis of BSA-malachite nanocomposite. Tertiary structural analysis of the protein in BSA−malachite nanocomposite was performed by steady-state fluorescence emission spectroscopy. The structure of BSA after cross-linking in BSA−malachite nanocomposite was compared with the native and adsorbed states as studied previously. The tryptophan emission fluorescence spectrum was collected in the wavelength range 320−500 nm at room temperature. The emission spectra of protein samples containing malachite nanoparticles were corrected using the baseline acquired from suspension of the same concentration of malachite nanoparticles without BSA. The amide I region (1600−1700 cm^{-1}) of FT-IR spectrum has been widely used to quantify the individual elements of secondary structure of a protein in liquid as well as lyophilized samples. FT-IR spectra of BSA−malachite nanocomposite were compared with lyophilized BSA samples in native and adsorbed states studied previously. Gaussian distribution analysis of amide I peak of the FT-IR spectra and the secondary structural content was analyzed as described in previous section. In each case, the secondary structure content was determined from two independently obtained spectra, the values were averaged, and the standard deviations were calculated (Appendix, Table A4.1).

Interaction studies of metal ions. Single- and multi-component adsorption studies of different metal ions on these two alternate surfaces, i.e., bare malachite nanoparticle (**I**) and BSA−malachite nanocomposite (**II**), were performed in batch mode. Herein, the following metal ions Cr^{3+}, Cu^{2+}, Ni^{2+}, Zn^{2+}, Pb^{2+}, Hg^{+}, Au^{3+}, Ag^{+} and Pd^{2+} were used for the adsorption studies on **I** and **II**. In a typical experimental setup, an amount of 10 mg L^{-1} of each metal ion solution was added separately (single-component) and in a mixed

solution (multi-component) to a fixed amount of **I** and **II** (5 g L^{-1}) individually at ionic strength of 0.001 M. The surface charge density (σ) of malachite nanoparticles was ~1.0 mC m^{-2} (at pH ~6.0). Adsorption kinetics of these metal ions was studied by withdrawing the samples at regular intervals and subsequent centrifugation (at 15000 rpm) to obtain suitable aliquots for analysis of metal ion concentration, until steady state is reached. The initial and residual metal ion concentrations after adsorption were measured by atomic absorption spectrometer in each case. The amount of metal ions adsorbed per unit weight of **I** and **II** (q_e, mg of metal ions/g of **I** and **II**) can be calculated from the initial (C_0, mg L^{-1}) and final (C_e, mg L^{-1}) metal ion concentration and concentration of **I** and **II** (g L^{-1}) in the sample. Solution pH of the adsorption experiments was varied from 4.0 to 9.0 to check the adsorption efficiency of **I** and **II** for various metal ions at different pH. The isotherm experiment was performed with different initial metal ion solutions, to get the maximum adsorption capacities of various metal ions on **I** and **II**. Metal adsorbed nanoparticles were further analyzed with FT-IR and steady-state fluorescence spectroscopy as stated before. The FT-IR spectra of both **I** and **II** after adsorption of metal ions were performed with 60 scans at 2 cm^{-1} resolution, whereas the fluorescence emission spectra of BSA−malachite nanocomposites (**II**) after adsorption of 'soft' metal ions were recorded in the range 320−500 nm.

The selective adsorption behavior of **I** and **II** from a synthetic wastewater source (prepared in the laboratory) was also studied. The average concentrations of the major metal ions present in two different nonferrous electroplating industry effluents (Delhi, India) are given as received in Table 4.4. The pH of the synthetic wastewater solution was set at ~5.0. After that, 5 mL of synthetic wastewater solution was stirred with 5 g L^{-1} of both **I** and **II** separately for 1 h (at ionic strength 0.001 M). Preliminary experiments revealed that this period of time is sufficient to ensure a steady state. After adsorption, the mixtures were centrifuged to separate the adsorbents and the supernatant was subjected to atomic absorption spectroscopy to measure unadsorbed metal ions. All these measurements were carried out twice, and the standard deviations were calculated from two replicates.

4.5.3. Characterization of BSA−malachite nanocomposites

BSA−malachite nanocomposites were resuspended in a varying pH solution to study desorption of protein from malachite surface in the pH range 4−12 (Figure 4.10a). Without cross-linking, BSA desorbed completely from the malachite surface at pH

> ~10. With the increase in glutaraldehyde concentration, the release of protein gets reduced at higher pH from malachite surface. Almost no release of protein from the surface was observed after cross-linking with 0.05 wt % glutaraldehyde even at higher pH. Therefore, cross-linking of BSA molecules (with 0.05 wt % glutaraldehyde solution) after adsorption on malachite surface results in a stable BSA−malachite nanocomposite in the wide pH range 4−12.

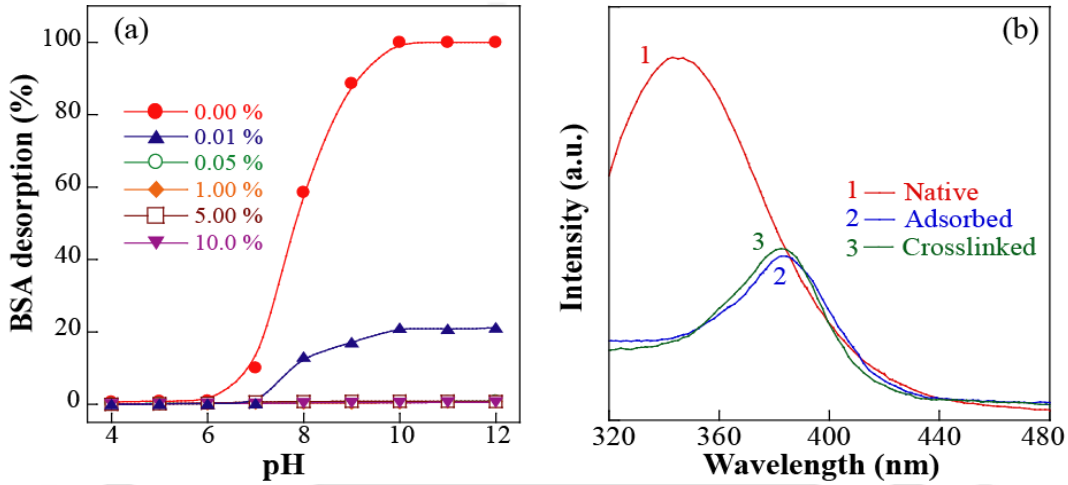

Figure 4.10. (a) Effect of crosslinking with 0-10 wt % glutaraldehyde on desorption of BSA from malachite surface at different pH. (b) steady-state fluorescence emission spectra of BSA in at native, adsorbed, and after cross-linking with glutaraldehyde on malachite nanoparticle surface.

Upon adsorption on malachite nanoparticle, emission spectra of BSA shifted from ~343 nm to ~386 nm with a mostly quenched intensity as found from steady-state fluorescence spectroscopy in our previous study. After cross-linking, steady-state fluorescence spectroscopy of BSA in nanocomposite is found to be changed little from that of emission spectra of the adsorbed BSA (Figure 4.10b). The quenching and red shift in fluorescence emission of BSA in nanocomposite indicate a partly unfolded state of the protein where the Trp molecule of the hydrophobic core of BSA[4.44] might be more exposed to the hydrophilic aqueous solution.

Secondary structural analysis of BSA in nanocomposite was done by Gaussian curve-fitting in the amide I region (1700−1600 cm^{-1}) of the FT-IR spectra.[4.31,4.54] The amide I band is mainly due to the C═O stretching and N—H bending vibration. The amide I region of IR spectra of BSA in adsorbed state and after cross-linking onto malachite surface are shown after subtracting the malachite spectrum (Figure 4.11). Secondary structural change of BSA upon adsorption and after cross-linking with glutaraldehyde

was compared. The Gaussian distribution peak at 1656 ± 2 cm^{-1} was assigned to α-helix, bands at 1689 ± 1, 1640 ± 1, and 1630 ± 1 cm^{-1} were assigned to β-sheet, and all other peaks were assigned to unordered structural elements including β-turns, random coils, and extended chains.[4.55] Results from previous section indicate a major decrease in secondary structure of BSA upon adsorption on the malachite nanoparticle. The α-helical content of native BSA (~31%) reduced to ~15% upon adsorption on malachite surface as studied previously. However, after cross-linking, the secondary structural content is close to that of adsorbed BSA as obtained from the area fraction of individual Gaussian peaks in the amide I region (Appendix, Table A4.1). This indicates a minor alteration in protein structure after cross-linking compared to adsorbed BSA. In addition, cross-linking results in a stable BSA−malachite nanocomposite throughout a wide pH range 4.0−12.0.

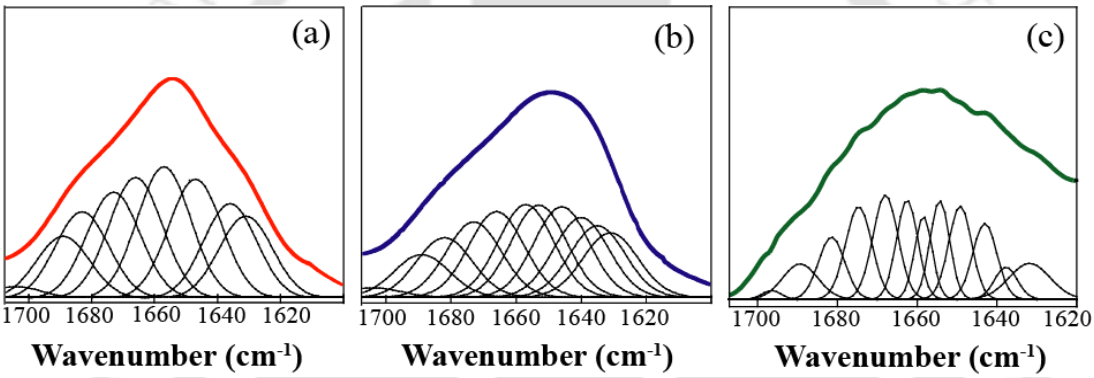

Figure 4.11. Gaussian distribution analysis of amide I region of FT-IR spectra of BSA at (a) native, (b) adsorbed on malachite surface, and (c) after cross-linking with glutaraldehyde.

4.5.4. Metal ion adsorption studies

Adsorption efficiency (%) of different metal ions from a competitive multi-component solution (10 mg L^{-1} of each metal ion) on **I** and **II** is shown in Figure 4.12a. The result from this study indicates a reversal in adsorption behavior of selected metal ions on **I** and **II**. The group of Cr^{3+} (~70%), Ni^{2+} (~30%), Zn^{2+} (~25%), and Cu^{2+} (~23%) ions were preferably adsorbed on malachite nanoparticle (**I**) and much less on BSA−malachite nanoparticle (**II**) (~1−3%); while Au^{3+} (~71%), Pd^{2+} (~68%), Ag^{+} (~33%), and Hg^{2+} (~60%) ions have preferential adsorption affinity toward **II** compared to **I** (~1−5%) (Table 4.4). Studies with single-component metal ion solution also reveal a similar type of adsorption behavior with higher adsorption efficiency (Figure 4.12b). The reduction in adsorption efficiency of each metal ion in the multi-component adsorption study is mainly due to the competitive adsorption of other metal ions present in the solution. This

controlled and reverse adsorption behavior of selected metal ions on **I** and **II** can be explained by Pearson's HSAB principle[4.63] and related to the nature and stability of the chemical interactions between the acid−base species. Due to the presence of 'hard' base (−CO_3 and −OH) on the surface of malachite [$CuCO_3$, $Cu(OH)_2$] nanoparticles, it prefers to bind 'harder' Lewis acids (e.g., Cr^{3+}, Ni^{2+}, Zn^{2+}, and Cu^{2+}) used in this study. The oxophilic nature of this group of metal ions also favors the better adsorption on **I** compared to the 'soft' metal ions studied here, while the 'soft' metal ions (e.g., Au^{3+}, Pd^{2+}, Ag^{+}, and Hg^{2+}) have a poor binding affinity toward the 'hard' base (−CO_3 and −OH) present on malachite surface (**I**). As a result, the 'harder' metal ions selectively adsorb on malachite nanoparticle (**I**) over the other 'soft' metal ions like Au^{3+}, Pd^{2+}, Ag^{+}, and Hg^{2+}.

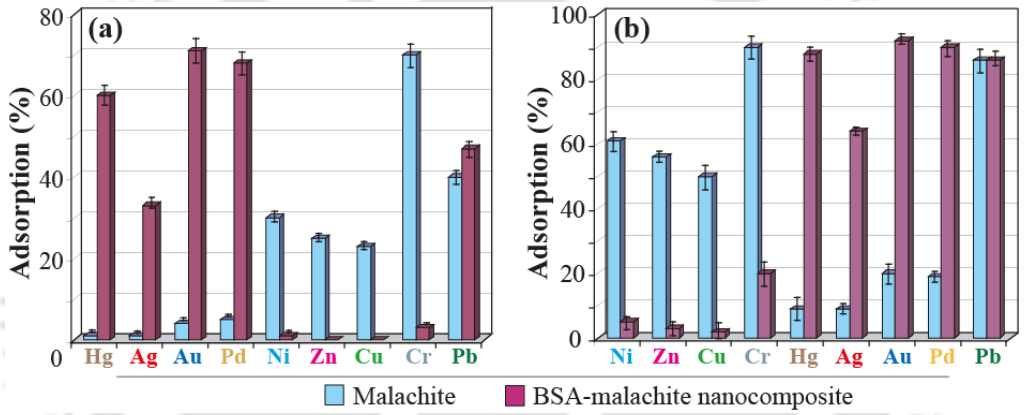

Figure 4.12. Adsorption efficiency of different metal ions (10 mg L^{-1} each) on both malachite nanoparticle (**I**) and BSA−malachite nanocomposite (**II**) from (a) equimolar multi-component solution, and from (b) single-component solution. The error bars represent the standard deviation from two replicates.

Again, the surface properties of 'hard' malachite nanoparticles can be changed upon coating with 'soft' BSA, as in the case of BSA−malachite nanocomposite (**II**). The 'soft' and precious metal ions, viz., Au^{3+}, Pd^{2+}, Ag^{+}, and Hg^{2+} were found to be adsorbed selectively on **II** over the 'harder' metal ions in this study. BSA was found to be a good candidate as an adsorbent for the precious metal ions.[4.62] The adsorption of specific precious metal ions by BSA can be attributed to several amino acid groups present in the protein molecule. The sulfhydryl group of the cysteine (Cys) residue and the nitrogen of the imidazole ring of histidine (His) are referred to as 'soft' bases in biological systems. BSA molecules contain ~35 Cys amino acid residues which have great binding affinity toward the 'soft' metal ions like Au^{3+}, Pd^{2+}, Ag^{+}, and Hg^{2+} over 'harder' metal ions. Successful complexation of 'soft' metal ions with Cys containing peptide has also been reported previously.[4.67-4.70] Again, all the amino-derived adsorbents were found to be

selective for 'soft' metal adsorption.[4.65] Therefore, nitrogen donor containing amino acids (His, Trp) in BSA and other amino acids like Tyr can selectively adsorb precious and 'soft' metal ions over the 'harder' ions, viz., Cr^{3+}, Ni^{2+}, Zn^{2+}, and Cu^{2+} from a mixed solution.[4.62,4.71]

Table 4.4. Adsorption efficiency and distribution coefficient (K_d) of different metal ions in a single- and in a competitive multi-component experiment (with 10 mg L^{-1} of each metal ion) on malachite nanoparticle (**I**) and BSA-malachite nanocomposite (**II**).

			Hg^{2+}	Ag^{+}	Au^{3+}	Pd^{2+}	Ni^{2+}	Zn^{2+}	Cu^{2+}	Cr^{3+}	Pb^{2+}
I	Adsorption (%)	*Single*	~9	~9	~20	~19	~61	~56	~50	~90	~86
		Mixed	~1	~1	~4	~5	~30	~25	~23	~70	~40
	K_d (L g^{-1})	*Single*	0.019	0.02	0.05	0.046	0.312	0.254	0.200	1.800	1.228
		Mixed	0.002	0.001	0.008	0.010	0.085	0.066	0.059	0.467	0.133
II	Adsorption (%)	*Single*	~88	~64	~92	~90	~5	~3	~2	~20	~86
		Mixed	~60	~33	~71	~68	~1	~1	~1	~3	~47
	K_d (L g^{-1})	*Single*	1.466	0.355	2.3	1.80	0.010	0.0061	0.004	0.05	1.22
		Mixed	0.30	0.085	0.487	0.425	0.001	0.002	0.004	0.006	0.177

As a result, the adsorption behavior of metal ions on **I** is reversed in the case of **II**, where the group of Au^{3+}, Pd^{2+}, Ag^{+}, and Hg^{2+} was preferably adsorbed compared to other metal ions. Hence, the adsorption behavior of these two groups of metal ions can be controlled by simple surface modification of malachite nanoparticles with BSA. Contrary to these two groups of metal ions, Pb^{2+} was adsorbed on both **I** and **II** equally. Pb^{2+} can bind well with imidazole containing His and with other coordinating amino acids of BSA which facilitate the adsorption on BSA−malachite nanocomposite (**II**). Complex of Pb^{2+} with different essential amino acids has been reported previously.[4.72] In addition, due to its oxophilic nature; Pb^{2+} can also adsorb on the $-CO_3$ group present on the malachite nanoparticle (**I**) surface. This results in similar adsorption capacity of Pb^{2+} on both surfaces. The malachite nanoparticles and BSA−malachite nanocomposites were also analyzed with FT-IR spectroscopy after adsorption of 'harder' (Cr^{3+}, Ni^{2+}, Zn^{2+}, Cu^{2+}, and Pb^{2+}) and 'soft' metal ions (Au^{3+}, Pd^{2+}, Hg^{2+}, Ag^{+}, and Pb^{2+}), respectively. Similarly, the adsorption of metal ions on BSA−malachite nanocomposites was studied with steady-state fluorescence emission spectroscopy. The fluorescence emission intensity of BSA in BSA−malachite nanocomposite was decreased to some extent after adsorption of different 'soft' metal ions (Appendix, Figure A4.11, A4.12). Among these, maximum quenching

occurs after adsorption of Au^{3+} on **II** compared to other ions studied. The decrease in fluorescence intensity is mainly due to the binding of metal ions with the 'soft' amino acid side chains of BSA in BSA−malachite nanocomposite, as described before.

4.5.5. Kinetics, pH dependence and isotherm of metal ion adsorption

Kinetic studies of all these metal ions in single-component adsorption on both **I** and **II** exhibit similar kinetic profiles. Adsorption kinetics is as fast as the steady state, reaching within ~1 h of different steady-state adsorption capacities in each case (Appendix, Figure A4.13) on both **I** and **II**. Adsorption kinetics curve is characterized by an initial slope indicating high affinity of ions toward the adsorbent surface followed by a plateau stage which reflects the steady state of adsorption of metal ions on both **I** and **II**. To evaluate the differences in adsorption kinetic rates, the kinetics of metal ion adsorption is described with pseudo first-order and second-order model. The kinetic rate constants and correlation coefficient values were calculated (Appendix, Table A4.2 and A4.3) from the fitted data. In analysis with kinetic models, it was found that the second-order model showed a better correlation coefficient (R) than the first-order model for all the metal ion adsorption on both **I** and **II**. Moreover, the error analysis of kinetic studies between experimental and modeled kinetic equations was performed by χ^2 tests. The calculated χ^2 values for both systems showed very good agreement between the experimental and second-order kinetic equations compared to the first-order model. This indicates that the adsorption kinetics of these metal ions preferably follows the second-order model, which might be due to the actual heterogeneous nature of both surfaces.

The influence of solution pH from 4.0 to 9.0 on the adsorption of all metal ions (single-component, 10 mg L^{-1} each) on **I** and **II** is shown in Figure 4.13. The adsorption capacity for 'harder' metal ions (*viz*., Cr^{3+}, Ni^{2+}, Zn^{2+}, Cu^{2+}) was higher on **I** but negligible on **II** in this pH range. Similarly, higher adsorption capacity for Au^{3+}, Ag^{+}, Hg^{2+}, and Pd^{2+} was achieved on **II** compared to **I**, in the pH range studied. On the contrary, the adsorption capacity of Pb^{2+} was similar on both surfaces in pH 4.0−9.0. Metal ions can bind with the groups present on the surfaces of **I** and **II** through electrostatic interaction and/or hydrogen bond. The effect of solution pH on adsorption efficiency is mainly attributed to the stability of metal−ligand complexes as per HSAB principle.[4.63] On malachite nanoparticle (**I**), the adsorption capacity for Ni^{2+}, Zn^{2+}, Cu^{2+}, and Pb^{2+} increases readily upon increasing the pH from 4.0 to 5.0. High adsorption capacity was achieved in the pH range ~5.0−6.0 for Ni^{2+}, Zn^{2+}, Cu^{2+}, and Pb^{2+}, while adsorption capacity for Cr^{3+} changed

little in the pH range ~4.0−6.0. On BSA−malachite nanocomposite, increase in the adsorption capacity for Ag^{+}, Hg^{2+}, and Pb^{2+} was observed upon increasing pH from 4.0 to 5.0 and high adsorption capacity was achieved in the pH range ~5.0−6.0. The adsorption capacity of $Au^{3+}$and Pd^{2+} on BSA−malachite nanocomposite remains unaltered in the pH range ~4.0−6.0. Beyond pH ~6.0, adsorption capacity decreases to some extent in almost each case. The decrease in adsorption capacity at higher pH on both **I** and **II** was mainly due to the precipitation of metal ions.

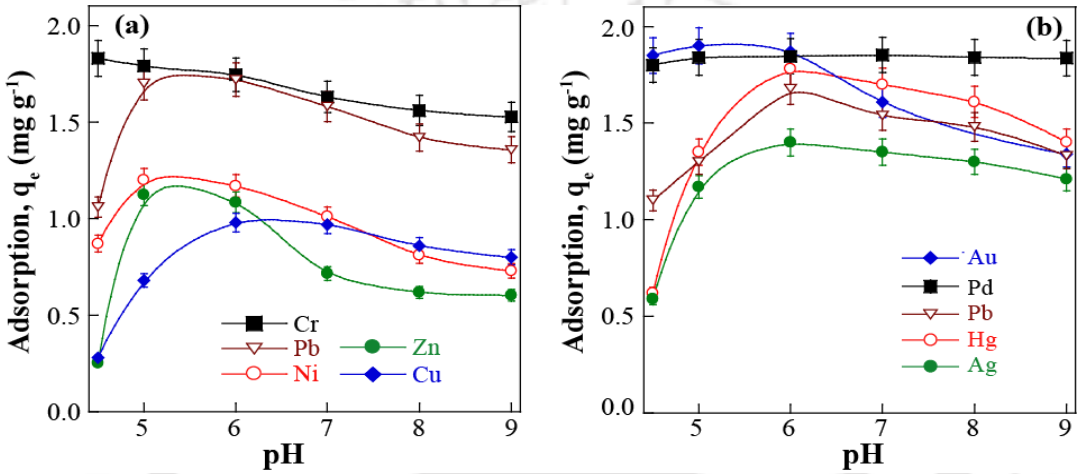

Figure 4.13. Influence of solution pH on the adsorption capacity of (a) Cr^{3+}, Pb^{2+}, Ni^{2+}, Zn^{2+}, and Cu^{2+} on malachite nanoparticles and (b) Au^{3+}, Pd^{2+}, Hg^{2+}, Pb^{2+}, and Ag^{+} on BSA−malachite nanocomposite. (The error bars represents the standard deviation from two replicates.)

The adsorption isotherm experiments were performed by adding 10−100 mg L^{-1} of different metal ions in a fixed amount of **I** and **II** (5 g L^{-1}). Figure 4.14a plots the adsorption isotherms of Cr^{3+}, Ni^{2+}, Zn^{2+}, Cu^{2+}, and Pb^{2+} on **I** which indicates different steady-state adsorption capacities of these metal ions on malachite nanoparticles. Similarly, the adsorption isotherms of Au^{3+}, Pd^{2+}, Ag^{+}, Hg^{2+}, and Pb^{2+} is also characterized by different steady-state adsorption capacity (q_e, mg g^{-1}) on BSA−malachite nanocomposite (**II**) (Figure 4.14b). Adsorption isotherm of Cr^{3+}, Ni^{2+}, Zn^{2+}, and Cu^{2+}on **II** and 'soft' and precious (*viz*., Au^{3+}, Pd^{2+}, Ag^{+}, Hg^{2+}) metal ions on **I** was not significant (figure not shown). The initial slope of the isotherm indicates high affinity of Cr^{3+}, Ni^{2+}, Zn^{2+}, Cu^{2+}, and Pb^{2+} for malachite nanoparticle (**I**) and Au^{3+}, Ag^{+}, Hg^{2+}, Pd^{2+}, and Pb^{2+} for BSA−malachite nanocomposite (**II**) surface. As the isotherm tends to plateau, it seems reasonable to assume that complete coverage of the adsorbent surface occurs and steady state is reached. Langmuir and Freundlich isotherm model has been

used to analyze the metal ion adsorption in each case. Different isotherm parameters of Langmuir and Freundlich models were calculated from the fitted curve and listed in Table 4.5. From the analysis, it was found that adsorption isotherms of Cr^{3+}, Ni^{2+}, Zn^{2+}, Cu^{2+}, and Pb^{2+} on **I** and Au^{3+}, Pd^{2+}, Ag^{+}, Hg^{2+}, and Pb^{2+} on **II** were fitted better with Langmuir isotherm model compared to Freundlich model.

Table 4.5. Adsorption isotherm parameters of Cr^{3+}, Ni^{2+}, Zn^{2+}, Cu^{2+}, Pb^{2+} on bare malachite nanoparticle (**I**) and Au^{3+}, Pd^{2+}, Ag^{+}, Hg^{2+}, Pb^{2+} on BSA-malachite nanocomposite (**II**).

		Langmuir isotherm				Freundlich isotherm		
		Q_m (mg g^{-1})	b (L mg^{-1})	R	R_L	K_f	n	R
on **I**	Ni^{2+}	8.7	0.035	0.990	0.740	0.523	1.63	0.987
	Zn^{2+}	3.3	0.101	0.999	0.497	0.734	3.03	0.987
	Cu^{2+}	3.4	0.056	0.993	0.641	0.506	2.47	0.990
	Cr^{3+}	9.5	0.235	0.999	0.298	2.118	2.51	0.967
	Pb^{2+}	7.2	0.274	0.999	0.267	2.018	3.04	0.920
on **II**	Hg^{2+}	12.6	0.227	0.996	0.305	2.38	2.17	0.915
	Ag^{+}	4.6	0.089	0.998	0.529	0.827	2.58	0.987
	Au^{3+}	22.6	0.126	0.992	0.442	2.588	1.477	0.975
	Pd^{2+}	14.2	0.586	0.998	0.145	4.68	3.26	0.944
	Pb^{2+}	8.1	0.237	0.998	0.296	2.046	2.816	0.935

This suggests monolayer coverage of metal ions on the adsorbent surface. As obtained from the Langmuir model, the maximum adsorption capacity (Q_m) of Cr^{3+} (~9.5 mg g^{-1}) is highest on **I** followed by Pb^{2+} (~7.2 mg g^{-1}), Ni^{2+} (~8.7 mg g^{-1}), Zn^{2+} (~3.3 mg g^{-1}), and Cu^{2+} (~3.4 mg g^{-1}). Similarly on BSA−malachite nanocomposite (**II**), the Q_m value of Au^{3+} (~22.6 mg g^{-1}) is higher than that of Pd^{2+} (~14.2 mg g^{-1}), Hg^{2+} (~12.6 mg g^{-1}), Pb^{2+} (~8.1 mg g^{-1}), and Ag^{+} (~4.6 mg g^{-1}). A "constant separation factor" or "equilibrium parameter", R_L, was calculated [$R_L = 1/(1 + bC_0)$] to evaluate the favorability of Langmuir adsorption process in each case (Table 4.5). For a favorable reaction process, the value of the constant separation factor should be $0 < R_L < 1$.[4.73] The R_L values obtained from the calculation supported the favorability of Langmuir isotherm model analysis. More generally, implementation of Langmuir model seemed to be more appropriate than Freundlich model in the case of adsorption of these metal ions on both **I** and **II**.

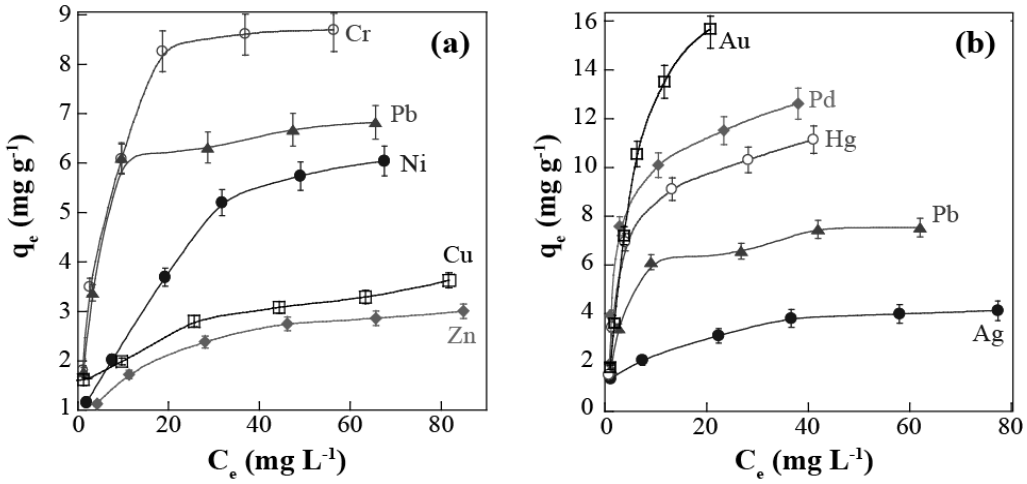

Figure 4.14. Adsorption isotherm plots of (a) Cr^{3+}, Pb^{2+}, Ni^{2+}, Zn^{2+} and Cu^{2+} on malachite nanoparticle and (b) Au^{3+}, Pd^{2+}, Hg^{2+}, Pb^{2+} and Ag^{+} on BSA-malachite nanocomposite. (The error bars represents the standard deviation calculated from two replicates.)

4.5.6. Adsorption characteristics of metal ions in competitive solution.

In a competitive and single-component study, the binding capacity of these metal ions on both type of surfaces (**I** and **II**) was analyzed with the respective distribution coefficient (K_d) values of each metal ion. The distribution coefficient (K_d) is described as the ability of adsorbents to remove a given ion from solution and can be expressed as,

$$K_d = \frac{C_s}{C_e} \tag{4.1}$$

where, C_s and C_e are steady state concentration of a given ion on adsorbent (mg g^{-1} of adsorbent) and in solution (mg L^{-1}) respectively. The K_d values of different metal ions for each single- and multi-component adsorption experiment have been calculated and given in Table 4.4. In both single and competitive study, the K_d values of Cr^{3+}, Ni^{2+}, Zn^{2+} and Cu^{2+} ions were relatively higher on the surface **I** compared to the 'soft' and precious metal ions. While, on BSA-malachite nanocomposite (**II**) this case reversed. Higher K_d values of Au^{3+}, Pd^{2+}, Hg^{2+} and Ag^{+} on BSA-malachite nanocomposite indicates higher binding capacity of these ions compared to the 'harder' metal ions (*viz.* Cr^{3+}, Ni^{2+}, Zn^{2+} and Cu^{2+}). Where as, Pb^{2+} has almost same K_d values (~1.2 L g^{-1} and 0.1 L g^{-1} in single and multiple component study respectively) for both **I** and **II**, which indicate equal binding capacity on both the surfaces, consistent with the results obtained previously. For each metal ion, K_d values in competitive study decreases from that of single-component study. In a mixed solution, decrease in K_d value of an ion, is mainly due to the competitive binding of other ions present in solution.

In the competitive study, the adsorption of different metal ions is mainly governed by the preferential binding affinity of the metal ions towards the binding site of the adsorbent. A selectivity coefficient (k) for the binding of a specific metal ion in presence of other competitive ions can be obtained from equilibrium binding data (Eq. 4.2, 4.3),[4.74]

$$m_1(solution) + m_2(adsorbent) \longrightarrow m_1(adsorbent) + m_2(solution) \quad (4.2)$$

$$k_1 = \frac{\{[m_1]_{adsorbent}[m_2]_{solution}\}}{\{[m_1]_{solution}[m_2]_{adsorbent}\}} = \frac{K_d(m_1)}{K_d(m_2)} \quad (4.3)$$

Where, K_d is the distribution coefficient of the metal ions and k_1 represents the ratio of K_d values of one metal ion (m_1) to another (m_2) used in the mixed solution. The selectivity coefficient k of **I** and **II** towards different metal ions in an equi-molar competitive solution was obtained and plotted (Figure 4.15 and Appendix). In the competitive experiment, the highest k values of **I** obtained for Cr^{3+} ($k_{Cr/Ag} = 2.7\times10^2$), Ni^{2+} ($k_{Ni/Ag} = 5.0\times10$), Zn^{2+} ($k_{Zn/Ag} = 3.8\times10$), Cu^{2+} ($k_{Cu/Ag} = 3.4\times10$) and Pb^{2+} ($k_{Pb/Ag} = 7.8\times10$), was much higher than other ions studied in the experiment (Appendix, Table A4.4). This preferential binding affinity of Cr^{3+}, Ni^{2+}, Zn^{2+}, Cu^{2+} and Pb^{2+} resulted in higher adsorption capacity of these ions on malachite nanoparticle (**I**) over the 'soft' metal ions. In case of BSA-malachite nanocomposite (**II**), the binding affinity of the metal ions is reversed. Here, the highest k values for Au^{3+} ($k_{Au/Ni} = 2.7\times10^2$), Pd^{2+} ($k_{Pd/Ni} = 2.3\times10^2$), Hg^{2+} ($k_{Hg/Ni} = 1.6\times10^2$), Pb^{2+} ($k_{Pb/Ni} = 9.8\times10$) and Ag^{+} ($k_{Ag/Ni} = 4.7\times10$) was found to be significantly higher than the 'harder' metal ions (Appendix, Table A4.5). As a result, the 'soft' and precious metal ions were adsorbed preferably on **II** compared to Cr^{3+}, Ni^{2+}, Zn^{2+} and Cu^{2+}.

Among the metal ions preferably adsorbed on **I**, the highest k values decreases in the order for Cr^{3+} ($k_{Cr/Ag} = 2.7\times10^2$) > Pb^{2+} ($k_{Pb/Ag} = 7.8\times10$) > Ni^{2+} ($k_{Ni/Ag} = 5.0\times10$) > Zn^{2+} ($k_{Zn/Ag} = 3.8\times10$) ≥ Cu^{2+} ($k_{Cu/Ag} = 3.4\times10$) as shown in Figure 4.15a. This indicates a decrease in adsorption capacity of 'harder' metal ions on **I** approximately in the order Cr^{3+} > Pb^{2+} > Ni^{2+} > Zn^{2+} ≥ Cu^{2+}, which is consistent with the experimental results obtained previously (Figure 4.12). Selectivity coefficient values (k) for Zn^{2+} and Cu^{2+} were found to be almost similar on **I**. Similarly among the ions get preferably adsorbed on BSA-malachite nanocomposite (**II**), the binding affinity (k value) decreases in the order of Au^{3+} ($k_{Au/Ni} = 2.7\times10^2$) > Pd^{2+} ($k_{Pd/Ni} = 2.3\times10^2$) > Hg^{2+} ($k_{Hg/Ni} = 1.6\times10^2$) > Pb^{2+} ($k_{Pb/Ni} = 9.8\times10$) > Ag^{+} ($k_{Ag/Ni} = 4.7\times10$) (Figure 4.15b). The maximum adsorption capacity (Q_m, Table 4.5) of these ions on **II**, also decreases in the order of Au^{3+} > Pd^{2+} > Hg^{2+} > Pb^{2+} > Ag^{+} according to the k value obtained. In addition with highest k values, other selectivity

coefficients (*k* values) also reflected the similar binding affinity of these metal ions on **I** and **II** (Appendix, Table A4.4 and A4.5).

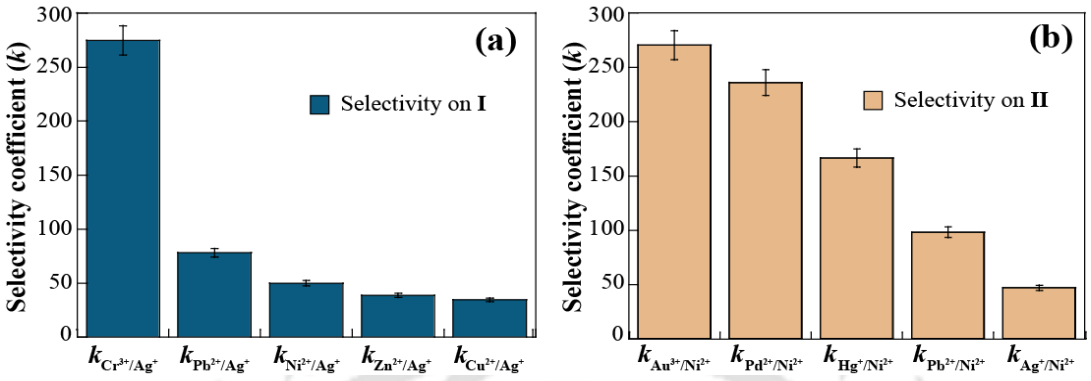

Figure 4.15. Comparison of selectivity coefficient (*k*) values for (a) Cr^{3+}, Pb^{2+}, Ni^{2+}, Zn^{2+} and Cu^{2+} on malachite nanoparticle and (b) Au^{3+}, Pd^{2+}, Hg^{2+}, Pb^{2+} and Ag^{+} on BSA-malachite nanocomposite. (The error bars represents the standard deviation calculated from two replicates)

4.5.7. Controlled interaction of metal ion from synthetic wastewater solution.

In addition with equi-molar competitive study, adsorption of these metal ions was also studied from a synthetic wastewater solution containing various metal ions of different concentrations. The mixed solution, prepared in the laboratory, consist of a relatively higher concentration of Au^{3+} along with Pd^{2+}, Zn^{2+}, Cu^{2+} and Cr^{3+} (Table 4.6). Adsorption behaviour of metal ions from this synthetic wastewater solution follows similar pattern as obtained in case of equi-molar competitive study (Figure 4.16). Table 4.6 summarizes the results of the adsorption of metal ions from synthetic wastewater solution on both the surfaces **I** and **II**. The adsorption of Au^{3+} and Pd^{2+} present in the synthetic wastewater is higher on BSA-malachite nanocomposite (**II**) and very low on malachite nanoparticle (**I**); while Cr^{3+}, Zn^{2+} and Cu^{2+} adsorbed more on **I** and hardly adsorb on **II**. Similarly, Pb^{2+} was adsorbed in equal amount from on both **I** and **II**. The K_d values for the metal ions obtained from this set of adsorption study listed in Table

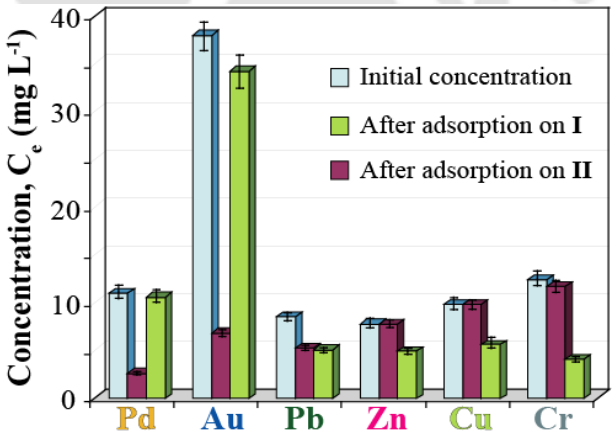

Figure 4.16. Adsorption behaviour of metal ions from synthetic wastewater solution on both malachite nanoparticles and BSA-malachite nanocomposite.

4.6. K_d values for Au^{3+} and Pd^{2+} was found higher on **II** and that for Cr^{3+}, Zn^{2+} and Cu^{2+} was higher on **I**. Moreover, the selectivity coefficient (*k*) calculation reveals the similar binding affinity in the order for $Au^{3+} > Pd^{2+} > Pb^{2+}$ on **II** and for $Cr^{3+} > Pb^{2+} > Zn^{2+}$, Cu^{2+} on **I** (Appendix, Figure A4.16 and Table A4.7) which is consistent with the equi-molar competitive study discussed previously. Therefore, the controlled adsorption of selective metal ions on two alternative nano-structured surfaces (malachite nanoparticle and BSA-malachite nanocomposite) has also succeeded in case of a synthetic wastewater solution having different metal ion concentration.

Table 4.6. Adsorption efficiency (%) and distribution coefficient (K_d) of different metal ions present in synthetic wastewater on malachite nanoparticle (**I**) and BSA-malachite nanocomposite (**II**).

Metal ion	Initial, C_0 (mg L^{-1})	Malachite nanoparticle **(I)**			BSA-malachite nanocomposite **(II)**		
		C_e (mg L^{-1})	Adsorption (%)	K_d (L g^{-1})	C_e (mg L^{-1})	Adsorption (%)	K_d (L g^{-1})
Au^{3+}	38.0	34.2	~10.0	0.022	6.8	~80.0	0.917
Pd^{2+}	11.0	10.6	~3.0	0.007	2.6	~76.0	0.646
Pb^{2+}	8.5	5.1	~40.0	0.133	5.2	~38.0	0.126
Zn^{2+}	7.7	5.7	~25.0	0.070	7.6	~1.0	0.0026
Cu^{2+}	9.8	7.8	~20.0	0.050	9.7	~1.0	0.0023
Cr^{3+}	12.4	4.1	~67.0	0.404	11.7	~5.0	0.011

4.5.8. Summary

In this present section, the reversal adsorption behaviour of selected metal ions, which can be controlled and reversed by simple surface modification of malachite nanoparticle with bovine serum albumin have been illustrated. BSA-malachite nanocomposite has been prepared by coating malachite nanoparticle with BSA and subsequent crosslinking with glutaraldehyde. Conformational analysis of protein in BSA–malachite nanocomposite reveals a partially unfolded state with reduced secondary structural elements of BSA compared to native state. Among the metal ions used in adsorption study, malachite nanoparticle (**I**) preferably adsorb the ions Cr^{3+}, Ni^{2+}, Zn^{2+} and Cu^{2+} over other ions *viz.* Au^{3+}, Pd^{2+}, Hg^{2+} and Ag^{+}. After surface modification with BSA, the BSA-malachite nanocomposite (**II**) exhibits a reverse preferential binding capacity for Au^{3+}, Pd^{2+}, Hg^{2+} and Ag^{+} compared to Cr^{3+}, Ni^{2+}, Zn^{2+} and Cu^{2+}. This reversal in adsorption behaviour is mainly attributed to the affinity of metal ions with the $–CO_3$ and –OH groups

present on the surface of **I** and several amino acid side groups of BSA present on **II**. In addition, Pb^{2+} was adsorbed on malachite nanoparticle and the BSA-malachite nanocomposite equally, due to its equal binding affinity towards these two surfaces. Kinetic analysis revealed that the adsorption phenomena can be expressed better with second order model in each case. Moreover, the adsorption isotherm of Cr^{3+}, Ni^{2+}, Zn^{2+}, Cu^{2+} and Pb^{2+} on **I** and Au^{3+}, Pd^{2+}, Hg^{2+}, Pb^{2+} and Ag^{+} on **II** is fitted well in Langmuir model compared to Freundlich model with a different maximum adsorption capacity (Q_m) value in each case. In equi-molar multi-component study, the calculated selectivity coefficient (*k*) values indicates a decrease in binding affinity in the order of $Cr^{3+} > Pb^{2+} > Ni^{2+} > Zn^{2+}$, Cu^{2+} on malachite nanoparticle (**I**) and in the order of $Au^{3+} > Pd^{2+} > Hg^{2+} > Pb^{2+} > Ag^{+}$ on BSA-malachite nanocomposite (**II**). Similar type of adsorption results were obtained with synthetic wastewater solution containing variable amounts of different metal ions on malachite nanoparticle and BSA-malachite nanocomposite. This supports the applicability of simple surface modification based controlled adsorption of selected metal ions from both equi-molar and variable amount multi-component solution.

References

[4.1] (a) Hurlbut, C.S.; Klein, C. *Manual of Mineralogy*, 20th ed.; John Wiley and Sons: New York, 1985. (b) Frost, R. L.; Ding, Z.; Kloprogge, J. T.; Martens, W. N. *Thermochimica Acta* 2002, 390, 133. (c) Salvado, N.; Pradell, T.; Pantos, E.; Papiz, M.Z.; Molera, J.; Seco M.; Vendrell-Saz, M. *J. Synch. Rad.* 2002, 9, 215. (d) Gilbert, B.; Denoel, S.; Weberc, G.; Allart, D. *Analyst* 2003, 128, 1213.

[4.2] Molchan, I.S.; Thompson, G.E.; Skeldon, P.; Andriessen, R. *J. Colloid Interface Sci.* 2008, 323, 282.

[4.3] Goldsmith, J.A.; Ross, S.D.; *Spectrochim. Acta, Part A: Mol. Biomol. Spectrosc.* 1968, 24, 2131.

[4.4] Frost, R.L.; Wain, D.L.; Martens, W.N.; Reddy, B.J. *Polyhedron* 2007, 26, 275.

[4.5] Tanaka, H.; Yamane, M. *J. Therm. Anal.* 1992, 38, 627.

[4.6] Brown, I.W.M.; Mackenzie, K.J.D.; Gainsford, G.J.*Thermochim. Acta* 1984, 74, 23.

[4.7] Gonzaletz, G.; Laskowski, J. *Electroanal. Chem. Int. Electrochem.* 1974, 53, 452.

[4.8] (a) Nakanishi, K.; Sakiyama, T.; Imamura, K. *J. Biosci. Bioeng.* 2001, 91, 233. (b) Field, S.; Udalova, I.; Ragoussis, J. *Adv. Biochem. Eng. Biotechnol.* 2007, 104, 87. (c) Vega, C.; Roos, Y.H. *J. Dairy Sci.* 2006, 89, 383. (d) Wang, A.J.; Arnold, M.A. *Anal. Chem.* 1992, 64, 1051. (e) Giacomelli, C.E.; Esplandin, M.J.; Oritz, P.I.; Avena, M.J.; De Pauli, C.P. *J. Colloid Interface Sci.* 1999, 218, 404.

[4.9] Lee, S.H.; Ruckenstein, E. *J. Colloid Interface Sci.* 1988, 125, 365.

[4.10] Koutsopoulos, S.; Patzsch, K.; Bosker, W.T.E; Norde, W.; *Langmuir* 2007, 23, 2000.

[4.11] Kondo, A.; Mihara, J.; *J. Colloid Interface Sci.* 1996, 177, 214.

[4.12] Kondo, A.; Oku, S.; Higashitani, K. *J. Colloid Interface Sci.* 1991, 143, 214.

[4.13] Larsericsdotter, H; Oscarsson, S.; Buijs, J. *J. Colloid Interface Sci.* 2005, 289, 26.

[4.14] Norde, W.; Favier, J.P. *Colloids Surf.* 1992, 64, 87.

[4.15] Bujis, J.; Norde, W.; Lichtenbelt, J.W.T. *Langmuir* 1996, 12, 1605.

[4.16] Su, T.J.; Lu, J.R.; Thomas, R.K.; Cui, Z.F. *J. Phys. Chem. B* 1999, 103, 3727.

[4.17] Yoon, J.Y; Park, H.Y.; Kim, J.H; Kim, W.S. *J. Colloid Interface Sci.* 1996, 177, 613.

[4.18] Norde, W.; Giacomelli, C.E. *J. Biotechnol.* 2000, 79, 259.

[4.19] Giacomelli, C.E.; Norde, W. *J. Colloid Interface Sci.* 2001, 233, 234.

[4.20] Kosmulski, M.; J. Colloid Interface Sci. 2004, 275, 214.

[4.21] Peng, Z.G.; Hidajat, K.; Uddin, M.S. *Colloids Surf B.* 2004, 33, 15.

[4.22] Giacomelli, C.E.; Avena, M.J.; Pauli, C.P.D. *J. Colloid Interface Sci.* 1997, 188, 387.

[4.23] Kopac, T.; Bozgeyik, K.; Yener, J. *Colloids Surf. A.* 2008, 322, 19.

[4.24] Oliva, F.Y.; Avalle, L.B.; Cámara, O.R.; Pauli, C.P.D. *J. Colloids Interface Sci.* 2008, 261, 299.

[4.25] Alkan, M.; Demirbas, O.; Dogan, M.; Arslan, O. *Micropor. Mesopor. Mater.* 2006, 96, 331.

[4.26] Wassell, D.T.H; Hall, R.C.; Embery, G. *Biomaterials* 1995, 16, 697.

[4.27] RCSB protein database. http://www.rcsb.org/.

[4.28] Rezwan, K.; Meier, L.P.; Rezwan, M.; Voros, J. Marcus Textor, M.; Gauckler, L.J. *Langmuir* 2004, 20, 10055.

[4.29] Yang, J. T.; Wu, C. S. C.; Martinez, H. M. *Methods Enzymol.* 1986, 130, 208.

[4.30] Brahms, S.; Brahms, J. *J. Mol. Biol.* 1980, 138, 149.

[4.31] Fu, K.; Griebenow, K.; Hsieh, L.; Klibnov, A. M.; Langer, R. *J. Control. Release* 1999, 58, 357.

[4.32] Wu, X.; Narsimhan, G. *Langmuir* 2008, 24, 4989.

[4.33] Sabatino, P.; Casella, L.; Granata, A.; Iafisco, M.; Lesci, I.G.; Monzani, E.; Roveri, N. *J. Colloid Interface Sci.* 2007, 314, 389.

[4.34] (a) Ho, Y. S.; McKay, G. *Water Res.* 2000, *34*, 735. (b) Reddad, Z.; Gérente, C.; Andrès, Y.; Ralet, M.-C.; Thibault, J.-F.; Le Cloirec, P. *Carbohydr. Polym.* 2002, *49*, 23. (c) Reddad, Z.; Gerente, C.; Andres, Y. Cloirec, P. L. *Environ. Sci. Technol.* 2002, 36, 2067.

[4.35] Shamim, N.; Liang, H.; Hidajat, K.; Uddin, M.S. *J. Colloid Interface Sci.* 2008, 320, 15.

[4.36] McMurry, J.; *Organic Chemistry*, 5th ed.; Brooks Cole: Belmont, CA, 1999.

[4.37] Yoon, J.Y.; Kim, J.H.; Kim, W.S. *Colloids Surf. B* 1998, 12, 15.

[4.38] Lassen, B.; Malmsten, M. *J. Colloid Interface Sci.* 1996, 180, 339.

[4.39] Sharma, S.; Agarwal, G. P. *J. Colloid Interface Sci*. 2001, 243, 61.

[4.40] Kanicky, J. R.; Shah, D.O. *J. Colloid Interface Sci*. 2001, 256, 201.

[4.41] Malmsten, M.; Emoto, K.; Van Alstine, J. M. *J. Colloid Interface Sci.* 1998, 202, 507.

[4.42] Bosker, W. T. E.; Patzsch, K.; Stuart, M. A. C.; Norde, W. *Soft Mater.* 2007, 3, 754.

[4.43] Nelson, D. L.; Cox, M. M. *Lehninger Principles of Biochemistry*, 4th ed.; W. H. Freeman: USA, 2004.

[4.44] Klajnert, B.; Stanislawska, L.; Bryszewska, M.; Palecz, B. *Biochim. Biophys. Acta* 2003, 1648, 115.

[4.45] Filenko, A.; Demchenko, M.; Mustafaeva, Z.; Osada Y.; Mustafaev, M. *Biomacromolecules* 2001, 2, 270.

[4.46] Lakowicz, J. R. *Principles of Fluorescence Spectroscopy*, 2nd ed.; Springer: New York, 2006.

[4.47] Pan, B. F.; Gao, F.; Ao, L. M. *J. Magn. Magn. Mater.* 2005, 293, 252.

[4.48] Patel, A. B.; Srivastava, S.; Phadke, R. S. *J. Biol. Chem.* 1999, 274, 21755.

[4.49] Sen, P.; Ahmad, B.; Khan, R.H. *Eur. Biophys. J.*, 2008, 37, 1303.

[4.50] Schwinte, P.; Ball, V.; Szalontai, B.; Haikel, Y.; Voegel, J.C.; Schaaf, P. *Biomacromolecules* 2002, 3, 1135.

[4.51] Weert, M.V.D.; Haris, P.I.; Hennink, W.E.; Crommelin, D.J.A. *Anal. Biochem.* 2001, 297, 160.

[4.52] Husband, F. A.; Garrood, M. J.; Mackie, A. R.; Burnett, G. R.; Wilde, P. J. *J. Agric. Food Chem.* 2001, 49, 859.

[4.53] Haris, P.I.; Severcan, F. *J. Mol. Cat. B.* 1999, 7, 207.

[4.54] Murayama, K.; Tomida, M. *Biochemistry* 2004, 43, 11526.

[4.55] Griebenow, K.; Klibnov, A. M. *J. Am. Chem. Soc.* 1996, 118, 11695.

[4.56] Griebenow, K.; Klibnov, A. M. *Proc. Natl. Acad. Sci. U.S.A.* 1995, 92, 10969.

[4.57] (a) Jiang, W.; Kim, B. Y. S.; Rutka, J. T.; Chan, W. C. W. *Nat. Nanotechnol.*, 2008, 3, 145. (b) Josephson, L.; Perez, J. M., Weissleder, R. *Angew. Chem. Int. Ed.*, 2001, 40, 3204.

[4.58] Meltzer, M.; Callahan, M.; Jensen, T. *Metal-bearing waste streams: minimizing, recycling and treatment*; Noyes Data Corp.: Park Ridge, NJ, 1990.

[4.59] Brown, J.; Mercier, L.; Pinnavaia, T. J. *Chem. Commun.* 1999, 1, 69.

[4.60] Liu, A. M.; Hidajat, S.; Zhao, D. Y. *Chem. Commun.* 2000, 13, 1145.

[4.61] (a) Zhang, Q.; Pan, B.; Pan, B.; Zhang, W.; Jia, K.; Zhang, Q. *Environ. Sci. Technol.*, 2008, 42, 4140. (b) Minamisawa, M.; Minamisawa, H.; Yoshida, S. Takai, N. *J. Agric. Food Chem.*, 2004, 52 5606. (c) Lam, K.F.; Yeung, K.L; McKay, G. *Environ. Sci. Technol.* 2007, 41, 3329. (d) Wang, J.; Chen, C. *Biotechnol. Adv.* 2009, 27, 195.

[4.62] Maruyama, T.; Matsushita, H.; Shimada, Y.; Kamata, I.; Hanaki, M.; Sonokawa, S.; Kamiya, N. Goto, M. *Environ. Sci. Technol.* 2007, 41, 1359.

[4.63] Peasron, R. G. *J. Am. Chem. Soc.* 1963, 85, 3533.

[4.64] Feng, X.; Fryxell, G. E.; Wang, L.-Q.; Kim, A. Y.; Liu, J.; Kemner, K. M. *Science* 1997, 276, 923.

[4.65] Lam, K. F.; Yeung, K. L.; McKay, G. *J. Phys. Chem. B* 2006, 110, 2187.

[4.66] Ishikawa, S.; Suyama, K.; Arihara, K.; Itoh, M. *Bioresource Technol.* 2002, 81, 201.

[4.67] Collman, P. M.; Freeman, M. C.; Guss, J. M.; Murata, M.; Moris, V. A.; Ramshaw, J. A.; Venkatappa, M. P. *Nature* 1978, 272, 319.

[4.68] Jalilehvand, F.; Leung, B.O.; Izadifard, M.; Damian, E. *Inorg. Chem.* 2006, 45, 66.

[4.69] Chen, X. H.; Zhu, L. G.; Duan, C. Y.; Liu, Y. J.; Kostic, N. M. *Acta Cryst.* 1998, C54, 909.

[4.70] Sasaki, Y. C.; Yasuda, K.; Suzuki, Y.; Ishibashi, T.; Satoh, I.; Fujiki, Y.; Ishiwata, S. *Biophys. J.* 1997, 72, 1842.

[4.71] Kang, T.; Park, Y.; Choi, K.; Lee, J. S.; Yi, L. *J. Mater. Chem.* 2004, 14, 1043.

[4.72] Burford, N.; Eelman, M. D.; LeBlanc, W.G.; Cameron, T. S.; Robertson, K. N. Chem. Commun. 2004, 3, 332.

[4.73] Hall, K.R.; Eagleton, L. C.; Acrivos, A.; Vermeulen, T. *Ind. Eng. Chem. Fundamen.*, 1966, 5, 212.

[4.74] Dai, S.; Burleigh, M.C.; Shin, Y.; Morrow, C.C.; Barnes, C.E.; Xue, Z. *Angew. Chem. Int. Ed.* 1999, 38, 1235.

Appendix

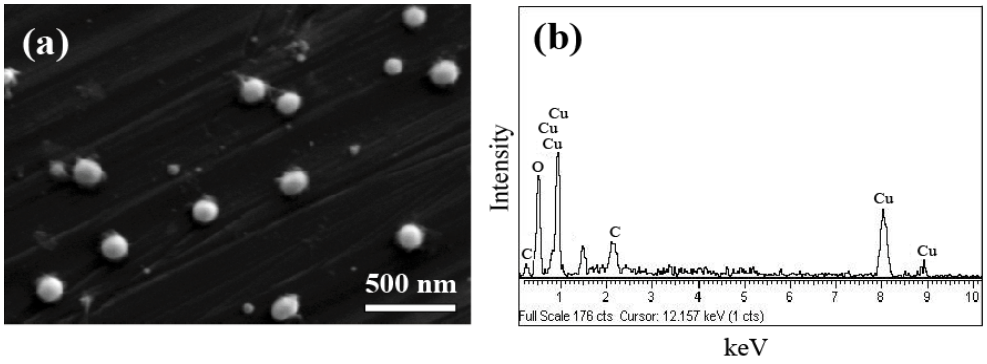

Figure A4.1. (a) SEM images of malachite NPs and (b) EDX spectra of malachite NPs showing the presence of Cu, C and O.

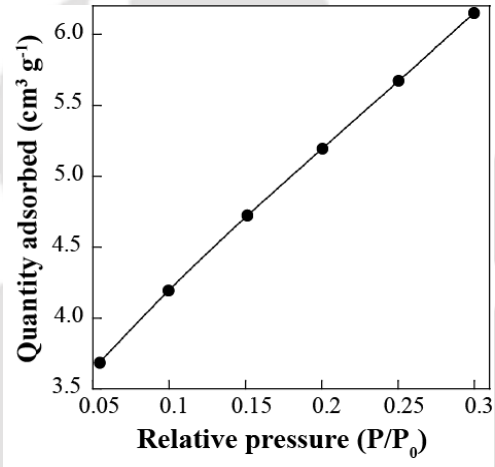

Figure A4.2. N_2 adsorption/desorption isotherms of malachite NPs measured from BET analysis.

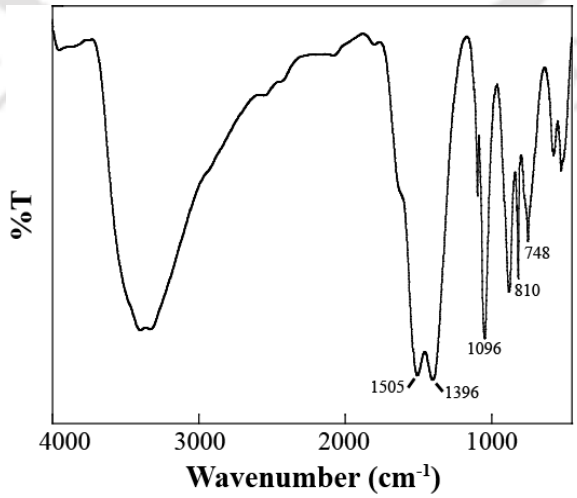

Figure A4.3. FT-IR spectra of malachite nanoparticles.

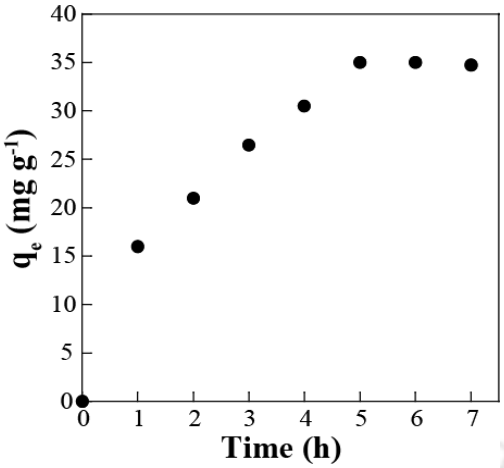

Figure A4.4. Adsorption kinetics with 1 mg L^{-1} BSA and 20 g L^{-1} malachite NPs at pH ~5.0. The steady state reaches within 5 h.

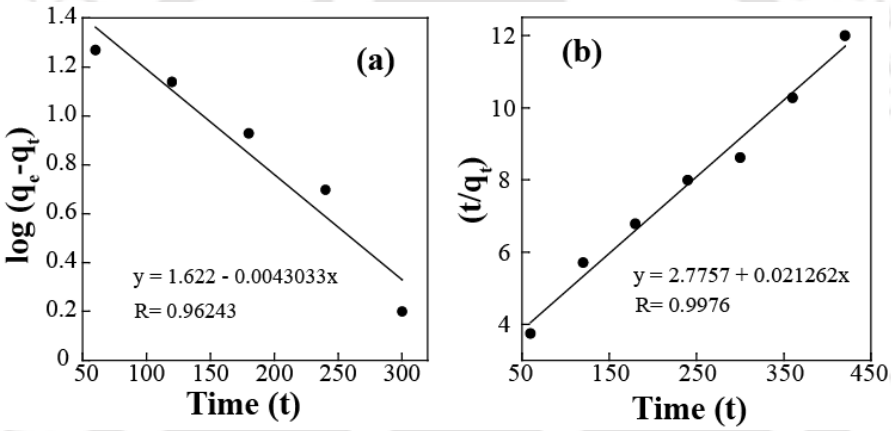

Figure A4.5. (a) Pseudo first order and (b) second order kinetics model of BSA adsorption studies on malachite performed with 1 mg mL^{-1} BSA and 20 g L^{-1} of malachite at pH ~5.0.

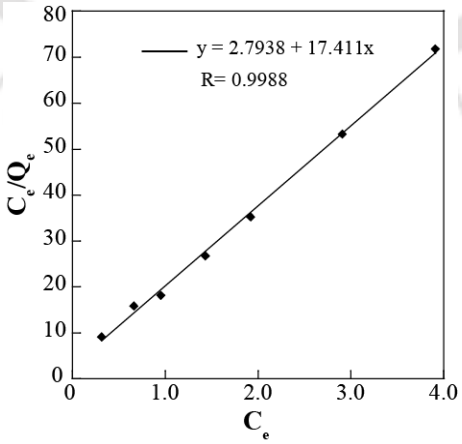

Figure A4.6. Scatchard plot of BSA adsorption on malachite NPs at different protein concentration. Correlation coefficient (R) value of 0.998 implies no significant co-operative effect.

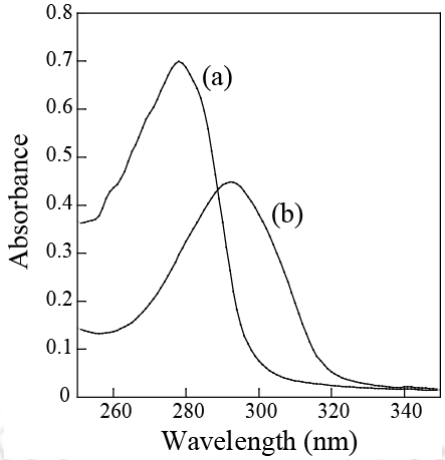

Figure A4.7. UV spectra of BSA in (a) native and (b) after desorption from malachite surface. Desorbed spectra shows a ~10 nm shift which is due to alteration in protein conformation upon adsorption-desorption cycle.

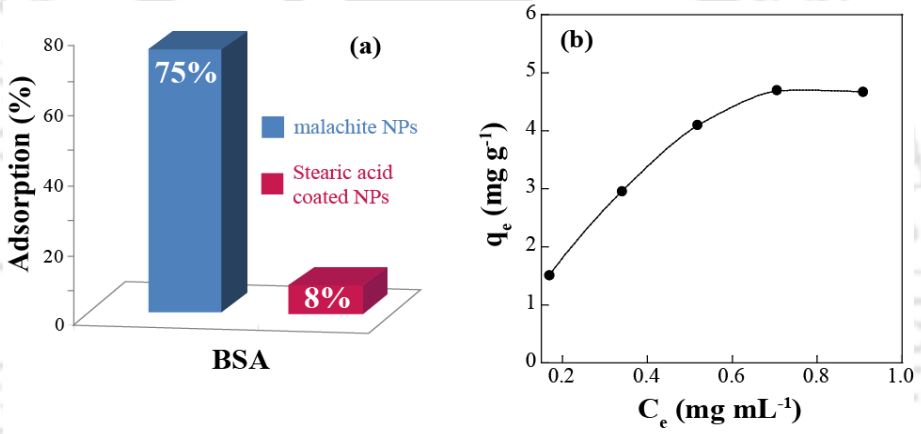

Figure A4.8. (a) Adsorption efficiency and (b) steady state adsorption isotherm of BSA on stearic acid coated malachite NPs at pH ~5.0. Maximum adsorption capacity was very much lower (~5 mg/g) compared to that on bare malachite surface (~50 mg g^{-1}).

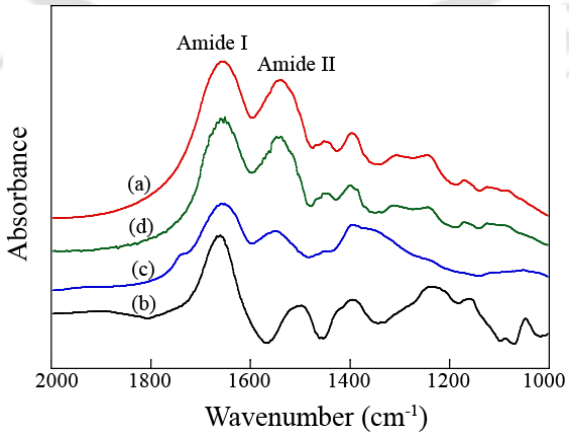

Figure A4.9. FTIR of lyophilized BSA in (a) native, (b) adsorbed (after subtraction of only malachite spectra), (c) desorbed and (d) after interaction with SA-malachite NPs.

Table A4.1. Secondary structural component analysis of BSA at different state of BSA-malachite nanocomposite. In BSA-malachite nanocomposite, the protein consist of ~15% α-helix and ~16% of β-sheet element compared to ~31% α-helix and ~20% of β-sheet content at native state.

Band position (cm^{-1})* Gaussian curve fit	Area (%) of Gaussian bands of BSA*			Assignment
	Native state	Adsorbed on malachite	Crosslinked (0.05% Glutaraldehyde)	
1704 ± 2	1 ± 1	2 ± 1	1 ± 1	Un-ordered
1689 ± 1	6 ± 1	7 ± 2	4 ± 1	β-sheet
1683 ± 2	8 ± 2	15 ± 1	8 ± 1	Un-ordered
1673 ± 1	11 ± 1	17 ± 1	10 ± 1	Un-ordered
1666 ± 2	8 ± 2	21 ± 2	35 ± 2	Un-ordered
1656 ± 2	31 ± 2	15 ± 1	14 ± 2	α-helix
1647 ± 1	7 ± 1	4 ± 1	10 ± 1	Un-ordered
1640 ± 1	5 ± 1	2 ± 1	8 ± 2	β-sheet
1635 ± 2	10 ± 1	8 ± 2	6 ± 1	Un-ordered
1630 ± 1	8 ± 2	6 ± 1	3 ± 1	β-sheet
1624 ± 2	5 ± 1	3 ± 1	1 ± 1	Un-ordered

* The ± values are the standard deviations calculated by analyzing two individual spectra in each case.

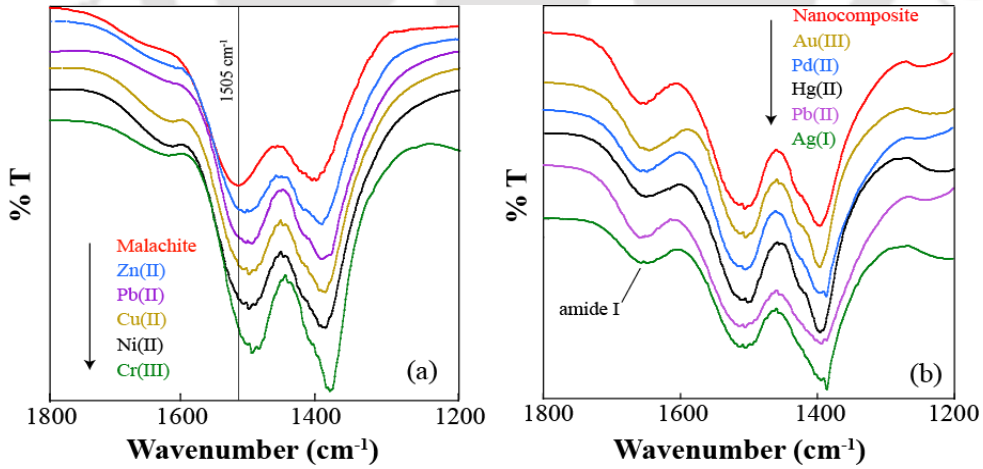

Figure A4.11. (a) FT-IR spectra of malachite nanoparticles after adsorption of Cr^{3+}, Zn^{2+}, Ni^{2+}, Cu^{2+} and Pb^{2+} ions (10 mg L^{-1} each). After adsorption of metal ions the band at ~1505 cm^{-1} shifted to ~1490 cm^{-1} in case, which is probably due to the binding of free $-(CO_3)^{2-}$ group with the metal ions in solution as anticipated in our discussion in the main text. (b) FT-IR spectra of BSA-malachite nanocomposite and after adsorption of Au^{3+}, Pd^{2+}, Hg^{2+}, Ag^{+} and Pb^{2+} (10 mg L^{-1} each). The band at ~1656 cm^{-1} represents the amide I region of BSA in BSA-malachite nanocomposite.

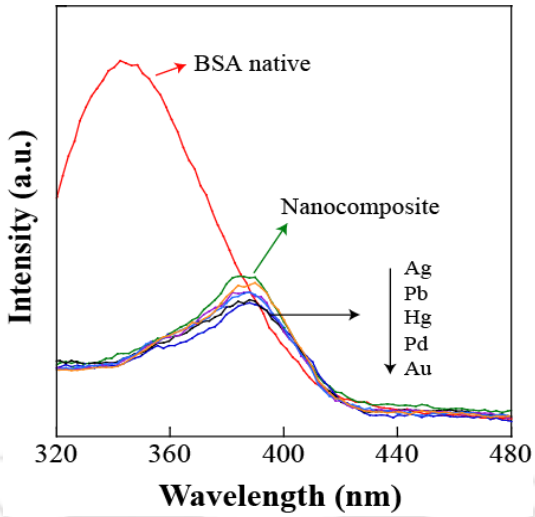

Figure A4.12. Steady state fluorescence emission spectra of BSA in BSA-malachite nanocomposite and after adsorption of different 'soft' metal ions (10 mg L^{-1}). Emission spectra of BSA is quenched and shifted to ~386 nm in BSA-malachite nanocomposite as described the main text. The emission intensity further decreased to some extent after adsorption of 'soft' metal ions. Maximum quenching occurs after adsorption of Au^{3+}, while least quenching observed in case of Ag^{+}. The decrease in intensity of metal-particle complexes is mainly due to the binding of metal ions with the side chains of different 'soft' amino acids of BSA in BSA-malachite nanocomposite.

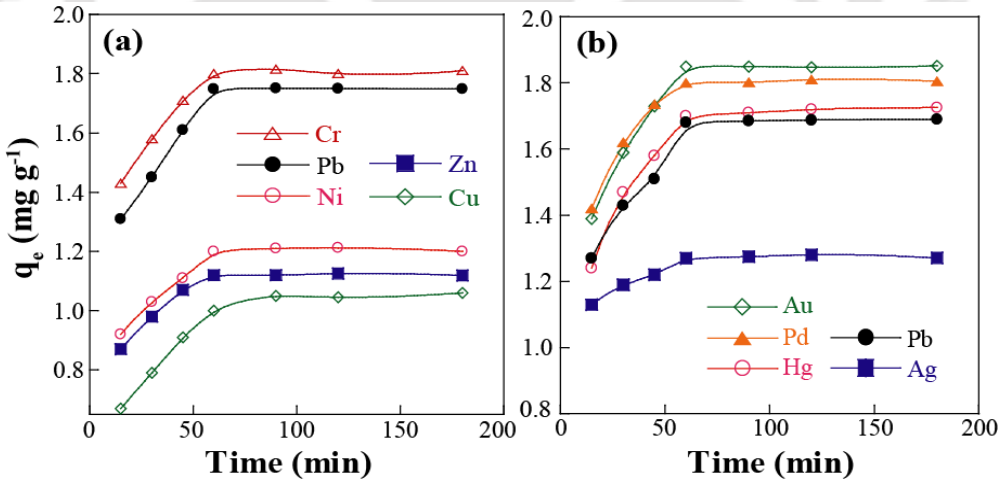

Figure A4.13. Adsorption kinetics with 10 mg/L of (a) Cr^{3+}, Ni^{2+}, Zn^{2+}, Cu^{2+} and Pb^{2+} on **I** and (b) Au^{3+}, Pd^{2+}, Ag^{+}, Hg^{2+} and Pb^{2+} on **II**. Almost for all metal ions adsorption reaches steady state within ~1 hr on both **I** and **II**.

Table A4.2: Adsorption kinetics parameters of Cr^{3+}, Ni^{2+}, Zn^{2+}, Cu^{2+} and Pb^{2+} on bare malachite (**I**) surface analyzed by pseudo first and second order kinetic model.

Metal ions	1st order kinetics			2nd order kinetics		
	R	k_1	χ^2	R	k_2	χ^2
Ni^{2+}	0.987	0.036	0.414	0.997	0.096	0.024
Zn^{2+}	0.987	0.046	0.206	0.999	0.111	0.034
Cu^{2+}	0.984	0.041	0.100	0.998	0.061	0.023
Cr^{3+}	0.988	0.046	0.370	0.998	0.077	0.012
Pb^{2+}	0.982	0.037	0.525	0.996	0.054	0.027

Table A4.3. Adsorption kinetics parameters of Au^{3+}, Pd^{2+}, Ag^{+}, Hg^{2+} and Pb^{2+} on BSA-malachite nanocomposite (II) analyzed by pseudo first and second order kinetic model.

Metal ions	1st order kinetics			2nd order kinetics		
	R	k_1	χ^2	R	k_2	χ^2
Hg^{2+}	0.980	0.044	0.268	0.998	0.057	0.031
Ag^{+}	0.988	0.034	1.11	0.999	0.254	0.007
Au^{3+}	0.986	0.044	0.334	0.998	0.057	0.048
Pd^{2+}	0.987	0.055	0.197	0.999	0.080	0.064
Pb^{2+}	0.987	0.029	1.18	0.998	0.064	0.037

Table A4.4. Selectivity coefficient ($k_{m1/m2}$) values for different metal ions adsorption on malachite nanoparticle (I) from equi-molar (10 mg L^{-1} each) competitive solution.

		m_1								
		Hg^{2+}	Ag^{+}	Au^{3+}	Pd^{2+}	Ni^{2+}	Zn^{2+}	Cu^{2+}	Cr^{3+}	Pb^{2+}
m_2	Hg^{2+}	-	0.850	4.00	5.00	42.50	33.0	29.5	233.5	66.50
	Ag^{+}	1.170	-	4.70	5.88	50.00	38.8	34.7	274.7	78.23
	Au^{3+}	0.250	0.212	-	1.25	10.62	8.25	7.37	58.37	16.62
	Pd^{2+}	0.200	0.17	0.800	-	8.500	6.60	5.9	46.70	13.30
	Ni^{2+}	0.023	0.023	0.094	0.117	-	0.776	0.694	5.49	1.564
	Zn^{2+}	0.030	0.025	0.121	0.151	1.280	-	0.899	7.07	2.015
	Cu^{2+}	0.033	0.028	0.135	0.169	1.440	1.11	-	7.91	2.254
	Cr^{3+}	0.004	0.003	0.017	0.021	0.182	0.141	0.126	-	0.284
	Pb^{2+}	0.015	0.012	0.060	0.075	0.639	0.496	0.443	3.51	-

Table A4.5. Selectivity coefficient ($k_{m1/m2}$) values for different metal ions adsorption on BSA-malachite nanocomposite (II) from equi-molar (10 mg L^{-1} each) competitive solution.

		m_1								
		Hg^{2+}	Ag^{+}	Au^{3+}	Pd^{2+}	Ni^{2+}	Zn^{2+}	Cu^{2+}	Cr^{3+}	Pb^{2+}
m_2	Hg^{2+}	-	0.283	1.62	1.416	0.006	0.006	0.0133	0.0200	0.590
	Ag^{+}	3.529	-	5.72	5.00	0.0211	0.023	0.047	0.0705	2.082
	Au^{3+}	0.616	0.174	-	0.872	0.003	0.0036	0.0082	0.0123	0.363
	Pd^{2+}	0.705	0.200	1.14	-	0.004	0.0047	0.0094	0.0141	0.416
	Ni^{2+}	166.6	47.22	270.5	236.1	-	1.11	2.22	3.333	98.333
	Zn^{2+}	150.0	42.5	243.5	212.5	0.900	-	2.00	3.00	88.500
	Cu^{2+}	75.0	21.25	121.7	106.2	0.450	0.500	-	1.5	44.250
	Cr^{3+}	50.0	14.16	81.16	70.83	0.300	0.333	0.666	-	29.500
	Pb^{2+}	1.694	0.480	2.75	2.401	0.010	0.011	0.0225	0.0338	-

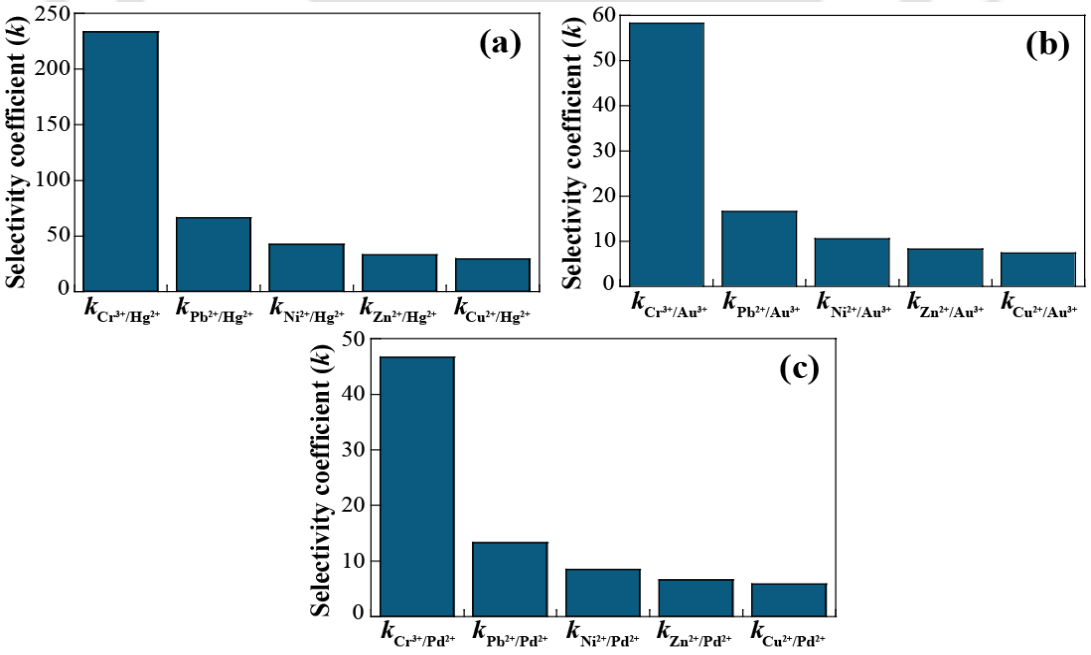

Figure A4.14. Selectivity coefficient for Cr^{3+}, Pb^{2+}, Ni^{2+}, Zn^{2+} and Cu^{2+} on malachite nanoparticle surface (**I**) from a competitive equi-molar solution having 10 mg L^{-1} of each metal ion. Selectivity coefficient values decreases (k) in the order $Cr^{3+} > Pb^{2+} > Ni^{2+} > Zn^{2+}$,$Cu^{2+}$; k values for Zn^{2+} and Cu^{2+} on **I** was found almost similar, indicating a similar binding affinity on **I**.

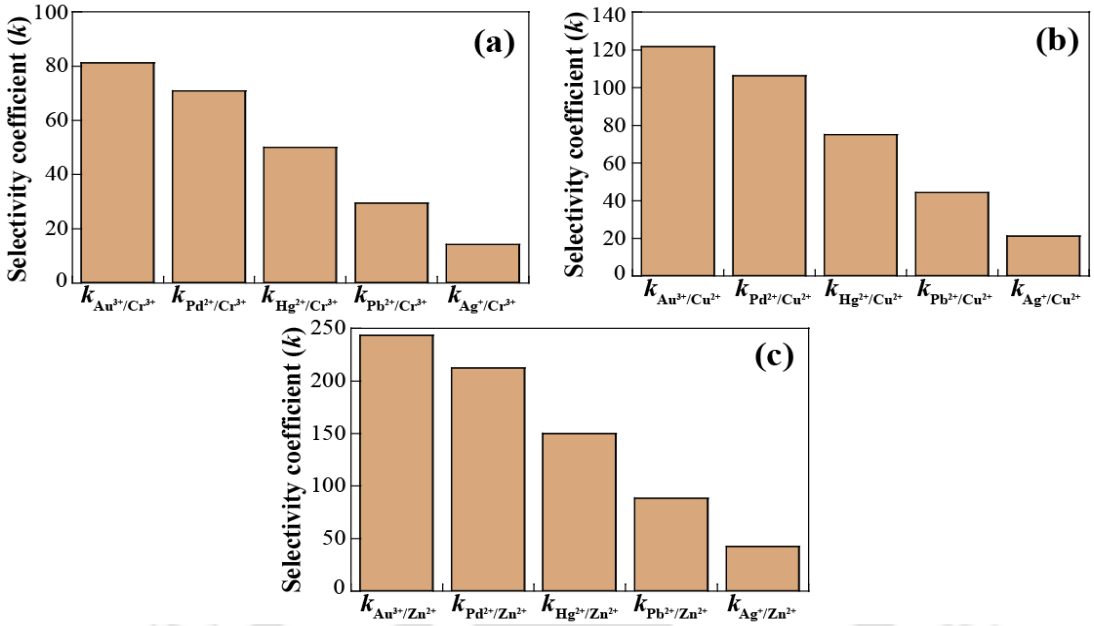

Figure A4.15. Selectivity coefficient for Au^{3+}, Pd^{2+}, Hg^{2+}, Pb^{2+} and Ag^{+} on BSA-malachite nanocomposite (**II**) from a competitive equi-molar solution having 10 mg L^{-1} of each metal ion. Selectivity coefficient decreases $Au^{3+} > Pd^{2+} > Hg^{2+} > Pb^{2+} > Ag^{+}$ on BSA-malachite nanocomposite.

Table A4.6. Selectivity coefficient ($k_{m1/m2}$) values for metal ions in a competitive adsorption study from synthetic wastewater on malachite nanoparticle (I).

Selectivity coefficient (k) on **I**		m_1					
		Au^{3+}	Pd^{2+}	Pb^{2+}	Zn^{2+}	Cu^{2+}	Cr^{3+}
m_2	Au^{3+}	-	0.340	6.045	3.181	2.27	18.36
	Pd^{2+}	2.930	-	19.00	9.333	6.667	57.71
	Pb^{2+}	0.164	0.056	-	0.526	0.375	3.037
	Zn^{2+}	0.314	0.107	1.900	-	0.714	5.771
	Cu^{2+}	0.440	0.150	2.660	1.400	-	8.080
	Cr^{3+}	0.054	0.018	0.329	0.173	0.123	-

Table A4.7. Selectivity coefficient ($k_{m1/m2}$) values for metal ions in a competitive adsorption study from synthetic wastewater on BSA-malachite nanocomposite (**II**).

Selectivity coefficient (k) on **II**		m_1					
		Au^{3+}	Pd^{2+}	Pb^{2+}	Zn^{2+}	Cu^{2+}	Cr^{3+}
m_2	Au^{3+}	-	0.704	0.137	0.0028	0.0025	0.011
	Pd^{2+}	1.419	-	0.195	0.0041	0.0035	0.017
	Pb^{2+}	7.277	5.126	-	0.020	0.018	0.087
	Zn^{2+}	352.6	248.4	48.46	-	0.884	4.230
	Cu^{2+}	382.1	280.8	54.78	1.130	-	4.78
	Cr^{3+}	83.36	58.72	11.45	0.236	0.209	-

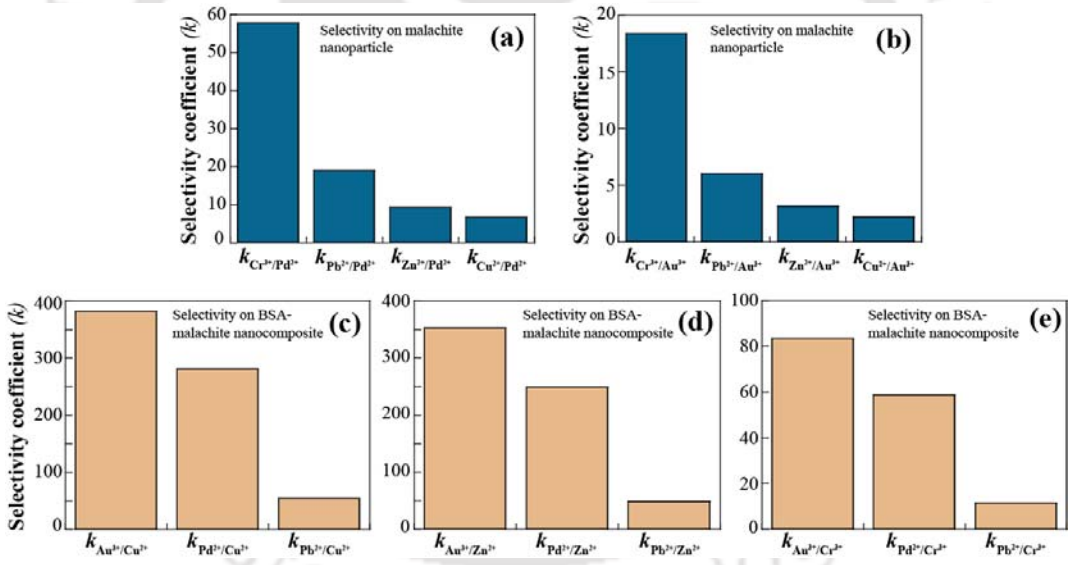

Figure A4.16. Comparison of selectivity coefficient values (k) from synthetic wastewater for Cr^{3+}, Pb^{2+}, Zn^{2+} and Cu^{2+} on malachite nanoparticle (**I**) [Figure (a) & (b)] and for Au^{3+}, Pd^{2+} and Pb^{2+} on BSA-malachite nanocomposite (**II**) [Figure (c) (d) & (e)]. Binding affinity of these metal ions reduce in the order Cr^{3+} > Pb^{2+} > Zn^{2+} > Cu^{2+} on malachite nanoparticle and Au^{3+} > Pd^{2+} > Pb^{2+} on BSA-malachite nanocomposite, which is consistent with the equi-molar competitive study.

Chapter 5

Interaction of Proteins on a ‘Soft’ Nanoparticle Surface

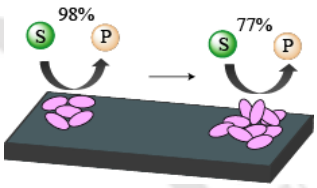

Chapter 5

5.1. Introduction

After studying the interaction on 'hard' surfaces, this chapter advances to describe the interaction of protein on a 'soft' nanoparticle surface. Herein, trypsin, a proteolytic enzyme has been taken for interaction studies on 'soft' CuS nanoparticle surface. The presence of sulfur group on the surface of CuS nanoparticle makes it a 'soft' surface which can easily interact with the protein. In addition, enzyme immobilized CuS nanoparticles have been also used for preliminary application on treating dairy wastewater.

5.2. Synthesis of 'soft' CuS nanoparticles

Ultrafine CuS nanoparticles were prepared via passing H_2S through a copper-acid complex solution (Scheme 5.1). Typically, aqueous solution of $Cu(CH_3COO)_2$ and pyridine-*2*,*3*-dicarboxylic acid (PDA) was mixed in a molar ratio of 1:2 to form a Cu-PDA complex, which precipitates out from the solution. The precipitated complex was further washed and re-dissolved into basic aqueous medium by adding piperidine base drop wise. The H_2S gas was then passed through this Cu-PDA complex solution in a controlled manner under vigorous stirring for 30 min. After that, the solution was stirred for additional 30 min. A colloidal greenish-black suspension was formed, which was separated by high speed centrifuge at 15000 rpm. Precipitate was further re-suspended with Milli-Q water and methanol to wash several times for removing the impurities. Finally, the washed CuS nanoparticles were collected after drying under vacuum and used for further interaction studies with trypsin.

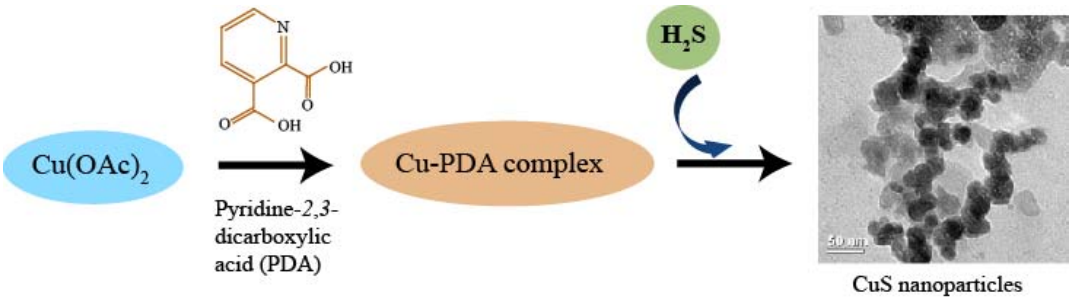

Scheme 5.1. Schematic illustration of synthesis of ultrafine CuS nanoparticles.

5.3. Characterization of CuS nanoparticles

The CuS nanoparticles have been synthesized in a facile two step process. Synthesized CuS nanoparticles were characterized by different analytical techniques. TEM images (Figure 5.1a) and corresponding particle size distribution analysis (Figure 5.1b) revealed the CuS nanoparticles are of regular shape with a size distribution in the range of 20−50 nm, which is fairly polydisperse. One control experiment has been also done by passing the H_2S gas into only $Cu(CH_3COO)_2$ solution, which resulted in precipitation of bulk CuS from solution. Due to the strong coordinating ability of carboxylate groups of PDA, it can bind strongly with metal center of Cu^{2+}.[5.1, 5.2] Therefore, the bi-dentate ligand PDA acted as a stabilizing agent in preparation of CuS nanoparticle. The analysis of the energy dispersive X-ray (EDX) spectra reveals that the presence of Cu and S in the CuS nanoparticle samples (Appendix, Figure A5.3).

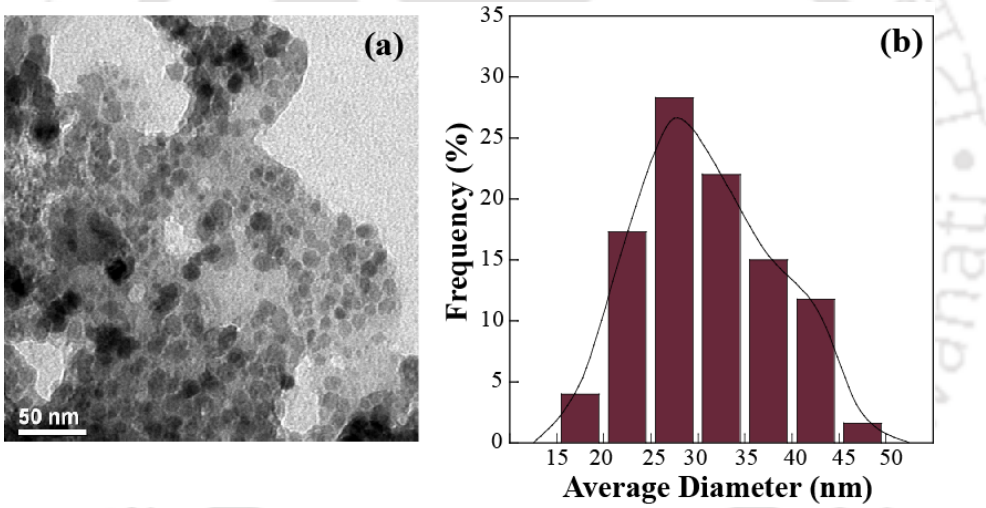

Figure 5.1. (a) TEM image and (b) size distribution analysis of synthesized CuS nanoparticles.

All peaks of the powder X-ray diffraction (PXRD) data shows the formation of crystalline nanoparticle (Figure 5.2a), and the peaks are matching well with the covellite phase of CuS (JCPDS file no. 00-006-0464).[5.3a] The average crystallite size of CuS nanoparticles was calculated ~25 nm using the Debye−Scherrer equation from the fwhm of the strongest peak, is consistent with the TEM and size distribution analysis. The N_2 adsorption isotherm of the BET analysis represents the type II isotherm according to Brunauer's classification (Appendix, Figure A5.4). From analysis, we found that CuS nanoparticles have a specific surface area of 60 $m^2 g^{-1}$ and a pore volume of 0.449 $cm^3 g^{-1}$. FT-IR spectra (Figure 5.2b) show the peaks characteristic of CuS. The weak metal-sulfur

band of CuS nanoparticles could be observed at ~617 cm^{-1} region (Appendix, Figure A5.5).[5.3b]

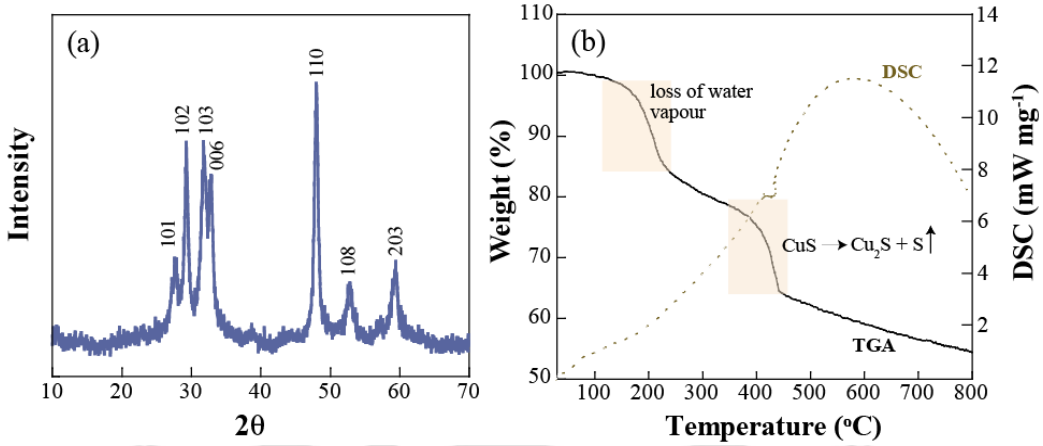

Figure 5.2. (a) PXRD spectra and (b) TGA-DSC spectra of CuS nanoparticles.

Thermal decomposition of CuS nanoparticles (in N_2 atmosphere), in the range of 25-100°C is shown in Figure 5.2b. At temperature range ~100-150°C the weight loss observed is mainly due to the release of water vapour associated with the material. The CuS nanoparticles undergo a desulfurization above 400 °C to give the product Cu_2S. Therefore, a further weight loss was observed in the temperature range of ~300-450°C, which is due to this decomposition of CuS to Cu_2S and release of sulfur that occurred up to ~430°C. [5.4]

$$2CuS \rightarrow Cu_2S + S\uparrow \qquad (5.1)$$

This decomposition pattern is in good agreement with the previous reports.[5.5] Moreover, the DSC pattern of CuS nanoparticles in this temperature range also reflects a change in phase from CuS to Cu_2S at this temperature range. The theoretical weight loss of CuS nanoparticles based on equation 5.1 is ~16.8%, whereas the measured weight loss from the TGA curve (Figure 5.2b) is about ~16.6%. Therefore, the theoretical and experimental weight losses were found to be close together, which supports the above mentioned discussion.

5.4. Controlled interaction trypsin with CuS nanoparticles

5.4.1. Background

Bio-nanotechnology is expected to have a large socioeconomic impact in practically all industrial activity fields. The use of nanomaterials is constantly increasing in all industrial sectors, in particular in biomedicine with applications in diagnostics and therapeutics.[5.6]

At the moment not much is known about the effects of nanoscale objects on biological systems, but recently the interaction of nanoparticles with proteins has emerged as a key parameter in nanotechnology, medicine, biomaterials etc. When nanoparticles (NPs) interact with proteins, they might alter protein conformation, expose new epitopes on the protein surface, or perturb the normal protein function, which can be important in various biotechnological application.[5.7] The information about protein structural changes upon binding to nanoparticles has been based mainly on infrared spectroscopy, circular dichroism, fluorescence, and other methods that can monitor changes in the secondary structure of proteins.[5.8] Moreover, the control over the interaction of proteins and its structure-function relationship is the most significant tool which can control the overall application. The controlled interaction of proteins/enzymes and its retention of functional activity is very much desirable in many industrial as well as research fields. Though many studies conducted on the in-depth analysis of structure-function relationship on proteins at interface, few could reach to conclusive results which can control the interaction at solid-liquid interface.

The use of different sulfide based mineral nanomaterials in a bio-interface has not been studied much. The fabrication of sulfide based nanomaterials like copper sulfides, silver sulfide (Ag_2S) etc. as semiconductor has been studied widely in recent years.[5.9] Copper sulfides exist as a range of stable and metastable phases ranging between copper 'poor' CuS (covellite) to copper 'rich' Cu_2S (chalcocite) at room temperature, common Cu_xS phases are $Cu_{1.75}S$(anilite), $Cu_{1.8}S$(digenite) and $Cu_{1.94}S$ (djurleite).[5.10] Copper sulfides have an important application in photonics as a semiconductor material for new-generation solar cells,[5.11] as a lithium battery cathode material,[5.12] as a catalyst and as a polymer-coating material.[5.13] However, the use of CuS in biological application has not been studied much. The presence of sulfur on the surface can make it a suitable tool to interact with biomolecules, where the sulfur on the surface can bind effectively with the thiol based amino acid side groups (like cysteine) of a protein. Trypsin is a proteolytic enzyme that cleaves peptide bonds at the carboxylic groups of arginine, lysine, and ornithine working optimally at pH 7.5-8.5.[5.14] In the human body the enzyme is excreted by the pancreas in the small intestine and takes part in the digestive deconstruction of food proteins and other biological processes. Trypsin is a medium-sized globular protein with applications in, *e.g.*, wound healing components, in washing agents, and in biotechnology (to perform enzymatic reactions).[5.15, 5.16]

In this section, the interaction of trypsin with ultrafine 'soft' CuS nanoparticles was investigated. Efforts were given to get control over the trypsin-CuS interaction and its structure-functional relationship. The surface coverage dependent structure and function of adsorbed trypsin was investigated. The conformational characteristics of the enzyme in the adsorbed state were analyzed in situ using CuS nanoparticles which, due to their extremely small size, do not significantly scatter or absorb light. Hence, the use of standard spectroscopic techniques such as circular dichroism and fluorescence spectroscopy is feasible.

5.4.2. Materials and methods

Enzyme. Prior to each experiment, fresh aqueous enzyme solutions of different concentrations were prepared in Tris-HCl buffer (pH 8.0) containing 10 mM of $CaCl_2$, optimum for trypsin activity. The use of $CaCl_2$ helps to prevent the autolysis of the enzyme as well as maintain its optimum activity.

Adsorption of trypsin. Batch adsorption experiment was performed in a 2 mL vial by adding different concentration of CuS nanoparticles into trypsin solution. For interaction studies, these vials were stirred in a temperature controlled end-over rotor in each case. The whole adsorption experiment was performed at pH 8.0 (with Tris-HCl buffer) as trypsin posses its optimum activity at this pH. Adsorption kinetics was studied by withdrawing the samples at regular interval and subsequent centrifugation to obtain suitable aliquots for analysis of protein concentration. Preliminary studies showed that this period of time is sufficient to ensure steady state. The amount of adsorbed enzyme (Γ_{trp}, mg m^{-2}) on nanoparticle surface was calculated from initial (C_0, mg L^{-1}) (C_e, mg L^{-1}) and final enzyme concentration and specific surface area (m^2 g^{-1}) of CuS nanoparticles. Once the steady state was reached, the enzyme bound nanoparticles were separated from unbound enzymes in solutions by centrifugation at 15000 rpm for 15 min. The initial and final protein concentration of individual trypsin was determined by Bradford assay procedure measuring at 595 nm. Binding stoichiometry and isotherm experiments were performed with different ratio of enzyme concentration and available surface area in terms of nanoparticle concentration. Isotherm analysis was done from the lower to higher surface coverage of trypsin and subsequent fitting of different isotherm models. The thermodynamic aspects of adsorption of protein adsorption have also been analyzed in a wide temperature range from 25°C to 50°C.

Fluorescence spectra for tertiary structure. The tertiary structure of trypsin in solution and in different adsorbed state was measured using tryptophan fluorescence emission technique in a steady-state spectrofluorimeter. Typically, the fluorescence spectra of adsorbed trypsin in function of time, concentration, temperature and surface coverage was measured to analysis the tertiary structure at different interaction level. Steady-state anisotropy measurement was also performed in all the cases. Time-resolved intensity decays of the proteins in different state were measured. The sample was excited by Pico-quant 290 nm laser source, and the decay was measured in a time scale of 0.0488 ns/channel. The decay curves were analyzed by FAST software using the discrete exponential method, and the mean lifetime (τ_m) of trypsin in different experimental conditions was also calculated.

Fourier transform infrared spectra. FT-IR spectra of lyophilized trypsin samples of native and in different adsorbed state were taken. All the spectra of lyophilized samples were measured with 1 mg samples in 200 mg of KBr as a pellet on the range of 2500−500 cm^{-1}. After background correction, Fourier self-deconvolution (FSD) was applied to the unsmoothed spectra for band narrowing (full width half-maxima, fwhm = 16 cm^{-1} and enhancement factor, k = 2.0).[5.17] Gaussian curve-fitting was then performed using GRAMS/AI software (Thermo Fisher Scientific, Massachusetts) on the Fourier self-deconvoluted amide I band region. The secondary structural content was calculated from the areas of the individual assigned bands and their fraction of the total area in the amide I region. In each case a linear baseline was fitted in addition to the Gaussian bands.

Enzymatic activity of trypsin. The enzymatic activity assay of trypsin in native and in adsorbed state at different surface coverage on CuS nanoparticles and temperature was measured in 50mM tris buffer (pH 8.0). The enzymatic activity of trypsin was measured using BAEE (*N*-α-benzoyl-L-arginin-ethyl ester) as substrate, according to the following reaction (Figure 5.3):[5.18]

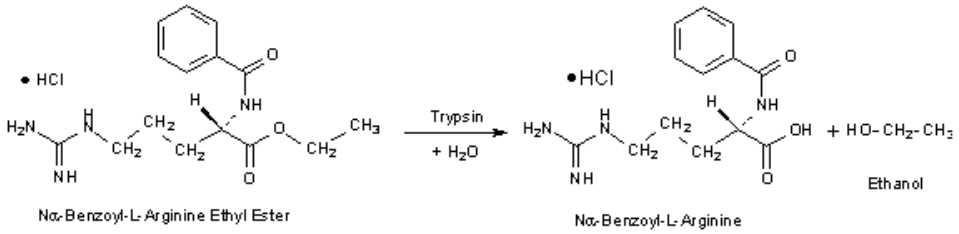

Figure 5.3. Reaction mechanism of trypsin using N-α-benzoyl-L-arginin-ethyl ester (BAEE) as substrate.

The enzymatic activity (U) represents conversion of 1 μmoL of the substrate per minute and the specific activity is defined as the enzymatic activity per mg of the enzyme (U mg^{-}

[1]). However, here the relative activity compared to native enzyme is presented in most of the cases. For the activity tests, BAEE was allowed to interact with free trypsin and CuS nanoparticle immobilized trypsin in a 1 mL vial. The hydrolysis of BAEE was determined spectrophotometrically at 253 nm by monitoring the increase of the reaction product (the esterolysis product is much more absorptive than BAEE at 253 nm) at a regular time interval until saturation reaches. The enzyme substrate mixture was mechanically stirred during the time lags between the spectroscopic measurements. In case of adsorbed trypsin, the enzyme loaded nanoparticles were separated from the solution after specific time interval by centrifugation at 15000 rpm. The absorbance was recorded every 5 min for a period of 30 min. The enzyme kinetic study for free and adsorbed trypsin was performed with 0.2−1.5 mM BAEE solution. Michaelis-Menten model was fitted to get the enzyme kinetic parameters in native and adsorbed state. The specific enzymatic activity of adsorbed trypsin was compared to the activity of trypsin free in solution (for sake of comparison, the samples contained equal amounts of trypsin).

Preliminary treatment of dairy wastewater. Immobilized trypsin molecules were also used to study its efficiency in reducing the total protein content from a dairy wastewater source. Dairy effluent was obtained from Central Dairy, Guwahati, Assam. The dairy effluents were allowed to settle for 12 h. After this simple pretreatment, a centrifugation at 10000 rpm was done to further remove non dissolved contaminants and solids. In a preliminary treatment, the supernatant was taken and incubated with free and immobilized trypsin at room temperature. Samples were collected for determination of total protein content and chemical oxygen demand (COD) initially and after 1 h of incubation with trypsin. Samples treated with nanoparticle immobilized trypsin were centrifuged to separate the nanoparticles prior to analysis. The total protein content was measured by UV-visible spectroscopy by measuring the absorption maxima at ~290 nm (was diluted equally with distilled water where required). A relative comparison in removal of total protein content (%) and COD (%) by immobilized and free trypsin has been presented.

5.4.3. Interaction of trypsin on CuS nanoparticles and time dependent studies

The interaction of trypsin (at pH 8.0) with CuS nanoparticles was studied for broad time duration. Time dependent adsorption behaviour of trypsin is shown in Figure 5.4a. Initially adsorption of trypsin on CuS surface is fast leading to almost steady state conditions after which adsorption capacity was linear and reached steady state within 3 h.

More than ~80% of the final amount of trypsin was adsorbed within first 1 h. The adsorption capacity for trypsin on CuS nanoparticles at steady state was found to be very high ~7 mg m^{-2}. On a 'soft' surface like CuS, binding of proteins may principally govern by electrostatic interactions. Previous studies reported the surface charge analysis (ζ-potential) of different CuS materials.[5.19] It was found that, covellite phase CuS nanomaterials have an isoelectric point (IEP) at pH ~3.0. In the other hand, the IEP of molecular trypsin is around pH ~9.0. Therefore, at pH ~8.0, the CuS surface will be negatively charged and trypsin molecule will be positively charged, which can lead to a strong electrostatic bonding between these two and resulted in high adsorption capacity for trypsin. Moreover, having the 'soft' sulfur group on the CuS surface may facilitate the binding of the particles with side chains of thiol containing amino acid like cysteine and other amino acids of trypsin,[5.20, 5.21] which also supports the high adsorption capacity for trypsin on CuS nanoparticle surface.

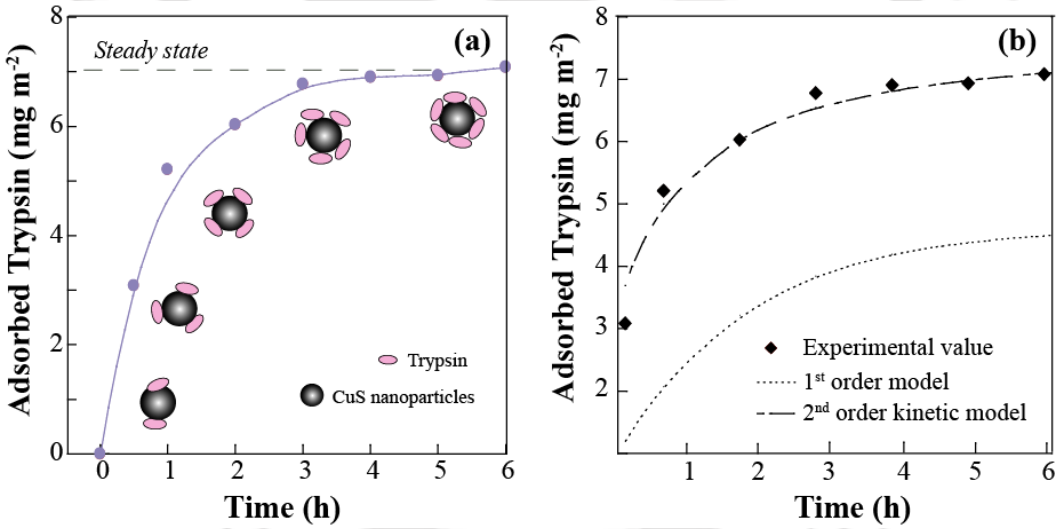

Figure 5.4. (a) Time dependent adsorption of trypsin on CuS nanoparticles and (b) Comparison of first and second order kinetic equation of adsorption.

The kinetics of trypsin adsorption on CuS nanoparticle surface was evaluated by first order and second order model. The linearized graph of first and second order model was plotted and the rate constant values were calculated (Appendix Figure A5.6). However, the adsorption of trypsin on CuS surface seemed to be described better by second order equation. Second order model showed a higher correlation coefficient (R^2) of 0.999 than that of first order model (R^2 = 0.977), which can be attributed to the actual heterogeneous distribution of CuS surface. The first and second order rate constants were 0.593 L min^{-1}

(k_1) and 0.233 g mg^{-1} per minute (k_2) respectively (Appendix, Table A5.1). Moreover, the experimental data were compared together with pseudo first and second order models (Figure 5.4b). The second order model matches well with the experimental data, as the first order model was far underestimated the actual amount of lysozyme adsorbed.

Further, the structural aspects of time dependent interaction of trypsin on CuS surface were analyzed with steady state fluorescence spectroscopy. Emission spectra of native and adsorbed trypsin at different time were taken in the range of 300-450 nm with an excitation wavelength of 295 nm.

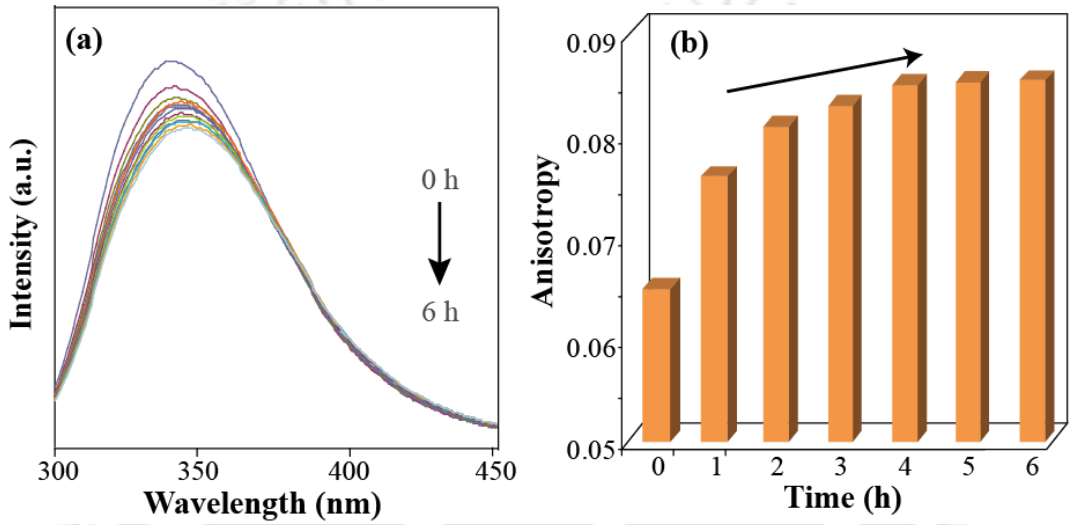

Figure 5.5. (a) Steady state fluorescence spectra and (b) anisotropy values of trypsin adsorbed on CuS nanoparticles in function of time.

Trypsin molecules contain four tryptophans that can be used as intrinsic fluorophores. The emission maximum of native trypsin in solution was observed at ~343 nm which indicates that specific tryptophan(s) of trypsin are partly exposed to the solvent. This observation is consistent with the structure of trypsin.[5.22] Upon binding with CuS surface, the fluorescence intensity of trypsin quenched to some extent with a red shift towards 350 nm. The red shift of the emission maximum suggests that in the adsorbed state, tryptophans are more exposed to the solvent. Decreased fluorescence intensity is relevant to the increased tryptophan quenching. This can be possible if the tertiary structure of trypsin molecule upon binding with CuS surface changes in such a way that the tryptophans occupy positions that are in close proximity of other fluorescence-quenching amino acids. Among different amino acids, cysteine is strong quenchers of tryptophan fluorescence and, therefore, in the native state tryptophans neighboring to cysteine

residues do not significantly contribute to the overall fluorescence emission.[5.23] In trypsin's three dimensional molecular structure, Cys 42 and 22 are located below and above the indol ring of Trp 141 (Appendix, Figure 5.7). Also, Cys 168 and 220 are very close to Trp 215; and Cys 232 is located in the proximity of Trp 237. Only Trp 51 is relatively far from cysteine groups, which can contribute a majority of the fluorescence intensity.[5.24] However, using the tryptophans of trypsin as a probe, the fluorescence spectroscopic data showed that adsorption on CuS surface results in partial conformational changes as the emission spectra quenched a little. However, the quenching of the intensity reduces gradually with time and almost constant once steady state reaches. This indicates that trypsin molecules undergo partial loss of tertiary structure and not totally denatured upon initial binding on nanoparticle surface, which remain constant after reaching steady state. Therefore, extensive molecular rearrangements of the protein are not likely to be the major driving force for the strong adsorption of trypsin at the solid/liquid interface, because structural analysis of trypsin adsorbed on CuS surface did not show dramatic conformational changes in the protein. The displacement of trypsin molecule from CuS surface (after reaching steady state), has also been studied by re-dispersing the enzyme loaded nanoparticles into a buffer solution containing no protein molecules. A time dependent study has been performed to check any displacement of the adsorbed enzyme back into the solution up to 1 h. From the analysis it was confirmed that no displacement of the enzyme occurs from the surface once it reaches steady state, possibly due to the strong binding interaction between 'soft' sulfur group and the amino acid side chains of trypsin.

The fluorescence anisotropy of trypsin binding on CuS surface in function of time has also been measured (Figure 5.5b). The anisotropy value of native trypsin in solution was found 0.064 which increases up to 0.085 upon binding on CuS surface. Increase in anisotropy values indicates an increased rigidity in the surrounding environment of the fluorophores upon binding on CuS surface. The increased anisotropy value can be attributed to the imposed motional restriction on the different fluorophores of trypsin, due to the adsorption. However, the anisotropy values remain almost constant after reaching steady state, which indicates no further alteration in three dimensional structures, an observation similar to previous emission spectroscopic analysis.

5.4.4. Influence of CuS nanoparticle concentration and binding stoichiometry

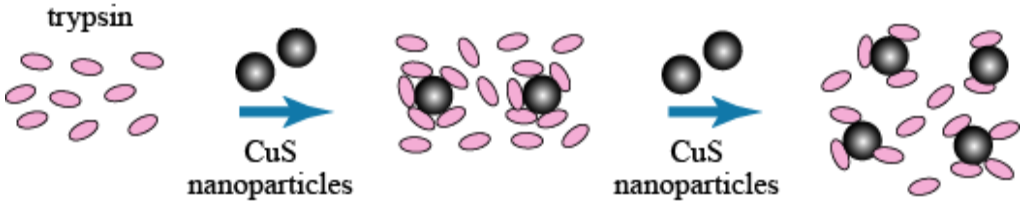

Scheme 5.3. Interaction of trypsin at different concentration of CuS nanoparticles

The influence of CuS nanoparticles in terms of its concentration on enzyme nanoparticle interaction was studied with a broad molar ratio of CuS to trypsin. An increasing amount of CuS nanoparticles (0.2 – 1.0 mg mL^{-1}) was added in a fixed amount of trypsin solution (0.5 mg mL^{-1}) (Scheme 5.3). The adsorption capacity of trypsin (Γ_{trp}) decreases from ~34.2 mg m^{-2} to ~7.7 mg m^{-2} with the increase in CuS concentration (Figure 5.6a), though the total adsorption efficiency increases. The binding stoichiometry of trypsin with CuS nanoparticles was also determined from the molar ratio of CuS to trypsin concentration, using Job's plot. The breakpoint of the plot gives the corresponding mole fraction which indicates the binding stoichiometry.[3,56] The binding isotherm plot (Figure 5.6b) of trypsin shows a breakpoint at the molar ratio of 0.47 of CuS to trypsin. This indicates a binding stoichiometry of 0.47 for CuS nanoparticles with trypsin in the solution.

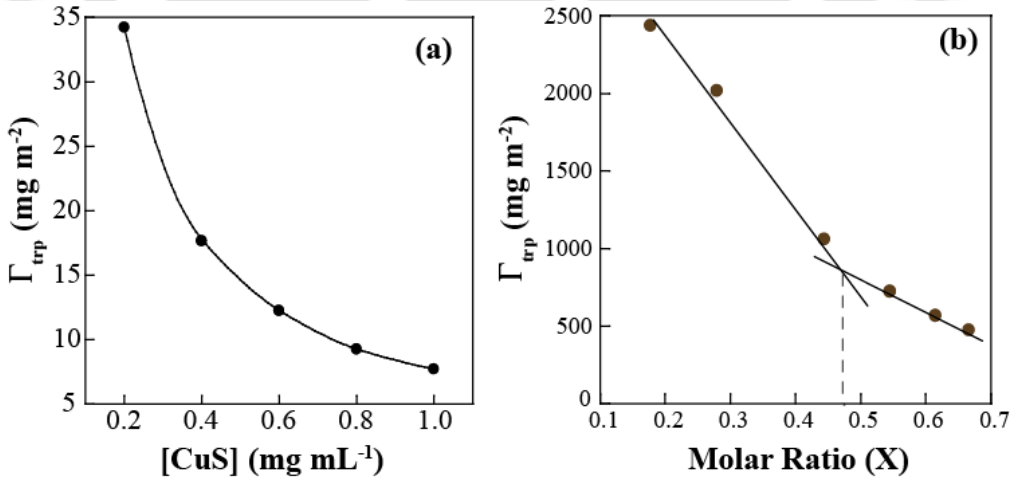

Figure 5.6. (a) Influence of CuS concentration on adsorption capacity of trypsin and (b) Jobs plot to determine the binding stoichiometry of trypsin and CuS nanoparticles. The molar ratio (X) calculated from the relation, X = [CuS] / [[CuS] + [trypsin]].

Moreover, the influence of CuS addition in increasing concentration on trypsin tertiary structure was also studied by steady state fluorescence spectroscopy. With the increase in

CuS concentration, the fluorescence intensity quenches with a slight red shift (Figure 5.7a). This indicates a partial unfolding of trypsin tertiary structure upon increasing concentration of CuS, as described previously. However, the intensity of quenching is comparatively higher at higher CuS concentration than previous case.

To get insight of CuS-trypsin interaction, the fluorescence lifetime of trypsin was measured upon addition of increasing concentration of CuS in the solution. The time-resolved decay of trypsin at different experimental conditions was taken at a emission wavelength of 345 nm. The data fitted well with the sums of two exponential decays with a χ^2 value close to 1.00. The decay profile of trypsin was different from native solution upon continuous addition of CuS nanoparticles (Figure 4.6). The individual lifetime values (τ_1 and τ_2) and amplitudes (α_1 and α_2) were calculated from the bi-exponential fit and are given in Table 5.1.[5.25] Initially there is small decrease in the τ_1 and τ_2 value of the fluorophore upon addition of CuS nanoparticles (up to 1 μg mL^{-1}), which further decreases rapidly with the increase in CuS concentration (~5 μg mL^{-1}). The mean lifetime (τ_m) was calculated and is given in Table 5.1. The mean fluorescent lifetime values clearly show the lifetime of trypsin reduces slightly in presence of less CuS but further reduces rapidly with increasing CuS concentration. The reduced mean lifetime (τ_m) is due to the alteration of polarity of the environment surrounding the fluorophores, which indicates partial unfolding and exposure of the fluorophore to the aqueous solvent upon binding on CuS nanoparticle surface.

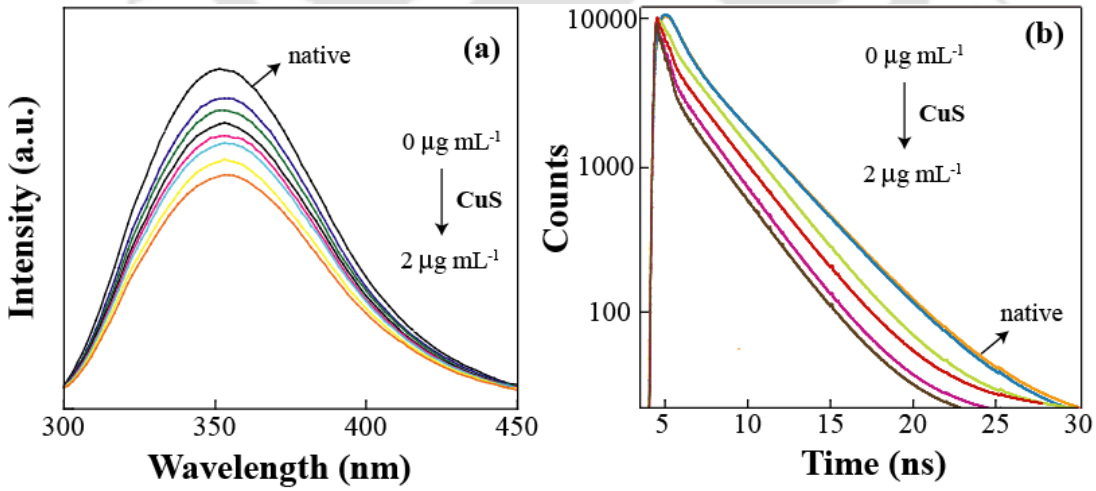

Figure 5.7. (a) Quenching of fluorescence intensity and (b) reduced lifetime of trypsin with increasing CuS nanoparticle concentration.

Table 5.1. Time-resolved fluorescence spectroscopic parameters of trypsin interacting with increasing concentration of CuS nanoparticles.

[CuS] ($\mu g\ mL^{-1}$)	λ_{em} *(nm)*	τ_1 *(ns)*	τ_2 *(ns)*	α_1	α_2	τ_m *(ns)*	χ^2
0 (native)		0.721	5.66	0.019	0.015	1.96	1.000
1	345	0.610	3.48	0.022	0.015	1.77	1.000
3		0.080	3.02	0.118	0.014	0.39	1.000
5		0.028	2.93	0.375	0.011	0.11	1.000

5.4.5. Surface coverage dependent structure and activity of immobilized trypsin

Adsorption isotherm studies at different surface coverage of trypsin on CuS surface was performed by adding a fix amount of CuS (1 mg mL^{-1}) to different concentration of trypsin (0.1 – 1.0 mg mL^{-1}) at pH 8.0 in room temperature. The steady state adsorption isotherm with increasing initial trypsin concentration on CuS surface is shown in Figure 5.8. The initial slope in the isotherm plot indicates high affinity of trypsin for CuS surface, which approaches a plateau indicating the steady state surface coverage of trypsin. Using the molecular dimensions of trypsin the maximum theoretical surface concentration could be calculated. On the basis of crystallographic information (Protein Data Bank entry 2PTN) (Appendix, Figure A5.7),[5.22] the conformation of the native trypsin molecule can be approximated as an ellipsoid with dimensions of 4.8 nm × 3.7 nm × 3.2 nm. Considering that the enzyme molecules are surrounded by a hydration layer of approximately 0.2 nm and that they adsorb in a *side-on* configuration, a tightly packed monolayer would contain about ~3.2 mg m^{-2} of unperturbed trypsin molecules. The initial steady state surface coverage (Γ_{trp}) on CuS with lower trypsin concentration was ~1-2 mg m^{-2} which is in line with the consideration of *side-on* monolayer coverage. However, with the increase of initial trypsin concentration, the steady state surface coverage approaching

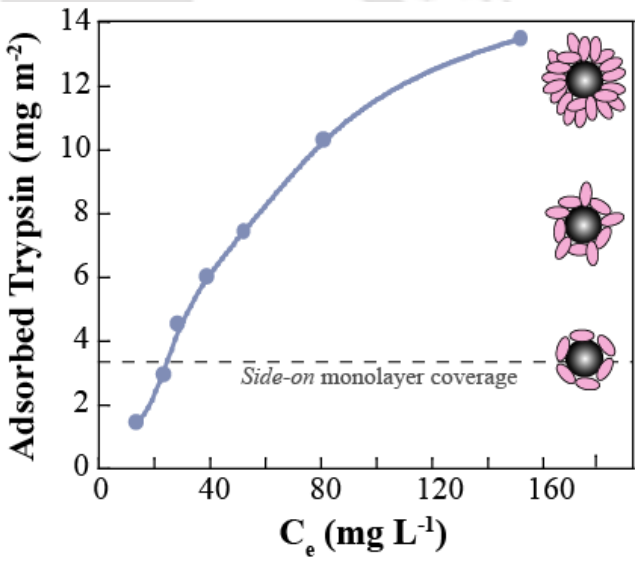

Figure 5.8. Steady state surface coverage of trypsin on CuS nanoparticles at different initial trypsin concentration.

plateau state and was found to be ~15 mg m^{-2}, which is significantly higher than the calculated *side-on* monolayer value. This indicates a tight packed crowding of trypsin molecule on the CuS nanoparticle surface. Further, the steady state adsorption isotherm of trypsin on CuS surface has been analyzed with Langmuir and Freundlich isotherm models. Langmuir model showed a good agreement with the experimental data compared to Freundlich model (Appendix, Figure A5.8). This indicates a monolayer coverage of trypsin on CuS surface at higher concentration. The constant values of both the isotherms were calculated from the linearized plots (Appendix, Table A5.2). The maximum calculated adsorption capacity ($\Gamma_{trp,m}$) of trypsin on CuS surface was found ~41.6 mg m^{-2} (from Langmuir model), which is quite high than the *side-on* monolayer coverage. This also supports the crowding of monolayer trypsin molecules on nanoparticle surface at higher concentration, which may lead to spatial restriction of the adsorbed enzymes. Moreover, the favouribility of Langmuir model was analyzed with a 'constant separation factor' or 'equilibrium parameter', R_L,[5.26] was also calculated. The value of R_L was found 0.86 which is consistent with the favorability of the adsorption process (for a favorable process $0 < R_L < 1$).

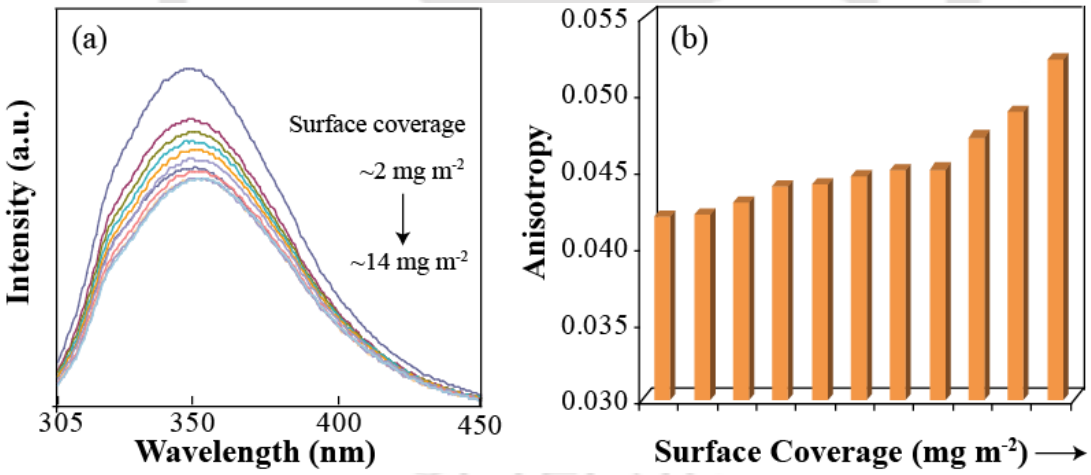

Figure 5.9. (a) Steady state fluorescence spectra and (b) anisotropy values of adsorbed trypsin at different surface coverage on CuS nanoparticles.

The tertiary structure of adsorbed trypsin at different surface coverage was also analyzed by fluorescence emission spectroscopy. The steady state fluorescence emission spectra of adsorbed trypsin with the increase in surface coverage are shown in Figure 5.9a. It was found that, the emission intensity of the adsorbed trypsin quenched further with the increase in surface coverage. The previous discussion of surface coverage dependent

spatial restriction can be useful to explain this result. As the crowding of enzyme on the surface increases, the adsorption sites become less available. This resulted in a perturbed tertiary structure of adsorbed trypsin that the enzyme adapted to get on the nanoparticle surface. However, the loss of tertiary structure upon increasing surface coverage is partial and very less at low surface coverage, as the emission intensity did not quenched totally. Moreover, the increased motional restriction o trypsin at higher surface coverage also confirmed from anisotropy values (Figure 5.9b). The anisotropy values of adsorbed trypsin increases with the increase in the surface coverage, which also supported the above description.

Surface coverage dependent enzymatic activity. The structure-function relationship of enzymes at interface is a very important parameter which determines a variety of processes. In this regard, the enzymatic activity of surface bound trypsin was measured using BAEE as substrate. BAEE hydrolysis activity of adsorbed trypsin at different surface coverage was determined and compared (% of retention) with the native enzyme activity. The specific activity of native trypsin was set to 100% and the relative activity of surface bound trypsin was compared and calculated (%). It was found that adsorbed trypsin at low surface coverage retains high enzymatic activity and reduces with higher surface coverage (Figure 5.10).

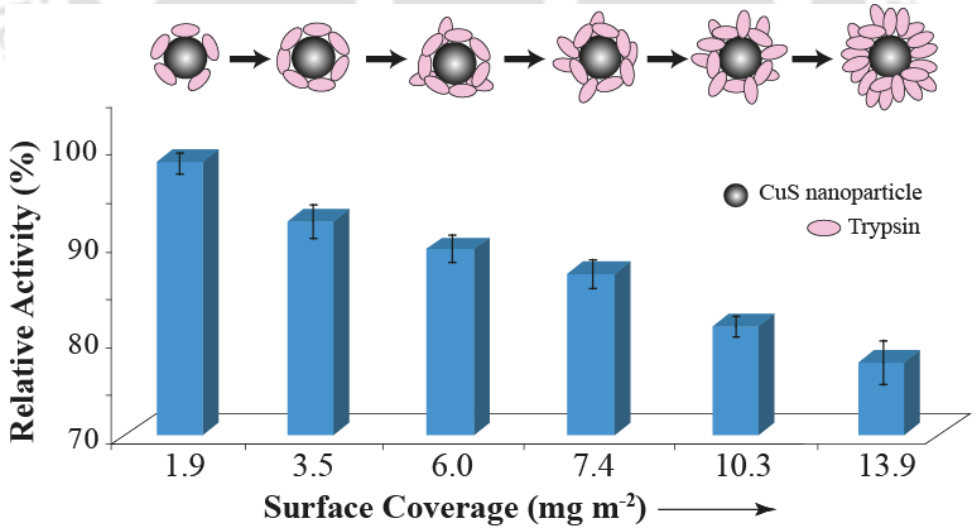

Figure 5.10. Surface coverage dependent enzymatic activity of trypsin using BAEE as substrate.

At a surface coverage of ~2 mg m^{-2} almost ~99% of the activity was retained by adsorbed trypsin (Table 5.2). At low surface coverage (~2 mg m^{-2}), enzyme molecules remains unperturbed with a small loss in tertiary structure as observed from previous fluorescence

spectroscopic results. This might help in retaining its activity almost upto ~98%. Upon increasing the surface coverage of trypsin, the crowding increases which resulted in more loss of tertiary structure of adsorbed proteins, as found from the previous results. Despite of a spatial restriction to accommodate on CuS surface at such higher monolayer coverage (~14 mg m^{-2}), the protein molecules do adsorb by adjusting more its conformation, due to strong binding affinity towards the CuS surface. This greater loss of protein conformation is directly proportional to activity of adsorbed enzyme. From results, it was found that trypsin activity reduced to ~77% at a higher surface coverage of ~14 mg m^{-2}. Therefore, a relationship between, the structure-functional aspect of protein-nanoparticle interaction could be obtained where the activity on the adsorbed enzyme could be controlled by controlling the enzyme concentration which in turn control the surface coverage.

Table 5.2. Enzymatic activity values of adsorbed trypsin on CuS nanoparticles at different surface coverage

Surface Coverage of trypsin (mg m^{-2})	*Retention of Enzymatic activity (%)*
1.9	98.3
3.5	92.1
6.0	89.2
7.4	86.7
10.3	81.3
14.0	77.5

5.4.6. FT-IR spectra for trypsin secondary structure

The FT-IR spectra of lyophilized trypsin in native and adsorbed at different surface coverage (on CuS nanoparticles) were taken from 4000 to 500 cm^{-1}. The 1700−1600 cm^{-1} region (amide I) band is mainly due to the C═O stretching and N−H bending vibration. The band at ~1540−1500 cm^{-1} corresponds to amide II, representing mainly the C−N stretch vibration.[5.27, 5.28] Although there were no significant peaks of only CuS at amide region of protein spectra, the IR spectrum of trypsin adsorbed onto CuS surface was analyzed after subtracting the CuS spectrum. Further, the individual secondary structural elements of adsorbed trypsin at different surface coverage were quantified by Gaussian deconvolution analysis of the amide I region (1700−1600 cm^{-1}) of the FT-IR spectra (Appendix, Figure A5.9).[5.17, 5.29, 5.30] The Gaussian distribution peak at 1654 ± 2 cm^{-1} was assigned to α-helix, bands at 1686 ± 1, 1644 ± 1, 1628 ± 1 and 1625 ± 1

cm^{-1} were assigned to β-sheet, and all other peaks were assigned to unordered structural elements which included β-turns, random coils, and extended chains.[5.31] The Gaussian analysis depicts that native trypsin has an α-helix content of ~11.3%, β-sheet of ~34.2% (rest ~54.5%was unordered elements) (Table 5.3). Similar results on secondary structural content of trypsin also reported previously.[5.32] From the results it was found that, upon adsorption on 'soft' CuS nanoparticles, the trypsin molecule almost retain its secondary structure, which is quite different compared to previous studies with 'hard' malachite nanoparticle surface. At lower surface coverage (~2 mg m^{-2}) almost all the secondary structural element was retained (Table 5.3). However, at higher surface coverage on CuS surface, only a small loss of helical structure of adsorbed trypsin was observed. A considerable amount of ~1-2% of α-helical content of native enzyme was decreased at higher surface coverage of ~14 mg m^{-2}. This is mainly the surface crowding of trypsin on nanoparticle surface which resulted in loss of structure and function of the enzyme.

Table 5.3. Secondary structural content (%) of trypsin in native and different adsorbed state.

	Native Trypsin	Surface coverage of adsorbed trypsin (mg m^{-2})				
		2.0	3.8	6.0	10.3	14.0
α-helix (%)	~11.3	~11.2	~11.0	~10.7	~10.1	~9.6
β-sheet (%)	~34.2	~31.8	~30.8	~32.3	~31.9	~33.1
Unorder (%)	~54.5	~58.5	~58.2	~57.0	~57.8	~57.3

5.4.7. Temperature dependent interaction and activity of immobilized trypsin

The protein-nanoparticle interaction was also studied at different temperature range of 10°C to 40°C and the thermodynamics aspect as well as the structure-functional features has been studied. The surface coverage of trypsin was high at low temperature, and decreases from ~30 mg m^{-2} at 10°C to ~14 mg m^{-2} with the increase in temperature to 40°C. The decrease in surface coverage at higher temperature indicates the adsorption process is exothermic in nature. The standard Gibb's free energy (ΔG^o) of trypsin adsorption on CuS surface was also calculated. The standard Gibb's free energy (ΔG^o) values were found to be negative in the whole temperature range which indicates the favouribility of this process (Table 5.4). The negative value of ΔG^o at the whole temperature range for adsorption of trypsin indicates that adsorption process is spontaneous and thermodynamically favourable. Moreover, the standard average enthalpy change (ΔH^o) and entropy change (ΔS^o) can be calculated from the Van't Hoff equation.

A linearized plot between ln(K_c) and 1/T was used to calculate the values of ΔH^o and ΔS^o (Appendix, Figure A5.10). The average change in entropy (ΔS^o) for trypsin adsorption was found to be -137.1 J K^{-1} mol^{-1}. The negative value of ΔH^o (-56 KJ mol^{-1}) also supports the exothermic nature of the adsorption process. Therefore, the adsorption of trypsin on CuS surface was found to be thermodynamically favourable and exothermic in nature in this temperature range at pH 8.0.

Table 5.4. Thermodynamic parameters of trypsin adsorption on CuS nanoparticles.

Temp (^oC)	*ΔG (KJ mol^{-1})*	*ΔS (J K^{-1} mol^{-1})*	*ΔH (KJ mol^{-1})*
10	-16.9		
25	-15.7	-137.1	-56
40	-12.7		

The structural features of native and adsorbed trypsin were at a temperature range of 25°C to 50°C under a continuous mode. In case of adsorbed trypsin, a lower surface coverage (~3 mg m^{-2}) was taken for temperature dependent studies. The emission spectra of native and adsorbed trypsin under a continuous increase of temperature are shown in Figure 5.11. In both the cases, the emission spectra quenched with a red shift with the increase in temperature, which indicates a partial unfolding of both native and adsorbed trypsin molecules at higher temperature. Importantly, the similar quenching of emission spectra of adsorbed trypsin (compared to native trypsin) indicates that, initially on CuS surface the enzyme molecules does not become denatured, rather acquires a partially unfolded molten-globule state, which undergoes further unfolding as temperature rises.

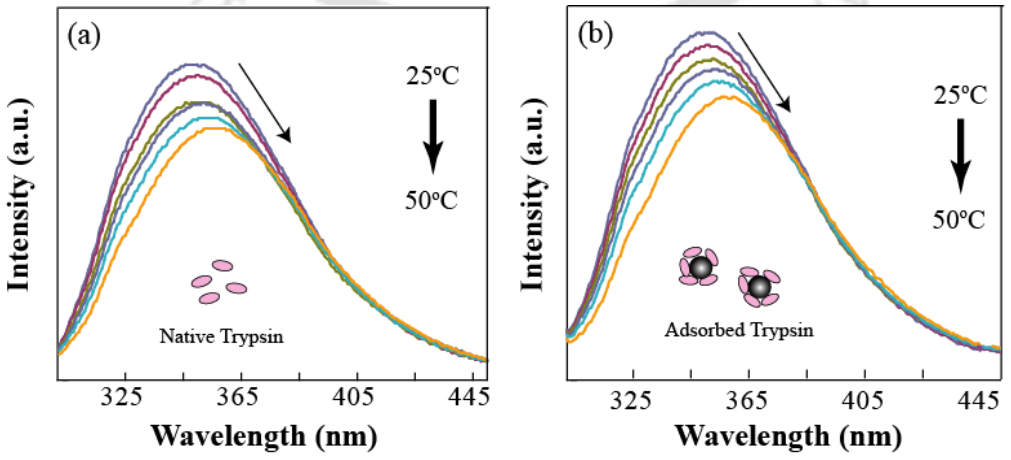

Figure 5.11. Steady state fluorescence emission spectra of (a) native and (b) adsorbed trypsin on CuS nanoparticles.

Moreover, the anisotropy values of native and adsorbed trypsin also reflects the similar situation. Here, unlike the previous anisotropy results, the anisotropy values decrease with the increase in temperature (Figure 5.12a). The decrease in anisotropy values at higher temperature is originated from the higher unfolding of proteins, which is also supported by the literature.[5.33] However, for both native and adsorbed trypsin, similar decrease in anisotropy values indicates the retention of most of its tertiary structure at room temperature (25°C) as described previously.

The activity of adsorbed trypsin was also measured at different temperature. The adsorbed trypsin molecules having low surface coverage on the surface has been taken for temperature dependent activity study. It was found that the activity of surface bound enzyme increased with the increasing with the temperature (Figure 5.12b). At low temperature of 10°C, adsorbed trypsin retains only ~40% of its native activity, which increases up to ~90% at high temperature of 40°C. Though the adsorbed trypsin tertiary structure was partially lost at higher temperature, but it seems that the temperature of the system has a dominant influence on trypsin activity.

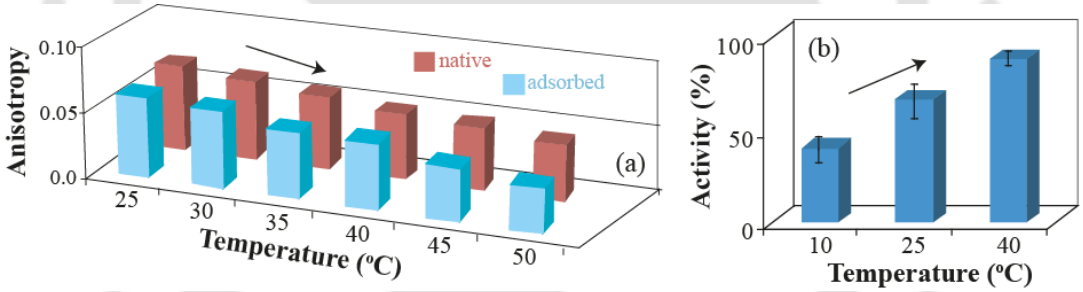

Figure 5.12. (a) Steady state anisotropy values of native and adsorbed trypsin and (b) enzymatic activity of adsorbed trypsin, at different temperature.

5.4.8. Enzyme kinetic analysis

The enzyme kinetics of adsorbed trypsin was performed with lower surface coverage enzymes and compared with native enzyme molecules. The rate of enzymatic activity, v (mg mL^{-1} min^{-1}) is calculated following the Michaelis-Menten kinetics[5.34] given by,

$$v = \frac{v_{\max}.[S]}{K_m + [S]} = \frac{k_{cat}.[E]_T.[S]}{K_m + [S]} \qquad (5.2)$$

Where, [S] is substrate concentration (mg mL^{-1}), v_{max} is the maximum rate attained at infinite concentration of substrate, K_m is the Michaelis-Menten constant. The term v_{max} can be further expressed by k_{cat} and $[E]_T$, which is turn over number and total enzyme concentration used for kinetics study, respectively.

The enzyme kinetic studies was performed with ~150 µg of adsorbed lysozyme per mg of CuS nanoparticles and relatively equal amount of free enzyme was added for sake of comparison in each case. Figure 5.13a shows the Michaelis-Menten plot for the hydrolysis of BAEE by free and adsorbed enzyme at pH 8.0 and 25°C. The values of maximum rate (v_{max}) and Michaelis-Menten constant (K_m) were calculated from a linearized Lineweaver-Burk plot for both free and adsorbed enzyme (Figure 5.13b). The kinetic parameters were calculated and given in Table 5.4.

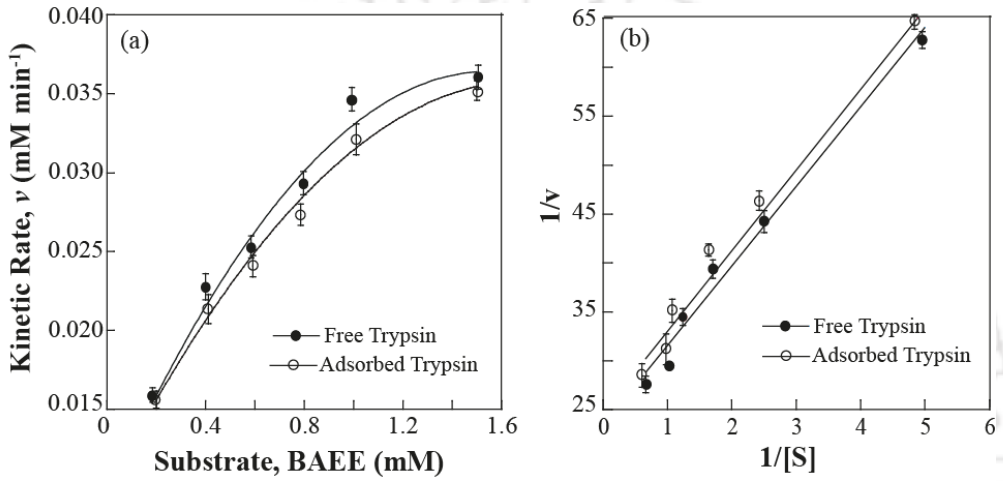

Figure 5.13. (a) Michaelis-Menten plot and (b) Lineweaver-Burk plot of free and adsorbed trypsin on CuS nanoparticles.

Table 5.4. Kinetic constants of enzyme activity study of free and adsorbed trypsin on CuS surface as calculated from Lineweaver-Burk plot.

	v_{max} (mM^{-1} min^{-1})	K_m (mM)
Free trypsin	0.042	0.347
Adsorbed trypsin	0.040	0.329

The maximum velocity (v_{max}) of free lysozyme activity was almost same after adsorption on TMA coated surface (0.042 and 0.04 mM min^{-1} respectively); *i.e.* adsorption of trypsin has a little influence on the release of product (here in terms of hydrolysis of BAEE) in the rate limiting step. The K_m value of trypsin reduces from 0.347 to 0.329 mM after adsorption CuS surface. The decrease in K_m value indicates an enhanced binding affinity of the adsorbed enzyme towards the hydrolysis of BAEE. This can be due to the specific re-orientation of enzyme molecule upon adsorption, which facilitates more specific binding of substrates. Hence, the binding of trypsin has affected the K_m value most, and

has a little effect on the kinetic velocity (v). Therefore, it can be an efficient means of controlling the activity of surface enzyme which significantly included a high adsorption capacity on nanoparticle surface.

5.4.9. Preliminary treatment of dairy wastewater

Dairy wastewater contains a large amount of non-degradable proteins which can be treated with some proteolytic enzymes like trypsin. Herein, the efficiency of adsorbed trypsin molecules in reducing the total protein content from dairy wastewater was investigated and compared with free enzyme. The adsorbed trypsin with a lower surface coverage (~3 mg m^{-2}) has been taken for this set of experiment. The total protein removal efficiency of free and adsorbed enzyme was found to be almost similar. In case of free enzyme ~53% removal was achieved, while with adsorbed enzyme reduction occurs up to ~46%. The initial COD values of wastewater and after treatment by both free and adsorbed trypsin have also been analyzed. However, a similar reduction in COD values with both free and adsorbed trypsin has been achieved. Moreover, the pH of the solution was also increased from ~2.3 to ~4.0 after treatment. These results indicated that, adsorbed trypsin can also perform quite well in treating dairy wastewater compared to the free enzyme. Therefore, the controlled interaction of trypsin with CuS nanoparticles can also be effectively used in practical wastewater treatment with an easy recovery of the surface bound enzyme.

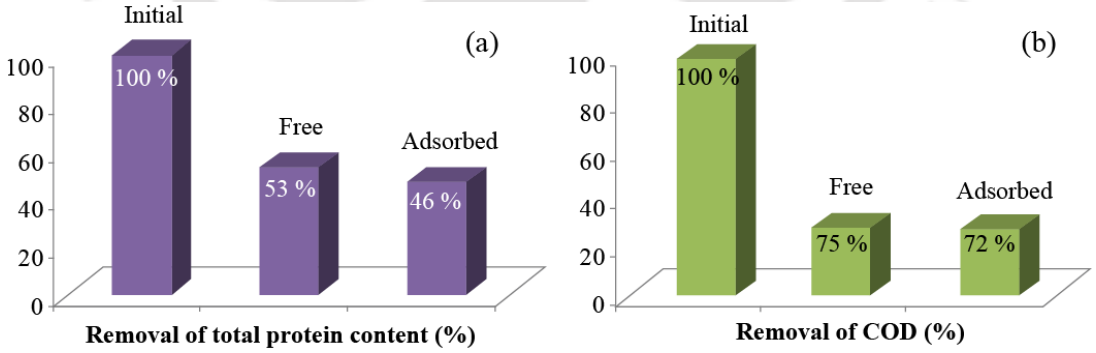

Figure 5.14. Comparative analysis of the removal efficiency (%) of (a) total protein content and (b) COD from dairy wastewater using free and adsorbed trypsin.

5.4.10. Summary

Ultrafine CuS nanoparticles was found to be a suitable tool for immobilization of proteolytic enzyme, trypsin. The 'soft' sulfur group present on the surface can easily bind with the amino acid side chains, which give rise to a high adsorption capacity for trypsin.

In general, the immobilized protein molecule on 'soft' nanoparticle surface was found to comparatively stable than on the 'hard' malachite nanoparticles as observed previously (chapter 4). Although a partial loss in tertiary structure has been observed upon binding on CuS surface. A rise in surface coverage of trypsin results in higher unfolding of enzyme molecule, although the secondary structure of adsorbed enzyme was almost similar. Significantly, a surface coverage dependent enzymatic activity was achieved from the study. At a low surface coverage on nanoparticle surface trypsin almost retains its full enzymatic activity, and with the increase in the surface crowding, activity of enzyme decreases. This finding is significant in terms of enzyme-nanoparticle interaction. Moreover, the surface bound trypsin molecules could be efficiently used in preliminary treatment of dairy wastewater. Adsorbed trypsin (at lower surface coverage) could effectively reduce the total protein content of the dairy wastewater compared to that of free enzyme. Therefore, CuS nanoparticles can be effective tool for immobilization of enzyme where the structure-functional aspect of the adsorbed enzyme can be controlled.

Reference

[5.1] Zhang, W.; Bruda, S.; Landee, C. P.; Parent, J.; Turnbull, M.M. *Inorg. Chim. Acta* 2003, 342, 193.

[5.2] Holmes, K. E.; Kelly, P. K.; Elsegood, M. *Dalton Trans*. 2004, 21, 3488.

[5.3] (a) Nagarathinam, M.; Saravanan, K.; Leong, W. L.; Balaya, P.; Vittal, J. J. Cryst. Growth Des. 2009, 9, 4461. (b) Chen, G.; Deng, B.; Cai, G.; Dong, W.; Zhang, W.; Xu, A. *Cryst. Growth Des.*, 2008, 8, 2137.

[5.4] Chen, Y.; Chen, L.; Wu, L. *Cryst. Growth Des*. 2008, *8*, 2736

[5.5] Godocikova, E.; Balaz, P.; Criado, J. M.; Real, C.; Gock, E. *Thermochim. Acta* 2006, 440, 19.

[5.6] (a) Panyam, J.; Labhasetwar, V. *Adv. Drug Delivery Rev.* 2003, 55, 329. (b) Michalet, X. *Science* 2005, 307, 538

[5.7] Lynch, I.; Dawson, K. A.; Linse, S. *Sci. STKE* 2006, 14.

[5.8] Gray, J. J. *Curr. Opin. Struct. Biol.* 2004, 14, 110

[5.9] Yao, W.-T.; Yu, S.-H. *Adv. Func. Mat.* 2008, 18, 1

[5.10] (a) Isac, L.; Duta, A.; Kriza, A.; Manolache, S.; Nanu, M. *Thin Solid Films* 2007, 515, 5755. (b) Grozdanov, I.; Barlingay, C. K.; Dey, S. K. *Integr. Ferroelectr.* 1995, 6, 205.

[5.11] [(a) Tian, B.; Zheng, X.; Kempa, T. J.; Fang, Y.; Yu, N.; Yu, G.; Huang, J.; Lieber, C. M. *Nature* 2007, 449, 885. (b) Beek, W. J. E.; Wienk, M. M.; Janssen, R. A. J. *Adv. Mater*. 2004, 16, 1009. (c) Chung, J. S.; Sohn, H. J. *J. Power Sources* 2002, 108, 226.

[5.12] Kuchmii, S. Y.; Korzhak, A. V.; Raevskaya, A. E.; Kryukov, A. I. *Theor. Exp. Chem*., 2001, 37, 36

[5.13] Kunita, M. H.; Girotto, E. M.; Radovanovic, E.; Gonc¸alves, M. C. O. P.; Muniz, E. C.; Rubira, A. F. *Appl. Surf. Sci*. 2002, 202, 223

[5.14] Barrett, A. J.; McDonald, J. K. *Mammalian Proteases: A Glossary and Bibliography, Vol. I, Endopeptidases*; Academic Press: London, 1980

[5.15] (a) Cheetham, P. S. J. The application of enzymes in industry. *Handbook of Enzyme Biotechnology*, 3rd ed.; Wisemann, A., Ed.; Ellis Horwood Ltd.: London, 1995; pp. 419-552. (b) Calleri, E.; Temporini, C.; Perani, E.; Stella, C.; Rudaz, S.; Lubda, D.; Mellerio, G.; Veuthey, J. L.; Caccialanza, G.; Massolini, G. *J. Chromatogr. A* 2004, *1045*, 99-109.

[5.16] (a) Nedelkov, D.; Tubbs, K. A.; Nelson, R. W. *Proteomics* 2002, *2*, 441-446. (b) Buckle, P. E.; Davies, R. J.; Kinning, T.; Yeung, D.; Edwards, P. R.; Pollardknight, D.; Lowe, C. R. *Biosens. Bioelectron.* 1993, *8*, 355-363. (c) Wang, C.; Oleschuk, R.; Ouchen, F.; Li, J.; Thibault, P.; Harrison, D. J. *Rapid Commun. Mass Spectrom.* 2000, *14*, 1377-1383.

[5.17] Fu, K.; Griebenow, K.; Hsieh, L.; Klibnov, A. M.; Langer, R. *J. Control. Release* 1999, *58*, 357.

[5.18] Schwert, G. W.; Takenaka, Y. *Biochim. Biophys. Acta* 1995, *16*, 570.

[5.19] Liu, J. C.; Huang, C. P. *Langmuir*, 1992, 8, 1851.

[5.20] Vlies, A. J. van der; O'Neil, C. P.; Hasegawa, U.; Hammond, N.; Hubbell, J. A. *Bioconjugate Chem.*, 2010, 21, 653.

[5.21] Rusmini, F.; Zhong, Z.; Feijen, J. *Biomacromolecules*, 2007, *8*, 1775.

[5.22] Walter, J.; Steigemann, W.; Singh, T. P.; Bartunik, H.; Bode, W.; Huber, R. *Acta Crystallogr. B* 1982, 38, 1462.

[5.23] Cowgill, R. W. *Biochim. Biophys. Acta* 1967, *140*, 37.

[5.24] Koutsopoulos, S.; Patzsch, K.; Bosker, W.T.E; Norde, W.; *Langmuir* 2007, *23*, 2000.

[5.25] Patel, A. B.; Srivastava, S.; Phadke, R. S. *J. Biol. Chem.* 1999, *274*, 21755.

[5.26] Hall, K.R.; Eagleton, L. C.; Acrivos, A.; Vermeulen, T. *Ind. Eng. Chem. Fundamen.*, 1966, *5*, 212.

[5.27] Schwinte, P.; Ball, V.; Szalontai, B.; Haikel, Y.; Voegel, J.C.; Schaaf, P. *Biomacromolecules* 2002, *3*, 1135.

[5.28] Weert, M.V.D.; Haris, P.I.; Hennink, W.E.; Crommelin, D.J.A. *Anal. Biochem.* 2001, *297*, 160.

[5.29] Haris, P.I.; Severcan, F. *J. Mol. Cat. B.* 1999, *7*, 207.

[5.30] Murayama, K.; Tomida, M. *Biochemistry* 2004, *43*, 11526.

[5.31] Griebenow, K.; Klibnov, A. M. *J. Am. Chem. Soc.* 1996, *118*, 11695.

[5.32] Huang, H; Zhao, M. *Eur. Food Res. Technol*. 2008, 227, 361

[5.33] (a) Kernchen, U.; Lipps, G. *Biochemistry*, 2006, 45, 594. (b) Wenz, J. J.; Barrantes, F. J. *Biochemistry*, 2005, 44, 398.

[5.34] Copeland, R. A. *Enzymes-A practical introduction to structure, mechanism and data analysis*, 2nd ed.; Wiley-VCH: New York, 2000.

Appendix

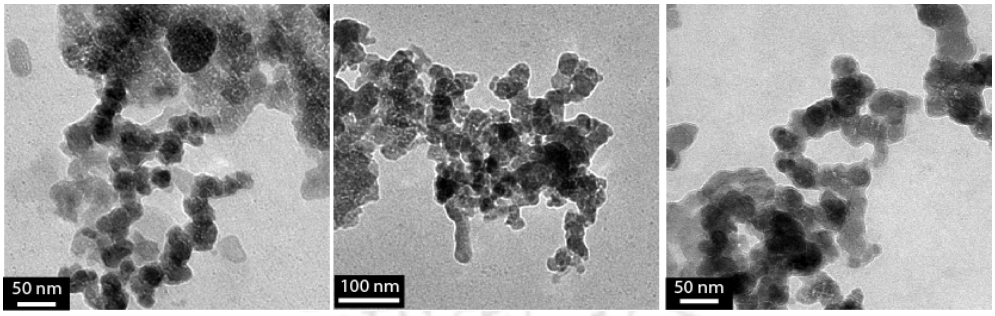

Figure A5.1. Additional TEM images of CuS nanoparticles (20-50 nm).

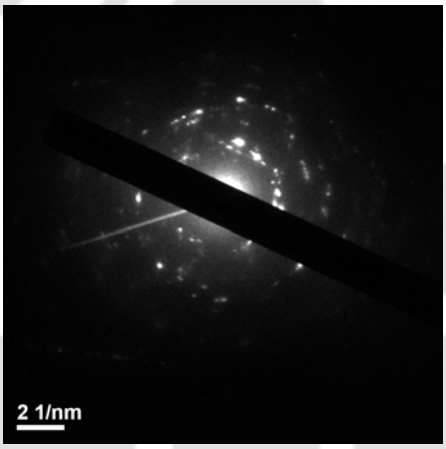

Figure A5.2. Selective area electron diffraction (SAED) of CuS nanoparticles.

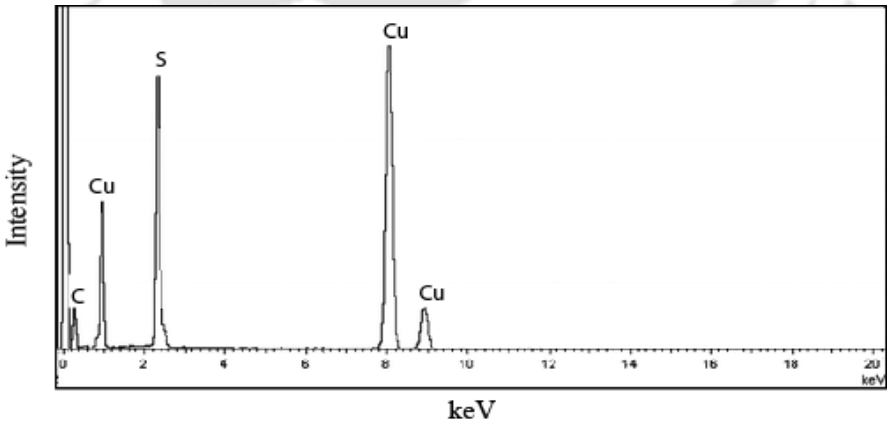

Figure A5.3. EDAX spectra of synthesized CuS nanoparticles, showing the presence of Cu and S.

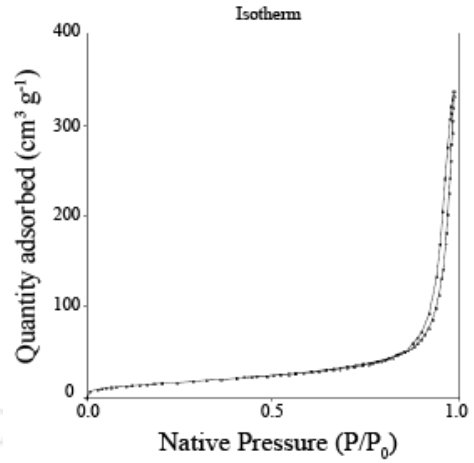

Figure A5.4. N_2 adsorption/desorption isotherms of CuS nanoparticles measured from BET analysis.

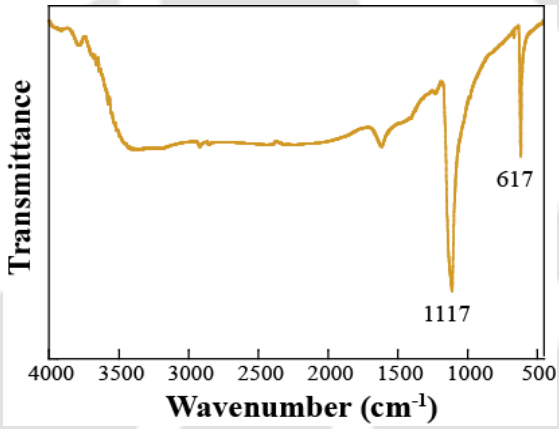

Figure A5.5. FT-IR spectra of CuS nanoparticles taken in the range of 4000-450 cm^{-1}, with a scan number of 20 (scan resolution 4cm^{-1})

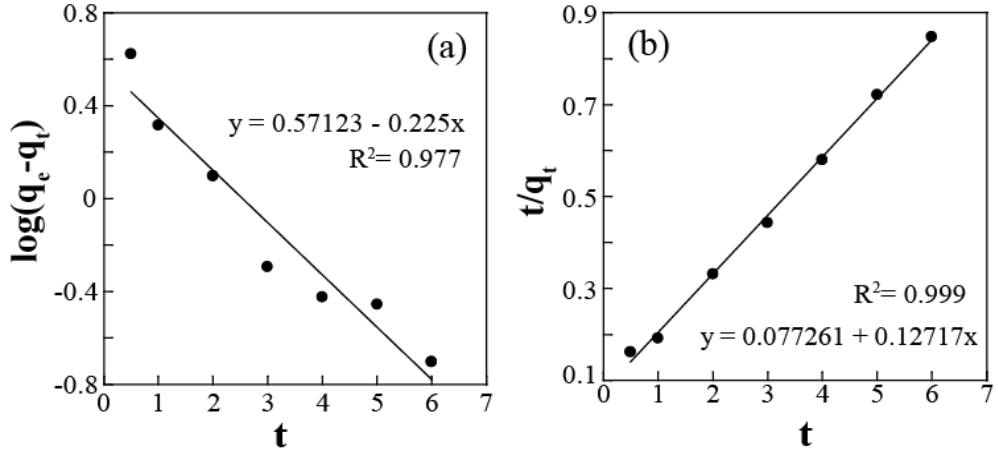

Figure A5.6. Adsorption kinetics of trypsin on CuS nanoparticles analyzed by (a) first order and (b) second order kinetic model.

Table A5.1. Kinetic parameters of trypsin adsorption on CuS nanoparticles

	Experimental q_e *(mg* m^{-2}*)*	**First order kinetics**			**Second order kinetics**		
		Calculated q_e *(mg* m^{-2}*)*	k_1 *(L* h^{-1}*)*	R^2	*Calculated* q_e *(mg* m^{-2}*)*	k_2 *(*m^2 mg^{-1} h^{-1}*)*	R^2
Trypsin	7.28	4.62	0.593	0.977	7.6	0.233	0.999

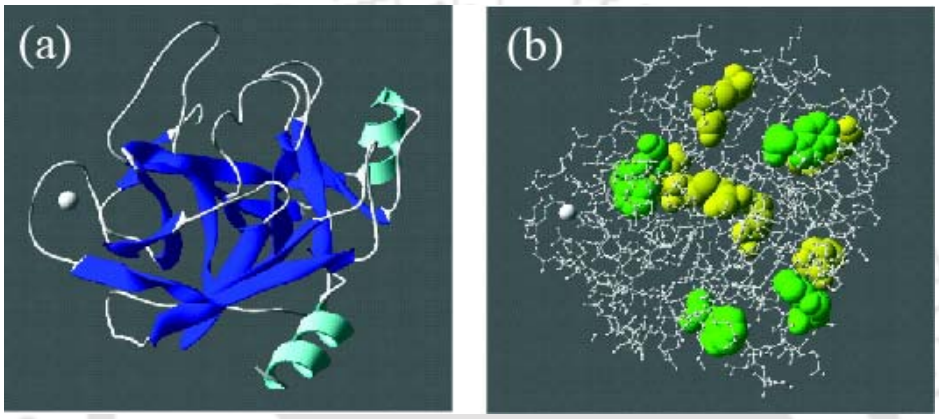

Figure A5.7. Molecular representation of trypsin based on crystallographic data: (a) secondary structural elements and (b) the position of the tryptophans in the three-dimensional structure. Color representation: blue and cyan ribbons denote β-structures and α-helices, respectively; green, yellow, and white balls stand for tryptophan and cysteine residues and the calcium ion, respectively (graphs were generated with Swiss PDB Viewer).

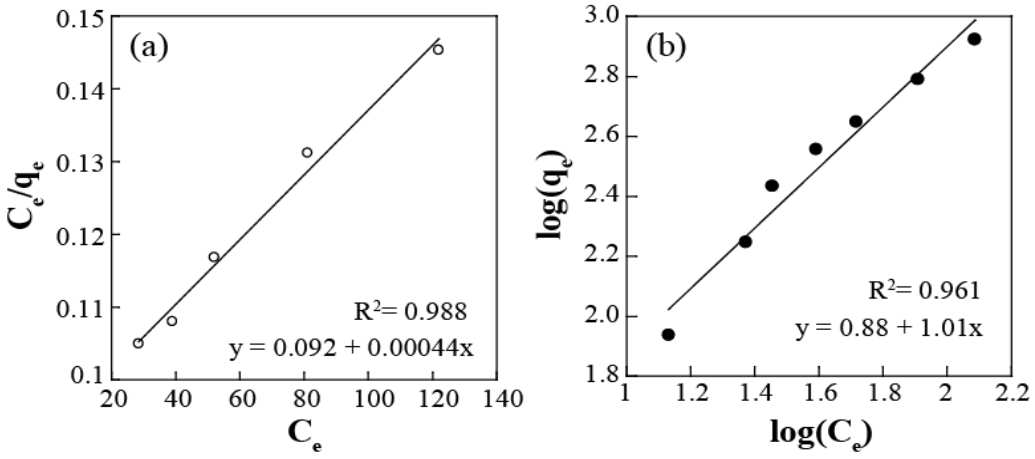

Figure A5.8. Adsorption isotherm of trypsin on CuS nanoparticles analyzed by (a) Langmuir and (b) Freundlich model.

Table A5.2. Isotherm parameters of trypsin adsorption on CuS nanoparticles

	Langmuir isotherm				Freundlich isotherm		
	$\Gamma_{trp,m}$ (mg m^{-2})	b (mL mg^{-1})	R^2	R_L	K_f (mg m^{-2})	n	R^2
Trypsin	41.6	0.0036	0.988	0.86	7.58	0.990	0.961

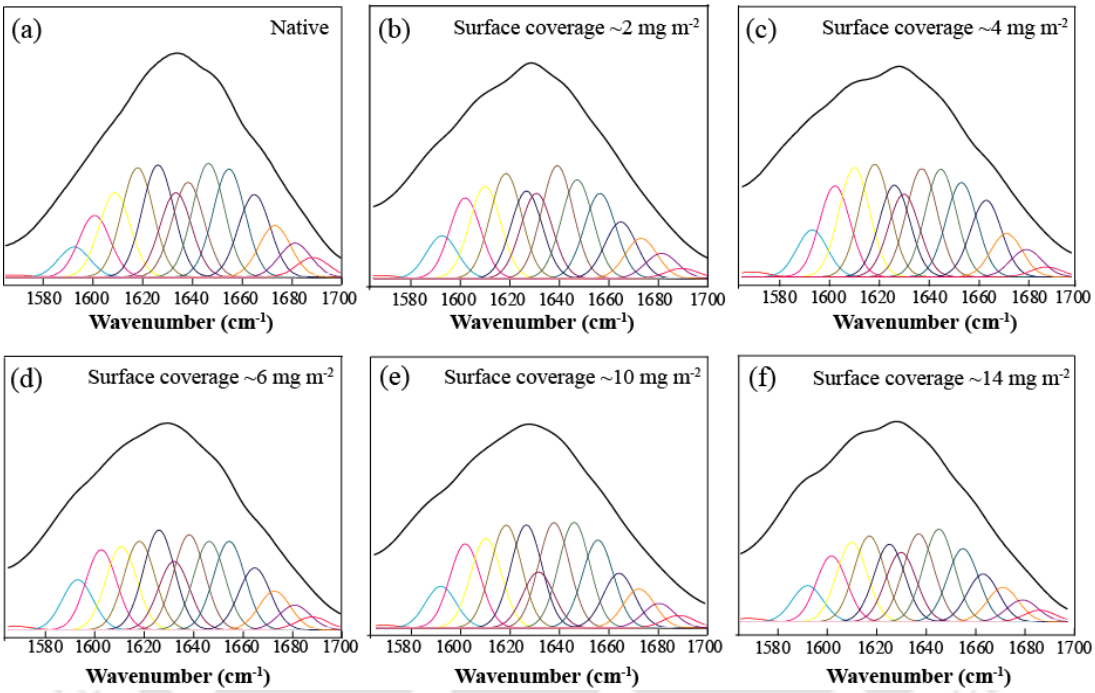

Figure A5.9. Gaussian distribution analysis for secondary structural content of trypsin in (a) native state; and adsorbed on surface CuS nanoparticles at surface coverage of (b) ~2 mg m^{-2}, (c) ~2 mg m^{-2}, (d) ~2 mg m^{-2}, (e) ~2 mg m^{-2}, and (f) ~2 mg m^{-2}.

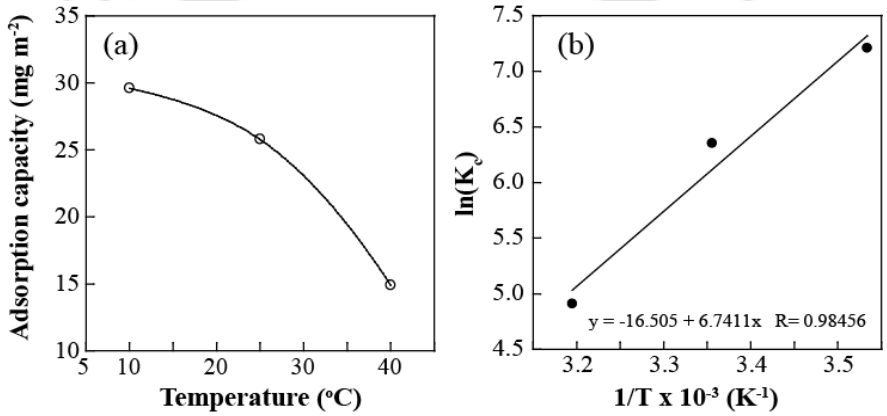

Figure A5.10. (a) Influence of temperature on adsorption capacity and (b) Van't Hoff plot of trypsin molecules adsorbed on CuS nanoparticles

Conclusion and Future Direction

In this thesis, the influence of different tailor-made surface properties on the interaction of different proteins and ionic pollutants at solid-liquid interface has been studied extensively. Different inorganic mineral based micro-to-nano structured materials have been prepared and used for these interaction studies. Significantly, the influence of 'hard' and 'soft' surfaces was found to be different on the interaction of proteins and ionic species. In addition with this, acidic or basic nature of the surface also found to control the interaction of these molecules affectively. Most importantly, an overall control over the interaction pattern of proteins and ionic species has been achieved by controlling the surface properties at micro/nano-scale level and by other parameters like pH, temperature, concentration etc. in each case. This is a major finding of this thesis. Moreover, the surface modification was also found to have a crucial role in controlling the interaction of different molecules.

The acidic 'hard' surface prepared by surface modification of alumina particles with TMA, was found to have a high binding capacity for toxic metal ions (Cu^{2+}, Fe^{3+} etc.) as well as anions like PO_4^{3-}. Moreover, the control interaction of biomolecules on acidic 'hard' surface also reflects a selective binding between two different proteins *viz.* BSA and lysozyme. The selective binding of lysozyme at physiological pH could also be supported with the control on enzyme activity. On a basic 'hard' malachite nanoparticle surface, the molecules were found to be interacting differently than the acidic surface. The adsorption capacity of BSA was found to be much higher and totally pH controlled, compared to acidic surface. Moreover, selective and reversal interaction behaviour of different metal ions has been achieved upon bare and BSA modified malachite nanoparticle surface. On the other hand, on 'soft' CuS nanoparticles, the interaction of protein molecules was found to be highly favourable with a high adsorption capacity. The surface bound enzyme molecules were much stable than previous cases and the structure-functional aspects of adsorbed trypsin could also be controlled. Significantly, the structure and activity of adsorbed enzyme could be controlled by controlling the surface coverage of trypsin on CuS nanoparticle surface.

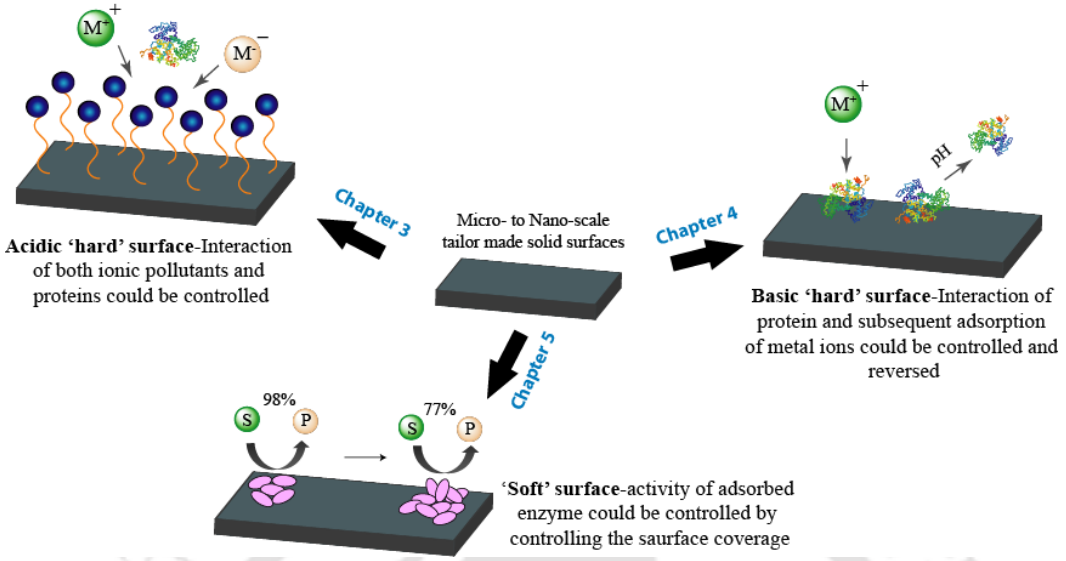

Scheme: A general outline of the present work of this thesis

Therefore, the studies performed in this thesis, reveals the in-sight of protein/ions interaction with tailor specific solid surfaces. The present work also finds several parameters to control the interaction phenomena at interface. The understanding of such interactions in scale-up process can help in construction of biochemical sensors, nanomaterial based drug delivery, biomaterial implants etc. Besides, scaling down to molecular level to understand more of these interactions can help to engineer at molecular level to control such interactions in more specific manner.

List of publication

(1) A rational approach for controlled adsorption of metal ions on covine serum albumin-malachite bionanocomposite. **Bedabrata Saha**, Saswati Chakraborty, Gopal Das, ***J. Phys. Chem. C***, 2010, 114, pp. 9817–9825.

(2) Malachite nanoparticle: a new basic hydrophilic surface for pH-controlled adsorption of bovine serum albumin with a high loading capacity. **Bedabrata Saha**, Gopal Das, ***J. Phys. Chem. C,*** 2009, 113, pp. 15667–15675.

(3) A mechanistic insight into enhanced and selective phosphate adsorption on a coated carboxylated surface. **Bedabrata Saha**, Saswati Chakraborty, Gopal Das, ***J. Colloid Interf. Sci.***, 2009, 331, pp. 21-26.

(4) A comparative metal ion adsorption study by trimesic acid coated alumina: a potent adsorbent. **Bedabrata Saha**, Saswati Chakraborty, Gopal Das, ***J. Colloid Interf. Sci.***, 2008, 323, pp. 26-32.

(5) Trimesic acid coated alumina: an efficient multi-cyclic adsorbent for toxic Cu(II). **Bedabrata Saha**, Saswati Chakraborty, Gopal Das, ***J. Colloid Interf. Sci.***, 2008, 320, pp. 30-39.

(6) Surface-modification-directed controlled adsorption of serum albumin onto magnetite nanocuboids synthesized in a gel-diffusion technique. Ballav M. Borah, **Bedabrata Saha**, Sandeep K. Dey, Gopal Das, ***J. Colloid Interf. Sci.***, 2010, 349, pp. 114-121.

(7) Efficient removal of chromate and arsenate from individual and mixed system by malachite nanoparticles. Jiban Saikia, **Bedabrata Saha**, G. Das, ***J. Hazard. Mater.***, 2011, 186, pp. 575-582.

(8) Selective and enhanced adsorption of different dyes on iron oxide nanoparticles: a comparative study. **Bedabrata Saha**, Sourav Das, Jiban Saikia, Gopal Das, ***J. Phys. Chem. C*** (*Manuscript under Minor Revision*).

(9) Tuning the selectivity of lysozyme adsorption with high retention of enzymatic activity on a charged carboxylated surface. **Bedabrata Saha**, Saswati Chakraborty, Gopal Das, (*Manuscript under Communication*).

(10) Influence of surface crowding on enzymatic activity of trypsin immobilized on ultrafine CuS nanoparticles. **Bedabrata Saha**, Jiban Saikia, Saswati Chakraborty, Gopal Das, (*Manuscript under Communication*).